Efficient Turbulence Modelling for Vortical Flows from Swept Leading Edges

M.Sc. Tony Di Fabbio

Vollständiger Abdruck der bei der
Fakultät für Luft- und Raumfahrttechnik
der Universität der Bundeswehr München
zur Erlangung des akademischen Grades eines

Doktor-Ingenieurs (Dr.-Ing.)

genehmigten Dissertation

Gutachter:
1. Prof. Dr.-Ing. habil. Markus Klein
2. Prof. Dr.-Ing. habil. Suad Jakirlic

Diese Dissertation wurde am 08.04.2024 bei der Universität der Bundeswehr München eingereicht und durch die Fakultät für Luft- und Raumfahrttechnik am 05.08.2024 angenommen. Die mündliche Prüfung fand am 05.08.2024 statt.

Abstract

This doctoral research addresses the complexities of aerodynamic design for high-performance fighter aircraft, focusing particularly on the prediction and analysis of leading-edge vortices in delta-wing configurations. The study stems from the necessity to enhance CFD methodologies for improving the fidelity of aerodynamic simulations, which are crucial for designing and optimizing future combat aircraft. It aims to contribute to the advancement of CFD by providing a more accurate, efficient, and versatile tool for predicting the aerodynamic performance of future fighter aircraft.

The dissertation delineates the theoretical foundations of vortex-dominated flows and the challenges in accurately simulating such phenomena, especially under high angles of attack and transonic flight conditions. Results from CFD simulations are validated against experimental data, employing both Unsteady RANS and scale-resolving simulations to assess the applicability of current CFD methods. The simulations investigate vortex-dominated flow, analyzing the patterns of leading-edge vortices, shock-vortex and vortex-vortex interactions, with a particular emphasis on accurately predicting the breakdown of leading-edge vortices. A theory and explanation for the occurrence of this phenomenon is provided. It elucidates the reasons behind the inaccuracies of RANS simulation predictions and identifies the limitations of the Spalart-Allmaras one-equation turbulence model. Aiming to significantly improve its predictive capabilities regarding vortex formation and breakdown, a straightforward modification to the SA model is proposed, and the enhanced accuracy of the developed model is presented. The model's application to complex aircraft configurations showcases its potential to impact the aerodynamic design process in academic research and industrial practice.

A novel aspect of this research is the integration of machine learning techniques to optimize RANS turbulence models. By employing a CFD-driven machine learning framework, specifically Gene Expression Programming, the dissertation innovates in calibrating and enhancing turbulence models. This approach addresses the specific aerodynamic challenges posed by delta wings and contributes broadly to the field of aerodynamics by offering insights into the fundamental physics governing turbulent flows. The developed one-equation RANS turbulence model represents a significant step forward for understanding and predicting complex vortex flows, with implications extending beyond aerospace engineering to include a wide range of fluid dynamics applications.

Zusammenfassung

Diese Doktorarbeit behandelt die Komplexität des aerodynamischen Entwurfs von Hochleistungs-Kampfflugzeugen. Der Fokus liegt insbesondere auf der Vorhersage und Analyse von Wirbelsystemen an Deltaflügel-Konfigurationen. Es ist notwendig, aktuelle CFD-Methoden zu verbessern und ihre Genauigkeit für aerodynamische Strömungen, welche für den Entwurf und die Optimierung zukünftiger Kampfflugzeuge von entscheidender Bedeutung sind, zu erhöhen. Die Arbeit versucht zur Weiterentwicklung von CFD beizutragen, indem Sie ein genaueres und vielseitigeres Werkzeug für die Vorhersage von aerodynamischen Strömungen bereitstellt.

Die Dissertation beschreibt die theoretischen Grundlagen von wirbeldominierten Strömungen und die Herausforderungen bei der genauen Simulation solcher Phänomene, insbesondere im hoch-Anstellwinkel und transsonischen Flugbereich. Es werden sowohl instationäre RANS, als auch skalenauflösende Simulationen mit experimentellen Daten verglichen, um ihre Anwendbarkeit zu bewerten. Die Simulationen untersuchen im Wesentlichen 3 Phänomene: die Form von Wirbelschleppen, Stöße und Wirbel-Stoß-Interaktionen. Dabei liegt der Schwerpunkt auf der präzisen Vorhersage des Wirbelaufplatzens. Eine neue Theorie erklärt das Auftreten von Wirbel-zerfall an der Flügelvorderkante. In diesem Zuge werden Gründe für Ungenauigkeiten von RANS-Simulationen erläutert und die Grenzen des Spalart-Allamaras Turbulenzmodells aufgezeigt. Anschließend, wird eine einfache Modifikation des Spalart-Allamaras-Modells vorgeschlagen, welche die Aussagekraft in Bezug auf Wirbelbildung und -aufplatzen deutlich verbessert. Die Anwendung dieses modifizierten Modells auf komplexe Flugzeug-Konfigurationen zeigt, dass das Modell das Potenzial hat, den aerodynamischen Entwurfsprozess in der akademischen Forschung und der industriellen Praxis zu verbessern.

Ein neuartiger Aspekt dieser Forschung ist die Integration von maschinellen Lernverfahren zur Optimierung von RANS-Turbulenzmodellen. Durch den Einsatz eines CFD-gesteuerten maschinellen Lernsystems, insbesondere von Gene Expression Programming, bietet die Studie innovative Möglichkeiten zur Kalibrierung und Verbesserung bestehender Turbulenzmodelle. Dieser Ansatz befasst sich mit den spezifischen aerodynamischen Herausforderungen von Deltaflügeln und leistet einen umfassenden Beitrag zur Aerodynamik, indem er Einblicke in die grundlegenden physikalischen Zusammenhänge turbulenter Strömungen bietet. Das entwickelte Ein-Gleichungs-RANS-Turbulenzmodell stellt einen bedeutenden Fortschritt für das Verständnis und die Vorhersage komplexer Wirbelströmungen dar, und hat Auswirkungen, welche über die Luft- und Raumfahrttechnik hinausgehen und ein breites Spektrum von Anwendungen der Strömungsdynamik umfassen.

Acknowledgement

Completing this PhD has been a profound journey, one marked not only by academic and personal dedication but also by the invaluable support I've received along the way. As I reach this moment of accomplishment, I wish to extend my deepest gratitude to those who have made this thesis possible.

First and foremost, I express my sincere appreciation to my advisor, Professor Markus Klein, for his unwavering support, patience, and guidance throughout this challenging process. His expertise and insightful critiques have been instrumental in shaping this research. You have been more than just an academic mentor; you have taught me, inspired me, and instilled in me a level of respect and admiration that I hope to one day earn from my own students, should I become a professor. I also extend my heartfelt thanks to my senior scientific supervisor, Eike, for our enriching discussions, forward-looking insights, and invaluable assistance in refining my English.

My gratitude goes to Professor Suad Jakirlic for agreeing to be part of the thesis committee despite tight deadlines. I am profoundly thankful for the financial support provided by Airbus Defense and Space, which was crucial to my research. Special thanks to Sebastian for trusting in my work and providing this opportunity.

I am indebted to my department and its staff, whose assistance and resources have been indispensable. In particular, I would like to thank Karthick for his friendship and collaborative spirit. Your roles as a man, father, and husband continue to be an inspiration to me. Many thanks also to the Australian team, led by Prof. Richard Sandberg. I appreciate your kindness and support in welcoming and assisting me. A special thank you, of course, goes to Yuan.

On a personal note, I extend my heartfelt thanks to my family, especially my parents and grandparents, for their sacrifices and unwavering belief in me. To Mirko, I apologize for being distant. Now it's time for us to reconnect and find each other again. To Giorgia, your understanding and strength have been my pillars of support. We have faced tough times, and, even though our paths eventually parted, with no small amount of turbulence, this work is also thanks to you.

Lastly, I want to thank my friends, who are more than just friends, for providing much-needed breaks and laughter. A special mention goes to Alessandro, Riccardo, Giuseppe and Simona: thank you for always being there at crucial moments.

This achievement is not mine alone; it belongs to all who have supported me on this journey. As I embark on new and even crazier adventures, I am ready for whatever comes next.

Contents

1 Introduction **1**
1.1 Background and motivation . . . 1
1.1.1 Advancements in fighter aircraft technology . . . 1
1.1.2 Challenges in CFD: complex flow phenomena . . . 4
1.2 Scopes and structure of the thesis . . . 6
1.2.1 Objectives . . . 6
1.2.2 Outline . . . 10

2 Literature Review **13**
2.1 Delta wing flow . . . 13
2.1.1 Leading-edge vortices . . . 13
2.1.2 Vortex development . . . 16
2.1.3 Vortex breakdown . . . 17
2.1.4 Unsteady flow phenomena . . . 19
2.1.5 Transonic vortical flows: compressibility effects . . . 20
2.1.6 Vortex flow experiment . . . 23
2.1.7 Generic delta wing planforms at transonic speeds . . . 25
2.1.8 Vortex interactions . . . 27
2.2 Advancements in CFD: turbulence modeling . . . 28
2.2.1 Previous CFD studies for delta wing flows . . . 28
2.2.2 RANS turbulence modeling: history and improvements . . . 35
2.3 Machine learning . . . 38
2.3.1 Role of evolutionary algorithms in machine learning . . . 38
2.3.2 Introduction to gene expression programming . . . 40
2.3.3 Machine learning applied to turbulence modeling . . . 40

3 Fluid Motion Theory and Turbulence Modeling **43**
3.1 Governing equations . . . 43
3.2 Introduction to turbulence . . . 45
3.2.1 Statistics of the flow . . . 46
3.2.2 Turbulent eddies and energy cascade . . . 47
3.3 Modeling and simulations . . . 49
3.3.1 Direct Numerical Simulation . . . 50
3.3.2 Large Eddy Simulation . . . 51
3.3.3 Reynolds Averaged Navier-Stokes equations . . . 54
3.3.4 Hybrid RANS/LES . . . 58
3.4 Methodology for delta wing flow . . . 59
3.4.1 The Spalart-Allmaras turbulence model . . . 60
3.4.2 Improved Delayed Detached Eddy Simulation . . . 64
3.4.3 The Menter Shear Stress Transport turbulence model . . . 68

3.4.4 Scale Adaptive Simulation 69

4 Software and Numerical Strategy 71
4.1 CFD codes overview 71
4.1.1 The DLR-TAU code 71
4.1.2 OpenFoam 72
4.2 Evolutionary computing 72
4.2.1 Evolutionary algorithms 72
4.2.2 Gene expression programming 77
4.2.3 Training frameworks: CFD-driven method 79
4.2.4 The EVE code 81
4.3 Numerical techniques 82
4.3.1 Finite volume method 82
4.3.2 Overview of the dual mesh approach 84
4.3.3 Conservative form of the governing equations 85
4.3.4 Spatial discretization schemes 86
4.3.5 Time discretization - solution techniques 88

5 Vortex-Dominated Flow over VFE-2 at Transonic Speed 93
5.1 Test case description 94
5.1.1 Mesh characteristics 94
5.1.2 Mesh convergence study 96
5.1.3 Numerical approach 96
5.2 Flow overview: instantaneous flow features 98
5.3 Mean flow features 100
5.3.1 Result validation and shock-wave locations 100
5.3.2 Vortex pattern analysis 103
5.4 Turbulence-related variables 107

6 Investigation of Transonic Aerodynamics on a Triple-Delta Wing in Side-Slip Conditions 111
6.1 Computational domain and numerical approach 112
6.1.1 Analysis of the mesh resolution 113
6.1.2 Mesh convergence study 114
6.1.3 Numerical setup and solution techniques 115
6.2 Vortex development: flow physics analysis 116
6.2.1 Vortex breakdown on the windward wing: $\alpha = 20°$ 116
6.2.2 Vortex breakdown fixed on the windward apex: $\alpha = 24°$ 122
6.2.3 Vortex breakdown on the leeward wing: $\alpha = 28°$ 127
6.3 Aerodynamic characteristic curves 131

7 Towards the Understanding of Vortex Breakdown for Improved RANS Turbulence Modeling 135
7.1 Extension of the Boussinesq assumption 136
7.2 Data comparison: validation of the CFD results 136
7.2.1 Enhancement of the aerodynamic coefficients 137
7.2.2 Investigation of the suction footprint 138
7.3 Vortex breakdown and turbulence modeling 140

7.4 Model impact on turbulence-related quantities . . . 144
7.4.1 Eddy viscosity: turbulence production and destruction . . . 144
7.4.2 Boussinesq assumption and Reynolds stress tensor . . . 147
7.5 Improved one-equation results . . . 151

8 Towards an Enhanced One-Equation Turbulence Model by Gene Expression Programming 155
8.1 Methodology for improved one-equation model . . . 156
8.1.1 Extra-Anisotropic Reynolds Stress Modeling . . . 156
8.1.2 The enhanced one-equation model . . . 157
8.2 NASA validation cases . . . 160
8.2.1 Flat plate . . . 162
8.2.2 Channel flow . . . 163
8.2.3 Wall-mounted hump . . . 164
8.2.4 Axisymmetric subsonic jet . . . 167
8.3 GEP training on the VFE-2 delta wing . . . 169

9 Conclusions and Outlook 175

References 195

Appendix 195

A Implementation-Ready Turbulence Models 197
A.1 Boussinesq Extension Models . . . 197
A.1.1 The PK Model . . . 197
A.1.2 Extra-Anisotropic Reynolds Stress Model . . . 197
A.2 RANS Turbulence Models . . . 198
A.2.1 Spalart-Allmaras . . . 198
A.2.2 Menter $k-\omega$ Shear Stress Transport . . . 200
A.2.3 Spalart-Allmaras with trained Production and Destruction . . . 201
A.2.4 Coupled Spalart-Allmaras . . . 201
A.2.5 Coupled Spalart-Allmaras with trained extra-anisotropy . . . 202
A.3 Hybrid RANS/LES Turbulence Models . . . 202
A.3.1 SA-based Improved Delayed Detached Eddy Simulation . . . 202
A.3.2 $k\omega$-based Scale Adaptive Simulation . . . 204

List of Figures

1.1 Design complexities of modern combat aircraft (inspired by Hitzel et al., 2020). 2
1.2 Insights into delta wing aircraft configurations: Concorde, Eurofighter and Space Shuttle created by OpenAI, 2024. 3
1.3 Visualization of flow around the single-delta wing VFE-2 (left) and the triple-delta wing ADS-NA2-W1 configuration (right). 8

2.1 Subsonic flow field above a delta wing (adapted from Zanin, 2013). . . . 14
2.2 Leading-edge vortex structure, including qualitative distribution of the vorticity, the axial and the tangential velocities (inspired by Nelson and Pelletier, 2003). 14
2.3 Various stages of vortex flow development (inspired by Moioli et al., 2022) 16
2.4 Insights into vortex breakdown (Lambourne and Bryer, 1961). 19
2.5 Categorization of flow behaviors over delta wings (inspired by Miller and Wood, 1984). 22
2.6 Proposed positions and shapes of shock systems over transonic delta wings: embedded cross-flow shock and rear/terminating shock (inspired by Donohoe and Bannink, 1997). 23
2.7 VFE-2 65° delta wing configuration. 24
2.8 ADS-NA2-W1: triple delta wing configuration 27
2.9 Vortex development on double delta wings: influence of leading-edge kink angle, $\Delta\varphi$, and angle of attack, α (inspired by Brennenstuhl and Hummel, 1982). 28

3.1 Turbulent energy spectrum (adapted from Greenshields and Weller, 2022). 49
3.2 Characteristics of the CFD modeling approaches. 51
3.3 RANS models 56
3.4 DES transition scheme (inspired by Spalart, 1997). 65

4.1 Scheme of the different genotype representations with binary (left) and string (right). A single allele is highlighted in green. 74
4.2 Selection schemes. 75
4.3 Tournament selection - The population is divided into m tournaments, each comprising t individuals, with winners granted the opportunity to reproduce. 75
4.4 Evolutionary process in an EA. 76
4.5 Expression tree for the chromosome in Eq. 4.4 78
4.6 Expression tree for the chromosome in Eq. 4.6 79
4.7 CFD-driven training scheme (inspired by Zhao et al., 2020). 80
4.8 EVE framework (inspired by Weatheritt and Sandberg, 2016) 82

4.9 Control volume. 83

5.1 VFE-2 geometry and mesh (Di Fabbio et al., 2023) 94
5.2 Vortex diameter (indicated by an arrow) based on the mean vorticity, IDDES results at $\xi = 0.4$. 94
5.3 Mean hybrid length scale over RANS length scale, and mean LES_{IQ_ν}, IDDES results at $\xi = 0.2, 0.6, 0.95$. 95
5.4 Relative deviation bar plot of the aerodynamic coefficients. "I" denotes the comparison between the IDDES results on the fine and extra-fine mesh (Di Fabbio et al., 2022a). 96
5.5 Time history of the lift coefficient, instantaneous (on the left) and run-time averaged (on the right) (Di Fabbio et al., 2023). 97
5.6 Mean convective CFL number at $\xi = 0.2$, comparison between the IDDES results with the time step size $\Delta t = 10\mu s$ and $\Delta t = 1\mu s$ (Di Fabbio et al., 2022a). 97
5.7 IDDES ($\Delta t = 1\mu s$) results for the VFE-2 geometry with $Ma_\infty = 0.8$, $Re_\infty = 2 \times 10^6$, $\alpha = 20.5°$ (Di Fabbio et al., 2023). 99
5.8 Mean surface coefficient of pressure, comparison between experimental and numerical data. The black contour lines indicate the sonic pressure coefficient $c_p^* = -0.43$ (Di Fabbio et al., 2022a). 101
5.9 Mean surface coefficient of pressure at $\xi = 0.2, 0.4, 0.6, 0.8, 0.95$ and at symmetry plane $\eta = 0$ (lower right), comparison between experimental, URANS and IDDES data (Di Fabbio et al., 2022a). 102
5.10 Mean x-direction vorticity distribution at $\xi = 0.5, 0.6, 0.7, 0.75$, comparison between experimental data (top) and IDDES outcomes (bottom). The black contour lines in the experimental data are related to the divergence of the in-plane velocity vector (Di Fabbio et al., 2022a). 104
5.11 Mean density gradient magnitude, mean normalized x-direction velocity, and mean normalized in-plane tangential velocity distribution, IDDES results at $\xi = 0.5, 0.6, 0.7, 0.8, 0.9$ (Di Fabbio et al., 2023). 105
5.12 Primary vortex core line extracted from the IDDES outcomes (Di Fabbio et al., 2023). 107
5.13 Turbulent viscosity ratio, comparison between URANS and IDDES results. 108
5.14 Resolved turbulence-related quantities along the wing from the IDDES results (note the different scale in the legend boxes). 109

6.1 ADS-NA2-W1 geometry and mesh (Di Fabbio et al., 2024a). 112
6.2 Vortex diameter (indicated by an arrow) based on the mean vorticity, IDDES results at chord-wise location $\xi = 0.55$. 113
6.3 Mean LES_{IQ_ν}, mean cell size over hybrid length scale, and mean hybrid over RANS length scale, IDDES results at $\xi = 0.35, 0.55, 0.75$ (Di Fabbio et al., 2024a). 114
6.4 Absolute deviation bar plots (Di Fabbio et al., 2022d). 115
6.5 Mean convective CFL number, IDDES results at $\xi = 0.35, 0.55, 0.75$. . . 116
6.6 Q-criterion instantaneous iso-surface with flood contour by instantaneous normalized helicity, comparison between SAnegRC-based URANS (left) and SAneg-based IDDES (right) results with $\alpha = 20°$ and $\beta = 5°$. . 117

6.7 Instantaneous x-vorticity and vortex stream-traces, comparison between SAnegRC-based URANS (left) and SAneg-based IDDES (right) results with $\alpha = 20°$ and $\beta = 5°$. 117
6.8 Instantaneous x-pressure gradient iso-surface with flood contour by instantaneous Mach number, comparison between SAnegRC-based URANS (left) and SAneg-based IDDES (right) results with $\alpha = 20°$ and $\beta = 5°$. Vortex stream-traces depicted in red. 119
6.9 Mean surface coefficient of pressure, comparison between experimental data (left), SAnegRC-based URANS (middle) and SAneg-based IDDES (right) results with $\alpha = 20°$ and $\beta = 5°$. Vortex stream-traces depicted in black. 120
6.10 Mean surface coefficient of pressure and mean normalized x-velocity contour plots at chord-wise locations $\xi = 0.35, 0.55, 0.75$, comparison between experimental data, SAnegRC-based URANS and SAneg-based IDDES with $\alpha = 20°$ and $\beta = 5°$. 121
6.11 Q-criterion instantaneous iso-surface with flood contour by instantaneous normalized helicity, comparison between SAnegRC-based URANS (left) and SAneg-based IDDES (right) results with $\alpha = 24°$ and $\beta = 5°$. . 123
6.12 Instantaneous x-vorticity and vortex stream-traces, comparison between SAnegRC-based URANS (left) and SAneg-based IDDES (right) results with $\alpha = 24°$ and $\beta = 5°$. 123
6.13 Instantaneous x-pressure gradient iso-surface with flood contour by instantaneous Mach number, comparison between SAnegRC-based URANS (left) and SAneg-based IDDES (right) results with $\alpha = 24°$ and $\beta = 5°$. Vortex stream-traces depicted in red. 124
6.14 Mean surface coefficient of pressure, comparison between experimental data (left), SAnegRC-based URANS (middle) and SAneg-based IDDES (right) results with $\alpha = 24°$ and $\beta = 5°$. Vortex stream-traces depicted in black. 125
6.15 Mean surface pressure coefficient and normalized mean x-velocity contour plots at chord-wise locations $\xi = 0.35, 0.55, 0.75$, comparison between experimental data, SAnegRC-based URANS and SAneg-based IDDES with $\alpha = 24°$ and $\beta = 5°$. 125
6.16 Q-criterion instantaneous iso-surface with flood contour by instantaneous normalized helicity, comparison between $k\omega$SST-based URANS (left) and SAS (right) results with $\alpha = 28°$ and $\beta = 5°$. 127
6.17 Instantaneous x-vorticity and vortex stream-traces, comparison between $k\omega$SST-based URANS (left) and SAS (right) results with $\alpha = 28°$ and $\beta = 5°$. 128
6.18 Instantaneous x-pressure gradient iso-surface with flood contour by instantaneous Mach number, comparison between $k\omega$SST-based URANS (left) and SAS (right) results with $\alpha = 28°$ and $\beta = 5°$. Vortex stream-traces depicted in red. 129
6.19 Mean surface coefficient of pressure, comparison between experimental data (left), $k\omega$SST-based URANS (middle) and SAS (right) results with $\alpha = 28°$ and $\beta = 5°$. Vortex stream-traces depicted in black. 130

6.20 Mean surface coefficient of pressure and normalized mean x-velocity contour plots at chordwise locations $\xi = 0.35, 0.55, 0.75$, comparison between experimental data, $k\omega$SST-based URANS and SAS with $\alpha = 28°$ and $\beta = 5°$. 130
6.21 Comparison of lift, rolling, and pitching moment coefficients across AoA: experimental versus numerical data at $Ma_\infty = 0.85$, $Re_\infty = 12.53 \times 10^6$, and $\beta = 5°$. 133

7.1 Q-criterion instantaneous iso-surface with flood contour by instantaneous normalized helicity H_n, IDDES results with $\beta = 5°$ and $\alpha = 20°$ (Di Fabbio et al., 2024a). 137
7.2 Comparison between state-of-the-art and PK model, experimental and numerical data with $Ma_\infty = 0.85$, $Re_\infty = 12.53 \times 10^6$ and $\beta = 5°$. Hi-Fi results are represented in red, while standard URANS results are in blue. PK turbulence model in green. One-equation and two-equation results are denoted with circle and star markers, respectively (Di Fabbio et al., 2024a). 138
7.3 Mean surface pressure coefficient, experimental and numerical data at $\beta = 5°$ and $\alpha = 20°$. The black lines show the extracted slice planes (Di Fabbio et al., 2024a). 139
7.4 Mean pressure coefficient profiles at $\xi = 0.35, 0.55, 0.75$, experimental and CFD data at $\beta = 5°$ and $\alpha = 20°$ (Di Fabbio et al., 2024a). 140
7.5 Iso-surfaces from streamwise pressure gradient and Q-criterion colored by Mach number, and slice planes showing the normalized x-velocity (Di Fabbio et al., 2024a). 141
7.6 x-pressure gradient contour field with Mach number contour lines and mean x-direction friction coefficient. Black lines indicate zero mean friction coefficient (Di Fabbio et al., 2024a). 142
7.7 Mean and instantaneous x-vorticity, URANS, and Hi-Fi results (Di Fabbio et al., 2024a). 143
7.8 Viscosity ratio in the windward inboard vortex (Di Fabbio et al., 2024a). 144
7.9 Source terms of the turbulence equations written in Table 7.1. All the values have been normalized (Di Fabbio et al., 2024a). 145
7.10 Normalized specific Reynolds stresses, R_{11} (Di Fabbio et al., 2024a). . . 147
7.11 Normalized specific Reynolds stresses, R_{22} (Di Fabbio et al., 2024a). . . 148
7.12 Normalized turbulent kinetic energy, K (Di Fabbio et al., 2024a). 149
7.13 Normalized specific Reynolds stress, R_{12}. 150
7.14 Normalized specific Reynolds stress, R_{13}. 150
7.15 Normalized specific Reynolds stress, R_{23}. 151
7.16 Relation between vorticity magnitude and turbulent kinetic energy through C_k (Di Fabbio et al., 2024a). 152
7.17 Aerodynamic coefficients deviation at $\alpha = 20°$ (Di Fabbio et al., 2024a). 152
7.18 PK outcomes: leading-edge vortices, vortex-shock interaction, streamwise separation, and vortex breakdown (Di Fabbio et al., 2024a). 153
7.19 PK outcomes: viscosity ratio; normalized turbulent kinetic energy and normalized normal Reynolds stresses (Di Fabbio et al., 2024a). 154

8.1 2DZP: friction coefficient and velocity profile (Di Fabbio et al., 2024b). 163
8.2 2DFDC: law of the wall (Di Fabbio et al., 2024b). 163
8.3 2DWMH: friction and pressure coefficients (Di Fabbio et al., 2024b). . . 164
8.4 2DWMH: velocity and Reynolds stress profiles (Di Fabbio et al., 2024b). 164
8.5 2DWMH: velocity contour plots (Di Fabbio et al., 2024b). 165
8.6 2DWMH: $f^{(1)}$, C_P, and C_D contours and streamlines (Di Fabbio et al., 2024b). 166
8.7 2DWMH: expressions as function of the invariants (Di Fabbio et al., 2024b). 167
8.8 ASJ: velocity profiles along the jet axis (Di Fabbio et al., 2024b). 167
8.9 ASJ: velocity and Reynolds stress profiles (Di Fabbio et al., 2024b). . . 168
8.10 ASJ: normalized velocity contour plots (Di Fabbio et al., 2024b). 168
8.11 ASJ: $f^{(1)}$, C_P, and C_D contours and streamlines (Di Fabbio et al., 2024b).169
8.12 ASJ: expressions as function of the invariants (Di Fabbio et al., 2024b). 169
8.13 VFE2: geometry and mesh. 170
8.14 VFE2: surface pressure coefficient at different ξ locations over the wing. 171
8.15 VFE2: surface pressure coefficient and normalized x-velocity. 172
8.16 VFE2: normalized x-velocity, contour and in-plane vectors at locations $\xi = 0.5, 0.6, 0.7, 0.8, 0.95$. 173
8.17 VFE2: $f^{(1)}$, C_P, and C_D contours and streamlines. 174
8.18 VFE2: expressions as function of the invariants. 174

List of Tables

2.1 Geometric details of the ADS-NA2-W1 27

5.1 VFE-2 computational domains (Di Fabbio et al., 2023). 96

6.1 Meshes details and aerodynamic coefficients (Di Fabbio et al., 2022d). . 114

7.1 Source terms of the turbulence equations illustrated in Fig. 7.9 146

8.1 2DZP: GEP expressions. Numbers rounded to the third decimal place. 163
8.2 2DFDC: GEP expressions. Numbers rounded to the third decimal place. 164
8.3 2DWMH: GEP expressions. Numbers rounded to the third decimal place. 166
8.4 ASJ: GEP expressions. Numbers rounded to the third decimal place. . 169
8.5 VFE2: GEP expressions. Numbers rounded to the third decimal place. 174

Nomenclature

Abbreviations

2DFDC	2D Fully-Developed Channel Flow at a high Reynolds number
2DWMH	2D NASA Wall-Mounted Hump with Flow Separation
2DZP	2D Zero Pressure Gradient Flat Plate
ADS	Airbus Defence and Spaces
AoA	Angles of Attack
AR	Aspect Ratio
ASJ	Axisymmetric Subsonic Jet
AVT	Applied Vehicle Technology Panel
CFD	Computational Fluid Dynamics
CFL	Courant-Friedrichs-Lewy number
CSA	Coupled Spalart-Allmaras
CTU	Convective Time Unit
DDES	Delayed Detached Eddy Simulation
DES	Detached Eddy Simulation
DLR	Deutsches Zentrum für Luft- und Raumfahrt
DNS	Direct Numerical Simulation
EA	Evolutionary Algorithm
EARSM	Explicit Algebraic Reynolds Stress Model
EC	Evolutionary Computing
EVM	Eddy Viscosity Model
FCAS	Future Combat Air System
FVM	Finte Volume Method
GA	Genetic Algorithm
GEP	Gene Expression Programming
GP	Genetic Programming
Hi-Fi	High-Fidelity
HRL	Hybrid RANS/LES
IDDES	Improved Delayed Detached Eddy Simulation
kωSST	Menter $k-\omega$ Shear Stress Transport
LE	Leading Edge
LES	Large Eddy Simulation
LHS	Left-hand side
ML	Machine Learning
NATO	North Atlantic Treaty Organization
NTF	National Transonic Facility
PIV	Particle Image Velocimetry
PK	Production of turbulent kinetic energy
PSP	Pressure-Sensitive Paint
QCR	Quadratic Constitutive Relation

RANS	Reynolds Averaged Navier-Stokes
RHS	Right-hand side
RTO	Research and Technology Organization
SA	Spalart-Allmaras
SA-RC	Spalart-Allmaras with Rotation/Curvature correction
SAneg	Spalart-Allmaras with negative turbulent viscosity correction
SAnegRC	Spalart-Allmaras with negative turbulent viscosity and Rotation/Curvature correction
SAS	Scale-Adaptive Simulation
SGS	Sub Grid Scale
SST	Shear Stress Transport
STO	Science and Technology Organization
UAV	Unmanned Aerial Vehicle
UCAV	Unmanned Combat Aerial Vehicle
URANS	Unsteady Reynolds Averaged Navier-Stokes
VFE	Vortex Flow Experiment
WMLES	Wall-Modeled Large Eddy Simulation

Greek symbols

α	Angle of attack [°]
$\bar{\phi}$	Time-averaged flow variable
β	Side-slip angle [°]
$\Delta\varphi$	Kink angle [°]
Δt	Time step size $[s]$
Δ	Characteristic cell size $[m]$
δ_{ij}	Kronecker delta
ϵ_{ijk}	Levi-Civita symbol
γ	Adiabatic index
$\hat{\phi}$	Filtered flow variable
λ	Second viscosity $[kg/(ms)]$
μ	Dynamic molecular viscosity $[kg/(ms)]$
μ_t	Turbulent eddy viscosity $[kg/(ms)]$
$\nabla\rho$	Density gradient $[kg/m^4]$
∇p	Pressure gradient $[Pa/m]$
ν	Kinematic viscosity $[m^2/s]$
ν_t	Kinematic eddy viscosity $[m^2/s]$
ω	Specific dissipation rate $[1/s]$
$\omega_x, \omega_y, \omega_z$	Vorticity components $[1/s]$
ϕ	Instantaneous flow variable
ϕ'	Fluctuating flow variable relative to the time-averaged
ϕ''	Sub-grid residual flow variable
ϕ'''	Fluctuating flow variable relative to the mass-averaged
ρ	Density $[kg/m^3]$
τ_w	Wall shear stress $[Pa]$
τ_{ij}	Viscous stress tensor $[Pa]$
τ_{ij}^R	Reynolds stress tensor $[Pa]$
θ	Momentum thickness
$\tilde{\nu}$	SA viscosity $[m^2/s]$

$\tilde{\phi}$	Mass-averaged flow variable
ε	Rate of dissipation of turbulent kinetic energy $[m^2/s^3]$
φ	Sweep angle [°]
ξ, η, ψ	Dimensionless Cartesian coordinates
Latin symbols	
$\tilde{d}$	Hybrid length scale $[m]$
a_{ij}	Anisotropic tensor $[Pa]$
b	Wing span $[m]$
c	Speed of sound $[m/s]$
c_f	Friction coefficient
C_k	Coefficient of the PK model
C_L	Lift coefficient
C_p	Specific heat capacity at constant pressure $[J/(kgK)]$
c_p	Pressure coefficient
c_p^*	Sonic pressure coefficient
c_r	Chord length $[m]$
C_v	Specific heat capacity at constant volume $[J/(kgK)]$
C_{m_x}	Rolling moment coefficient
C_{m_y}	Pitching moment coefficient
d	RANS length scale $[m]$
d_{ω_x}	Vortex diameter $[m]$
H_n	Normalized helicity
I_k	Invariants
K	Normalized turbulence kinetic energy
k	Turbulent kinetic energy $[m^2/s^2]$
k_{SA}	Spalart-Allmaras turbulent kinetic energy $[m^2/s^2]$
L	Characteristic length $[m]$
LES_{IQ_ν}	Index of Resolution Quality
Ma	Mach number
N_{ω_x}	Grid points inside vortex diameter $[m]$
p	Pressure $[Pa]$
p_0	Total pressure $[Pa]$
Pr	Prandtl number
Q	Q-criterion $[1/s^2]$
R	Specific gas constant $[J/(kgK)]$
R_t	Turbulent eddy viscosity over dynamic molecular viscosity
R_{ij}	Specific normalized Reynold stress tensor
Re	Reynolds number
Re_θ	Reynolds number based on momentum thickness
S_{ij}	Strain rate tensor $[1/s]$
S_{ij}^*	Deviatoric strain rate tensor $[1/s]$
St	Strouhal number
t	Time $[s]$
U	Velocity magnitude $[m/s]$
u',v',w'	Velocity fluctuations components $[m/s]$
u,v,w	Velocity components $[m/s]$
u^+	Non-dimensional velocity

u_τ	Friction velocity $[m/s]$
u_t	In-plane tangential velocity $[m/s]$
V	Cell volume $[m^3]$
V_{ij}^k	Basis tensor
W_{ij}	Vorticity tensor $[1/s]$
x,y,z	Cartesian coordinates $[m]$
y^+	Non-dimensional wall-normal distance

1

Introduction

This chapter serves as the introduction to the dissertation. It offers an in-depth exploration of the background and motivations underpinning this study, as well as its scopes and objectives. Additionally, the structure of the thesis is meticulously detailed, furnishing a exhaustive roadmap for the reader.

1.1. Background and motivation

The development and design of an aircraft represents a complex intersection of academic and industrial research efforts. They are constrained by time and cost considerations, scientific validity, market competition, and the necessity to meet pre-defined requirements and targets. This task gains complexity as technology advances, global competition intensifies, and requirements evolve. Consequently, increasing collaboration between academia and industry is imperative to address pertinent scientific questions and promote further progress. This necessity is a key driver in developing this research project that amalgamates these two perspectives towards a common goal.

Different aircraft types and mission profiles necessitate distinct characteristics. This research focuses on high-agility and performance aircraft with notably stringent challenges. Agile military aircraft operate under extreme flight conditions characterized by intricate flow fields, and often incorporate low aspect ratio wings with swept leading-edges. The aerodynamic efficacy of these delta wings is significantly influenced by the vortex-dominated flows originating at their swept leading-edges, underlining the importance of understanding and precisely predicting the vortical flow system within the aircraft design.

1.1.1. Advancements in fighter aircraft technology

In recent years, the aerodynamic design of future fighter aircraft has become a focal point of advanced aeronautical engineering research. Hitzel et al., 2020 has specifically addressed the multifaceted challenges and considerations in developing aerodynamically efficient designs that meet the rigorous demands of modern combat scenarios. Modern combat aircraft are mandated to encompass a broad spectrum of performance metrics and maneuverability capabilities, as illustrated in Fig. 1.1a. Furthermore, the

design considerations extend to conforming with signature limitations, as evidenced in Fig. 1.1b, alongside achieving specific operational ranges and payload capacities. Recent analyses of mission scenarios have intensified the requirements for swift, dynamic controllability, especially at elevated angles of attack (AoA). Historically, many advanced combat aircraft have adopted delta-wing configurations to benefit from the slender design and the advantageous non-linear lift properties provided by leading-edge vortex flows. The augmented lift and enhanced aerodynamic properties significantly boost agility, particularly at low speeds, thus steering the widespread adoption of delta wing platforms in designing various intricate configurations (Anderson, 2016).

Understanding and precisely controlling vortex flows is imperative, as these significantly influence the aircraft's aerodynamic characteristics, affecting its agility and response in various flight conditions. As depicted in Fig. 1.1a, numerous instabilities and flow phenomena present significant challenges in extending the operational envelope of fighter aircraft. Additionally, the influence of aircraft design parameters such as planform, wing sweep, and leading-edge configurations on vortex behavior has to be explored. The aim is to enhance the flight envelope regarding control power, maneuverability, and performance while maintaining acceptable stability, structural integrity, and longevity. The design process requires exceptional precision across all disciplines to meet these demands and aerodynamics plays a crucial role.

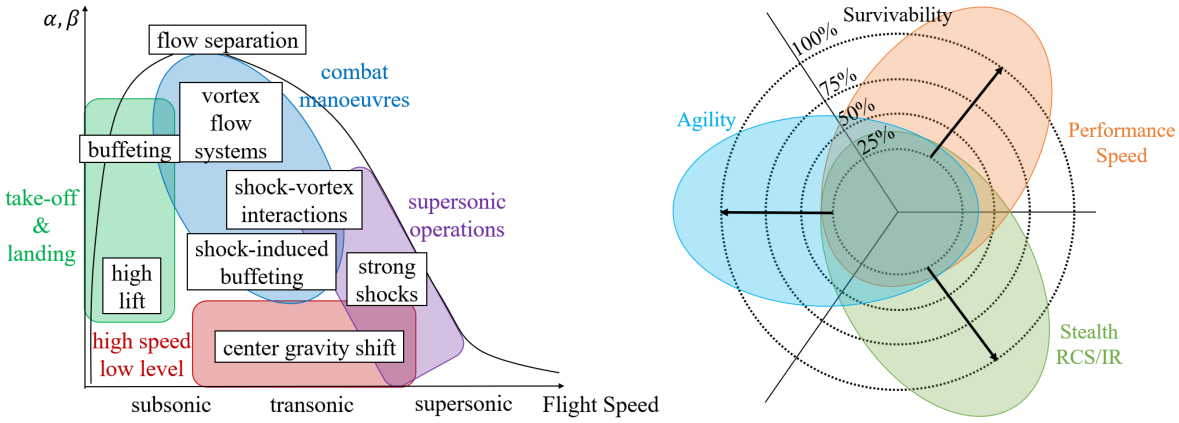

(a) Typical agility envelope and flow phenomena. **(b)** Maneuverability and signature triangle.

Figure 1.1: Design complexities of modern combat aircraft (inspired by Hitzel et al., 2020).

A significant portion of aerodynamic research and development is devoted to explore flow phenomena that become prominent as the angle of attack increases. The downstream movement of the flow detaching at the leading-edges culminates in the formation of coherent vortical structures above the leading-edge, contributing substantially to the lift force produced by the wing. The efficacy of these lift-augmenting wing vortices intensifies with the angle of attack until these structures destabilize and disintegrate into a turbulent state. This degradation in the coherence of the flow structure atop the wing is noted to adversely impact the aerodynamic properties, precipitating abrupt changes in the forces and moments imposed on the vehicle.

As illustrated in Fig. 1.1, the expanded operational envelope of many contemporary aircraft includes manoeuvres being conducted at transonic speeds, which also introduce the phenomenon of shock waves interacting with leading-edge vortices. These shocks arise from localized supersonic regions, and as the flow behavior evolves with an increase in incidence, both the location and intensity of the shocks are subject to change. These alterations can influence the overall flow dynamics and, by extension, impact the aircraft's performance during manoeuvres within this flight regime. Consequently, a profound understanding of the flow behavior, particularly the interactions between the shock and vortical flows, is paramount in aerospace research. Furthermore, pioneering research observed that the flow over the delta wing is unsteady, particularly when leading-edge vortices transition into a turbulent state. This unsteadiness adds layers of complexity to an already intricate flow behavior. Coupled with interactions with the wing surface and other aircraft structures, aeroelastic effects follow, inducing fatigue and, in extreme scenarios, precipitating catastrophic failure (Lambourne and Bryer, 1961). This type of unsteady flow, known as buffet, concerns all aircraft configurations incorporating swept edges into their design. Understanding the dynamics of this unsteady force is pivotal to mitigating any resultant structural responses. This holds paramount importance for the analysis of current complex fighter configurations and the design of futuristic ones.

Notable aircraft within this category, depicted in Fig. 1.2, include the Concorde, the Eurofighter and the Space Shuttle. Analogous considerations are also prevalent in Unmanned Aerial Vehicles (UAVs) and Unmanned Combat Aerial Vehicles (UCAVs). UCAVs, commonly referred to as combat drones, are unmanned aircraft designed for roles including intelligence, surveillance, target acquisition, and reconnaissance. The advent and proliferation of new UAV and UCAV technologies, particularly those adopting planforms where vortical dynamics are crucial, reemphasize the necessity for an in-depth understanding of vortex flows.

Figure 1.2: Insights into delta wing aircraft configurations: Concorde, Eurofighter and Space Shuttle created by OpenAI, 2024.

Given the dualistic nature of these vortical flows, exhibiting both positive and negative impacts on aircraft aerodynamics, extensive research and development have been undertaken to dissect and ameliorate wing behavior under diverse flight conditions.

A challenge is thus posed for researchers in both experimental and numerical fields. Historically, aerodynamic flow behavior were predominantly studied using experimental methodologies, including extensive wind tunnel testing and flight tests. However, flight tests, offering the highest accuracy by evaluating the device in its actual application environment, are feasible only after a prototype has been evaluated, constructed, and deemed safe to fly. Consequently, they incur the highest costs in both time and money. Therefore, although less accurate due to boundary condition limitations, wind tunnel tests are more cost-effective and can be conducted with preliminary designs to elucidate flow dynamics across various flight conditions.

An increasingly instrumental tool in investigating intricate flow regimes is Computational Fluid Dynamics (CFD). CFD produces numerical solutions for a set of partial differential equations governing fluid motion. Utilizing discrete methodologies, CFD's primary aim is to qualitatively and quantitatively decode physical phenomena within the flow, subsequently contributing to advancements in engineering design. Over time, CFD has emerged as an essential complement to conventional wind tunnel experiments, pivotal in designing and developing contemporary high-performance aircraft. Specifically, CFD simulations, especially those targeting vortical flow over delta wings, continue to accumulate significant interest. Numerical simulation offers the best turnaround time, albeit at a compromise in accuracy quality, contingent on the chosen numerical methodology. Each method has then its advantages and drawbacks, primarily evaluated in terms of accuracy and cost, both temporal and economic.

CFD's role in understanding vortical flows is critical for advancing future air-vehicle concepts. Unconventional wing planforms demand the application of high-fidelity CFD to predict their high angle of attack aerodynamics accurately. Hitzel et al., 2020 has critically reviewed the existing knowledge landscape in vortex dynamics and pinpoints specific lacunae that necessitate attention for the discipline's advancement. The improvement of CFD tools (and experimental facilities) is imperative to facilitate more precise analyses and the assimilation of intricate flow characteristics into the design schema. A more profound and extensive understanding of vortex flows, with enhanced simulation capabilities, will catalyze the formulation of more resilient and pioneering aerodynamic configurations. Such progressions will substantially strengthen the performance and adaptability of future fighter aircraft, ensuring their continued efficacy and capability in the progressively complex scenario of aerial warfare. This necessity is underscored in various ongoing development initiatives, notably the Future Combat Air System (FCAS) project, an European defense initiative, which is providing financial support for this doctoral research.

1.1.2. Challenges in CFD: complex flow phenomena

Since the mid-1960s, the advancement of CFD methods for computing flow has undergone remarkable progress. The advancement in high-speed computation has revolutionized engineering analysis across various fields. This evolution has been propelled by the substantial growth in computer memory, coupled with notable advancements in numerical algorithms for solving fluid-dynamic equations.

CFD has become an increasingly valuable tool for understanding aerodynamic flow behavior. It minimizes the need for expensive, large-scale testing programs by identifying regions of interest in flow regimes before physical testing begins. Integrating CFD with experimental testing in research and industrial design processes is gaining recognition among scientists and engineers. CFD has played a pivotal role in augmenting the understanding of flow physics, especially in turbulence. It enables the examination of situations that may be impractical in wind tunnels, such as more realistic flight conditions and scenarios. This advancement, in turn, translates into reducing project risk and a heightened analysis of system performance before flight. Additionally, it opens the door for developing tools capable of understanding unexpected flight behavior that may arise during flight tests.

Although computations of viscous flow under cruise conditions are now routine, accurately predicting complex effects at high angles of attack remains a formidable challenge. Key challenges, as delineated in previous studies (Hitzel, 2022a,b; Lovell, 2001), are here briefly outlined.

- The computational methods for predicting vortex flows have to be validated.
- Tools enabling the rapid computations of vortex flows around complex configurations are in research stage.
- Accurate predictions of the strength and position of the primary vortex core require a suitable grid and turbulence model.
- Refinement studies should be conducted to demonstrate grid convergence.
- Prediction of vortex breakdown for complex configurations proves challenging.
- Consideration of scale, compressibility, and unsteady effects is essential.

Challenges then include the accurate modeling of turbulence and transition in vortical and extensively separated flows, alongside the need for suitable numerical algorithms, and the difficulties associated with generating grids that facilitate precise simulation of the flow field (Cummings et al., 2003a). The inherent complexities of delta wing flow directly impact turbulence stresses and scales, necessitating ongoing development and improvement in prediction methods. Addressing these challenges is crucial for advancing the predictive capabilities of CFD in the complex aerodynamic regimes.

Currently, CFD is acknowledged as an experimental technique when applied to delta wing flows and unsteady effects. For this reason, it typically requires support from experiments for almost all such problems (Spalart and Bogue, 2003). Despite advancements, further development is imperative to enhance the accuracy and reliability of CFD techniques for industrial applications. The overarching challenge lies in achieving time-accurate CFD simulations of a complete aircraft configuration at high angles of attack and flight Reynolds numbers. The ongoing challenge in developing CFD methods for vortex-flow simulations lies in the search for an optimal balance between computational efficiency and fidelity.

1.2. Scopes and structure of the thesis

The objectives of the thesis are detailed in Section 1.2.1, whereas its structure, which closely adheres to these objectives, is outlined in Section 1.2.2. Moreover, a summary of the thesis objectives in bullet points is provided. This format provides a compact overview where all essential information is included, ensuring both readability and ease of understanding.

1.2.1. Objectives

The investigation of leading-edge vortices of swept wings with low aspect ratio has been subject to several research projects in recent decades. Also, unsteady phenomena like the vortex breakdown at high angles of attack have been investigated in detail. In many configurations, the flow separation, which forms the initial stage of vortex formation, is fixed by the sharp leading-edge. Therefore, the main challenge of turbulence models is to correctly produce formation and further development of the vortical flow system along the wing surface. As the complexity of the configuration escalates, including multiple leading-edge angles, variations in edge contours, and additional flow control devices, current state-of-the-art methods render it impracticable to predict flow behavior without recourse to detailed simulation or costly wind tunnel testing. Computational fluid dynamics experts have been striving to numerically estimate the behavior of these intricate and challenging flow patterns. However, despite considerable efforts, no definitive and universally applicable solution has been discovered. Therefore, it is essential to assess several turbulence treatments to determine their suitability for addressing these wing configurations' specific and demanding requirements.

Turbulence models and approaches capture the complex turbulence fluctuations in the delta wing flow. The Reynolds Averaged Navier-Stokes (RANS) approach is widely preferred in industrial settings primarily because it demands significantly less computational resources compared to high-fidelity (Hi-Fi) simulations like Direct Numerical Simulations (DNS) and Large Eddy Simulation (LES). Nevertheless, RANS often falls short in its predictive accuracy when dealing with complex geometries and flow dynamics. In the RANS momentum equation, the turbulent fluctuations are represented by the Reynolds stress tensor. Different assumptions are used for modeling the Reynolds stress tensor, which categorizes the turbulence model used in the solver. The commonly used Boussinesq hypothesis assumes a linear relationship between the Reynolds stress tensor and the mean strain rate tensor.

Boussinesq postulated that the momentum transfer caused by turbulent eddies could be modeled using an eddy viscosity. Several eddy-viscosity models (EVMs) can be classified according to the number of transport equations solved to compute the eddy viscosity. Among the various established models, the Spalart-Allmaras (SA) model is widely recognized as a standard RANS closure method in aerodynamic applications. However, while the SA model is widely adopted in the (aerospace) industry due to its simplicity and robustness, its inherent limitations and drawbacks become more evident when applied to complex configurations. Notably, it frequently exhibits excessive eddy

viscosity production within the vortex, affecting the unburst vortex size, type, and velocities. Therefore, both the academic and industrial worlds remain keenly invested in improving the predictive accuracy of SA-based RANS models, especially in the aerodynamic design validations within the aerospace sector. Since a substantial requirement exists for a model that can predict flows dominated by leading-edge vortices with both time efficiency and high accuracy, a sustained interest persists in developing novel one-equation turbulence models with the potential to enhance RANS outcomes.

The primary objective of this dissertation is to develop an efficient one-equation RANS turbulence model, specifically tailored for the prediction of leading-edge vortex formation and interaction in multiple delta configurations. Emphasis is placed on the accurate prediction of leading-edge vortex breakdown. The SA model serves as the foundational reference, with the goal of refining its predictive capabilities. This thesis aims to extend its practical use in both academic research and industrial applications, particularly in military aircraft design and engineering. The roadmap to achieving this goal involves several distinct steps, which can be categorized into intermediate objectives.

First of all, it is imperative to cultivate knowledge and expertise in vortex-dominated flows over delta wings. This process necessitates acquiring high-fidelity data to elucidate complex flow patterns over the wing. Reviewing existing numerical methods is essential to evaluate their suitability for modeling swept leading-edge vortex phenomena. While LES may offer a more general approach to turbulence resolution, its computational cost renders it impractical for routine in aerodynamic applications. Given the complexity of these simulations, the hybrid RANS/LES (HRL) approach is then identified as a viable alternative. It aims to accurately capture the unsteady characteristics of the vortices with a manageable computational effort by resolving parts of the turbulence spectrum in the flow away from the wall rather than modeling the entire spectrum.

The HRL approach based on the SA one-equation turbulence model requires rigorous validation against established, straightforward configurations. For this purpose, the well-documented and sharply contoured leading-edge configuration of the Vortex Flow Experiment (VFE-2) delta wing is utilized to examine the vortex-dominated flow thoroughly, as depicted in Fig. 1.3. The CFD simulations have been performed using the DLR-TAU code, developed by the Deutsches Zentrum für Luft-und Raumfahrt (DRL, German Aerospace Center). In addition to evaluating sensitivity to spatial and temporal resolutions, the research uncovers physical characteristics not readily discernible from experimental data, necessitating scale-resolving simulation approaches. The study explores the complex pattern of leading-edge vortices, including embedded shocks and the subsequent interactions between shocks and vortices. The shock-vortex interaction is detailed, and a theory behind the occurrence of the vortex breakdown is introduced. Accurate outcomes are obtained, supported by Hi-Fi data derived from scale-resolving simulations. The analysis also extends to turbulence-related metrics such as eddy viscosity and resolved Reynolds stresses, providing insights into their dynamics during the vortex formation and sustenance processes.

After the methodology validation, the focus is directed towards the Airbus Defense and Space (ADS) NA2-W1 configuration to elucidate the flow field behavior over such intricate geometries, as depicted in Fig. 1.3. The vortex-dominated flow around the triple-delta wing is meticulously examined to enhance understanding of the flow physics phenomena, especially under side-slip and transonic conditions. Both Unsteady RANS and scale-resolving simulations based on the SA turbulence model are utilized to assess the range of applicability of current CFD methods. The aerodynamic coefficients are examined across various flight conditions to elucidate the reasons behind the persisting prediction inaccuracies. The deficiencies of URANS outcomes are demonstrated, and significant enhancements are achieved using the HRL method. The Hi-Fi data notably uncovers physical aspects previously unobserved with sufficient accuracy in URANS, such as vortex-vortex, shock-vortex interactions and vortex breakdown. These phenomena elucidate the improved prediction of surface pressure coefficients over the aircraft and, consequently, the aerodynamic force and moment coefficients.

Furthermore, the triple-delta wing is employed for additional analyses and considerations on the vortex breakdown phenomenon and its underlying causes. Numerical results obtained from two-equation turbulence methods are included as well. The flow physics derived from different turbulence modeling approaches is then compared. The study aims to identify the limitations of the SA one-equation model in addressing such complex applications. The physical and modeling reasons behind the one-equation model's misprediction are investigated to enhance its accuracy. The influence of turbulence treatment on CFD results is then discussed. A straightforward modification to the Boussinesq assumption when utilizing the SA model for complex configurations is assessed, and the improved URANS results are compared with the state-of-the-art outcomes.

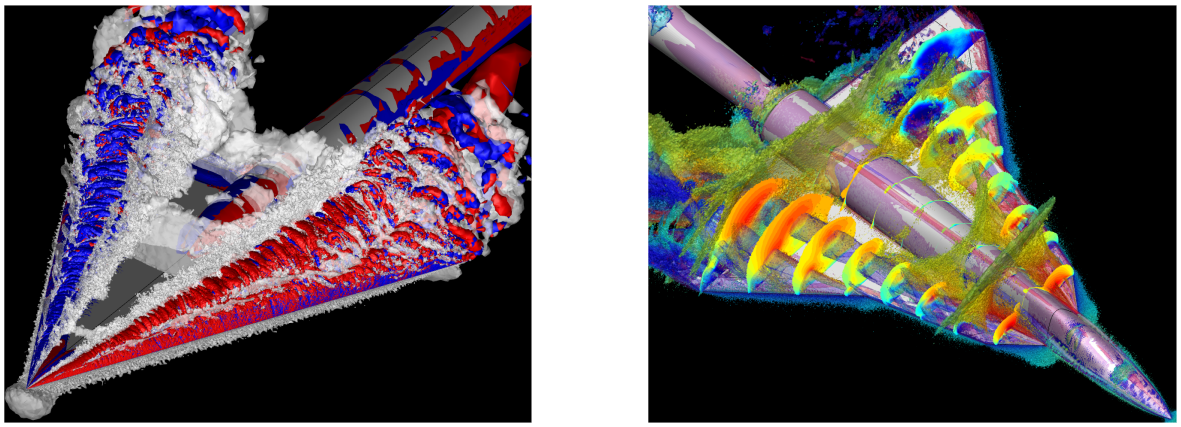

Figure 1.3: Visualization of flow around the single-delta wing VFE-2 (left) and the triple-delta wing ADS-NA2-W1 configuration (right).

Based on the expertise gained analyzing the vortex-dominated flows on both configurations, this research progresses to conceptualizing and developing an enhanced one-equation turbulence model. A CFD-driven machine learning (ML) framework, utilizing

the Gene Expression Programming (GEP) methodology, is used to advance RANS models. The study investigates two distinct strategies: firstly, challenging the Boussinesq hypothesis, and secondly, constructing a new one-equation turbulence model designed to predict a broad spectrum of turbulent wall-bounded flows accurately. A comparative analysis is conducted on these methodologies to assess their potential in enhancing RANS modeling capabilities. At the first stage, four fundamental flows of the NASA challenge validation cases, the flat plate, channel, jet, and wall-mounted hump, are employed to perform the training process. Subsequently, the VFE-2 delta wing configuration is then trained and investigated numerically. The CFD code used within the GEP training framework is OpenFoam Version 7.0. Utilizing pre-existing training data, the symbolic regression applied in this study not only formulates constitutive relations for specific user-defined expressions but also provides deep insights into fundamental physics by negating ineffective methodologies. Consequently, the role of machine learning in this context transcends the mere development of a turbulence closure for a particular instance, signifying its broader application and impact in aerodynamics and fluid mechanics research.

Concise summary of thesis objectives: a bullet point overview

Primary Goal → Enhancement of SA Model: Improve the predictive accuracy of the SA turbulence model via the RANS method to extend its applicability in both academic and industrial sectors. Address the SA model's limitations by developing an optimized model for predicting the formation and breakdown of leading-edge vortices in multi-delta configurations.

The intermediate objectives of the thesis are concisely articulated in bullet points and arranged logically and sequentially.

1. **Understanding vortex-dominated flows:** deepen the understanding of vortex-dominated flows over the VFE-2 delta wing at transonic conditions, concentrating on predicting the formation and breakdown of leading-edge vortices.
    - Explore the feasibility and applicability of HRL methods. Evaluating sensitivity to spatial and temporal resolutions necessary for accurate scale-resolving simulations.
    - Employ scale-resolving simulations to investigate vortex-dominated flow, analyzing the pattern of leading-edge vortices, and shock-vortex interactions.
    - Focus on the accurate prediction of the breakdown of leading-edge vortices. Provide a theory and explanation behind the occurrence of the leading-edge vortex breakdown.
    - Uncovering physical characteristics not evident from experimental data and extending the analysis to turbulence-related metrics.

2. **ADS-NA2-W1 aircraft configuration:** analyze the flow field behavior over the triple-delta wing aircraft, particularly at side-slip and transonic conditions.
    - Utilize both URANS and scale-resolving simulations to assess the applicability of current CFD methods.
    - Examine vortex-vortex and shock-vortex interactions, vortex breakdown and their impact on aerodynamic force and moment coefficients.
    - Explore the vortex breakdown phenomenon and its underlying causes, comparing flow physics from different turbulence modeling approaches.
    - Elucidate reasons behind inaccuracies of the RANS simulations predictions. Identify limitations of the SA one-equation model.
    - Propose a straightforward modification to the SA model.
3. **Enhanced turbulence model development:** conceptualize and develop an enhanced one-equation turbulence model for a broad spectrum of turbulent flows through a CFD-driven machine learning framework.
    - Conduct a comparative analysis of novel methodologies to assess their potential in enhancing RANS modeling capabilities.
    - Highlight the broader application and impact of machine learning in aerodynamics research.

1.2.2. Outline

The structure of the thesis is delineated to reflect the logical progression of the objectives previously outlined.

Chapter 2 includes the literature review. Section 2.1 provides a comprehensive examination of delta wing flows, considering various aspects such as the formation of leading-edge vortices, vortex breakdown, unsteady flow phenomena and transonic vortical flows. The VFE-2 and the ADS-NA2-W1 configurations investigated in this thesis are also introduced, discussing the experimental framework. A review of the state-of-the-art in CFD as it pertains to delta wing flows is presented in Section 2.2. Section 2.3 introduces the concept of ML, with a focus on the fundamentals of evolutionary algorithms (EAs). It provides an introduction to GEP and concludes with an overview of the application of machine learning in turbulence modeling.

Chapter 3 is dedicated to the theoretical foundations of fluid motion and modeling. The governing equations and the nature of turbulence are discussed in Sections 3.1 and 3.2, respectively. Section 3.3 provides a comprehensive overview of modeling and simulation techniques. Subsequently, Section 3.4 offers a detailed examination of the modeling approaches and turbulence models employed for analyzing delta wing aerodynamics in this dissertation.

Chapter 4 outlines the software and the numerical strategy. Section 4.1 briefly introduces the CFD codes employed in this dissertation, particularly TAU and OpenFOAM.

Section 4.2 discusses evolutionary computing strategies, placing particular emphasis on GEP with a focus on the CFD-driven approach. It then introduces EVE, the GEP code employed in this thesis. Section 4.3 provides a detailed exposition of the conservative equations fundamental to the Finite Volume Method (FVM). It subsequently explores the numerical methods employed for solving these equations, highlighting spatial and temporal discretization techniques.

Chapter 5 focuses on scale-resolving simulations of the vortex-dominated flow around the VFE-2 wing, exploring complex vortex patterns and shock interactions. It discusses the rigorous validation of the HRL approach and its significant contributions to understanding the flow physics in transonic conditions.

Chapter 6 applies the HRL and URANS approaches to the complex ADS-NA2-W1 configurations, analyzing vortex-dominated flow at side-slip and transonic conditions. It assesses the applicability and limitations of current CFD methods, highlighting significant improvements in predicting flow behavior and aerodynamic coefficients through Hi-Fi data. The deficiencies of the SA model in predicting vortex breakdown are highlighted.

Chapter 7 focuses on understanding the vortex breakdown phenomenon and its causes. It evaluates the limitations of the SA one-equation model, investigates the reasons behind its inaccuracies, and propose an extension to the Boussinesq assumption to enhance its accuracy.

Chapter 8 explores potential advancements in the SA model developed through a CFD-driven machine learning framework. It challenges traditional hypotheses and significantly improves the state-of-the-art in predictive accuracy. It underscores the pivotal role of machine learning in enhancing RANS capabilities and its broader impact on research in aerodynamics and fluid mechanics.

The thesis concludes with Chapter 9, synthesizing the main findings and delineating potential directions for future investigations.

Finally, a detailed, implementation-ready specification of the employed turbulence models and their associated coefficients is provided in the Appendix.

2

Literature Review

This chapter delineates the background and conducts a literature review pertinent to the studies undertaken in this dissertation. It is divided into three sections. Section 2.1 delves into the complex aerodynamics of delta wing flows, offering an in-depth examination of various characteristics and analyses. Section 2.2 reviews the state-of-the-art CFD methods and approaches applied to delta wing flows. Specifically, one- and two-equation models are discussed, with an emphasis on providing an overview of the proposed models along with their modifications or improvements. The chapter concludes with Section 2.3, which introduces the concept of ML. Particular attention is devoted to Evolutionary Algorithm (EAs) and GEP, detailing the utilization of ML within the context of turbulence modeling.

2.1. Delta wing flow

Delta wing designs are critical in many high-speed aircraft. The aerodynamic flow around these wings is complex and present unique challenges and opportunities in aeronautical engineering. One of the most notable features of delta wing aerodynamics is the formation of coherent vortices along the leading-edges. Understanding these flow patterns is crucial for optimizing aircraft performance, stability, and control, especially in high-speed flight regimes.

2.1.1. Leading-edge vortices

The subsonic aerodynamic characteristics of delta wings with leading-edge separation are documented in existing literature, resulting in a well-established understanding of the flow topology (Anderson, 2016). The schematic representation of the flow pattern around a sharp-edged delta wing is illustrated in Fig. 2.1.

The predominant feature of the subsonic flow over delta wings, particularly noteworthy for wings with leading-edge sweep angles exceeding 45°, is the formation of vortical structures. Upon encountering the sharp leading-edge, a geometrical singularity denoted as the primary separation line S_1 in Fig. 2.1, the flow separates. This phenomenon initiates the formation of a free shear layer that extends into the outer

non-dissipative flow. Under the influence of the vorticity within it, the free shear layer undergoes a spiral roll-up, forming the compact and steady primary vortex.

As illustrated in Fig. 2.2, the vortex structure in a cross-flow plane comprises three distinct components: the vortex sheet or free shear layer, the rotational core, and the inner viscous sub-core. The vortex contains a viscous core, and the surrounding vortex flow is inviscid. The primary vortex remains embedded within the shear layer, continually acquiring vorticity along the entire wing's leading-edge length. This vorticity is transported through the free shear layer, enhancing the strength and cross-sectional dimension of the vortex core downstream. The diameter of the rotational core is approximately one-third of the local wing span and is marked by intense tangential velocities. In contrast, the viscous sub-core, constituting about 5% of the local span, is predominantly influenced by dissipation effects.

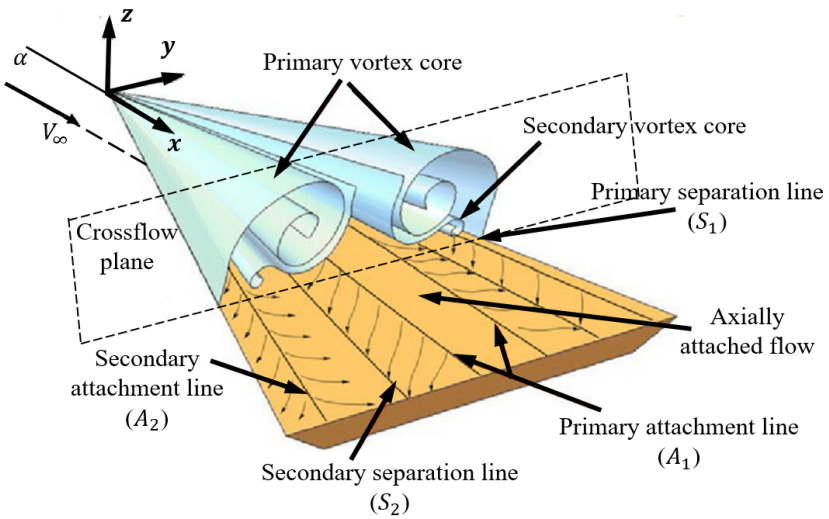

Figure 2.1: Subsonic flow field above a delta wing (adapted from Zanin, 2013).

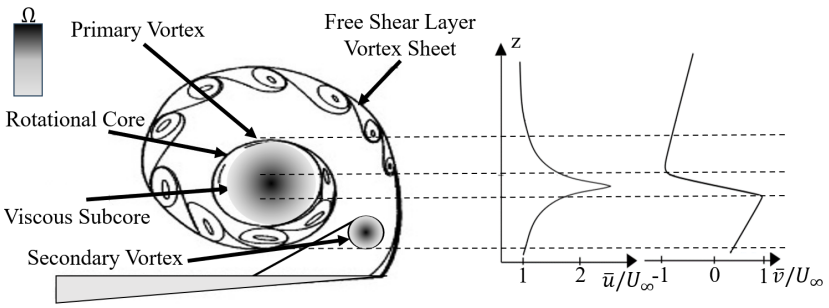

Figure 2.2: Leading-edge vortex structure, including qualitative distribution of the vorticity, the axial and the tangential velocities (inspired by Nelson and Pelletier, 2003).

The presence of the primary vortex significantly influences the local velocity and pressure distributions on the wing by introducing additional velocities, with the immediate

effect of establishing a low-pressure region beneath the vortex core (Délery, 1994). The rotational core exhibits high axial and azimuthal velocities. Within the inner core, axial velocity can reach up to threefold the free-stream velocity. For instance, axial velocities exceeding three times the free-stream velocity are recorded in the vortex core by Payne et al., 1986. The high rotational velocities extend beyond the core, interacting with the wing surface and generating a suction footprint. According to Hummel, 1981, the peak of additional velocity, which occurs beneath the vortex axis, coincides with the lowest point in the pressure distribution.

The vortex sheet loops over the wing and reattaches along the primary attachment line A_1. The streamlines on the vortex sheet follow helical paths, diverging from attachment lines and converging towards separation lines where they detach from the surface. Inboard of the primary attachment lines A_1, the surface streamlines remain attached. Outboard these attachment lines, the flow captured by the primary vortex moves outward beneath the primary vortex core toward the leading-edge. This flow may separate near the wing surface at S_2 due to the adverse pressure gradient encountered in the span-wise direction. The separated flow can then give rise to an oppositely rotating secondary vortex. Beyond the secondary vortex, the flow reattaches at A_2 and approaches the leading-edge. These secondary vortices can further spawn tertiary vortices through a similar process. At the leading-edge, the flow again separates and combines with the flow from the lower surface in the shear layer (Anderson, 2016).

The occurrence of secondary and tertiary vortices is contingent upon the type of separation in the cross-flow. In general, these smaller vortices impact the primary vortex, causing a displacement of its position inboard and lifting it away from the wing surface. Consequently, the presence of the secondary vortex may alter the location of the primary suction peak, shifting it out from a precise alignment below the primary vortex core (Jupp et al., 1999; Lowson, 1991). The nature of the boundary layer influences the location, size and strength of the secondary separation, specifically whether it is laminar or turbulent, which depends on the Reynolds number. The laminar boundary layer, more susceptible to adverse pressure gradients, experiences earlier separation, thus manifesting further inboard on the delta wing surface. Consequently, a transition from laminar to turbulent flow on a delta wing may be signaled by an outboard inflection of the secondary separation line. For a laminar boundary layer and separation, the formation of the secondary and subsequent vortices leads to a peak in the surface pressure distribution greater than that caused by the primary vortex. Conversely, for turbulent boundary conditions and separation, this peak is relatively flat and, consequently, less pronounced than the peak resulting from the primary separation.

The suction peak results in the so-called vortex lift, augmenting the potential lift achieved with fully attached flow (Polhamus, 1971). Consequently, the relationship between lift and incidence becomes nonlinear. Furthermore. leading-edge vortices supply the central regions of the wing with fresh air, mitigating the propensity for two-dimensional boundary layer separation, which is the primary factor contributing to the stall in conventional wings. The suction effect produced by strong and stable leading-edge vortices, in conjunction with this phenomenon, contributes to an increase in the lift coefficient (C_L) for a delta wing. Notably, this increase in C_L occurs at angles of attack where conventional wing planforms typically experience stall. Between 30%

and 60% of the total lift at high AoA is attributed to the leading-edge vortices (Wentz and Kohlman, 1971). Consequently, the presence of leading-edge vortices generally enhances the performance of delta wings. Ultimately, as the angle of attack continues to increase, a limit to the favorable effects induced by the vortex system is encountered, marked by large-scale vortex breakdown occurring above the wing, leading to an unsteady flow field.

2.1.2. Vortex development

The evolution of the large-scale vortex on a delta wing undergoes various stages, contingent on flow conditions and geometrical parameters, such as angle of attack (α), sweep angle (φ), and leading-edge (LE) roundness, as shown in Fig. 2.3. The angle of attack is the primary variable in differentiating its developmental stages. Variations in the sweep angle similarly impact the vortex stage, often mirroring the effects of an inverse angle of attack change (Hummel, 1981). For a given wing geometry, positive sweep angle adjustments results in equivalent vortex stages at higher AoA. The leading-edge shape critically determines the initial vortex separation (Moioli et al., 2022). A sharp leading-edge or small radius induces a fixed position for flow separation, simplifying the flow dynamics and inducing the development of vortices along the entire leading-edge, even at low AoA (Hummel, 1981). Conversely, an increased leading-edge radius enhances the separation's sensitivity to flow conditions. This effect is attributed to the radius's relative size in comparison to the wing, which can modify the effective angle of attack and subsequently influence the flow dynamics.

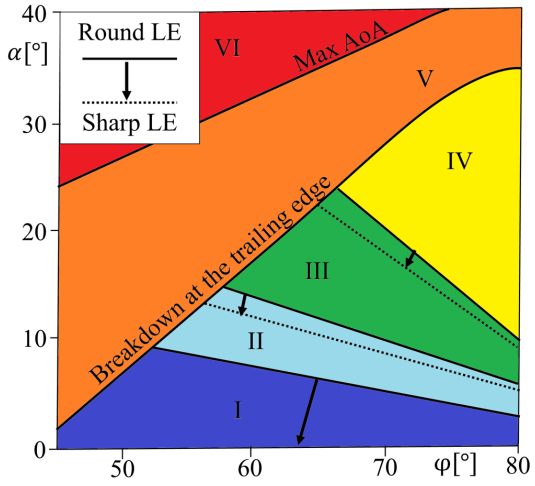

Figure 2.3: Various stages of vortex flow development (inspired by Moioli et al., 2022)

For a rounded leading-edge, no noticeable vortex separation occurs at low angles of attack (Stage I). As the angle of attack increases, the flow begins to roll into a vortex from a specific onset point on the leading-edge, identified as the partially developed vortex stage (Stage II). This stage corresponds to the initial stage of a sharp leading-edge wing. Further increase in the angle of attack causes the vortex to advance, with its separation onset moving toward the wing apex. A fully developed vortex stage (Stage III) is achieved upon reaching the apex. Beyond this point, the separation onset remains fixed at the apex, with the vortex axis moving inward at larger AoA until it stabilizes (Stage IV). At a certain threshold value of the angle of attack, a drastic alteration occurs in the vortex flow field over the wing, significantly impacting aerodynamics. The vortex breakdown stage (Stage V) is defined by the angle of attack

at which this instability first appears, starting from the trailing-edge and moving upward with increasing angle of attack, eventually leading to vortex shedding and stall conditions (Stage VI) (Moioli et al., 2018, 2022).

At lower incidence angles, breakdown may occur, but the bursting point is downstream of the trailing-edge, exerting no influence on the vortex lift generated by the wing. Subsequent increments in the angle of attack result in a rapid forward displacement of the vortex breakdown onset location. This movement is initially rapid and later exhibits a more gradual progression with increasing incidence (Délery, 1994; Huang and Hanff, 1992; Lowson and Riley, 1995). Beyond the angle of attack corresponding to the breakdown location at the apex, the shear layer separating from the leading-edges fails to form a swirling flow with axial motion. Instead, vortex shedding from the wing initiates (Gursul, 1994). Increased leading-edge sweep amplifies the strength of the leading-edge vortex and simultaneously delays vortex breakdown (Hemsch and Luckring, 1990). Wentz and Kohlman, 1971 note that for sweep angles exceeding 75°, breakdown becomes independent of the sweep angle.

Vortex breakdown plays a crucial role in delta wing aerodynamics, primarily due to its sudden modification of the wing's aerodynamic characteristics. This phenomenon significantly influences lift generation, underlining its importance in aerodynamic performance. Accurate prediction of the breakdown location and intensity is then crucial in designing and developing delta wing aircraft. While the theoretical framework proposed by Polhamus, 1971, based on a leading-edge suction analogy, is commonly used to describe the vortex lift contribution, it becomes invalid when vortex breakdown occurs over the wing, limiting its applicability. Wentz and Kohlman, 1971 and Johari and Moreira, 1998 reveal that for wings with a sweep angle exceeding 70°, the point where breakdown passes over the trailing-edge aligns with maximum lift. However, the coupling between vortex burst and lift is weak for wings with sweep angles of 70° or less, and maximum lift is not attained until the breakdown is near the apex of the wing, close to stall (Kengelman and Roos, 1989). Therefore, the relationship between vortex breakdown and lift generation is complex, with factors like incidence angle, sweep angle and vortex strength playing crucial roles (Lee and Ho, 1990).

2.1.3. Vortex breakdown

Vortex breakdown is a complex and unresolved challenge in fluid mechanics. The core of a leading-edge vortex undergoes a sudden expansion in cross-sectional area as the angle of incidence surpasses a critical value, contingent on the wing's sweep angle. Upstream of this phenomenon, the flow exhibits steadiness, contrasting with the downstream region where unsteady flow phenomena are consistently observed (Délery, 1994; Gursul, 1994), as discussed in Section 2.1.4.

Despite the profound alterations in the flow field over a delta wing associated with breakdown, the overall strong circulatory flow pattern does not abruptly disappear when vortex breakdown occurs. Breakdown involves a sudden reduction in the axial and circumferential velocity, leading to a turbulent wake flow downstream (Lambourne and Bryer, 1961). More intricate measurements conducted by Kengelman and Roos,

1990 and Délery, 1994 reveal that along the vortex axis, the axial velocity component increases until the breakdown location, where it experiences an abrupt decrease. Within the vortex core, the total pressure loss remains relatively constant until it reaches the breakdown location, where it suddenly increases. The vortex region characterized by elevated total pressure losses diminishes until the breakdown point, then experiences a sharp increase and starts to include the entire vortex sheet. Subsequently, total pressure losses begin to decrease downstream of the breakdown. During breakdown, the initially x-direction vorticity, concentrated near the vortex core axis, tends to disperse into regions beyond the axis and reorients itself along a transverse direction (Gursul, 2005; Nelson and Pelletier, 2003).

Various forms of breakdown are identified in literature. Lambourne and Bryer, 1961 are the pioneers in differentiating between spiral and bubble-type breakdown, as depicted in Fig. 2.4. In a spiral breakdown, a rapid deceleration of the core flow occurs. Immediately downstream, the vortex core filament undergoes an abrupt bending, initiating a spiral motion around the axis of the structure and creating a distortion of the vortex core. This spiral structure may persist for one or two turns before transitioning into large-scale turbulence (Payne et al., 1987). For leading-edge vortices, the sense of the spiral winding is opposite to the direction of rotation of the upstream vortex. However, the winding's rotation aligns with the rotation of the upstream vortex. The bubble type is characterized by a stagnation point on the vortex axis, succeeded by an oval-shaped recirculation zone. The upstream portion of the recirculation zone can be nearly axisymmetric, with the core flow symmetrically spreading out at the stagnation point and smoothly passing around the recirculation zone. The downstream half is typically open and irregular, with the flow shedding from the aft end resembling the shedding from a blunt solid body (Payne et al., 1987). Payne et al., 1986 observe that the bubble is single-celled, with the recirculation flow moving upstream along the vortex axis. The bubble typically spans two or three upstream core diameters in length. Downstream of the bubble, the vortex becomes turbulent and rapidly diffuses with distance.

Understanding the flow parameters influencing these two types of vortex breakdown and unraveling the underlying physical processes of the breakdown mechanism remain among the most challenging fundamental research problems in fluid dynamics. As outlined in Section 1.2, this thesis aims to offer additional insights and potential explanations for this phenomenon through Hi-Fi data.

Numerous investigations have explored vortex breakdown's movement and sensitivity to internal and external parameters over delta wings and within vortex tubes. Breakdown must be initiated by a destabilizing factor, such as the adverse longitudinal pressure gradient in the vicinity of the trailing-edge, which, in turn, is contingent on factors like incidence and sweep (Lambourne and Bryer, 1961). Several theories have been proposed to elucidate the cause of vortex breakdown, encompassing analogies to a 2-dimensional boundary layer, hydrodynamic instability, and critical state (wave) theories (Délery, 1994; Escudier, 1988). Additionally, substantial efforts have been dedicated to theories positing the existence of a critical parameter or relationship at which stagnation and mass disorganization occur in the flow. These criteria typically hinge on internal parameters such as swirl velocity, axial velocity, and adverse pressure

gradient. They include a critical value of swirl ratio (or Rossby number), rooted in critical states theory and vortex stability (Robinson et al., 1994; Spall et al., 1987), a critical value of helical angle (Ashley et al., 1991; Mitchell and Délery, 2001), a switch in the sign of azimuthal vorticity (Brown and Lopez, 1990; Towfighi and Rockwell, 1993), and a critical value of circulation (Jumper et al., 1993).

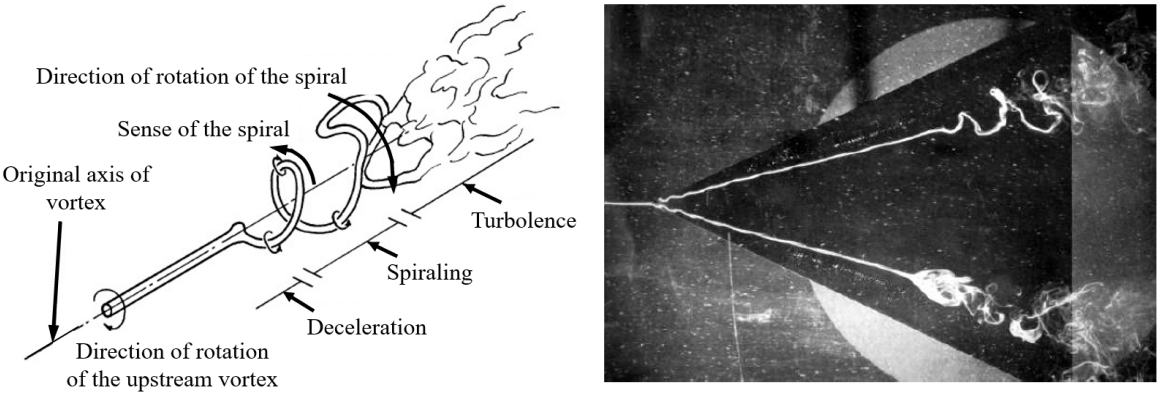

(a) Stages in the behavior of the axial filament and the orientation of the spiral during a spiral breakdown on the left.

(b) Visualization in a water tunnel depicting spiral (top) and bubble-type (bottom) vortex breakdown over a delta wing.

Figure 2.4: Insights into vortex breakdown (Lambourne and Bryer, 1961).

Numerous external factors significantly influence the behavior of vortex breakdown. Geometric considerations, such as the presence of center-bodies or sting geometries (Ericsson, 2003), sweep angle, and leading-edge properties (Lowson and Riley, 1995; Srigrarom and Kurosaka, 2000), as well as the proximity of wind tunnel walls (Allan et al., 2004, 2005), play also crucial roles. The vortex breakdown may also be contingent, to some extent, on the behavior of the secondary vortex, considering that it is identified by a twist in the secondary separation line. When the rate of vorticity feeding from the leading-edge surpasses what can be convected downstream, the vortex filaments constrict, resulting in breakdown (Huang and Hanff, 1992). Numerous potential causes have been then proposed to account for this phenomenon. However, a universally accepted explanation has yet to be established.

2.1.4. Unsteady flow phenomena

The vortex system over delta wings comprises flow structures characterized by unsteadiness across various scales, which include nonlinear interactions. An understanding of the unsteady behavior in delta wing flows can be drawn from the literature. Gursul, 1994 extensively reviews the primary unsteady elements in delta wing flow. Several concepts are briefly introduced for clarity and completeness, even though unsteady effects are not the focus of this thesis. Understanding these fundamental principles, however, aids in comprehending the complexity of this phenomenon.

- Helical mode instability of vortex breakdown: characterized by spiral-type vortex breakdown at typical Reynolds numbers and ratios of vortex-induced to free-stream velocity, the vortex core flow experiencing burst exhibits helical mode instability (Breitsamter, 2008; Lambourne and Bryer, 1961).
- Shear layer instabilities (Kelvin-Helmholtz instability): at high Reynolds numbers, the shear layer rolls up periodically, forming discrete vortical substructures that feed into the primary vortices (Lowson, 1991).
- Vortex shedding: observed at high angles of attack, it occurs when the vortex breakdown location reaches the wing apex, with vortices periodically shed from the trailing-edge in a symmetric mode (Rediniotis et al., 1993).
- Vortex core rotation (vortex wandering): upstream of the vortex breakdown, significant velocity fluctuations are observed in the vortex core, even without breakdown. These fluctuations correlate with the Kelvin-Helmholtz instability and are explained by a Biot-Savart induction of the small-scale vortices on the primary vortex (Gursul and Xie, 2000; Gursul, 1994).
- Vortex breakdown oscillation: the breakdown location of the vortex exhibits unsteady fluctuations along the vortex axis. This motion, which is anti-symmetric on the two halves of a delta wing, may lead to an undesired periodic rolling moment, as the oscillation frequency is significantly lower than that of the helical mode instability (Délery, 1994; Gursul and Yang, 1995).

Menke et al., 1999 performed an analysis of the vortex-dominated flow behavior and a schematic of the frequency spectrum was created to classify the unsteady frequencies. Characteristic frequencies can be associated with each of these phenomena. The majority of the frequencies assigned to the helical mode instability fall between a Strouhal number $St = 1 - 2$ and similarly, for the oscillation of vortex breakdown location, the majority of the investigations show this to occur between $St = 0.04 - 0.2$. The Strouhal number is a dimensionless number that describes oscillating flow mechanisms. It is defined as follows

$$St = \frac{fL}{U} \tag{2.1}$$

where f is the frequency of vortex shedding, L is a characteristic length, and U is the velocity of the flow. Further insights into the unsteady behavior of flow over delta wings are provided by Gursul, 2004, 2005.

2.1.5. Transonic vortical flows: compressibility effects

The role of flow compressibility in the evolution and development of vortex flows presents an additional fluid dynamics characteristic of significance. Compressibility effect are determined by the Mach number, Ma. It is a dimensionless ratio, defined as the speed of an object, U, divided by the speed of sound, c, as follows

$$Ma = \frac{U}{c}. \tag{2.2}$$

In the context of high-performance aircraft, which predominantly operate in high subsonic ($Ma < 1$), transonic, and supersonic regimes ($Ma > 1$), the impact of compressibility becomes critical. The speed of sound in an ideal gas is given by

$$c = \sqrt{\gamma RT} \tag{2.3}$$

where γ is the adiabatic index (also known as the heat capacity ratio, C_p/C_v, where C_p is the heat capacity at constant pressure, and C_v is the heat capacity at constant volume), R is the specific gas constant, and T is the temperature of the gas. The specific gas constant R and the adiabatic index γ vary depending on the gas. For dry air at standard conditions, γ is approximately 1.4, and R is approximately $287 J/(kgK)$. This relationship indicates that the speed of sound increases with the square root of the temperature, showing that sound travels faster in warmer air. In air at sea level, at a temperature of $293.15K$, the speed of sound is approximately $343 m/s$.

Compressibility primarily influences the stability and structure of the vortex. As the free-stream Mach number is elevated to transonic levels, $Ma > 0.7$, the vortical flow undergoes a transition and exhibits behavior different from that of the subsonic regime. In the experiments conducted by Erickson and Rogers, 1987, an increase in Mach number from 0.4 to 0.95 results in a notable transformation of the leading-edge vortex. The vortex assumed a flatter, more elliptical shape, progressively approaching the wing's surface. Additionally, as the Mach number increases across the transonic regime, the suction induced on the wing's surface by the leading-edge vortices diminishes due to a reduction in the up-wash generated by the leading-edges.

Moreover, as the Mach number increases, the flow locally becomes supersonic, leading to shock waves that further modify the behavior of the leading-edge vortices. Stanbrook and Squiref, 1964 establish a correlation between the change in the behavior of the leading-edge separated flow by considering the Mach number and the incidence, both normal to the leading-edge, defined respectively as

$$M_N = M_\infty \sqrt{1 - \sin^2(\Lambda)\cos^2(\alpha)} \quad \text{and} \quad \alpha_N = \tan^{-1}\left(\frac{\tan(\alpha)}{\cos(\Lambda)}\right). \tag{2.4}$$

Utilizing these flow parameters, the flow behavior could be categorized into two primary types: separated and attached. Miller and Wood, 1984 extend the consideration of flow types over delta wings to transonic and supersonic regimes based on experimental results for various delta wings with different sweep angles, Mach numbers, and angles of incidence. Their analysis classify the flow into six types of behavior, also characterized by the normal Mach number and incidence used by Stanbrook and Squiref, 1964, leading to a redefined classification diagram depicted in Fig. 2.5. Transonic flow over delta wings generally falls into the category of leading-edge separation. This flow regime is characterized by the formation of leading-edge vortices and the emergence of shock waves, which are dependent on the Mach number.

A multitude of investigations, including both experimental and numerical studies, scrutinize the occurrence and dynamics of shock waves in vortical flows under transonic conditions (Donohoe and Bannink, 1997; Donohoe et al., 1995; Longo, 1995). These

studies document several shock-wave systems, and among them, two primary systems are identified: the cross-flow shock, positioned underneath the primary vortex at a relatively constant span-wise location just outboard of the primary suction peak, and the rear/terminating shock, located on the aft section of the wing, close to the trailing-edge and perpendicular to the plane of symmetry. Fig. 2.6 shows the behavior of these shocks in the flow, drawing insights from experiments conducted on a 65° delta wing at $Ma = 0.8$ (Donohoe and Bannink, 1997).

The cross-flow shock, also known as the separation shock, is theorized to induce secondary separation beneath the primary vortex. As incidence increases for a specific Mach number, the shock materializes beneath the vortex, generating a substantial adverse pressure gradient that leads to boundary layer separation. This phenomenon explains the inward movement of the secondary separation previously discussed. Although cross-flow shocks may manifest as tightly contoured pressure coefficient regions in surface isobar plots, their position may not be distinctly discerned in span-wise pressure coefficient distributions.

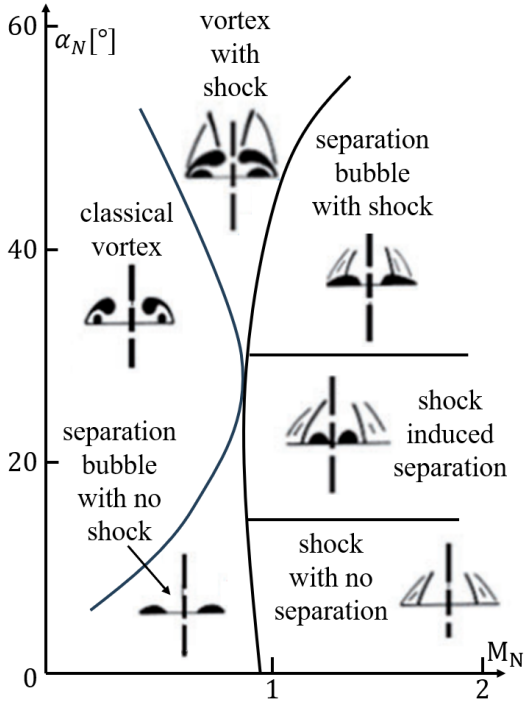

Figure 2.5: Categorization of flow behaviors over delta wings (inspired by Miller and Wood, 1984).

The presence of the rear shock is identified through the analysis of the chord-wise pressure coefficient distribution along the plane of symmetry. At low angles of incidence and low Mach numbers, the distribution gradually decreases toward the trailing-edge as the flow conditions approach free-stream conditions. However, at moderate angles of incidence and increasing Mach numbers, a sharp change in distribution near the trailing-edge signifies the presence of a shock wave in this region. The rear shock appears perpendicular to the symmetry plane at the wing's centerline but then curves downstream toward the primary vortices, seemingly intersecting the vortex region. Side-view visualizations reveal that the shock, starting perpendicular to the wing surface at the symmetry plane, curves upward toward the apex before returning to a perpendicular direction until it dissipates. The rear/terminating shock can exist for low to moderate angles of incidence without vortex breakdown. Donohoe and Bannink, 1997 hypothesize that the shock wave is situated above the vortex region, seemingly not interacting with the core. However, the dynamics at this point remain poorly understood, and conclusive knowledge about interaction is lacking. Insights from the study of the interaction between longitudinal vortices and normal shocks in supersonic flow suggest that a vortex can pass through a normal shock without being weakened sufficiently to induce breakdown (Kalkhoran and Smart, 2000).

The presence of these shock-wave systems in the flow introduces intricate interactions (Délery, 1994). This complexity becomes crucial when examining the behavior of vortex breakdown in transonic flows. It differs significantly from that observed in subsonic vortical flows, where the onset of breakdown is relatively gradual with increasing incidence (Jobe, 2004). A thorough investigation of the delta wing flow behavior can be performed by conducting an in-depth analysis of the VFE-2 experimental datasets.

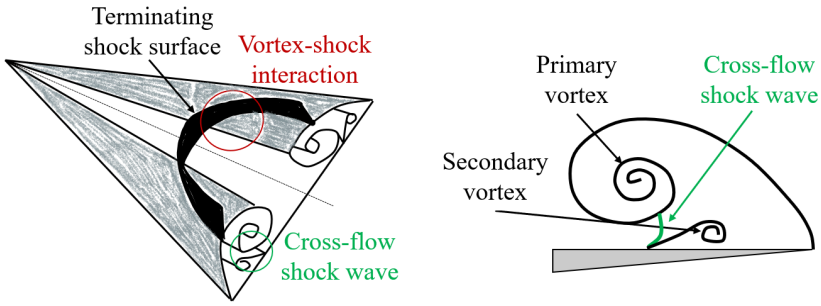

Figure 2.6: Proposed positions and shapes of shock systems over transonic delta wings: embedded cross-flow shock and rear/terminating shock (inspired by Donohoe and Bannink, 1997).

2.1.6. Vortex flow experiment

The Vortex Flow Experiment is a notable research project in aerodynamics, particularly focusing on the characteristics of vortex flow over delta wings. The geometry utilized in the VFE-2 study is initially examined in experiments conducted by Chu, 1996a,b,c,d at the National Transonic Facility (NTF) of NASA Langley. These investigations focus on a delta wing with a $\varphi = 65°$ sweep, featuring four types of leading-edge profiles: one sharp and three rounded with varying radii. The geometry of all leading-edge profiles is defined analytically. Fig. 2.7 illustrates the wing positioned within the NTF wind tunnel, along with detailed geometric information. The experiments span a comprehensive range of conditions, encompassing subsonic and transonic velocities, as well as test and flight Reynolds numbers.

Considering the purpose of this dissertation, only the sharp leading-edge profile at transonic conditions is considered, with further details provided in Chapter 5. In the study of transonic flow over sharp leading-edge wings ($Ma = 0.85$, $Re = 6 \times 10^6$), a significant chord-wise variation in flow structure is observed (Chu, 1996a). With increasing angles of incidence, the suction peak intensifies and shifts inboard, especially noticeable between 19.6° and 20.6°. Beyond 20.6°, secondary peaks emerge without inboard movement. A critical observation is the collapse of the primary vortex suction peak and disappearance of secondary peaks and cross-flow shock at angles equal to or greater than 24.6°, indicating vortex breakdown.

The findings of Konrath et al., 2006, 2013 involve a detailed analysis of aerodynamic phenomena on the VFE-2 delta wing utilizing Pressure-Sensitive Paint (PSP) and Particle Image Velocimetry (PIV) techniques. The study reveals how vortex structures

form and evolve, particularly noting the significant effects of changes in flow conditions. A vital aspect of the research is its exploration of vortex breakdown. As the incidence rises, the magnitude of the suction peaks increases. The inboard motion of the vortical system is also observable. However, the most prominent feature is the sudden asymmetric breakdown at 24.3°, where it unexpectedly occurs on the right side of the wing. This asymmetry in breakdown aligns with NASA data for a similar Mach number, although the critical onset angle is slightly higher (Chu, 1996a). The experimental tests consistently show this behavior for other transonic conditions. The asymmetry always appears on the same side of the wing, indicating the potential sensitivity of transonic vortex breakdown to surface disturbances within experimental tests. However, as also investigated by Chu, 1996a, this behavior transitions to a symmetric breakdown with an increase in the angle of incidence. It is also noted that the PSP suction peak heights are underestimated due to temperature effects. Furthermore, in contrast to the observations made by Donohoe and Bannink, 1997, Konrath et al., 2006 reports the presence of two terminating shocks: one close to the sting tip curving downstream and a second located over the sting between the x/c_r = 0.8 and 0.9 streamwise locations. A curving of the vortex core trajectory is observed in the vicinity of the sting shock from these tests.

Analysis of cross-flow behavior upstream and downstream of breakdown can be inferred from the PIV results. For the post-breakdown case, α = 25.7°, a secondary vortex is evident under the vortex, near the leading-edge. The breakdown appears to occur between x/c_r = 0.6 and 0.7, and the flow behavior shifts to a large region of reversed flow, expanding downstream and exhibiting a relatively circular nature. Inboard this breakdown region the flow remains supersonic and accelerating.

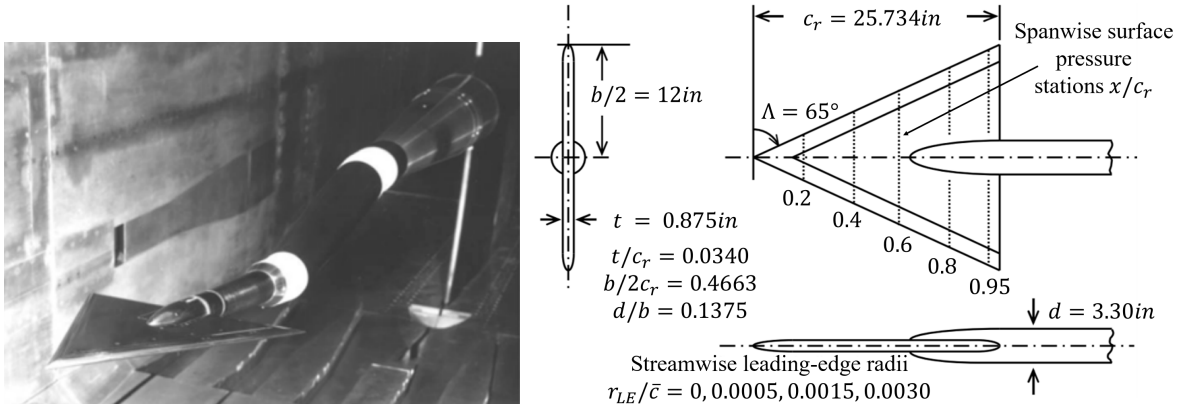

(a) Wing in NTF Facility (Chu, 1996a). **(b)** Wing geometry (adapted from Luckring, 2013).

Figure 2.7: VFE-2 65° delta wing configuration.

A critical repository of information on the state-of-the-art in numerical simulations of vortex flows is also included in the VFE-2, where internationally recognized academies, research establishments, and industries apply their best practices to a uniform wing geometry (Fritz and Cummings, 2008). The outcomes of these experiments provide,

for example, a crucial foundation for the studies conducted by Luckring, which investigate the effects of Reynolds number (Luckring, 2002a,b) and compressibility (Luckring, 2004) on wings with both sharp and rounded leading-edges. Significant discrepancies are noted by comparing steady surface pressure measurements with numerical results in prior extensive research (Crippa and Rizzi, 2008; Cummings and Schütte, 2013; Fritz and Cummings, 2008). Significant numerical challenges include predicting the breakdown type, position, vortex structure, development stage, and suction levels. More pronounced deviations from experimental data are observed in the breakdown position and vortex development with increasing angle of attack. These discrepancies vary across different numerical grids, turbulence model definitions, and solver implementations, indicating a fundamental source of error associated with the Boussinesq assumption.

At transonic conditions, discrepancies are primarily found in the breakdown strength and position, closely tied to the shock wave's position on the wing's upper surface (Fritz and Cummings, 2008; Schiavetta et al., 2009). This shock wave coincides with the vortex's transition to a chaotic wake flow. Employing Detached Eddy Simulation (DES) and Delayed DES (DDES) models may offer more detailed insights into the impact of small-scale turbulence on the vortex flow (Cummings and Schütte, 2013). However, this approach increases computational costs and complexity in setting up stable numerical simulations with adequately refined meshes and settings. Furthermore, it does not assure improved alignment of numerical solutions with experimental data (Cummings and Schütte, 2013). For this reason, as outlined in Section 1.2, this manuscript initially applies and validates the HRL approach, which aims to acquire Hi-Fi data using the SA turbulence model, to the VFE-2 delta wing. Subsequently, this approach is employed for the more complex flow analysis of the ADS-NA2-W1 configuration. Further insight into previous CFD studies for delta wing flows are given in Section 2.2.1.

2.1.7. Generic delta wing planforms at transonic speeds

To achieve a more practically relevant configuration, the lambda-shaped SACCON is investigated within the NATO-RTO task group AVT-161 (Cummings and Schütte, 2012). This configuration exhibits leading-edge contours in the span-wise direction, incorporating sharp and rounded segments with radii significantly larger than those in the VFE-2 cases. Consequently, it results in a complex system of primary and secondary vortices, extensively documented for this specific configuration but posing challenges for turbulence models regarding accurate reproduction. With a heightened emphasis on the separation process, the NATO-STO task group AVT-183 investigate a diamond-shaped geometry with rounded leading-edges (Luckring et al., 2016). Another noteworthy configuration, the SAGITTA also adopts a diamond-shaped wing and incorporates span-wise variations of the leading-edge contour to control the formation of the leading-edge vortex (Seifert, 2012).

Within the framework of the NATO-STO AVT-316 task group (Hövelmann et al., 2020; Pfnür and Breitsamter, 2019), a generic multi-swept delta wing configuration is subject to both experimental and numerical investigations (Hitzel et al., 2020; Schütte

and Marini, 2020). The project aims to investigate the vortex interaction effects relevant to military air vehicle performance (NATO Science and Technology Organization, 2018), by using CFD simulations and wind tunnel experiments across subsonic, transonic, and supersonic conditions. These configurations are particularly relevant for combat aircraft, which often operate in high angle of attack conditions, necessitating designs that maintain stability and control even in extreme flight regimes. Geometry and flow condition variations are included, where differing wing sweep angles notably enhance flow complexity. The geometric discontinuity at the leading-edge corresponds to vortices generation, each varying in strength, stability, and nature, influenced by the sweep angles from which they originate. Furthermore, these vortices interact or merge in various ways depending on the angles of attack and side-slip. Additionally, as mentioned above, in transonic flow conditions, the shock-vortex interaction further contributes to this complexity. The primary goals are to deepen the understanding of vortex-related flow phenomena and enhance the predictive accuracy of current CFD methods, particularly in turbulence modeling. The task group's findings are extensively disseminated across the scientific literature. For instance, Hitzel, 2022a presents an overview of the research program, whereas Hitzel, 2022b provides a detailed summary of the findings. Additionally, Russel et al., 2022 delves into the analysis of results under transonic conditions, and Schütte and Werner, 2022 investigates the effects of turbulence models on the prediction of transonic vortex interactions.

Hövelmann et al., 2020 introduce a combined experimental and numerical investigation based on URANS computations into the aerodynamics of a generic triple-delta wing configuration at transonic speeds. The focus is on understanding vortex flow phenomena, including vortex development, vortex-vortex and vortex-shock interactions. The experimental investigate the ADS-NA2-W1 triple delta wing, which consists of a 52.5° sweep in the negative strake, a 75° sweep in the mid-wing section, and a 52.5° sweep in the rear wing section. The wind tunnel model for this planform, characterized by a thickness of $8mm$, is equipped with a sharp leading-edge. Figure 2.8 and Table 2.1 illustrate the specific characteristics of the aircraft configuration. The results include flow conditions at $Ma = 0.5$ and 0.85, covering different angles of attack (up to 40°) and non-symmetric flows (with non-zero side-slip angles). The experimental datasets includes force and moment measurements and digital representations of processed steady PSP measurements. These PSP data provide a high-resolution pressure distribution on the surface, offering a valuable experimental basis for validating the numerical results. The detailed illustration of the experimental data is presented in Chapter 6, where they are compared with the numerical results obtained in this dissertation.

Findings indicate that the experimental and computational results generally agree at lower to medium angles of attack. However, as the angle of attack increases, discrepancies emerge, particularly in predicting vortex breakdown effects. These discrepancies are more pronounced in lateral motion cases, where the experimental and numerical results emphasize different predictions of vortex breakdown effects. The CFD computations presented by Hövelmann et al., 2020 employ the one-equation Spalart-Allmaras with negative turbulent viscosity correction (SAneg) turbulence model. A detailed discussion of this specific turbulence model is provided in Section 3.4, as it constitutes a focal point of this dissertation. The discrepancies underline the need for further

research, possibly involving different turbulence models or enhancing existing ones. The application of alternative turbulence models demonstrates the sensitivity of flow phenomena to these models (Schütte and Marini, 2020). This observation is critical as it indicates that current state-of-the-art CFD tools might inaccurately predict flow characteristics, leading to substantial uncertainties regarding the stability and control of such planforms during preliminary development phases.

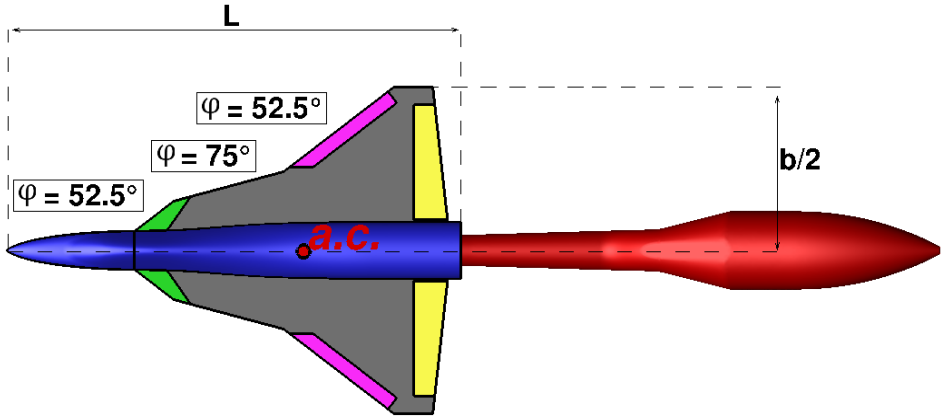

Figure 2.8: ADS-NA2-W1: triple delta wing configuration

Table 2.1: Geometric details of the ADS-NA2-W1

Model length	Root chord length	Mean aerodynamic chord	Wing span	Moment reference point aft of nose	Wing thickness	Wing reference area
$[m]$	$[m]$	$[m]$	$[m]$	$[m]$	$[mm]$	$[m^2]$
0.580	0.401	0.234	0.417	0.380	8	0.082

2.1.8. Vortex interactions

Within the framework of the NATO-STO AVT-316 task group, the complexity of vortex interactions in high-performance aircraft, especially those featuring multi-swept delta wing configurations, is investigated. The multiple wing sections with different sweep angles lead to the generation and interaction of various vortical structures, as detailed in literature (Hitzel et al., 2020; Schütte and Marini, 2020). While horizontal surfaces downstream of the main wing do not significantly affect other vortical structures, vortices from canard wings or deployed slats may interact or merge with the main wing vortex, depending on flow conditions. Furthermore, additional complexity arises in configurations with rounded leading-edge geometries, where multiple vortices may separate at different positions along the leading-edge. The interaction and merging of these vortices increase then the flow complexity, introducing cross-dependencies

in their evolution. The vortices can interact in various ways, leading to complex aerodynamic behaviors. The interaction can change the aircraft's lift, drag, and stability. The interaction of vortices can enhance lift, but it can also lead to increased drag or potentially dangerous flight conditions like vortex-induced vibrations or buffeting. Understanding vortex interactions is crucial for the design and optimization of aircraft for improved performance, efficiency, and safety.

In a straked double-delta wing, the vortex-vortex interaction evolves progressively with the angle of attack. At low angles of incidence, the vortices show minimal interaction. However, as the angle of attack increases, the interaction strength grows due to the cross-sectional increase of the vortices (Brennenstuhl and Hummel, 1982). Eventually, the inner vortex merges into the outer vortex, with the merging position moving upstream as the angle of attack increases, as illustrated in Fig. 2.9. These configurations have different sections with varying sweep angles. The point where the sweep of the wing changes is known as the kink and it is a critical design feature that influences the aerodynamic performance of the aircraft.

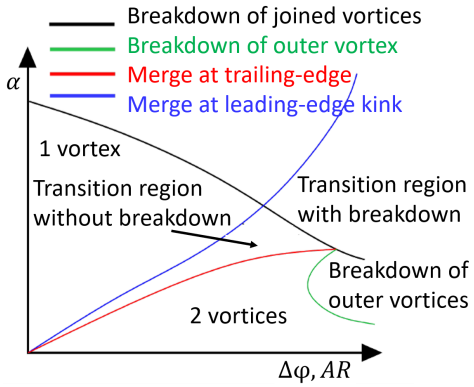

Figure 2.9: Vortex development on double delta wings: influence of leading-edge kink angle, $\Delta\varphi$, and angle of attack, α (inspired by Brennenstuhl and Hummel, 1982).

A parameter closely associated with these phenomena is the kink angle $\Delta\varphi$, defined as the difference between the strake and aft wing sweep angles. The angle of attack at which merged vortices' breakdown decreases with increasing $\Delta\varphi$ as the outer vortex becomes less stable. Employing multiple vortical flows increases the complexity of physical understanding and predicting aerodynamic behavior. This complexity challenges numerical methodologies and physical modeling, such as turbulence models, in maintaining consistent accuracy across varying flow conditions. The vortex-vortex interaction is primarily investigated in Chapter 6, where the CFD simulations conducted on the ADS-NA2-W1 configuration are discussed at various angles of attack.

2.2. Advancements in CFD: turbulence modeling

A review of the state-of-the-art in CFD as it pertains to delta wing flows is presented. This discussion includes an examination of the RANS turbulence models, with a focus on one and two-equation models, reflecting their utilization in this dissertation.

2.2.1. Previous CFD studies for delta wing flows

One of the most critical considerations in applying CFD, especially for delta wings, is the selection of a turbulence model (Cummings et al., 2003a). Various approaches and

methods exist for turbulence treatments and modeling, differing in complexity, accuracy, and computational expense. In ascending order of complexity, these techniques include inviscid, laminar, RANS, hybrid RANS/LES, LES, and DNS. The choice of a turbulence model typically involves a trade-off between computational expense and solution accuracy. Chapter 3 elaborates on various techniques and approaches, with particular emphasis in Section 3.4 on the methodology adopted to achieve this dissertation's outcomes.

The following section provides an overview of CFD studies focusing on vortex flow over delta wings, considering the advantages and disadvantages of each numerical approach. While informative, it is essential to note that this review may not cover the entirety of the available literature and predominantly emphasizes simulations at high angles of attack, where vortex breakdown occurs. The RANS and HRL methodologies are examined in greater detail, as these are the approaches utilized in this thesis. Consequently, the literature review is primarily focused on the VFE-2 and the ADS-NA2-W1 configurations, as detailed in Sections 2.1.6 and 2.1.7, respectively.

Inviscid methods: solving the Euler equations

Inviscid methods, notably through solving Euler equations, are extensively applied in simulating flow over delta wings, favored for their reduced computational demands compared to Navier-Stokes solutions. Despite their inability to account for boundary layers and predict separation, these methods are particularly effective for delta wings with sharp leading-edges, where separation is inherently fixed, thereby providing reasonable flow approximations (Allan et al., 2005).

Pioneering studies by Rizzi and Eriksson, 1985 illustrate the Euler equations' effectiveness in capturing leading-edge separation and vortex formation. The critical role of numerical dissipation in defining separation at sharp edges and the necessity for dense grids to accurately model vortex-shock interactions are emphasized (Murman and Rizzi, 1986; Rizzi and Eriksson, 1985; Rizzi and Purcell, 1987).

The capacity of Euler equations to predict vortex breakdown, albeit with outcomes highly dependent on grid resolution affecting vortex strength and breakdown characteristics, is validated by Newsome, 1986. Further researches explore the dynamics of vortex breakdown, highlighting the influence of grid refinement on the phenomenon (Kumar, 1999). J. Müller and Hummel, 1999 report the observation of periodic oscillations in aerodynamic forces attributed to vortex breakdown, significantly affected by numerical damping.

Finally, the comparative analysis of Euler and Navier-Stokes solutions points out the inviscid methods' shortcomings, and accentuates the importance of viscous effects for an accurate depiction of flow separation and vortex breakdown mechanisms (Agrawal et al., 1992; Rizzi and B. Müller, 1988).

Laminar methods: solving the Navier-Stokes equations

Laminar flow modeling, which accounts for viscosity effects while neglecting turbulence, is pivotal for elucidating flow dynamics over delta wings, especially under conditions

dominated by viscous effects. This methodology demonstrates the laminar boundary layer's heightened sensitivity to adverse pressure gradients, resulting in more pronounced separation phenomena than those observed in turbulent flows (Agrawal et al., 1992). Nonetheless, the applicability of such computations is primarily at low Reynolds numbers, where viscous forces significantly outweigh inertial forces.

Comparative analyses of Euler and laminar Navier-Stokes solutions highlight distinct differences in the mechanisms of vortex initiation and separation over delta wings with rounded edges (Rizzi and B. Müller, 1988). Laminar models, initiating vortices at the wing apex, align more closely with experimental findings than Euler solutions, underscoring the critical influence of grid resolution and axial pressure gradients on accurately predicting vortex dynamics (Ekaterinaris and Schiee, 1990a,b).

Further research into the unsteady characteristics of flow following vortex breakdown uncovers intricate interactions between breakdown structures and the wing boundary layer (Gordnier, 1997; Visbal, 1996). Time-accurate laminar simulations reveal detailed behaviors of spiral and bubble-type breakdowns, elucidating the complex onset and evolution of vortex breakdown over delta wings (Cummings et al., 2003b,c; Visbal and Gaitonde, 1999). However, as the flow transitions towards turbulent, the necessity for employing advanced modeling techniques becomes paramount to accurately depict the complex vortex dynamics inherent to such conditions.

Reynolds Averaged Navier-Stokes

For enhanced accuracy in computational solutions of delta wing flows, it is imperative to consider and model the turbulent behavior of the flow. Reynolds averaging, which simplifies the instantaneous Navier-Stokes equations into mean flow equations, represents a prevalent approach for treating turbulence. The principles and applications of Reynolds averaging, along with several turbulence models, are elaborated in Chapter 3. Not all turbulence models are suitable for analyzing delta wings and vortical flows. Consequently, researchers dedicate substantial efforts to identifying appropriate models and modifying existing ones to yield the most accurate results compared to experimental data.

Morton et al., 2002 examine the impact of turbulence modeling on the unsteady behavior of flow over a 70° semi-span delta wing, operating at $Ma = 0.069$, $Re = 1.56 \times 10^6$, and $\alpha = 27°$. The investigation utilizes five turbulence models: three RANS models (SA, SA-RC, SST) and two HRL approaches based on the SA and Menter's SST models. The analysis of the frequency content of unsteady results indicates that while the SA and SST models struggled to resolve the majority of the spectrum's frequencies, the SA-RC model exhibits an improved spectrum due to its correction, which reduced turbulence dissipation within the vortex core. However, this model faces challenges with specific frequencies associated with post-breakdown turbulence scales. A comparison with experimental data by Mitchell et al., 2000 reveals that all turbulence models, except the SST, produce breakdown positions comparable to experimental observations.

Fritz and Cummings, 2008 provide insights into the VFE-2 delta wing flows. They perform RANS simulations, initially with algebraic turbulence models and subsequently

with one- and two-equation turbulence models. There are good agreement between numerical results and experiments for subsonic sharp leading-edge test cases, but predicting vortex breakdown remains challenging. The simulations are able to predict secondary (and even tertiary) vortex separation. However, issues with turbulence models lead often to poor predictions of surface pressures, especially regarding the location and strength of the secondary vortices. In transonic conditions, the shock position is often predicted too far upstream, leading to premature vortex breakdown compared to experimental observations.

Crippa and Rizzi, 2008 focus on CFD analysis of the VFE-2, involving simulations across a range of Reynolds numbers at subsonic speeds and low incidences, and comparing the results to experimental data. The numerical simulations reveal a wide, thin inner vortex forming early in the apex region, attaching to the symmetry plane. However, these findings differ from experimental data, which suggest the inner vortex is located further outboard, stronger, and more compact than the numerical predictions. The computations consistently under-predict the strength of the inner vortex at its origin, leading to mismatches in its further development. This under-prediction aligns with the detailed analysis of skin friction lines, where there is no distinct convergence of lines leading to the formation of inner vortical flow. The recognized separations are primarily due to primary and secondary leading-edge vortices. The need for time-accurate computations is justified, as the formation of complex multi-vortex systems and time-dependent sub-vortices upstream of primary separation are crucial for understanding and accurately modeling these flow characteristics.

Rizzi et al., 2009 focus on numerical simulations of the F-16XL aircraft using various CFD solvers and RANS methods. They compare simulations with flight-test measurements across different flight Reynolds/Mach number combinations. The challenges and discrepancies encountered in the simulations, particularly in replicating complex flow phenomena like vortex breakdown and the interaction of vortices over the aircraft, are emphasized. Specifically, for FC70, a high-Mach, high-Reynolds condition, although there is a remarkable agreement among state-of-the-art computational tools, the agreement with actual flight measurements is not close. It is suggested that this discrepancy is due to the poor prediction of a concentrated leading-edge vortex and its interaction with a shock.

Schütte et al., 2012b analyze the SACCON UCAV configuration using wind tunnel experiments and numerical calculations. The basic flow pattern around the SACCON configuration, characterized by a 53° swept and rounded leading-edge, consists of an apex vortex and a tip vortex, separated by a primarily attached flow region at the leading-edge. With increasing angle of attack, the intermediate flow region disappears, leading to a flow dominated by two vortices. This change in flow topology is responsible for a characteristic dip in the pitching moment slope as AoA increases. Schütte et al., 2012b emphasize the effectiveness of the SA turbulence model in accurately predicting aerodynamic coefficients and surface pressure distributions, highlighting its suitability for complex aerodynamic analyses. Slight differences are noted in the AoA at which the dip in the pitching moment curve occurs. Numerical simulations significantly overpredict the pitching moment coefficient at very high AoAs (above 20°), likely due to vortex

breakdown, indicating a need for improvement in numerical simulations to account for this phenomenon.

Schütte et al., 2012a conduct a comprehensive investigation of the complex aerodynamics of the X-31 aircraft utilizing various CFD solvers, including the DLR-TAU Code. They perform a detailed comparison of numerical results obtained using a range of RANS turbulence models, such as SA, SA-RC, $k-\omega$, and others, against experimental data. The focus is on the necessity for precise prediction of complex flow phenomena, especially around fighter aircraft configurations at high angles of attack, where intricate vortical structures are prevalent. The research emphasizes the crucial role of amalgamating CFD predictions with experimental data to deepen aerodynamic understanding and enhance the model validation process.

Schütte and Marini, 2020 focus on the computational analysis of the sharp leading-edge triple delta wing NA2-W1 fighter configuration. The study highlights the significant impact of grid resolution on the representation of suction peaks of vortices and pressure recovery near attachment lines. Although a final grid convergence is not achieved, a medium-size grid is used for the analysis, suggesting a need for further grid assessment after selecting an optimal turbulence model. The pitching moment coefficient is significantly influenced by the chosen turbulence models. The SA turbulence model, compared with two versions of the $k-\omega$ models and a Reynolds-Stress turbulence model, shows significant differences in predicting flow topology. The SA turbulence model fails to provide accurate flow physics and aerodynamic performance. The $k-\omega$ models yields reasonable results in some areas but inaccurate in others, such as overpredicting suction in secondary vortices. The Reynolds-stress model provides the best overall results across the range of angle of attack and side-slip.

While classical RANS models are computationally efficient, their ability to accurately predict highly vortical flows, especially at high angles of attack and side-slip, is limited. EVMs often struggle to accurately predict the fundamental characteristics of vortices, primarily due to the misprediction of eddy viscosity production/destruction in vortex flow regions. This limitation, inherent in standard RANS models, typically results in excessive eddy viscosity, affecting the vortex's size, type, and velocities, and leading to significant discrepancies in suction peak and pressure distribution compared to experimental findings. Numerical solutions inaccurately predict vortex breakdown in terms of position and intensity, negatively affecting the accuracy of delta wing aerodynamic coefficients. This constraint generates interest across academic and industrial communities in advancing the accuracy of RANS models, notably within the aerospace industry. Despite advancements in computational power, turbulence modeling remains then a vital area of research aimed at accelerating engineering design processes. This topic is further explored in Section 2.2.2, which provides a comprehensive review of modifications to the RANS model. Additionally, Section 2.3.3 highlights innovations that incorporate machine learning techniques to improve classical models.

LES and DNS

The most accurate methods for predicting turbulent flows are LES and DNS. DNS directly solves the Navier-Stokes equations for all scales of motion, which makes it

highly accurate but computationally expensive, typically limiting its application to low-Reynolds number flows (Shan et al., 2000; Visbal and Gordnier, 2003). LES simulates large-scale flow structures directly while modeling smaller scales, allowing for coarser grid resolutions and application to higher Reynolds numbers, albeit with greater computational demands than RANS methods.

Mary, 2003 employ LES to study vortex breakdown over a delta wing, using localized mesh refinement and various wall treatments to explore near-wall effects, revealing the sensitivity of flow behavior to wall conditions and mesh resolution. Similarly, Shan et al., 2000 and Visbal and Gordnier, 2003 utilize DNS to investigate vortex shedding and the structure of vortical flows over delta wings, highlighting the technique's ability to capture intricate flow phenomena even at modest Reynolds numbers.

Despite their computational demands, LES and DNS have are feasible for detailed flow analysis of simple and selected test cases, particularly in studying complex phenomena like vortex breakdown and shear layer instabilities. However, the substantial computational resources required for these simulations often render them impractical for routine applications, especially at higher Reynolds and Mach numbers. In this context, the hybrid RANS/LES methodology offers a more feasible alternative, balancing accuracy with computational efficiency for complex flow conditions (Gordnier and Visbal, 2005).

Hybrid RANS/LES

To mitigate the demanding spatial and temporal requirements of LES, particularly within boundary layer regions, researchers employ HRL methods. These hybrid techniques leverage the strengths of RANS and LES by applying RANS models to boundary layer regions and LES to the rest of the flow domain. Hybrid RANS/LES emerges as a significant field in analyzing vortical flows, and many researchers assess this method to simulate delta wing flows. Further elaboration on the formulation of such methods is provided in Chapter 3.

Morton et al., 2002 simulate the flows over a 70° wing and compare RANS with two DES formulations based on the SA and SST models. Given DES's inherent sensitivity to time step size and grid resolution, they conduct both time accuracy and grid dependence studies. The DES methods are able to capture the full range of frequencies present in delta wing flows. Their analysis of vortex breakdown behavior further reveal that breakdown is more distinctly resolved in the DES solutions, concluding that DES methods provide a more accurate prediction of flow behavior, demonstrating their potential as a valuable tool for capturing complex turbulent flows over delta wings.

Mitchell et al., 2006 explore the presence of vortical substructures in delta wing flows using DES based on the SA turbulence model. They conduct meticulous time step and grid resolution analyses, employing Adaptive Mesh Refinement to enhance grid resolution in critical areas, particularly within the vortex core region. The results show good concordance with experimental observations, revealing small, spatially stationary sub-vortices in the shear layer on the finest and adapted grids. These structures identified in the adapted grid solution mirror the experimental results more closely than

those on the finest grid, suggesting that the manifestation of these structures is highly grid-dependent. While DES is endorsed for its solution accuracy, the study emphasizes the criticality of meticulous grid creation due to the significant sensitivity of the results to vortex region resolution.

Goertz, 2003; Goertz and Le Moigne, 2003 conduct DES investigations on a 70° delta wing at a Mach number of 0.2 and a Reynolds number of 1.56×10^6. The study perform a time step analysis on a semi-span wing to expedite calculation times. Although the signal duration is insufficient to detect frequencies associated with vortex breakdown oscillation, flow visualizations in agreement with experimental data indicate an accurate prediction of the unsteady behavior of the breakdown location. Overall, the study concludes that while DES accurately predicts unsteady vortex breakdown locations, further research into grid refinement is necessary.

Riou et al., 2010 focus on the impact of compressibility on vortical flow over the VFE-2 delta wing at different Mach numbers (0.4 and 0.8) and an angle of attack of 25.5°. The simulations utilize a combination of DDES and Zonal DES approaches, enhancing the decay of eddy-viscosity in LES regions. The study highlights the influence of the Mach number on the leading-edge vortex core development. Notably, two perpendicular shock waves to the wing's symmetry plane are observed, with the shock at $x/c = 0.55$ interacting with the leading-edge vortex. This interaction results in a decrease in longitudinal velocity and Rossby number, indicating vortex breakdown. The presence of the normal shock wave leads to an earlier vortex breakdown in the transonic case. Additionally, five cross-flow shocks around the vortical flow are noted, with one shock moving laterally at frequencies characteristic of shock/boundary layer interactions. The HRL method demonstrate a commendable correlation with experimental data, enabling an in-depth analysis of phenomena not accurately discernible through experimental methods alone.

Tangermann et al., 2012 conduct DDES on the VFE-2 delta wing, achieving results that largely concur with experimental findings. They highlight the pivotal role of initial vortex formation in influencing the overall vortex system. High resolution in the apex region is crucial for accurate vortex development, while downstream areas can be modeled with coarser grids and smaller time steps. Discrepancies are observed between simulations and experiments, particularly in the predicted locations of vortex breakdown, which occurs further downstream and develops more suddenly in simulations. Accurate prediction of vortex behavior, especially vortex breakdown, is found to be contingent on fine resolution near the wing apex despite the fixed flow separation due to the sharp leading-edge.

Numerical simulations of the flow at subsonic conditions for the VFE-2 delta wing configuration with rounded leading-edges are carried out by Cummings and Schütte, 2013 using RANS and several hybrid turbulence models. The work focuses on the dual primary vortex flow topology and its sensitivity to varying angles of attack and Reynolds number effects. The simulated flow field resulting from SA-DDES simulations shows significant improvements compared to other hybrid turbulence model simulations, and the results are promising for understanding the flow field.

Peng and Jirasek, 2016 perform RANS and HRL computations, taking into account the flow around the VFE-2 delta wing at a low-speed subsonic Mach number $Ma = 0.14$ and an angle of attack $\alpha = 23°$. The HRL computations reproduce the mean flow more reasonably than the RANS computation, conducted with the SA model and the Explicit Algebraic Reynolds Stress Model (EARSM). The HRL approach enables a reasonable vortex evolution and bursting prediction as the flow approaches the wing trailing-edge, aligning better with experimental data than the RANS models. It adequately represents the presence of inner, primary, and secondary vortices in terms of the resolved instantaneous vortical flow structures.

A promising research contribution in the filed of HRL approach is also given by Zhou et al., 2019. The study focuses on simulating the turbulent flow around the VFE-2 delta wing at a low subsonic Mach number using the HRL approach. An automated mesh generation methodology is employed for a sharp leading-edge delta wing and the DDES approach is used with a shear layer adapted sub-grid scale model. The simulations employ three different mesh densities and compare the results with experimental data, highlighting the importance of mesh adaptation and resolution in capturing essential flow physics, especially in leading-edge and vortex core regions.

These studies collectively suggest that HRL approaches offer significant advancements in accurately simulating complex turbulent flows, particularly for configurations such as delta wings. These HRL methods demonstrate an enhanced capability to capture the intricate details of vortex formation, development, and breakdown. The importance of high-resolution meshing in critical areas like the wing apex for precise vortex prediction is underscored, while also acknowledging the method's sensitivity to grid and time step choices. Overall, HRL methods emerge as a promising tool for studying vortical flows, providing a balance between computational feasibility and the need for detailed flow physics representation, especially in areas where standard RANS models fall short.

2.2.2. RANS turbulence modeling: history and improvements

Historically, a diverse array of turbulence models have been proposed, spanning from rudimentary algebraic models such as Prandtl's mixing length hypothesis to comprehensive stress-transport models like the Launder–Reece–Rodi (Launder et al., 1975). Nonetheless, the escalated complexity of these turbulence models and their heightened computational demands when applied to practical technical challenges do not always correlate with a marked enhancement in solution quality. A review of several prevalent and widely adopted turbulence models can be found in literature (Wilcox, 1998). The following overview is concentrated on one and two-equation turbulence models, reflecting their utilization in this dissertation.

Over the past decade, one-equation turbulence models have gained significant attention. Their rising popularity is primarily attributed to their numerical simplicity in comparison to conventional two-equation models such as $k - \epsilon$ (Jones and Launder, 1972) and $k - \omega$ (Wilcox, 1988). While algebraic models, exemplified by the established Baldwin–Lomax model (Baldwin and Lomax, 1978), are computationally efficient, they often lack universality and omit specific effects like transport and diffusion. In contrast,

one-equation models are the most rudimentary form of turbulence models that account for transport effects, positioning them as a favorable middle ground between algebraic and traditional two-equation models.

As the state-of-the-art, the widely used one-equation model is formulated for the turbulent eddy viscosity ν_t by Spalart and Allmaras, 1992, prioritizing numerical stability. Subsequently, Menter, 1997 delineate a comprehensive technique for extrapolating one-equation models from their two-equation counterparts, culminating in a novel model rooted in the conventional $k-\epsilon$ equations. Additionally, Nagano et al., 2000 extrapolate another one-equation model from the low-Reynolds-number $k-\epsilon$ model. Their model register commendable performance against DNS and experimental data for wall-adherent flows such as boundary layers and planar wall jets.

The efficacy and predictive accuracy of numerous models, including the Baldwin–Barth, Spalart–Allmaras, standard $k-\epsilon$, $k-\omega$, and the SST (Menter, 1993) are extensively detailed in several studies (Spalart, 2000; Wilcox, 1988). As detailed in Section 2.2.1, RANS models frequently face challenges in predictive accuracy, and a universal solution to address their shortcomings has yet to be identified.

Over the years, turbulence modeling has seen numerous modifications and new approaches to enhance the fidelity of RANS models. A notable focus is addressing accuracy issues in complex flow scenarios like highly curved, rotating, or recirculating flows. Diverse curvature and rotation corrections are developed for RANS turbulence models over the years, even though introducing streamline curvature directly into model equations often fails due to the lack of Galilean invariance (Howard et al., 1980; Launder et al., 1977). For instance, Howard et al., 1980 explore $k-\epsilon$ model adjustments considering the Coriolis force, while Launder et al., 1977 introduce a term in the epsilon transport equation for curved boundary layers. Similarly, Degani and Schifft, 1986 identify and correct an over-prediction issue in the Baldwin-Lomax model. Shur et al., 2000 introduce a streamline curvature correction that modifies the source term of the SA model (SA-RC) by applying a correction function to the production term in the eddy viscosity transport equation. This modification is later adapted for the SST turbulence model by Smirnov and Menter, 2009, with correction constants calibrated for a global formulation. It significantly influences the vortex core and is highly responsive to the vortex characteristics and strength. However, while it is effective in improving solutions for many delta wing simulations, it is observed to be ineffective or even detrimental in other cases.

Recent researches in turbulence modeling highlight the potential of empirical and physical modifications to improve the accuracy of specific flow classes. These modifications progressively address increasingly complex flow scenarios, comparing their performance with experimental data. W. Zhang et al., 2010 implement a rotation correction based on the formulation by Hellsten, 1998, focusing on simplification and computational efficiency. Unlike the SA-RC model, which requires higher-order velocity derivatives, Zhang's correction is based on a general definition of the Richardson number and utilizes only first-order velocity derivatives. Arolla and Durbin, 2013 modify the production term of ω based on streamline curvature, following the concept of Reif et al., 1999.

Similarly, Stabnikov and Garbaruk, 2016 propose a correction that multiplies turbulent kinetic energy transport equation, showing improvements in various test cases, including vortex flows.

Asnaghi et al., 2019 comprehensively compare various curvature corrections concerning separating a Rankine tip vortex. The sensitivity of vortex separation to turbulence modeling is highlighted. Different rotation corrections have varying impacts on eddy viscosity distribution. X. Zhang and Agarwal, 2018 introduce a Richardson model-based correction to the model by Wray and Agarwal, 2015, demonstrating mild accuracy improvements without additional computational costs.

An alternative strategy involves the development of an optimized and enhanced turbulence model, using an existing database of Hi-Fi data. Menter et al., 2020 propose the Generalized $k-\omega$ model, highlighting the importance of minimizing other error sources and using experimental data for model adaptation. Moioli et al., 2018, 2022 aim to adapt the one-equation SA model specifically for delta wing applications using an experimental database and a gradient-based optimization process. However, since the model terms are modified to better agree with measured data from experiments, such development leads to very specialized turbulence models suitable only for specific applications.

As introduced in Section 2.2.1, EVMs based on Boussinesq's hypothesis, are developed to compute eddy viscosity from flow characteristics but struggle with accuracy in complex flows. These models, simplifying turbulence to kinetic energy and using eddy viscosity, neglect turbulence's anisotropic nature. The assumption that Reynolds stress aligns with the mean strain rate fails in vortical flows, such as those around delta wings. The concept, while widely adopted for its simplicity, falls short in conditions where stress and strain rates are misaligned or in situations of rapid stress redistribution, especially at high AoA and side-slip. Further details are given in Section 3.3.

Since the Boussinesq assumption limits the potential accuracy of RANS numerical simulation of vortex flows, different approaches are proposed to remedy some of the shortcomings of the linear eddy-viscosity models (Spalart, 2000). Pope, 1975 introduces a more realistic effective-viscosity formulation. It aims to better represent the turbulent viscosity, which is a key factor in determining the momentum transfer and mixing in turbulent flows. Pope's formulation enhances turbulence modeling by integrating turbulence anisotropy and strain rate effects into effective viscosity calculations. This approach, achieved by introducing additional transport equations or modifying existing ones, offers a more refined representation of turbulent flow physics. It accounts for the distribution of turbulent energy across various scales and directions, providing a more accurate depiction of turbulence's dissipative actions. By accounting for the anisotropy of turbulence, the effective-viscosity formulation can more accurately predict the behavior of turbulent flows, especially in complex scenarios where traditional models may fail.

Therefore, research efforts focus on incorporating non-linear terms into turbulence models. Shih, 1997 demonstrate accuracy improvements in swirling flows by including a cubic Reynolds stress-strain term in the $k-\epsilon$ model. Craft et al., 1996 further expand on the development of non-linear eddy-viscosity models. Dol et al., 2002 explore the

capabilities of non-linear eddy viscosity models in predicting flow behavior over delta wings, comparing them with standard linear two-equation models, both with and without rotation correction. Both the rotation-corrected and non-linear models improve significantly upon the standard model's predictions, with the non-linear model showing strong agreement with experimental results at higher angles of incidence. Furthermore, Rumsey et al., 2020a propose the Quadratic Constitutive Relation (QCR) which employs a non-linear turbulent stress/strain equation, extending the linear Boussinesq relation. This approach accounts for the anisotropy property of Reynolds's normal stresses, addressing their incorrect behavior.

In general, while these advancements in turbulence modeling show potential in specific cases, their application often requires preliminary testing and lacks consistent flexibility and accuracy across different flow scenarios. The exploration of these corrections continues to be integral to advancing RANS model fidelity. Future research directions include model extensions to complex physical flows and more universal applicability.

2.3. Machine learning

Machine learning represents a transformative branch of artificial intelligence, aiming to empower machines to learn from and make data-based decisions. It includes the development of algorithms capable of processing, analyzing, and learning from data to autonomously make predictions or execute tasks without the need for explicit programming for each specific scenario. Machine learning algorithms progressively improve as they are exposed to more data, enhancing their ability to make more accurate predictions and informed decisions. This field is rapidly evolving, continually pushing the boundaries of machine capabilities and finding new applications across nearly every sector of society and industry. The primary categorizations of machine learning are outlined and the integration of EAs into the machine learning framework in discussed. This discussion encompasses the application of machine learning techniques in a broad context, with a particular focus on their specific utilization within the fields of aerodynamics and turbulence modeling.

2.3.1. Role of evolutionary algorithms in machine learning

Machine learning algorithms are broadly categorized based on how they learn and operate. One approach within this field is EAs, which draw inspiration from biological evolution. Evolutionary Algorithms complement traditional machine learning approaches by addressing optimization challenges that are intractable for gradient-based methods, thus expanding the applicability of machine learning.

EAs are highly flexible and can adapt to solve a wide range of optimization problems without the need for gradient information, which is often unavailable or difficult to compute for turbulent flows. This makes EAs particularly suitable for optimization in turbulence research where the problem landscapes are highly nonlinear and multimodal. Unlike gradient-based optimization methods that are prone to getting stuck in local minima, EAs are designed to perform global searches by maintaining a population

of solutions. This characteristic is particularly beneficial in exploring the vast solution spaces inherent in turbulence models, enhancing the likelihood of finding optimal or near-optimal solutions. Furthermore, the intrinsic exploratory nature of EAs enables them to discover novel solutions that might be overlooked by methods that optimize based on gradient descent, which is particularly relevant in the innovative field of turbulence research where new phenomena are frequently discovered.

While traditional ML techniques, such as deep learning, have shown success in turbulence research, they often rely on large amounts of labeled data and may struggle with extrapolation outside the training datasets. In contrast, EAs do not require labeled data to explore the solution space, making them more versatile in situations where data is scarce or expensive to obtain. EAs are inherently parallelizable, as each individual in the population can be evaluated independently. This feature is highly advantageous for computational efficiency, especially given the computationally intensive nature of turbulence simulations (Deb et al., 2002; Fleming and Purshouse, 2002).

At the heart of EAs is the concept of the evolutionary cycle, which involves the generation of a population of individuals (solutions), the evaluation of these individuals based on a fitness function (how well they solve the problem), and the application of evolutionary operators such as selection, crossover (recombination), and mutation to create a new generation of individuals. This process is repeated over many generations, with the population ideally converging towards an optimal or satisfactory solution. pressure within the algorithm.

Several types of EAs exist, each with its own strengths and optimal applications for specific types of problems. Among these, Genetic Algorithms (GA) and Genetic Programming (GP) form the foundational concepts behind GEP. GAs represent a subset of EAs that employ mechanisms inspired by biological evolution, including reproduction, mutation, recombination, and selection. Within this framework, candidate solutions to an optimization problem serve as individuals in a population, with the fitness function assessing the quality of these solutions. GP, a branch of evolutionary computation, focuses on evolving programs or algorithms tasked with specific functions. The foundational concept of GP is articulated by Koza, 1994 and further elaborated by Kramer, 2017. GP extends GAs by operating on populations of tree-structured programs rather than fixed-length strings, thereby enhancing the adaptability and scope of evolutionary computation in problem-solving (Langdon et al., 2008). This structural aspect of representing individuals is also integral to GEP.

Evolutionary Algorithms represent a versatile and powerful toolkit for solving optimization problems across a wide range of domains. In general engineering, EAs are employed to address many problems (A. Johnson et al., 2019; Parmee, 2012). The adaptability of EAs extends to areas such as turbulence modeling (Sandberg et al., 2018; Schoepplein et al., 2018), as well as health technologies (Ling et al., 2016). Recent crises further demonstrate the utility of EAs, examining the coevolutionary dynamics of SARS-CoV-2 (Govinda et al., 2021), and enhancing real-time flood predictions through EA-neural network integrations (Suddul et al., 2020). Beyond engineering challenges, EAs venture into creative domains, generating art and music (Hofmann, 2015; Secretan et al., 2011).

The continuous evolution and diversification of EAs underscore then their versatility and growing impact across various fields.

2.3.2. Introduction to gene expression programming

Gene Expression Programming is a type of EAs developed by Ferreira, 2002 that combines the advantages of GAs and GP. GEP evolves populations of individuals encoded in linear chromosomes, which are then expressed as tree structures for evaluation. The linear chromosome representation facilitates the application of genetic operators such as mutation, recombination, and transposition, while the tree structure expression allows for the direct evaluation of evolved expressions (Ferreira, 2006b). This dual nature of GEP enables it to efficiently search the solution space for optimal or near-optimal solutions. Ferreira, 2006a introduced the notion of the Open Reading Frame to articulate the linear string of the genome, wherein the symbolic expression is termed k-expression, derived from Karva-language. Further research efforts are ongoing to develop more accurate and faster GEP codes (Kasten et al., 2022a; Weatheritt and Sandberg, 2015, 2016).

The GEP's ability to evolve concise, yet complex models offers significant advantages for symbolic regression and the modeling of complex systems. As research continues, GEP is expected to find even broader applications and achieve greater optimization performance. While black box models offer the advantage of handling highly complex problems with potentially higher accuracy, the transparency, interpretability, and adaptability of GEP make it a preferred choice for applications where understanding the model's decision-making process is crucial. GEP's ability to produce human-readable models that can evolve and adapt over time provides a unique blend of flexibility and transparency that is highly valued in many domains.

2.3.3. Machine learning applied to turbulence modeling

Recent progress in data science has reinvigorated scientific research focused on turbulence modeling. In the field of turbulence modeling, machine learning has achieved significant advancements (Duraisamy et al., 2019). The evolution of more efficient and complex deep neural networks and machine learning tools presents an opportunity for synergistic improvements in physical modeling, particularly in accuracy and computational feasibility. Applying deep neural networks to analyze extensive datasets from high-fidelity simulations or experimental studies holds promise for advancing traditional RANS turbulence models to their optimal performance thresholds.

Various machine learning techniques are employed to improve the predictive capacity of conventional RANS models. These methodologies include the calibration of model parameters via the Bayesian approach (Edeling et al., 2014), the introduction of a neural network-informed correction component for the turbulence production term (Z. Zhang and Duraisamy, 2015), and the integration of a spatially varying correction field employing field inversion and Gaussian Process techniques (Parish and Duraisamy, 2016), among others. Beyond merely introducing corrections to pre-existing model parameters, attempts to devise new Reynolds stress closures using physics-informed

machine learning are conducted. Wang et al., 2017 employ a random forest method to train Reynolds stress discrepancy functions based on the eigenvalues of the anisotropy tensor. Ling et al., 2016 use a deep neural network to train the Reynolds stress tensor conserving Galilean invariance.

Initially, most of these efforts have focused on simple individual test cases. Milano and Koumoutsakos, 2002 use neural networks to recreate the near-wall velocity fields in turbulent channel flows. Weatheritt and Sandberg, 2016 showcase promising outcomes for the backwards-facing step and periodic hill flows using GEP. Tracey et al., 2015 probe the capabilities of kernel regression in modeling the NACA 0012 airfoil flow, while Wang et al., 2017 enhance predictions for the periodic hill flow. Besides, more recent turbulence modelers broaden the horizons of ML techniques to consider more challenging flow cases. Significant advancements are observed in predicting wake loss profiles across both low- and high-pressure turbine instances (Akolekar et al., 2019; Zhao et al., 2020) and in depicting turbulent boundary layers at high Mach number (Wang et al., 2019). Moreover, although considering a single test case, some researchers have tried assessing turbulence models under different flow conditions. Examples include formulating ML models tailored for periodic hill flows across a range of Reynolds numbers (Z. Zhang et al., 2021), airfoil flows subjected to varying free-stream conditions and geometrical configurations (Zhu et al., 2022), and vertical natural convection cases under distinct Rayleigh numbers (Xu et al., 2022). Only a handful of studies incorporate diverse flow contexts within their training framework, like channel and duct flows (Jiang et al., 2021). Consequently, there's a growing inclination in engineering to develop more comprehensive models aimed at achieving higher accuracy across diverse flow test cases.

Moreover, various data analysis instruments have been introduced with the advancement of high-performance computing, enabling more complex simulations and state-of-the-art experimental tools, that provide comprehensive datasets. These instruments can derive essential physical insights from the data to enhance RANS modeling (Brunton et al., 2020; Duraisamy et al., 2019, 2017; Durbin, 2018). Nevertheless, although data has historically been instrumental in refining model coefficients and assessing the model uncertainty (Brunton et al., 2020), the capacity to exploit this expansive datasets remains predominantly underutilized. Indeed, while the adoption of ML in turbulence model development is increasing, challenges remain in training these models for practical engineering applications. Integrating the resulting neural network into standard RANS solvers present several challenges, and many of the devised corrections often lack clear physical interpretability.

Recent advancements in turbulence modeling are marked by Singh et al., 2017, who integrate a neural network with an inference tool to modify the Spalart-Allmaras turbulence model. This modification involves a correction factor applied to the production term within the flow domain. The process begins with solving an inversion problem to determine a pointwise correction factor that closely matches experimental data. This corrected field then serves as a training target for the neural network. The enhanced model, equipped with the trained neural network, is designed to predict the appropriate correction factor in new test cases and flow fields. Initial results are promising, particularly in airfoil flows and other two-dimensional scenarios, indicating the method's

potential for broader application and improvement in more complex flow conditions. Parallel to this, Zhu et al., 2019 and Wu et al., 2018 develop similar methodologies to integrate high-fidelity data into additional terms of their turbulence models. Their approach focuses on rectifying the discrepancies between the true Reynolds stresses from DNS and those predicted by RANS models, employing neural networks to learn and adjust based on the input flow. The regression function resulting from this learning process is then utilized to enhance the turbulence models' predictive accuracy.

Weatheritt and Sandberg, 2016 pioneer the use of GEP to enhance the Boussinesq approximation within the RANS approach. GEP is the choice for the ML framework used in this dissertation, owing to its previously demonstrated efficacy in addressing challenges related to turbulence closures, heat flux, and transition models (Akolekar et al., 2021; Haghiri et al., 2020; Lav et al., 2021, 2019a,b; Wilsby and Sandberg, 2019; Xu et al., 2022; Zhao et al., 2020). Its adaptability is particularly highlighted in turbulence closures, where its utility extends from two-equation closures to developing second-order closure models (Alaya et al., 2022). Further studies in the field of turbulence modeling can be found in the literature (Fang et al., 2023; Kasten et al., 2022b; Reissmann et al., 2021).

Nevertheless, previous ML research efforts (Ling et al., 2016; Wang et al., 2017) and GEP studies (Akolekar et al., 2019; Weatheritt and Sandberg, 2015, 2017) have primarily used time-averaged Hi-Fi data for model assessments, employing a method known as frozen training. In this context, frozen implies that the Hi-Fi data used during the training phase remains unchanged. Despite the potential for applying this methodology across various data types, including experimental and theoretical data, the approach faces limitations due to inconsistencies between Hi-Fi data and the RANS framework, such as fluctuations in turbulent dissipation rates (Duraisamy et al., 2019). The discrepancies between RANS modeling and Hi-Fi training data often lead to ineffective model enhancements when applied in RANS contexts, as evidenced by efforts to refine Reynolds stress models using DNS data (Parneix et al., 1998). This challenge raises doubt on the efficacy of development approaches that rely on accurately modeling the Reynolds stress tensor using Hi-Fi data for predicting mean flow dynamics. The separation of learning and prediction stages often results in discrepancies between a priori and a posteriori assessments.

To address these limitations, recent researches have introduced an innovative CFD-driven training methodology, which integrates CFD simulations into the model training iterations, aiming for models that align more closely with RANS predictions of turbulence metrics. A comprehensive understanding of GEP's application in CFD-driven training is elaborated by Fang et al., 2023; Zhao et al., 2020. Zhao et al., 2020 apply machine learning techniques to devise an algorithm for identifying the most effective enhancements to a baseline turbulence model. Within the proposed framework, the effectiveness of proposed models is directly evaluated through RANS calculations, bridging the gap between theoretical model development and practical application. The CFD-driven framework based on GEP used in this dissertation is detailed in Section 4.2.

3

Fluid Motion Theory and Turbulence Modeling

This chapter scrutinizes fluid motion theory, starting with the presentation of the governing equations in Section 3.1, followed by an introduction to turbulence in Section 3.2. The discussion then progresses to the modeling aspect, where numerical approaches are detailed in Section 3.3. Section 3.4 then presents a thorough examination of the modeling approaches and turbulence models employed for the analysis of delta wing aerodynamics in this dissertation.

3.1. Governing equations

The Navier-Stokes equations are a set of differential equations that describe the motion of viscous fluid substances, such as liquids and gases. These equations are fundamental in fluid dynamics and are used to model the behavior of the fluid's velocity, pressure, temperature, and density. They are derived from applying Newton's second law to fluid motion and assuming that fluid stress is the sum of a diffusing viscous term and a pressure term. The continuum approach is employed, based on the assumption that the Knudsen number is lower than 0.01. This assumption allows the examination of fluid behavior through macroscopic properties such as velocity, pressure, and density.

The Navier-Stokes equations play a pivotal role in the fundamental understanding and prediction of fluid dynamics across diverse scientific and engineering domains. These equations govern mass, momentum, and energy within fluid flows.

The principle of mass conservation, commonly known as the continuity equation, is articulated in its differential form as follows

$$\underbrace{\frac{\partial \rho}{\partial t}}_{\text{Transient term}} + \underbrace{\frac{\partial (\rho u_i)}{\partial x_i}}_{\text{Convective term}} = 0, \tag{3.1}$$

where ρ represents the fluid density, u_i the velocity components, and x_i the spatial coordinates. The first term, referred to as the transient term, represents the rate of

mass change in time, whereas the second term, known as the convective term, illustrates the net mass flow exiting an infinitesimal element.

The conservation of momentum, or the momentum equation, is given by

$$\frac{\partial(\rho u_i)}{\partial t} + \frac{\partial(\rho u_i u_j)}{\partial x_j} = -\frac{\partial p}{\partial x_i} + \frac{\partial \tau_{ij}}{\partial x_j}, \tag{3.2}$$

where p is the pressure, and τ_{ij} the viscous stress tensor. Subscripts i and j indicate that the stress component acts in the i-direction on a surface normal to the j-direction.

In Newtonian fluids, the viscous stresses are directly proportional to the deformation rates as follows

$$\tau_{ij} = \mu\left(\frac{\partial u_i}{\partial x_j} + \frac{\partial u_j}{\partial x_i}\right) + \lambda\left(\frac{\partial u_k}{\partial x_k}\right)\delta_{ij}, \tag{3.3}$$

where μ is the the dynamic viscosity, and λ the second viscosity, which correlate stresses to volumetric deformation, and δ_{ij} the Kronecker delta. The second viscosity is typically approximated as $\lambda = -\frac{2}{3}\mu$. For an incompressible fluid, it is crucial to note that the divergence of velocity ($\nabla \cdot \mathbf{u}$) equals zero.

Furthermore, the viscous strain-rate tensor, S_{ij}, is defined as

$$S_{ij} = \frac{1}{2}\left(\frac{\partial u_i}{\partial x_j} + \frac{\partial u_j}{\partial x_i}\right), \tag{3.4}$$

which can be substituted into Eq. 3.3 to derive the viscous stress tensor expressed as

$$\tau_{ij} = 2\mu S_{ij} - \frac{2}{3}\mu\left(\frac{\partial u_k}{\partial x_k}\right)\delta_{ij}. \tag{3.5}$$

The dynamic viscosity is governed by Sutherland's law, relating it to temperature, as follows

$$\frac{\mu}{\mu_0} = \left(\frac{T}{T_0}\right)^{3/2}\frac{T_0 + X}{T + X}, \tag{3.6}$$

where $\mu_0 = 1.7894 \times 10^{-5} kg/(ms)$ is the reference viscosity at the reference temperature $T_0 = 288.16K$, and $X = 110K$.

The energy equation, representing the conservation of energy, is expressed as

$$\frac{\partial(\rho E)}{\partial t} + \frac{\partial\left(\rho u_j E\right)}{\partial x_j} = -\frac{\partial\left(p u_j\right)}{\partial x_j} + \frac{\partial}{\partial x_j}\left(\tau_{ij} u_i - q_j\right). \tag{3.7}$$

Here, E is the total energy of the fluid, defined as the sum of internal and kinetic energy, as

$$E = e + \frac{1}{2}u_i u_i, \tag{3.8}$$

and q_i is the heat flux vector defined by Fourier's Law as

$$q_j = -\kappa_T \frac{\partial T}{\partial x_j} \quad \text{where} \quad \kappa_T = \frac{1}{(\gamma - 1)\, M_\infty^2}\frac{\mu}{Pr}. \tag{3.9}$$

It represents the thermal conductivity of the fluid. Here, T is the temperature of the fluid, γ is the specific heat ratio, M_∞ is the free-stream Mach number, and Pr is the Prandtl number.

These equations, along with the following equations of state for a perfect gas

$$H = E + \frac{p}{\rho}, \quad \text{and} \quad p = \rho RT, \tag{3.10}$$

provide a complete description of the flow and heat transfer of a three-dimensional Newtonian fluid.

The Navier-Stokes equations are highly nonlinear and, except for simple cases, cannot be solved analytically. Instead, numerical methods and simulations for specific boundary conditions and scenarios often obtain solutions. Despite this inherent complexity, these equations are indispensable for predicting and elucidating fluid behavior across many contexts, including aerodynamic flows.

3.2. Introduction to turbulence

Turbulence is distinguished by irregular, rapid fluctuations in flow properties, occurring over a broad scale range and associated with structures known as turbulent eddies. Their behavior is complex and non-linear, with interactions across various wavelengths facilitated by vortex stretching, an inherently three-dimensional property crucial for turbulence production.

The Reynolds number is a crucial parameter for ascertaining the onset and intensity of turbulence in fluid flow. It is defined as follows

$$Re = \frac{\rho U L}{\mu}, \tag{3.11}$$

where ρ represents the fluid density, U the velocity, L a characteristic linear dimension, and μ the dynamic viscosity. The Reynolds number effectively juxtaposes the inertial forces against the viscous forces within the fluid, facilitating the prediction of the flow being either laminar or turbulent. In the laminar flow regime at low Reynolds numbers, viscous stresses and vorticity diffusion suppress small-scale instabilities. However, with increased Reynolds numbers, inertial effects progressively become more dominant. The viscosity no longer maintains order, transitioning from laminar to turbulent flow.

Understanding turbulence is crucial for predicting and managing turbulent systems in various scientific and engineering applications. Turbulence's complexity arises from several aspects, which can be summarized as follows (Tsinober, 2001).

- Intrinsic spatial-temporal randomness: turbulent flows, sensitive to minute perturbations, lack repeatability. However, their statistical properties remain largely stable against disturbances.
- Intermittency: turbulence can sporadically appear in time and space, interacting with non-turbulent flows.

- Wide range of non-locally interacting scales: turbulent flows comprise a broad spectrum of scales, ranging from large systems to minute eddies.
- Continuous self-production of vorticity and three-dimensionality: vortex dynamics, including stretching and spinning, are central to sustaining turbulence, inherently a three-dimensional phenomenon. Notably, two-dimensional vortices cannot stretch; thus, true two-dimensional turbulence is non-existent.
- Strong diffusion: turbulence necessitates an energy source (like velocity gradients or buoyancy) to sustain. Energy is supplied at larger scales and dissipated at smaller ones. Turbulent fluctuations enhance the stretching and distortion of fluid elements, dramatically increasing the transport and mixing of properties like heat and momentum.

Despite its complexity, turbulence can be modeled using deterministic Navier-Stokes equations, although solutions are highly sensitive to initial and boundary conditions. Consequently, field variables are often treated as random to understand turbulent flows, and statistical analysis is employed to extract meaningful information.

3.2.1. Statistics of the flow

Due to the inherent complexity of turbulent flows, they are predominantly analyzed through statistical analysis tools. Some of the more frequently employed single-point and multi-point statistical measures are then elucidated.

The simplest statistical property to consider is the mean. The mean value of a random variable at a specific spatial location can be determined by averaging its long-term measurement as follows

$$\bar{\phi}(\boldsymbol{x}) = \lim_{T\to\infty} \frac{1}{T} \int_{t_0}^{t_0+T} \phi(\boldsymbol{x},t)\, dt, \tag{3.12}$$

where $\bar{\phi}$ denotes the mean value of the random variable ϕ. The time-averaging process is meaningful only when the flow is characterized as statistically steady, ensuring that the result is independent of the initial time t_0 and invariant for sufficiently large values of T.

Furthermore, the ensemble average is articulated as follows

$$\bar{\phi}(\boldsymbol{x},t) = \lim_{N\to\infty} \frac{1}{N} \sum_{i=1}^{N} \phi(\boldsymbol{x},t), \tag{3.13}$$

where the summation spans a set of samples, N, acquired at the same spatial location, $\mathbf{x}$, and identical instant, t, across N distinct realizations or experiments.

Finally, the n-th order central moment can be computed from

$$\overline{(\phi(\boldsymbol{x},t) - \bar{\phi}(\boldsymbol{x}))^n}, \tag{3.14}$$

assuming that the averaging process is properly defined and converges. A hierarchy of moments can be established to characterize the statistical state of a random variable, among which the velocity field is a pertinent variable in turbulent flow analysis. Denoting ϕ' as the fluctuating component of the random variable, ϕ can be expressed as

$$\phi(\boldsymbol{x},t) = \bar{\phi}(\boldsymbol{x}) + \phi'(\boldsymbol{x},t). \tag{3.15}$$

Beyond the mean value, the second central moment, or variance, emerges as the next critical statistical attribute of turbulence, expressed as follows

$$\mathrm{var}(\phi) = \overline{(\phi(\boldsymbol{x},t) - \bar{\phi}(\boldsymbol{x}))^2}. \tag{3.16}$$

This metric provides a quantitative assessment of the expected magnitude of deviations from the mean value. This concept is often articulated as turbulence intensity, which is essentially the square root of the second central moment, or the root mean square of the velocity fluctuation, $\sqrt{u'^2}$.

The moments defined above are single-point moments, meaning they contain only information about a random variable at a point. In turbulent flow, it is essential to have some statistical measure of spatial and temporal information about the flow. Turbulence is characterized by chaotic and irregular fluid motion that involves a wide range of time scales and eddy sizes. Understanding how velocities or other turbulent quantities are correlated in time at a fixed point or between two points in space provides insights into the energy cascade process, dissipation mechanisms, and mixing efficiency within the flow.

The two-point temporal correlation function gives an estimate of the time interval over which the fluctuation velocity component $u'(t)$ is correlated. The integral turbulent time scale, τ_0, computed from the two-point temporal correlation function, represents an averaged inverse rotational frequency of the predominant large eddy, indicating the time over which $u'(t)$ retains its historical influence. The integral time scale is important for understanding the persistence of velocity fluctuations in a turbulent flow and estimating the time it takes for energy to cascade from large to smaller scales.

The integral length scale, l_0, is connected to this, representing the large scales in the flow field and serving as a measure from which velocity fluctuations are predominantly uncorrelated. It is computed using the two-point spatial correlation function. It is also important for understanding energy distribution across different scales in the flow. Indeed, the Fourier transform is used to compute the energy spectrum from two-point spatial correlation function. The energy spectrum describes how energy is distributed across different spatial scales or frequencies.

3.2.2. Turbulent eddies and energy cascade

The presence of numerous interacting eddies characterizes turbulent flow. The turbulent flow can be decomposed into a series of eddies of various sizes l_e, speeds u_e and time scale $\tau_e \approx \frac{l_e}{u_e}$, which interact with each other. They significantly influence the overall flow field through a kinetic energy transfer from larger to smaller eddies, a

phenomenon known as the energy cascade. The cascade process commences with the largest eddies, which possess the highest turbulent kinetic energy per unit mass. Energy is then transferred from these large eddies to smaller ones, with the energy of the smaller scales eventually dissipating due to viscous action. Larger eddies migrate also across the flow, carrying smaller eddies. This movement, known as turbulent mixing, significantly enhances the diffusion of mass, momentum, and energy within the fluid, thus characterizing the intricate and chaotic nature of turbulent flows.

Kolmogorov, 1991 develops a series of hypotheses that define turbulence behavior, conceptualizing eddies as moderately coherent turbulent motions within a region of scale l_e. Kolmogorov's hypotheses address crucial questions regarding the quantification of length scales, their proportions, interdependencies, and the relationship with flow characteristics.

The first hypothesis pertains to the local isotropy of turbulence. It asserts that small-scale turbulent motions are statistically isotropic for sufficiently high Reynolds numbers. This is contrary to the anisotropic scales, which are prevalent only in the largest length scales of the flow. Indeed, the anisotropic turbulence, or the energy containing range, significantly influences the mean flow as it contains most of its energy. This concept suggests that the anisotropy evident at the largest scales dissipates during the energy cascade towards the smallest scales. As a result of losing the large-scale flow information at the smallest scales, the statistical characteristics of small-scale flow become universal across all turbulent flows, depending solely on the energy dissipation rate per unit mass, ε, and the kinematic viscosity, ν. This hypothesis, combined with dimensional analysis, leads to the definitions of the Kolmogorov scales as follows

$$\eta = \left(\frac{\nu^3}{\varepsilon}\right)^{1/4}, \quad u_\eta = (\varepsilon\nu)^{1/4}, \quad \text{and} \quad \tau_\eta = \left(\frac{\nu}{\varepsilon}\right)^{1/2}. \tag{3.17}$$

The Reynolds number is approximately one at the smallest scale, indicating the prominence of dissipation effects. The dissipative range or viscous range refers then to the smallest turbulent scales where energy is dissipated to heat by molecular viscosity.

Kolmogorov's second similarity hypothesis postulates that the intermediate scales in the energy cascade, the inertial subrange situated between the largest flow scale and the Kolmogorov scales, are uniquely determined by the dissipation rate of turbulent kinetic energy, ε while being independent of the kinematic viscosity, ν. At these intermediate scales, the Reynolds number is sufficiently high to minimize the influence of viscous dissipation effects. The rate of dissipation, e.g. for homogeneous isotropic turbulence, balances the rate of change of turbulent kinetic energy, and it can be defined as

$$\varepsilon = -\frac{dk}{dt}. \tag{3.18}$$

It is influenced primarily by the flow's largest eddies and establishes then a scale range within the turbulent flow, expanding with the increase in Reynolds number. Consequently, the ratios between the largest and smallest scales of length, velocity, and time

in turbulent flow can be represented as

$$\frac{l_0}{\eta} \propto Re^{\frac{3}{4}}, \quad \frac{u_0}{u_\eta} \propto Re^{\frac{1}{4}}, \quad \text{and} \quad \frac{\tau_0}{\tau_\eta} \propto Re^{-\frac{1}{2}}, \tag{3.19}$$

where l_0, u_0, and τ_0 denote the characteristic length, velocity, and time scale of the largest eddies, respectively. This highlights the vast scale disparity between the smallest and largest turbulent scales and their dependency on the Reynolds number.

As mentioned before, Kolmogorov's first hypothesis posits that for sufficiently large Reynolds numbers, turbulence becomes isotropic. Subsequently, the energy spectrum $E(\kappa)$ becomes solely a function of the rate of energy dissipation, ε, and the eddy size, r. This hypothesis leads to the formulation of Kolmogorov's five-thirds law for the inertial subrange where $\eta \ll r \ll l_0$, defined as

$$E(\kappa) = C_k \varepsilon^{2/3} \kappa^{-5/3}, \tag{3.20}$$

where C_k is the Kolmogorov constant. Here, $C_k \approx 1.5$ for $Re \to \infty$. The exponents of 2/3 and 5/3 are chosen to ensure dimensional consistency for E, which has dimensions of L^3/T^2, and to account for the relationship $r \propto \kappa^{-1}$.

Fig. 3.1 shows the energy spectrum, $E(\kappa)$ vs κ, which adheres to the Kolmogorov $-5/3$ slope in the inertial subrange. The horizontal axis represents the wave number, κ, indicative of the number of eddies per unit length and inversely proportional to the eddy size. This spectrum represents how the kinetic energy is distributed among different sizes of eddies or wave numbers. It offers then a profound understanding of the energy distribution within turbulent flows. This $-5/3$ slope on a log-log plot of the energy spectrum versus wave number is a fundamental result of Kolmogorov's theory. It suggests that the energy cascade process is self-similar and universal across these scales, independent of the specific nature of the large-scale energy input or the small-scale dissipative mechanisms. This concept is foundational in turbulence research and is used extensively in analyzing and modeling turbulent flows.

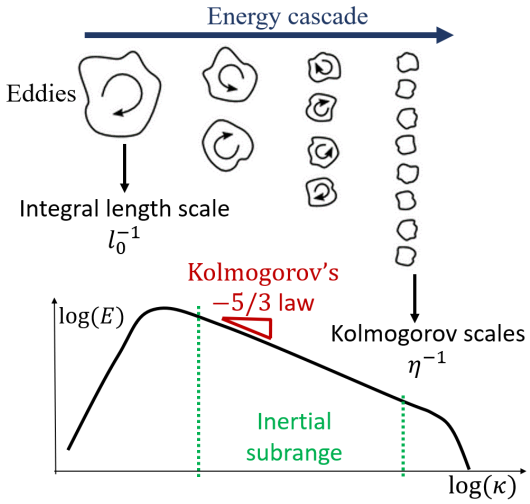

Figure 3.1: Turbulent energy spectrum (adapted from Greenshields and Weller, 2022).

3.3. Modeling and simulations

In CFD simulations, accurately modeling turbulence is paramount, considering the predominance of turbulent flows in engineering applications. The fidelity of turbulence

modeling is fundamental to securing reliable CFD results. This discussion delves into the intricacies, challenges, and methodologies pertinent to simulating turbulent flows, underscoring its significance as a critical domain of scientific investigation.

3.3.1. Direct Numerical Simulation

By the early 1980s, computational advancements and increased resource availability have enabled the numerical solution of the Navier-Stokes Equations. DNS, a full-field simulation approach, has emerged as a vital tool for acquiring insights into turbulence. DNS facilitates a deeper understanding of turbulence physics and its modeling, elucidating the temporal evolution of turbulence fields, eddy life histories, and multi-point correlations. However, DNS necessitates resolving the extensive range of temporal and spatial scales in turbulent flow, from the very large to the very small, down to the Kolmogorov length scale, η, introduced in Eq. 3.17.

In turbulent flow simulations, the equations are solved for three-dimensional, time-dependent velocities, including the full spectrum of turbulence scales. As expressed in Eq. 3.19, the computational cost can be assessed considering the dependence of length and time scales on the Reynolds number. Spatial discretization in three dimensions must be sufficiently fine to capture the smallest turbulent scales, implying that the number of grid points in each direction scales with $\mathrm{Re}^{3/4}$. Consequently, for three dimensions, the total number of spatial discretization points, $N_{\Delta x}$, scales with $\mathrm{Re}^{9/4}$.

Considering the time discretization executed using an explicit method, the time step Δt, is constrained by a Courant number less than one as follows

$$C = \frac{u_0 \Delta t}{\Delta x} < 1, \tag{3.21}$$

where Δx represents the spatial discretization. The number of time steps for the simulation duration, T, is approximately as

$$N_{\Delta t} \sim \frac{T}{\Delta t} \sim \frac{T u_0}{l_0} \mathrm{Re}^{3/4}. \tag{3.22}$$

Combining spatial and temporal discretization, the computational cost of a DNS simulation scales proportionally with Re^3, rendering this methodology feasible only for a limited set of cases at low Reynolds numbers, simple geometries, and small domains.

Turbulence modeling is introduced to account for a proportion of the small-scale turbulent fluctuations and consequently reduces the computational expense in resolving all the scales of turbulence. As illustrated in Fig. 3.2a, the resolved scales refer to the range of turbulent motions directly computed in a simulation. The approach's choice determines the extent to which the scales of turbulence are resolved or modeled, balancing between computational expense and the level of physical detail captured in the simulation.

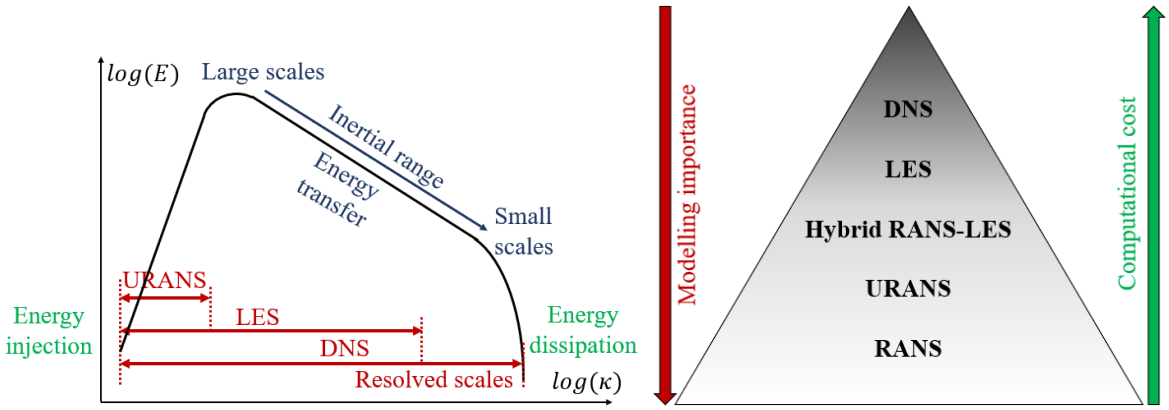

(a) Scales in turbulence modeling.

(b) Turbulence modeling approaches.

Figure 3.2: Characteristics of the CFD modeling approaches.

In engineering, the focus often lies on mean or integral quantities. Turbulence models are sufficient for this purpose and are recommended, as they provide reliable solutions efficiently and cost-effectively. Fig. 3.2b illustrates the common approaches to solving turbulent flows, with the computational cost of a CFD simulation escalating from the RANS approach to DNS. As a result, scale-resolving methodologies such as DNS and LES are typically employed for elementary geometries and academic settings. Conversely, hRL (in selected test cases), Unsteady RANS (URANS), and steady RANS are utilized for complex industrial applications. Two strategies are employed in this dissertation for modeling the Navier-Stokes equations and managing turbulence: the URANS and hRL.

3.3.2. Large Eddy Simulation

Large Eddy Simulation was initially proposed to mitigate the computational demands associated with DNS. The foundational philosophy of LES is the explicit resolution of large-scale motions coupled with the modeling of smaller scales. By focusing only on the larger scales, LES permits using significantly coarser grids and time steps than DNS. Consequently, LES is practicable at much higher Reynolds numbers, balancing accuracy and computational efficiency.

The smallest turbulence scales are spatially filtered out, while the largest and most energy-dense scales are directly resolved. This methodology relies on the assumption that, at very small scales, flow structures are similar across various applications, allowing for the application of more universal and simpler turbulence models compared to those employed in the RANS approach, as discussed in Section 3.3.3. These models require less tuning and can be broadly applied across diverse scenarios. Nevertheless, smaller scales are critical in ensuring a complete and accurate solution. Consequently, their influence, encompassed within scales smaller than the grid cell dimensions, needs to be accurately modeled.

An LES filter can be applied to a spatial and temporal field $\phi(\boldsymbol{x},t)$ and perform a spatial filtering operation, a temporal filtering operation, or both. The filtered field, denoted with an hut, is defined as follows

$$\hat{\phi}(\boldsymbol{x},t) = \int_{-\infty}^{\infty}\int_{-\infty}^{\infty} \phi(\boldsymbol{r},\tau)G(\boldsymbol{x}-\boldsymbol{r},t-\tau)d\tau d\boldsymbol{r} \tag{3.23}$$

where G is the filter convolution kernel, $\boldsymbol{x}$ and $\boldsymbol{r}$ represent position vectors in physical space. This operation can also be concisely given by

$$\hat{\phi} = G \star \phi. \tag{3.24}$$

The filter kernel in physical space is mathematically defined as follows

$$G(\boldsymbol{x}-\boldsymbol{r}) = \begin{cases} 1/\Delta^3, & \text{if } |\boldsymbol{x}-\boldsymbol{r}| \leq \Delta/2, \\ 0, & \text{otherwise.} \end{cases} \tag{3.25}$$

where Δ denotes the characteristic length scale of the filter, determining the spatial extent over which the filter operates.

This filter kernel is a simple yet effective way to apply a uniform averaging process within a defined radius around a point. The choice of Δ is crucial, as it determines the scale of features that are smoothed out or retained in the filtered data. LES employs filtering techniques to differentiate between these scales, using the following maximum cell dimensions of the grid as the filter width:

$$\Delta = \max(\Delta_x, \Delta_y, \Delta_z). \tag{3.26}$$

Scales smaller than these are eliminated from $\hat{\phi}$. Using the above filter definition, any field ϕ may be split up into a filtered and sub-filtered (denoted with a prime) portion, as follows

$$\phi(\boldsymbol{x},t) = \hat{\phi}(\boldsymbol{x},t) + \phi''(\boldsymbol{x},t). \tag{3.27}$$

It is important to note that the LES filtering operation does not satisfy the properties of a Reynolds operator. Flow variables are then partitioned into resolvable (filtered, $\hat{\phi}$) and sub-grid (residual, ϕ'') components to capture the complex dynamics of turbulent flows. The sub-grid component accounts for the remaining unresolved turbulent fluctuations.

The governing equations for LES are derived by applying a filtering operation to the Navier-Stokes equations, which govern the dynamics of the flow field, as introduced in Section 3.1. The transition from incompressible to compressible LES formulations necessitates the adoption of a modified filtering operation. Specifically, for compressible flows, the Favre-averaging technique, detailed in Section 3.3.3, has to be employed. This approach distinguishes between mass-weighted (Favre-averaged) and conventional filtering operations, reflecting the distinct treatment required for compressible flow.

For incompressible flow and constant viscosity, by applying these techniques and as-

suming that filtering and taking derivatives commutes, the Navier-Stokes momentum equations for the filtered component of the flow are obtained as follows

$$\rho\frac{\partial\hat{u}_i}{\partial t}+\rho\frac{\partial(\widehat{u_iu_j})}{\partial x_j}=-\frac{\partial\hat{p}}{\partial x_i}+\mu\frac{\partial}{\partial x_j}\left(\frac{\partial\hat{u}_i}{\partial x_j}+\frac{\partial\hat{u}_j}{\partial x_i}\right)=-\frac{\partial\hat{p}}{\partial x_i}+2\mu\frac{\partial\hat{S}_{ij}}{\partial x_j}, \tag{3.28}$$

where $\hat{p}$ is the filtered pressure field and $\hat{S}_{ij}$ is the rate of strain tensor evaluated using the filtered velocity. The nonlinear filtered convective term $\widehat{u_iu_j}$ introduces the Sub Grid Scale (SGS) or residual stress tensor, τ_{ij}^{SGS}, due to the difference between the filtered product and the product of two filtered variables (Leonard, 1975), as follows

$$\widehat{u_iu_j}=\tau_{ij}^{SGS}+\hat{u}_i\hat{u}_j\rightarrow\tau_{ij}^{SGS}=\widehat{u_iu_j}-\hat{u}_i\hat{u}_j \tag{3.29}$$

The filtered Navier-Stokes equations become

$$\rho\frac{\partial\hat{u}_i}{\partial t}+\rho\frac{\partial(\hat{u}_i\hat{u}_j)}{\partial x_j}=-\frac{\partial\hat{p}}{\partial x_i}+\mu\frac{\partial}{\partial x_j}\left(\frac{\partial\hat{u}_i}{\partial x_j}+\frac{\partial\hat{u}_j}{\partial x_i}\right)-\rho\frac{\partial\tau_{ij}^{SGS}}{\partial x_j} \tag{3.30}$$

with the residual stress tensor, τ_{ij}^{SGS}, grouping all unclosed terms.

The primary objective is to address the unknown terms in the filtered Navier-Stokes equations, identified as SGS stresses. They represent the effects of the smaller, unresolved scales on the resolved scales and are crucial for accurately capturing the dynamics of turbulent flows. This SGS stress tensor is further decomposed into deviatoric and its trace as follows

$$\tau_{ij}^{SGS}=\tau_{ij}^{*,SGS}+\frac{2}{3}k_r\delta_{ij}, \tag{3.31}$$

where k_r is the residual kinetic energy given by

$$k_r=\frac{1}{2}\tau_{ii}^{SGS}. \tag{3.32}$$

Smagorinsky's approach treats the deviatoric part of the stress tensor in a similar way to the Boussinesq approximation (see Section 3.3.3), associating it with an eddy viscosity as follows

$$\tau_{ij}^{*,SGS}=-2\nu_{SGS}\hat{S}_{ij}. \tag{3.33}$$

The Smagorinsky eddy viscosity is defined as

$$\nu_{SGS}=(C_s\Delta)^2\sqrt{2\hat{S}_{ij}\hat{S}_{ij}}, \tag{3.34}$$

where C_s is the Smagorinsky constant. This provides a linear relation for the sub-grid scale stress tensor expressed as

$$\tau_{ij}^{SGS}=-2\nu_{SGS}\hat{S}_{ij}+\frac{2}{3}k_r\delta_{ij}. \tag{3.35}$$

Recognizing that the physics modeled by the SGS stress tensor in LES significantly dif-

fers from those in RANS is crucial. In LES, the energy contained in the sub-grid scales constitutes a smaller portion of the total flow energy than in RANS. Consequently, only the smallest isotropic scales need to be modeled, implying that model accuracy may be less critical for SGS modeling than for (U)RANS computations, which must consider anisotropic scales. For further details and a comprehensive understanding of LES, readers are referred to Pope, 2000.

3.3.3. Reynolds Averaged Navier-Stokes equations

The RANS equations transform the Navier-Stokes equations into averaged forms that depict the mean behavior of fluid flows. While these modified equations resemble their initial counterparts, they include supplementary terms known as Reynolds stress terms. Originating from the averaging procedure, these terms embody turbulent fluctuations and are unknown. Therefore, developing turbulence models is imperative to achieve closure of these equations.

Turbulence models approximate turbulence's impact and are typically categorized based on the number of supplementary equations they incorporate. The complexity and fidelity of these models escalate by including more equations, ranging from simple algebraic expressions to intricate multi-equation systems. The RANS models are extensively employed in industrial applications, primarily when pursuing steady-state solutions. For scenarios involving moving components or periodic flow features, the unsteady variant URANS offers an enhanced representation by resolving the transient characteristics.

Reynolds averaging approach

The Reynolds averaging approach depends on the decomposition of the instantaneous flow into a mean flow and turbulent fluctuations, a technique known as Reynolds decomposition (Reynolds, 1895). It's imperative to note that the term mean flow here refers to the slowly varying flow behavior, which isn't necessarily static over time. This decomposition is subsequently integrated into the Navier-Stokes equations, followed by an application of an averaging process. Among the various methods for averaging the flow (time averaging, spatial averaging, and ensemble averaging), time averaging is predominantly employed in engineering flows. Further insights into alternative methods can be explored in literature (Wilcox, 1998).

Recalling the definitions in Section 3.2.1, the basic principle of Reynolds decomposition involves splitting a flow variable, ϕ, into its mean (time-averaged) component $\bar{\phi}$ and its fluctuating component ϕ'. Mathematically, this is represented in Eq. 3.15. The variables ϕ, $\bar{\phi}$, and ϕ' are consistently used to represent the instantaneous, mean, and fluctuating terms, respectively. These variables are conceptually different from the ones expressed in the LES approach discussed in Section 3.3.2.

In cases of statistically stationary turbulence, where the turbulent flow's mean does not fluctuate with time, the true time average of instantaneous variables is defined in Eq. 3.12. The term $T \to \infty$ implies that the integration period T must be substantially long compared to the period of the maximum fluctuation. For $\bar{\phi}$ to be a well-defined

term, the limit must be independent of the initial conditions at t_0. This time averaging of the instantaneous velocity decomposes into the time average of the mean flow, which, due to its stationary nature, equates to the mean, and the time average of the turbulent fluctuations, which are then zero, $\bar{\phi'} = 0$. It is critical to note that the time average of the mean flow does not necessary equate to the stationary mean. This distinction underscores the intricate nature of turbulence and the careful considerations needed in its mathematical interpretation.

Nonetheless, it remains analytically challenging to determine an upper bound for T. In applying time-averaging in numerical simulations, the following formulation,

$$\bar{\phi}(\boldsymbol{x}) = \frac{1}{T}\int_{t_0}^{t_0+T} \phi(\boldsymbol{x},t)dt, \tag{3.36}$$

is used. The sample time T is selected to be significantly larger than the small-scale fluctuations characteristic of turbulence but smaller than the scales of the mean flow oscillations. This approach is based on the premise that time averaging is only valid when the oscillation periods of the mean flow are substantially larger than the turbulent motion's timescales. This assumption is a complex aspect of turbulence, as turbulent fluctuations can sometimes be quite pronounced. Nevertheless, as introduced in Section 2.1.4, considering that the majority of characteristic flow features typically occur at low non-dimensional frequencies ($St < 10$), it is often feasible to assume that the turbulent fluctuations are relatively small for vortical flows.

By applying Reynolds decomposition, each instantaneous quantity is split into its time-averaged and fluctuating components. The Navier-Stokes equations are then time-averaged. Many terms derived from the Reynolds decomposition vanish due to the time averaging of the turbulent fluctuations, where $\bar{\phi'} = 0$. Consequently, assuming constant density and viscosity, the incompressible Navier-Stokes momentum equations reads

$$\rho\frac{\partial \bar{u}_i}{\partial t} + \rho\frac{\partial(\overline{u_i u_j})}{\partial x_j} = -\frac{\partial \bar{p}}{\partial x_i} + \mu\frac{\partial}{\partial x_j}\left(\frac{\partial \bar{u}_i}{\partial x_j} + \frac{\partial \bar{u}_j}{\partial x_i}\right) = -\frac{\partial \bar{p}}{\partial x_i} + 2\mu\frac{\partial \bar{S}_{ij}}{\partial x_j}, \tag{3.37}$$

where $\bar{S}_{ij}$ is the mean rate of strain tensor evaluated using the mean velocity field.

However, this procedure introduces two new non-linear terms arising from the convective term, due to the time-averaging of the product, $\overline{u_i u_j}$. Given that $\bar{u'} = 0$, this yields

$$\overline{u_i u_j} = \overline{\left(\bar{u}_i + u_i'\right)\left(\bar{u}_j + u_j'\right)} = \overline{\bar{u}_i\bar{u}_j + \bar{u}_i u_j' + u_i'\bar{u}_j + u_i'u_j'} = \overline{\bar{u}_i\bar{u}_j} + \overline{u_i'u_j'} \tag{3.38}$$

In the context of stationary turbulence, the time-averaged mean flow equates to the mean flow itself, thereby simplifying the term $\overline{\bar{u}_i\bar{u}_j}$ to $\bar{u}_i\bar{u}_j$. The second term, $\overline{u_i'u_j'}$, however, cannot be simplified in the same manner and is applicable to both stationary and non-stationary turbulence. Consequently, this introduces six new unknowns, represented by $-\rho\overline{u_i'u_j'} = \tau_{ij}^R$, which constitute the Reynolds stress tensor. Accordingly,

the RANS momentum equations for incompressible flow are formulated as follows

$$\rho\frac{\partial\bar{u}_i}{\partial t}+\rho\frac{\partial(\bar{u}_i\bar{u}_j)}{\partial x_j}=-\frac{\partial\bar{p}}{\partial x_i}+2\mu\frac{\partial\bar{S}_{ij}}{\partial x_j}-\rho\frac{\partial\overline{u_i'u_j'}}{\partial x_i}, \tag{3.39}$$

and $\bar{\tau_{ij}}=2\mu\bar{S}_{ij}$ is the mean viscous stress tensor (see Eq. 3.3). A comparable outcome is achieved for the energy equation (Eq. 3.7).

The nonlinear Reynolds stress term requires additional modeling to close the RANS equation for solving and lead to the development of various turbulence models. Turbulence modeling methodologies are divided into EVMs and non-EVMs, often called second-moment closure models. The first category includes turbulent viscosity models, based on Boussinesq's assumption and designed to determine the eddy viscosity relative to the flow field quantities. These models can be structured either algebraically or using one or more transport equations. The second category involves directly modeling Reynolds stresses via dedicated transport equations. This approach eliminates the need for an eddy viscosity term but introduces increased complexity, higher computational demands, and potentially additional numerical instabilities. Fig. 3.3 catalogs the more common models, indicating the increasing computational cost.

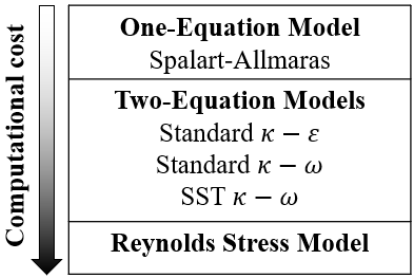

Figure 3.3: RANS models

Solution to the closure problem: the Boussinesq's assumption

The Reynolds stresses introduce a closure problem, necessitating a new set of equations to compute them from known mean quantities. A prevalent strategy is founded by Boussinesq, 1877. Boussinesq's assumption establishes an analogy that equates the influence of Reynolds stresses to viscous stress, as defined in Eq. 3.3 (Schmitt, 2007). Specifically, Boussinesq's assumption is often formulated as

$$\tau_{ij}^R=-\rho\overline{u_i'u_j'}=\mu_t\left(\frac{\partial\bar{u}_i}{\partial x_j}+\frac{\partial\bar{u}_j}{\partial x_i}\right)-\frac{2}{3}\rho k\delta_{ij}=2\mu_t\bar{S}_{ij}-\frac{2}{3}\rho k\delta_{ij}, \tag{3.40}$$

where μ_t denotes the eddy viscosity, a quantity that is not an inherent fluid property but must be modeled based on the flow field characteristics. Here, k represents the turbulent kinetic energy per unit mass, defined by $k=\frac{1}{2}\overline{u_i'u_i'}$, effectively representing half the trace of the Reynolds stress tensor. The first term on the RHS represents the anisotropic or deviatoric part of the turbulent stresses, modeled similarly to the viscous stresses but using the turbulent viscosity μ_t, and the second term accounts for the isotropic part, which is related to the turbulent kinetic energy k.

The terms anisotropy part and deviatoric part of the Reynolds stress tensor are related but distinct concepts within the context of turbulence modeling and fluid dynamics. Both refer to aspects of the Reynolds stress tensor that arise due to turbulence. The anisotropy part of the Reynolds stress tensor refers to the component that specifically

represents the directional dependence of the turbulent stresses. It essentially captures how turbulence intensities vary in different directions. Anisotropy is critical in understanding and modeling complex turbulent flows because it dictates how energy is distributed among various turbulent structures. In mathematical terms, the anisotropic tensor a_{ij} can be derived from the Reynolds stress tensor normalized by the turbulent kinetic energy k (to make it dimensionless) and subtracting the isotropic part (which is one third of the tensor's trace), as follows

$$a_{ij} = \frac{\overline{u_i' u_j'}}{2k} - \frac{1}{3}\delta_{ij}. \tag{3.41}$$

The deviatoric part of the Reynolds stress tensor, on the other hand, is a broader concept that includes all the shear and normal stresses due to turbulence but excludes the isotropic part. The deviatoric part is essentially the Reynolds stress tensor without its isotropic component, and it focuses on the shear and distortion effects rather than the volumetric expansion or contraction. It can be expressed as follows

$$\tau_{ij}^{*} = -\rho\overline{u_i' u_j'} - \frac{1}{3}\rho k\delta_{ij}. \tag{3.42}$$

The Boussinesq approximation fundamentally relies on two assumptions. Firstly, the mean velocity gradients can characterize the anisotropic Reynolds stresses at each point in space and time. Secondly, the turbulent eddy viscosity is a scalar property of the flow, indicating a linear relationship between anisotropy and velocity gradients. Despite these assumptions, the Boussinesq approximation offers the advantage of retaining the same form as the Navier-Stokes equations for the Reynolds averaged equations and simplifies the closure problem by reducing the unknowns in the system to one. The turbulent eddy viscosity is often defined as the product of velocity and length scales. Most (U)RANS turbulence models are applied in the direct or indirect calculation of the eddy viscosity, with the specification of these scales differing among various models.

It's worth noting that EVMs have significant limitations in accurately predicting flow fields. The primary issue with EVMs is that they represent turbulence using a scalar quantity and kinetic energy and employ the eddy viscosity assumption, disregarding turbulence anisotropy. These models assume that the Reynolds stress tensor is instantaneously in equilibrium with the mean strain rate. This presumption forces the main axes of $\overline{u_i' u_j'}$ and the main rate of deformation $\bar{S_{ij}}$ to align, which is valid in purely stressed flows but not in flows with mean vorticity, such as delta wing flows.

Favre-averaging for compressible flows

Incorporating fluctuations in field variables for compressible flows introduces a significant increase in the complexity of the Navier-Stokes equations. When applied to these equations with density defined as the sum of its mean and fluctuating parts, the Reynolds averaging procedure yields additional terms involving correlations with fluctuating density, ρ', necessitating more complex turbulence closure models.

With a density-weighted averaging technique, this challenge was addressed by Favre, 1965. Like Reynolds averaging, the Favre-averaging method decomposes the instantaneous flow variables, ϕ, into mass-averaged, $\tilde{\phi}$, and fluctuating components, ϕ''', as follows

$$\phi(\boldsymbol{x},t) = \tilde{\phi}(\boldsymbol{x}) + \phi(\boldsymbol{x},t)'''. \tag{3.43}$$

The mass average of the variable field is defined as follows

$$\tilde{\phi}(\boldsymbol{x}) = \frac{1}{\bar{\rho}} \lim_{T\to\infty} \frac{1}{T} \int_{t}^{t+T} \rho\phi(\boldsymbol{x},t)dt, \tag{3.44}$$

where $\bar{\rho}$ is the time-averaged density. The mass average of the variables may be then expressed as

$$\tilde{\phi} = \frac{\overline{\rho\phi}}{\bar{\rho}}. \tag{3.45}$$

Therefore, the time average of the product of the density and a variable, ϕ, can be represented in terms of the Reynolds-averaged density and the Favre-averaged variable as follows

$$\overline{\rho\phi} = \bar{\rho}\tilde{\phi}. \tag{3.46}$$

Applying Favre averaging to the momentum Navier-Stokes equation yields

$$\frac{\partial(\bar{\rho}\tilde{u}_i)}{\partial t} + \frac{\partial(\bar{\rho}\tilde{u}_i\tilde{u}_j)}{\partial x_j} = -\frac{\partial\bar{p}}{\partial x_i} + \frac{\partial}{\partial x_j}\left(\bar{\tau_{ij}} + \tau_{ij}^R\right), \tag{3.47}$$

These Favre-averaged equations are analogous to the incompressible RANS equations but incorporate the Reynolds stress tensor defined as

$$\tau_{ij}^R = \overline{-\rho u_i''' u_j'''}. \tag{3.48}$$

The Boussinesq approximation adapts accordingly by using the deviatoric strain-rate tensor for calculating the anisotropic part as follows

$$S_{ij}^* = \tilde{S_{ij}} - \frac{1}{3}\frac{\partial\tilde{u_k}}{\partial x_k}\delta_{ij}. \tag{3.49}$$

Despite the similarity of the Favre-averaged equations to RANS equations, it's crucial to understand that Favre averaging is a mathematical simplification and does not eliminate the effects of density fluctuations on turbulence in the flow. The turbulent closure and applicable turbulence models remain consistent due to the analogous form of the equations.

3.3.4. Hybrid RANS/LES

Section 3.3.2 outlines LES as an approach to reduce the computational demands inherent in DNS. However, the applicability of LES is limited by several factors, most notably its marginal increase in feasible Reynolds numbers, approximately only an order of magnitude greater than that of DNS. These limitations primarily arise from the

challenges of implementing LES near domain walls, where turbulent length scales diminish to the scale of the boundary layer. Precise modeling of flow behavior near walls necessitates grid refinement approaching that of DNS, thereby reintroducing substantial computational limitations. This is particularly pertinent in practical engineering applications, such as aircraft simulations.

Various hybrid RANS/LES models have been developed to surmount these challenges. These models combine the fidelity of LES with the computational efficiency of RANS in contexts where exclusive use of LES would be prohibitively demanding. This approach will be discussed and analyzed in Section 3.4, based on the methodology adopted in the current manuscript.

3.4. Methodology for delta wing flow

A diverse range of turbulence models has evolved in RANS simulations, each garnering a unique position among various user groups and application contexts. The nature of turbulence, marked by its inherent complexity, unpredictable behavior, and non-linear properties, is a critical factor in flow types relevant to industrial and academic research. A spectrum of turbulence models with empirical foundations has been developed to address specific flow categories (Wilcox, 2001). The decision-making process for selecting the optimal turbulence model is often intricate, as the effectiveness of a model is closely tied to the distinct features of the flow scenario in question.

The inherently unsteady behavior of delta wing vortical flows is discussed in Section 2.1.4, highlighting the time-variant nature of the mean flow and its resultant non-stationary turbulence. Despite the non-stationary nature, Reynolds decomposition remains applicable as elucidated in Section 3.3.3. The fluctuation of an unsteady mean flow necessitates understanding turbulence models' predictive capabilities regarding the behavior of velocity gradients and turbulence production in such flows.

The velocity gradients in turbulent flows are components of a second-order tensor, decomposable into isotropic, symmetric-deviatoric, and anti-symmetric parts. A comprehensive elucidation of second-order tensors is provided by Pope, 2000. The decomposition of the velocity gradient tensor is elaborated in Eq. 3.50, wherein the symmetric component is identified as the strain rate tensor, S_{ij}, and the anti-symmetric component is associated with the rotation tensor, W_{ij}.

$$\frac{\partial u_i}{\partial x_j} = \underbrace{\frac{1}{3}\frac{\partial u_k}{\partial x_k}\delta_{ij} + S^*_{ij}}_{S_{ij}} + W_{ij} \tag{3.50}$$

The strain-rate tensor is defined in Eq. 3.4, and the rotation tensor is given by

$$W_{ij} = \frac{1}{2}\left(\frac{\partial u_i}{\partial x_j} - \frac{\partial u_j}{\partial x_i}\right). \tag{3.51}$$

This rotation tensor is directly related to the flow's vorticity, as expressed in

$$\omega_i = -\epsilon_{ijk} W_{jk}, \tag{3.52}$$

where ϵ_{ijk} is the Levi-Civita symbol, defined as

$$\epsilon_{ijk} = \begin{cases} 1, & \text{if } (i,j,k) \text{ are cyclic, i.e., 123, 231, or 312} \\ -1, & \text{if } (i,j,k) \text{ are anti-cyclic, i.e., 321, 132, or 213} \\ 0, & \text{otherwise} \end{cases} \tag{3.53}$$

In shear layers, it is generally observed that the velocity gradients are dominated by the normal gradients, rendering the strain rate and rotational tensors roughly equal. However, as the flow approaches the vortex core, it tends towards a purely rotational state, and the rotational tensor predominates.

The production of turbulent kinetic energy is defined as the product of the Reynolds stress tensor and the velocity gradient, formulated as

$$P_k = \tau_{ij}^R \frac{\partial u_i}{\partial x_j}. \tag{3.54}$$

This equation describes the energy transfer from the mean flow to the fluctuating velocity field, facilitated by the interaction between mean velocity gradients and Reynolds stresses through vortex stretching. Notably, only the symmetric part of the velocity gradient tensor and the anisotropic part of the Reynolds stress tensor contribute to turbulent kinetic energy production. The kinetic energy production is then proportional to the strain-rate tensor. In the context of delta wing vortical flows, this suggests that turbulence production primarily occurs within the shear layer and surrounding flow rather than the highly rotational vortex core, which may exhibit low turbulence and approach a laminar state. An effective turbulence model for this flow type should accurately predict such behavior.

The turbulence models and approaches adopted in this manuscript are elucidated herein, aligning with the theoretical framework on turbulence modeling previously delineated. As outlined in Section 1.2, both URANS and hRL simulations are conducted using the DLR-TAU code for simulating the delta wing flows. Within the URANS framework, two EVMs are utilized: the one-equation Spalart-Allmaras with negative and Rotational/Curvature correction (SAnegRC) model, and the two-equation $k-\omega$ Shear-Stress Transport model ($k\omega$SST). Furthermore, for the hRL approach, the Improved Delayed Detached Eddy Simulation (IDDES) based on the SAneg model, in addition to the Scale-Adaptive Simulation (SAS) based on the $k\omega$SST model, are employed.

3.4.1. The Spalart-Allmaras turbulence model

The Spalart-Allmaras model for eddy viscosity turbulence is built around a solitary transport equation for the eddy viscosity variable, ν_t (Spalart and Allmaras, 1992).

Its design goals included numerical stability, local validity, and Galilean invariance. The local approach of the model allows for the computation of ν_t at individual points independently of the domain's other points, significantly benefiting its application to unstructured grid frameworks. The SA model is robust in handling both wall and free-stream boundary conditions. Its convergence rate, stability, and accuracy efficiency have been validated through numerous applications, especially in scenarios involving attached or mildly separated flows, making it a popular choice in contemporary numerical studies. The logic behind the SA is explained step by step in the following. For the sake of clarity, the filtering operation is not explicitly detailed. The methodology adopted adheres to the notation prevalent in the literature (Spalart and Allmaras, 1992; Wilcox, 1998).

SA formulation for free shear flows. The eddy viscosity in the SA model establishes a linear relation $-\overline{u_i u_j} = \nu_t S_{ij}$, aligning with the Boussinesq assumption (see Section 3.3.3). Contrary to certain two-equation models, the k term is neglected. The material derivative of ν_t on the left-hand side (LHS) of the equation finds a balance with the right-hand side (RHS) terms, incrementally added to an initial formulation for free-shear flows, each signifying singular additional phenomena.

The RHS principally includes a production and a diffusion term in a free-shear flow scenario. A scalar norm S, essential for evaluating the deformation tensor $\partial u_i/\partial x_j$, must accompany ν_t. This norm is invariant, and in the original formulation, the vorticity norm Ω was used mainly because, in the targeted applications, areas with dominant vorticity usually exhibit significant turbulence. However, other metrics like strain rate or the complete tensor norm could be equally effective. For consistency with the original formulation, Ω will be represented as S. Thus, the baseline production term becomes $c_{b1} S \nu_t$.

The diffusion term is formulated based on the spatial derivative of the turbulent viscosity, ν_t, utilizing the operator $\nabla \cdot ((\nu_t/\sigma)\nabla\nu_t)$, where σ denotes the Prandtl number. This diffusion term is further modified to $(1/\sigma)\left[\nabla \cdot (\nu_t \nabla \nu_t) + c_{b2}|\nabla\nu_t|^2\right]$, incorporating the term $c_{b2}|\nabla\nu_t|^2$ to account for the enhanced diffusion effect. Therefore, the model considered appropriate for free shear flow scenarios is expressed as

$$\frac{\partial \nu_t}{\partial t} + u_j \frac{\partial \nu_t}{\partial x_j} = c_{b1} S \nu_t + \frac{1}{\sigma}\left[\frac{\partial}{\partial x_j}\left(\nu_t \frac{\partial \nu_t}{\partial x_j}\right) + c_{b2}\frac{\partial \nu_t}{\partial x_i}\frac{\partial \nu_t}{\partial x_i}\right]. \tag{3.55}$$

The term $c_{b2}|\nabla\nu_t|^2$ specifically accounts for the additional diffusion of ν_t due to the turbulence itself, beyond what would be predicted by molecular diffusion alone. This term ensures the model's responsiveness to variations in the spatial gradients of ν_t, allowing for better adaptation to the evolving structure of turbulence. This adaptability is crucial for accurately simulating complex flows that exhibit significant differences in turbulence intensity and scale.

SA formulation for wall-bounded flows. Incorporating wall effects destroys the Reynolds shear stress, dependent on the wall distance d. The term $-c_{w1}\left(\nu_t/d\right)^2$ is integrated for this purpose. This term becomes negligible in free-shear flows where the distance approaches infinity, ensuring it does not modify the previous calibration

suitable for free-shear flows. Applications demonstrate accurate replication of the log-layer in boundary layers but tend to underestimate skin friction coefficients over flat plate flows. To rectify this, a non-dimensional smoothing function f_ω, based on the dimensionless mixing length,

$$r = \frac{\nu_t}{S\kappa^2 d^2}, \tag{3.56}$$

is applied to the destruction factor. The function is defined as follows

$$f_\omega(r) = g\left[\frac{1+c_{\omega3}^6}{g^6+c_{\omega3}^6}\right]^{\frac{1}{6}}, \quad \text{where} \quad g = r + c_{\omega2}(r^6 - r). \tag{3.57}$$

Spalart and Allmaras, 1992 also considered the buffer and viscous sub-layer modeling, introducing a modified eddy viscosity[1], $\tilde{\nu}$, equivalent to ν_t except in the viscous region. A smoothing function f_{v1} is applied, equalizing eddy viscosity to $\kappa y u_\tau$ in both the log and buffer layers, as follows

$$\nu_t = \tilde{\nu} f_{v1}, \quad \text{where} \quad f_{v1} = \frac{\chi^3}{\chi^3 + c_{v1}^3} \quad \text{with} \quad \chi = \frac{\tilde{\nu}}{\nu}. \tag{3.58}$$

The production term requires another smoothing function f_{v2}, ensuring appropriate behavior across different boundary layer stages. Consequently, S is replaced by $\tilde{S}$ as follows

$$\tilde{S} = S + \frac{\tilde{\nu}}{\kappa^2 d^2} f_{v2}, \quad \text{with} \quad f_{v2} = 1 - \frac{\chi}{1+\chi f_{v1}}, \tag{3.59}$$

to maintain log-layer dependence as $\tilde{S} = u_\tau/(\kappa y)$.

The final formulation step considers laminar and transition regions. However, the transition-triggering term is omitted here, as our research focuses on fully turbulent cases for which the model is predominantly utilized. The addition for laminar regions ensures $\tilde{\nu} = 0$ as a stable solution of the model equation, assuming $\tilde{\nu}$ should be at most of the order of ν in laminar conditions. The production term is thus modified with $1 - f_{t2}$, and the destruction term is accordingly balanced. The function f_{t2} is formulated as follows

$$f_{t2} = c_{t3} \exp\left(-c_{t4}\chi^2\right). \tag{3.60}$$

The term f_{t2}, which appears in both the production and destruction components, is specifically designed to suppress turbulence in laminar regions.

In the end, after all the previous steps, the model's equation for the modified eddy viscosity, $\tilde{\nu}$, is presented in its incompressible form as follows

$$\frac{\partial\tilde{\nu}}{\partial t} + u_j\frac{\partial\tilde{\nu}}{\partial x_j} = c_{b1}(1-f_{t2})\tilde{S}\tilde{\nu} - \left[c_{w1}f_w - \frac{c_{b1}}{\kappa^2}f_{t2}\right]\left(\frac{\tilde{\nu}}{d}\right)^2 + \frac{1}{\sigma}\left[\frac{\partial}{\partial x_j}\left((\nu+\tilde{\nu})\frac{\partial\tilde{\nu}}{\partial x_j}\right) + c_{b2}\frac{\partial\tilde{\nu}}{\partial x_i}\frac{\partial\tilde{\nu}}{\partial x_i}\right], \tag{3.61}$$

[1]It is important to clarify that the notation employing the tilde should not be confused with the Favre averaging discussed in Section 3.3.3.

with

$$\begin{aligned} c_{b1} &= 0.1355, \quad \sigma = \frac{2}{3}, \quad c_{b2} = 0.622, \quad \kappa = 0.41, \\ c_{w1} &= \frac{c_{b1}}{\kappa^2} + \frac{1 + c_{b2}}{\sigma}, \quad c_{w2} = 0.3, \quad c_{w3} = 2.0, \\ c_{v1} &= 7.1, \quad c_{t3} = 1.1, \quad c_{t4} = 0.5. \end{aligned} \tag{3.62}$$

The original SA model, which does not explicitly include the density term, is applicable to both incompressible and compressible flows and is considered the standard formulation for compressible analysis. Nevertheless, an equivalent conservation form can be derived by integrating the SA model with the mass conservation equation (Allmaras and F. Johnson, 2012). For compressible flow simulations, additional compressibility corrections are introduced in solvers such as the DLR-TAU code, exemplified by

$$C_{\tilde{\nu}} = -\frac{1}{\sigma}(\nu + \tilde{\nu})\frac{\partial \rho}{\partial x_k}\frac{\partial \tilde{\nu}}{\partial x_k} \tag{3.63}$$

Consequently, the **compressibility-corrected SA** equation is expressed as

$$\begin{aligned} \frac{\partial(\rho\tilde{\nu})}{\partial t} + \frac{\partial(\rho\tilde{\nu}u_j)}{\partial x_j} = {} & c_{b1}\left(1 - f_{t2}\right)\tilde{S}\rho\tilde{\nu} - \left[c_{w1}f_w - \frac{c_{b1}}{\kappa^2}f_{t2}\right]\rho\left(\frac{\tilde{\nu}}{d}\right)^2 \\ & + \frac{1}{\sigma}\left[\frac{\partial}{\partial x_j}\left(\rho\left(\nu + \tilde{\nu}\right)\frac{\partial \tilde{\nu}}{\partial x_j}\right) + c_{b2}\rho\frac{\partial \tilde{\nu}}{\partial x_i}\frac{\partial \tilde{\nu}}{\partial x_i}\right] \\ & - \frac{1}{\sigma}(\nu + \tilde{\nu})\frac{\partial \rho}{\partial x_k}\frac{\partial \tilde{\nu}}{\partial x_k}. \end{aligned} \tag{3.64}$$

This model has gained widespread usage in external aerodynamic flow studies, particularly in attached flow conditions, where it exhibits optimal performance in terms of accuracy due to its formulation and calibration procedure. It demonstrates significant numerical stability and robustness, with minimal sensitivity or critical outcomes relative to initial and free-stream conditions. A typical free-stream value for $\tilde{\nu}$ is significantly larger than ν, aiding in resolving potential solver issues where rounding errors or divisions by $\tilde{\nu}$ are involved in the model's implementation.

The SA model with negative eddy viscosity correction (**SAneg**), an extension of the standard SA model proposed by Allmaras and F. Johnson, 2012, is activated when the turbulence variable $\tilde{\nu}$ is negative, a condition that is physically non-realistic and thus needs mitigation. Under these circumstances, the modified transport equation becomes

$$\frac{\partial \tilde{\nu}}{\partial t} + u_j\frac{\partial \tilde{\nu}}{\partial x_j} = c_{b1}(1 - c_{t3})\Omega\tilde{\nu} + c_{w1}f_w\left(\frac{\tilde{\nu}}{d}\right)^2 + \frac{1}{\sigma}\left[\frac{\partial}{\partial x_j}\left(\left(\nu + \tilde{\nu}f_n\right)\frac{\partial \tilde{\nu}}{\partial x_j}\right) + c_{b2}\frac{\partial \tilde{\nu}}{\partial x_i}\frac{\partial \tilde{\nu}}{\partial x_i}\right], \tag{3.65}$$

with

$$f_n = \frac{c_{n1} + \chi^3}{c_{n1} - \chi^3} \qquad \text{and} \qquad c_{n1} = 16. \tag{3.66}$$

The production term becomes positive because the coefficient c_{t3} being set at 1.2. Indeed, the factors multiplying $\tilde{\nu}$, and, $\tilde{\nu}$ itself, are negative.

Shur et al., 2000 further augmented the SA model with a streamline curvature correction (**SA-RC**), modifying the production term with a rotation function as follows

$$f_{r1} = (1 + c_{r1})\frac{2r^*}{1 + r^*}\left[1 - c_{r3}tan^{-1}(c_{r2}\tilde{r})\right] - c_{r1}. \tag{3.67}$$

Specifically, the first term on the RHS of the SA-RC equation is given by

$$c_{b1}(f_{r1} - f_{t2})\hat{S}\hat{\nu}. \tag{3.68}$$

The various terms are defined as follows

$$\begin{aligned}
&r^* = \frac{S}{\omega}, \qquad \tilde{r} = \frac{2\omega_{ik}S_{jk}}{D^4}\left(\frac{DS_{ij}}{Dt} + (\varepsilon_{imn}S_{jn} + \varepsilon_{jmn}S_{in})\Omega'_m\right),\\
&S_{ij} = \frac{1}{2}\left(\frac{\partial u_i}{\partial x_j} + \frac{\partial u_j}{\partial x_i}\right), \qquad \omega_{ij} = \frac{1}{2}\left[\left(\frac{\partial u_i}{\partial x_j} - \frac{\partial u_j}{\partial x_i}\right) + 2\varepsilon_{mji}\Omega'_m\right],\\
&S^2 = 2S_{ij}S_{ij}, \qquad \omega^2 = 2\omega_{ij}\omega_{ij}, \qquad D^2 = \frac{1}{2}\left(S^2 + \omega^2\right),\\
&c_{r1} = 1.0, \qquad c_{r2} = 12, \qquad c_{r3} = 1.0.
\end{aligned} \tag{3.69}$$

3.4.2. Improved Delayed Detached Eddy Simulation

The DES approach proposed by Spalart, 1997 has become notably prominent among the hRL method. DES integrates LES modeling in regions distant from wall boundaries while transitioning to RANS modeling in near-wall boundary layer regions. Adopting DES in industrial settings is increasingly preferred, as it addresses some of the intrinsic limitations of RANS models and enhances solution quality.

The integration of the SA model within the **DES** framework is based on the interplay between the production and destruction terms in the model's governing partial differential equation, as delineated in Eq. 3.61. This interplay yields a relationship wherein the eddy-viscosity, $\widetilde{\nu}$, is proportional to the product of modified vorticity, $\widetilde{S}$, and the square of the distance to the nearest wall, d^2, expressed as

$$\widetilde{\nu} \propto \widetilde{S}d^2. \tag{3.70}$$

The analogous nature of this relationship becomes evident when considering the SGS model, particularly its formula for eddy viscosity. Here, a similar proportionality is observed, with the grid spacing term, Δ (defined in Eq. 3.26), replacing the distance d, as indicated in

$$\nu_{SGS} \propto \widetilde{S}\Delta^2. \tag{3.71}$$

This resemblance led to the proposition that substituting d with Δ in the wall destruction term would enable the SA model to mimic a Smagorinsky LES model. Consequently, for the SA model to exhibit both URANS and LES behavior, the distance d is replaced with a modified distance $\widetilde{d}$, defined as

$$\widetilde{d}_{DES} \equiv \min\left[d, \Delta_{DES}\right], \quad \text{with} \quad \Delta_{DES} = C_{DES}\Psi\Delta. \tag{3.72}$$

Here, C_{DES} is a constant set to 0.65 as recommended for homogeneous turbulence conditions, and Ψ is a low Reynolds number correction. This formulation enables the model to function as a RANS model when $d \ll \Delta$ and as an SGS model when $d >> \Delta$, thereby localizing URANS to near-wall areas and facilitating LES application elsewhere, as illustrated schematically in Fig. 3.4.

Employing DES allows the application of LES to the vortical regions above the wing. The Boussinesq approximation is limited to the unresolved scales and near wall region, ensuring that all large-scale rotations, stresses, and strains are fully resolved on the grid. This leads to a more accurate prediction of turbulence production and the overall behavior of the leading-edge vortex system. Typically, the sub-grid contribution to turbulence will be minimal, thereby maintaining low and realistic turbulence levels within the vortex core region. However, to ensure this minimal contribution, the grid must be adequately refined to resolve most flow scales, significantly increasing the computational expense compared to traditional RANS turbulence models.

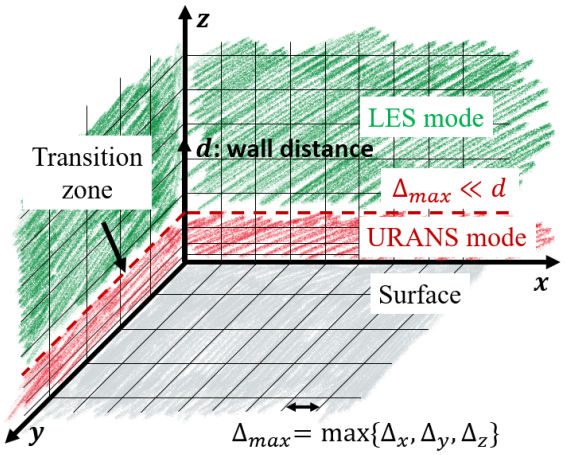

Figure 3.4: DES transition scheme (inspired by Spalart, 1997).

A notable limitation of the original DES methodology manifests when the grid is locally refined in multiple directions in regions not intended for scale-resolving. This situation commonly occurs in areas of high geometric curvature or near junctures where multiple solid surfaces converge. As the DES transition criterion (Eq. 3.72), directly contrasts the RANS length scale with the maximum grid cell dimension, the eddy viscosity may experience a significant reduction within the boundary layer without a corresponding mechanism to convert the resolved turbulence energy into modeled energy. For a typical RANS grid characterized by a high aspect ratio within the boundary layer, where the wall-parallel grid spacing often surpasses the boundary layer thickness, δ, Eq. 3.72 ensures that the DES model operates in RANS mode throughout the entire boundary layer. However, the DES limiter may inadvertently trigger the LES mode within the boundary layer in scenarios characterized by an ambiguous grid definition, specifically where $\Delta \ll \delta$. Such a situation is problematic as the grid might not be sufficiently refined to support resolved turbulence. This poses a considerable constraint for more complex flow applications, such as delta wing flows, where local refinements are indispensable.

In response to these and other shortcomings of the original DES, several modifications to the basic DES concept are proposed in the literature. A notable evolution of this methodology is the **IDDES** approach, as introduced by Shur et al., 2008. The IDDES framework incorporates two major advancements beyond the standard DES methodology.

The first advancement, leading to the **DDES** approach as articulated by Spalart et al., 2006, addresses the issue mentioned above by inhibiting the transition from RANS to LES mode within attached boundary layers due solely to grid design specifics. This modification is achieved by altering the DES length scale to include a flow-dependent shielding function that upholds the RANS length scale in regions of attached boundary layer flows. This ensures a more accurate and reliable simulation in complex geometric configurations. DDES is specifically designed to maintain the RANS mode across the entirety of the boundary layer, thereby mitigating premature transition to LES mode due to sub-optimal grid definitions.

In the DDES model, the hybrid length scale, $\widetilde{d}$, becomes

$$\widetilde{d}_{DDES} \equiv d - f_d \max\left[0, d - \Delta_{DES}\right], \tag{3.73}$$

where the shielding function f_d is defined as

$$f_d = 1 - \tanh\left((8r_d)^3\right), \quad \text{with} \quad r_d = \frac{\mu + \mu_t}{\rho(\kappa d^2)\max\left[\sqrt{\frac{\partial u_i}{\partial x_j}\frac{\partial u_i}{\partial x_j}}, 10^{-10}\right]}. \tag{3.74}$$

The variable r_d is designed to approximate unity within the sub-layer and logarithmic regions of the boundary layer, and it asymptotically approaches zero near the boundary layer's edge. Consequently, f_d remains near zero until the defect layer is encountered, rapidly ascending towards unity as $r_d \ll 1$.

The second enhancement introduced by Shur et al., 2008 was incorporating Wall-Modeled Large Eddy Simulation (**WMLES**) functionality into the IDDES formulation. Generally, the IDDES framework can provide a WMLES response if resolved turbulent content is available as an inflow or initial condition. The model defaults to a DDES response without such resolved turbulence. This dual capability enables IDDES to adaptively respond to the specifics of the flow field and the available simulation data, thereby enhancing its applicability and accuracy for a broad range of complex flow scenarios.

The WMLES branch of the IDDES is designed to activate only under specific conditions. When the inflow conditions are resolved, turbulent content and the grid resolution are sufficient to resolve at least the largest energy-containing eddies of the boundary layer. This branch employs the hybrid length scale, $\widetilde{d}_{WMLES}$, defined as follows

$$\widetilde{d}_{WMLES} = f_\beta(1 + f_e)d + (1 - f_\beta)\Delta_{DES}. \tag{3.75}$$

Here, f_β, the empirical blending function, is expressed as

$$f_\beta = \min\left[2\exp\left(-9\alpha^2\right), 1\right], \quad \text{with} \quad \alpha = 0.25 - \frac{d}{\Delta}. \tag{3.76}$$

This function transitions from 0 (LES mode) to 1 (RANS mode) and facilitates a rapid switch between these modes as the wall distance spans 0.5Δ and Δ. The secondary empirical function, f_e, is designed to prevent an excessive reduction of the RANS Reynolds

stresses near the RANS/LES interface, thus addressing the log-layer mismatch common in hRL models. It is defined as

$$f_e = \max\left[(f_{e1} - 1), 0\right] \Psi f_{e2}, \tag{3.77}$$

where f_{e_1} and f_{e2} are given by

$$\begin{aligned} f_{e_1} &= \begin{cases} 2\exp(-11.09\alpha^2), & \text{if } \alpha \geq 0 \\ 2\exp(-9.0\alpha^2), & \text{if } \alpha < 0 \end{cases} \\ f_{e_2} &= 1 - \max\left[\tanh\{(c_t^2 r_{d_t})^3\}, \tanh\{(c_l^2 r_{d_l})^{10}\}\right]. \end{aligned} \tag{3.78}$$

Here, Ψ represents an optional low Reynolds number correction, while r_{d_t} and r_{d_l} denote the turbulent and laminar portions of the r_d parameter (Eq. 3.74). The constants c_t and c_l ensure that f_{e_2} approaches zero when either r_{d_t} or r_{d_l} is close to 1.0. The optimal values for these constants vary based on the specific RANS model employed. For instance, Shur et al., 2008 determined that $c_t = 1.63$ and $c_l = 3.55$ are effective with the SA model, as evidenced by fully developed channel flow simulations. The correction Ψ is the same low Reynolds number correction introduced in the definition of Δ_{DES} in Eq. 3.72 when employing the SA model. It is set to unity for RANS models that do not incorporate low Reynolds number corrections.

The DDES and WMLES length scales, as denoted in Eq. 3.73 and Eq. 3.75, respectively, are not readily blended in a manner that guarantees the realization of the desired branch, contingent on the presence of resolved turbulent content within the boundary layer. However, a modified DDES length scale expression allows for such a possibility as follows

$$\widehat{d}_{DDES} = \widetilde{f}_d d + (1 - \widetilde{f}_d)\Delta_{DES}, \tag{3.79}$$

where

$$\widetilde{f}_d = \max\left[1 - f_{d_t}, f_\beta\right], \quad f_{d_t} = 1 - \tanh\left[(8 r_{d_t})^3\right]. \tag{3.80}$$

This functional replacement for the DDES length scale essentially facilitates the blending of the DDES and WMLES length scale definitions through the following expression:

$$\widetilde{d}_{IDDES} = \widetilde{f}_d(1 + f_e)d + (1 - \widetilde{f}_d)\Delta_{IDDES}. \tag{3.81}$$

The IDDES hybrid length scale ensures the desired WMLES behavior in simulations containing resolved turbulent content within the boundary layer (since $r_{d_t} \ll 1 \Rightarrow f_{d_t} \approx 1$ so that $\tilde{f}_d = f_\beta$). Conversely, in simulations devoid of resolved turbulence within the boundary layer, $f_e \approx 0$ and $f_{d_t} \approx 0$, which implies $\tilde{f}_d = 1$.

Additionally, the DES filter width in the IDDES formulation is explicitly modified to include the wall distance, d, as follows

$$\Delta_{IDDES} = \min\left\{\max\left[C_w d, C_w\Delta, \Delta_n\right], \Delta\right\}. \tag{3.82}$$

Here, Δ_n denotes the grid spacing in the wall-normal direction, which can be ambiguous for complex geometries with multiple walls. A potential method to assess this quantity

involves averaging the cell center values of the wall distance to grid nodes, facilitating the computation of an effective wall-normal grid spacing as the discrepancy between the maximum and minimum nodal values for each grid cell. Fully developed channel flow simulations determined the coefficient $C_w = 0.15$.

3.4.3. The Menter Shear Stress Transport turbulence model

Within the $k-\omega$ model framework, the turbulent kinetic energy, k, and the dissipation rate, ω, are determined through the solution of their respective transport equations. The transport equation for turbulent kinetic energy is given by

$$\frac{\partial(\rho k)}{\partial t} + \frac{\partial(\rho k u_j)}{\partial x_j} = P_k - \beta^k \rho\omega k + \frac{\partial}{\partial x_j}\left[(\mu + \sigma_k \mu_t)\frac{\partial k}{\partial x_j}\right]. \tag{3.83}$$

Similarly, the transport equation for the dissipation rate is expressed as

$$\frac{\partial(\rho\omega)}{\partial t} + \frac{\partial(\rho\omega u_j)}{\partial x_j} = \frac{\gamma_\omega \omega}{k} P_k - \beta^\omega \rho\omega^2 + \frac{\partial}{\partial x_j}\left[(\mu + \sigma_\omega \mu_t)\frac{\partial \omega}{\partial x_j}\right] + \frac{\rho\sigma_d}{\omega}\frac{\partial k}{\partial x_j}\frac{\partial \omega}{\partial x_j}. \tag{3.84}$$

The turbulent eddy viscosity is given by

$$\mu_t = \frac{\rho k}{\omega}, \tag{3.85}$$

and the turbulence production term $P_{k\omega}$ is defined as

$$P_k = \tau_{ij}^R \frac{\partial u_i}{\partial x_j}, \tag{3.86}$$

where the Reynolds stress tensor τ_{ij}^R is evaluated using the Boussinesq assumption expressed in Eq. 3.40. In these equations β^k, β^ω, γ_ω, σ_k, σ_ω, and σ_d are closure coefficients that vary between the different versions of the $k-\omega$ model present in the literature.

Menter baseline model. Menter, 1994 proposed a hybrid approach that combines the $k-\omega$ model in the near-wall regions with the standard $k-\varepsilon$ model in the free-stream. This integration involves transforming the ε-equation into a transport equation for ω, introducing the cross-diffusion term, which effectively suppresses the free-stream model sensitivity. The $k-\omega$ model enhances accuracy in near-wall regions, whereas the $k-\epsilon$ model is more effective outside these areas. The transition between the $k-\omega$ and $k-\varepsilon$ models is facilitated through a smooth variation of the closure coefficients as defined by

$$\phi = F_1 \phi^{(i)} + (1 - F_1)\phi^{(o)}, \tag{3.87}$$

where $\phi = \{\beta_k, \beta_\omega, \gamma_\omega, \sigma_k, \sigma_\omega, \sigma_d\}$, and the indices i and o denote values in the near-wall (inner) and free-stream (outer) regions, respectively. The blending function, F_1, is determined as

$$F_1 = \tanh\left(G_1^4\right), \tag{3.88}$$

where G_1 is calculated by

$$G_1 = \min\left[\max\left(\Gamma_1, \Gamma_2\right), \Gamma_3\right]. \tag{3.89}$$

The arguments are defined as

$$\Gamma_1 = \frac{\sqrt{k}}{0.09\omega d}, \qquad \Gamma_2 = \frac{500\mu}{\rho\omega d^2}, \qquad \Gamma_3 = \frac{2\sigma_d^{(o)} k}{\mathrm{CD}_\omega^{(o)} d^2}, \tag{3.90}$$

with

$$\mathrm{CD}_\omega^{(o)} = \max\left(\sigma_d^{(o)} \frac{\rho}{\omega} \frac{\partial k}{\partial x_j} \frac{\partial \omega}{\partial x_j}, 10^{-20}\right). \tag{3.91}$$

Here, d represents the distance from the wall, that is, the projected distance to the nearest point on the wall. The function F_1 is specifically designed to transition from a value of 1 in close proximity to the wall, to 0 approximately at the midpoint of the boundary layer. This design facilitates accurate modeling of turbulence dynamics from the near-wall region to the outer layers of the boundary layer.

Menter SST model. Alongside the Baseline (BSL) model, Menter, 1993, 1994 introduced the so-called SST model. This model represents an extension of the BSL model, enhancing its sensitivity to positive pressure gradients and flow separation. This enhancement is achieved by modulating the eddy viscosity as follows

$$\mu_t = \frac{\rho a_1 k}{\max(a_1\omega, \Omega F_2)}, \tag{3.92}$$

with $a_1 = 0.31$, and he blending function, F_2, given by

$$F_2 = \tanh\left(G_2^2\right), \qquad \text{with} \qquad G_2 = \max\left(2\Gamma_1, \Gamma_2\right). \tag{3.93}$$

The function F_2 assumes a value of 1 in proximity to walls and transitions to 0 at the edge of the boundary layer. This gradation effectively confines the eddy-viscosity reduction (SST limitation) to the boundary layers. Notably, the parameters for Γ_1 and Γ_2 are consistent with those utilized for the F_1 function in the BSL model.

3.4.4. Scale Adaptive Simulation

The SAS approach is an advanced technique that bridges traditional RANS models and the more computationally intensive LES. Included within the hRL methods, SAS can provide more accurate results than RANS in various scenarios but does not fully resolve all the scales of turbulence as LES does. Consequently, it is considered a compromise between the accuracy of LES and the computational efficiency of RANS. Developed to enhance the accuracy of turbulence modeling while maintaining reasonable computational costs, SAS aims to adaptively resolve the larger energy-containing scales of turbulence based on local flow conditions. Its advantage over traditional RANS lies in its capability to capture unsteady and complex flow features without incurring the complete computational expense of LES, proving particularly useful in the context of

flows dominated by large, unsteady vortices. The employed SAS approach is based on the Menter SST $k-\omega$ model (Menter, 1994).

SAS's turbulence model can alter its behavior depending on the local flow structure. It incorporates an additional source term or function, Q_{SAS}, into the turbulence dissipation rate equation (Eq. 3.84) that responds to locally resolved turbulence. This term is mathematically expressed as

$$Q_{SAS} = \max\left[\rho\zeta_2 S^2\left(\frac{L_m}{L_{vK}}\right)^2 - F_{SAS}\frac{2\rho k}{\sigma_\phi}\max\left(\frac{1}{k^2}\frac{\partial k}{\partial x_j}\frac{\partial k}{\partial x_j}, \frac{1}{\omega^2}\frac{\partial \omega}{\partial x_j}\frac{\partial \omega}{\partial x_j}\right), 0\right], \tag{3.94}$$

with $\zeta_2 = 1.755$, $\sigma_\phi = \frac{2}{3}$, and $F_{SAS} = 1.25$. The length L_m is defined as follows

$$L_m = c_\mu^{-\frac{1}{4}}\frac{\sqrt{k}}{\omega}, \tag{3.95}$$

with $c_\mu = 0.09$ and $\kappa = 0.41$. The von Kármán length scale, $L_{\nu K}$, is defined as

$$L_{\nu K} = \kappa\frac{U'}{U''}, \quad \text{where} \quad U' = \sqrt{2S_{ij}S_{ij}} \quad \text{and} \quad U'' = \sqrt{\frac{\partial^2 u_i}{\partial x_k^2}\frac{\partial^2 u_i}{\partial x_j^2}}. \tag{3.96}$$

As proposed by Menter and Egorov, 2010, SAS represents an innovative methodology to facilitate the partial resolution of turbulent structures in unsteady flow regimes. Conceptualized as a URANS model with scale-resolving capabilities, SAS exhibits LES-like behavior under certain conditions. In contrast to LES, a unique feature of SAS is its well-defined nature, even on coarser mesh cells. When the flow is well-resolved (as in LES), the model acts more like an LES model, resolving larger scales of turbulence. Conversely, when the flow is not well-resolved (as in RANS), it behaves more like a RANS model. This model's adaptability stems from the integration of the von Kármán length scale into the scale-determining equation. This inclusion facilitates a dynamic transition from RANS to LES-like behavior in regions exhibiting unsteady flow, such as vortices and shear stress regions observed in delta wing flows.

4

Software and Numerical Strategy

This chapter outlines the software and numerical strategies. Section 4.1 introduces the CFD codes utilized, while Section 4.2 addresses Evolutionary Computing (EC), specifically presenting the GEP code and its CFD-driven framework. Finally, Section 4.3 discusses the numerical techniques, including the FVM and the numerical schemes.

4.1. CFD codes overview

The CFD simulations are conducted using two CFD codes, TAU and OpenFoam. These tools are briefly described below, with pertinent references provided for more in-depth exploration by the reader.

4.1.1. The DLR-TAU code

The German Aerospace Center has developed TAU, a widely recognized computational tool in aerodynamics and fluid dynamics. It is a sophisticated CFD code that simulates complex, three-dimensional flow fields. It is particularly notable for its versatility in handling various types of flow, ranging from incompressible to hypersonic regimes.

TAU employs the FVM for discretizing the Navier-Stokes equations. One of its key strengths lies in its ability to work with unstructured grids, which makes it highly adaptable for complex geometries often encountered in aerospace applications. This flexibility is crucial for accurately simulating flow over intricate designs, such as delta wings, where the flow field can be highly irregular and challenging to model.

The code supports a range of turbulence models and boundary conditions and has capabilities for both steady-state and transient simulations. Its robustness and efficiency make it a tool for various aerodynamic research and industrial applications. Flux computation is facilitated via either upwind or central schemes. Viscous fluxes for one-equation turbulence models with central schemes are discretized using central differences, while two-equation models employ an upwind-type discretization.

For those looking to delve deeper into its functionalities and applications, references such as Gerhold, 2002 and Kroll et al., 2014 provide comprehensive insights and are frequently cited in academic and industry research.

4.1.2. OpenFoam

OpenFOAM Version 7.0 is an open-source CFD software widely utilized for modeling complex fluid dynamics scenarios. OpenFOAM is, first and foremost, a C++ library used primarily to create executables known as applications. The applications fall into two categories: solvers, which are each designed to solve a specific problem in continuum mechanics, and utilities, which are designed to perform tasks that involve data manipulation. The interfaces to the pre-and post-processing are OpenFOAM utilities, thereby ensuring consistent data handling across all environments (Greenshields, 2019).

Two distinct OpenFOAM solvers, simpleFoam and rhoPimpleFoam, each tailored to specific types of fluid flow simulations, are employed in this thesis. simpleFoam is adept at handling steady-state simulations in scenarios involving incompressible, turbulent fluid flow. The principal characteristic of these simulations is the constancy of flow over time, which necessitates a steady-state solution. The underlying algorithm of simpleFoam is the Semi-Implicit Method for Pressure-Linked Equations (SIMPLE). In contrast, rhoPimpleFoam is engineered for simulations that demand the analysis of compressible, turbulent flow, especially in cases characterized by unsteady dynamics and high Mach numbers. The solver synthesizes methodologies from both the Pressure Implicit with Splitting of Operators (PISO) and SIMPLE algorithms.

OpenFOAM is a tool of choice in academic research and is widely used in various industrial applications due to its flexibility and capabilities. Users are encouraged to refer to the official OpenFOAM documentation and community resources for more detailed information (Greenshields, 2019).

4.2. Evolutionary computing

EC is a branch of artificial intelligence that draws inspiration from the mechanisms of natural evolution to solve complex problems. It includes a variety of algorithms and techniques, including evolutionary algorithms, genetic programming, and evolutionary strategies, among others. These algorithms simulate the process of natural selection by evolving solutions to problems over many generations, optimizing for the best possible results.

4.2.1. Evolutionary algorithms

The fundamental objective of all EAs is to emulate the process of evolution (Langdon et al., 2008). These algorithms incorporate numerous concepts from natural evolution into their codes. Initiating with a specific population, the pivotal concept is the Darwinian principle of natural selection, colloquially known as the survival of the fittest (Man et al., 2001). This principle is implemented via a fitness function applied to potential solutions (individuals), which is iteratively refined across generations. The fitness function, which may vary based on individual characteristics, must facilitate a comparative evaluation of individuals concerning their problem-solving efficacy. An individual's fitness determines its likelihood of reproduction and prolonged survival

across generations. In engineering contexts, fitness functions often use error metrics, measuring the discrepancy between an individual's performance, I, and the desired solution across the problem's domain, f. Mathematically, this can be expressed as

$$fitness(I) = \sum_{domain} |I - f|^n. \tag{4.1}$$

Here, $n > 1$ enhances the differentiation between similar individuals by amplifying the error metric. In many engineering applications, the domain is three-dimensional, and the computational efforts of calculating fitness for each individual escalates with the domain's size. Moreover, this computation must be repeated for every new individual in each generation, making computational efficiency crucial while defining a fitness function to be optimized.

Once individual fitness is assessed, a selection scheme determines which individuals will reproduce to create the next generation. The fittest individuals are selected for reproduction to produce offspring of the next generation. They operate through a selection, crossover, mutation, and replacement cycle to evolve a population of candidate solutions towards an optimal solution. The choice of selection scheme significantly influences the selection pressure within the algorithm.

Terminology and methodologies

In EC, various processes are utilized across different segments. The terminology and methodologies employed in basic EA, GP, and GEP are elucidated as referenced in the literature (Ferreira, 2002; Holland, 1992; Koza, 1994). This discussion establishes the foundation for comprehending EVE, the GEP code used in this dissertation.

The Search Space $\mathbb{S}$ is inherently defined by the problem at hand. EAs are typically employed for problems with relatively large search spaces, where exhaustively trying every possible solution is infeasible.

The population $\mathbb{P}$ is a subset of the search space $\mathbb{S}$, consisting of all current computational individuals. With a population size p_s, the population can be defined as $\mathbb{P} = \{I_1, ..., I_{p_s}\}$.

An individual I represents a potential solution characterized by its chromosome and fitness derived from that chromosome. After decoding the chromosome, its fitness is typically calculated via a related fitness function.

A chromosome or genotype represents a sequence of parameters delineating a potential solution, where each parameter is termed an allele. Chromosomes can be constructed in various ways, with binary and string representations being common, as depicted in Fig. 4.1. A chromosome comprises at least one gene but can contain multiple genes in multi-genetic chromosome scenarios.

The phenotype is the tangible manifestation or solution corresponding to a genotype. It is derived from the genotype through specific encoding and decoding functions.

The genotype space $\mathbb{G}$ is translated into the search space $\mathbb{S}$ using a decoding function $f_{decode} : \mathbb{G} \to \mathbb{S}$. Conversely, phenotypes from the search space are converted back to genotypes using an encoding function $f_{encode} : \mathbb{S} \to \mathbb{G}$.

The concept of fitness is crucial to emulate survival of the fittest. Fitness functions or cost functions calculate an individual's fitness using its decoded chromosome, $f_{fitness} : \mathbb{S} \to \mathbb{R}$, allowing for comparative evaluation of solutions relative to an exact solution or a target condition.

Figure 4.1: Scheme of the different genotype representations with binary (left) and string (right). A single allele is highlighted in green.

The concept of selection pressure plays a pivotal role in the evolution of solutions. It is the driving force behind creating new individuals and is intrinsically linked to an individual's fitness. Selection pressure determines an individual's likelihood of being chosen as a parent based on their fitness. High selection pressure implies that individuals with extreme fitness values (very high or very low, depending on the optimization goal) have a significantly higher chance of being selected for reproduction. Conversely, low selection pressure suggests that fitness has minimal or no influence on the selection probability. Various selection schemes are employed to regulate this pressure, with some of the most common being the Roulette wheel, tournament, and truncation selection.

The roulette wheel selection, a probabilistic selection mechanism in EAs, assigns a reproductive probability to each individual based on fitness, as illustrated in Fig. 4.2a. As elucidated by Baker, 1987, this method ensures that individuals with superior fitness are more likely to be selected for reproduction, directly correlating fitness with reproductive probability.

The truncation selection employs a fitness threshold to determine reproductive eligibility (Mühlenbein and Schlierkamp-Voosen, 2005), as illustrated in Fig. 4.2b. Individuals exceeding this threshold (superior fitness in maximization problems or inferior fitness in minimization problems) can reproduce. This selection method correlates fitness with reproductive probability, as individuals must surpass a predefined fitness level to contribute genetically to the subsequent generation.

The tournament selection is illustrated in Fig. 4.3. As discussed by Blickle and Thiele, 1996, it divides the population into groups (tournaments) of a specified size. In each tournament, the individual exhibiting the highest fitness is identified as the winner and granted the opportunity to reproduce. This selection method indirectly relates fitness to reproductive probability by increasing the likelihood that individuals with superior fitness will win their respective tournaments. The size of the tournament directly influences the selection pressure; larger tournaments generally increase the chances of the fittest individuals being selected, enhancing the overall selection pressure.

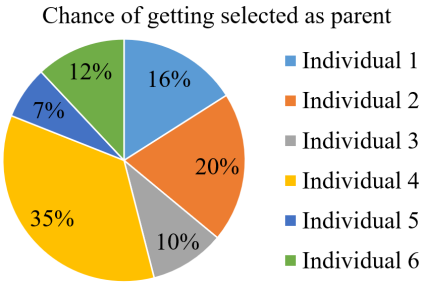

(a) Roulette selection - Individuals are given a probability of being selected for reproduction based solely on their fitness.

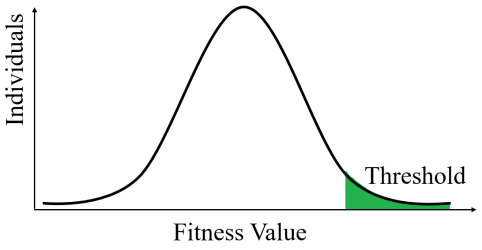

(b) Truncation selection - Only individuals surpassing a specified fitness threshold can reproduce.

Figure 4.2: Selection schemes.

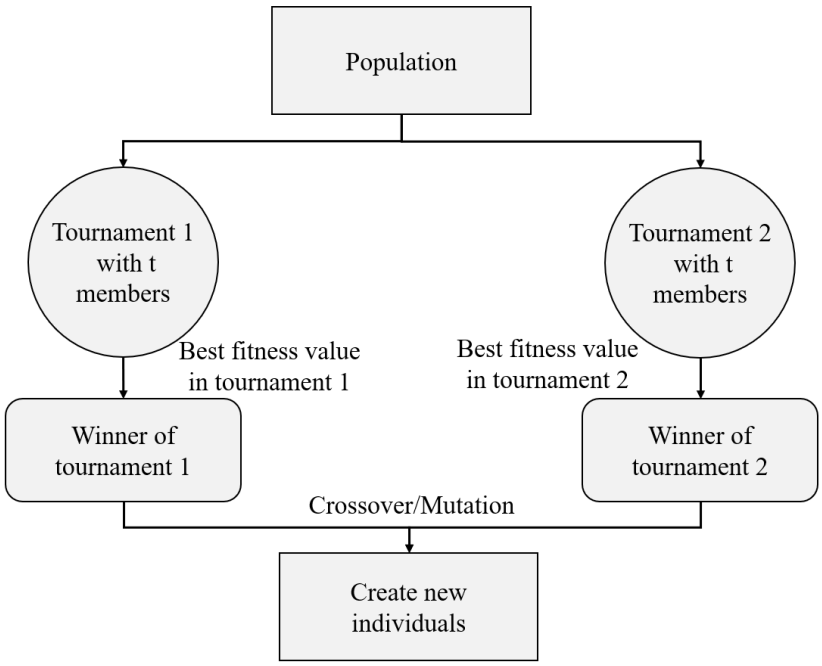

Figure 4.3: Tournament selection - The population is divided into m tournaments, each comprising t individuals, with winners granted the opportunity to reproduce.

Crossover and mutation are two fundamental mechanisms in EAs. Crossover is a process where two selected parents combine parts of their chromosomes to create a new individual (Zaharie, 2009). The specific crossover mechanism can vary depending on the EA type. Mutation introduces variability and innovation into the population by altering the alleles of an individual's chromosome. This process is crucial as it maintains a low probability of discovering global optima and ensures the exploration of the search space (Kramer, 2017).

Reinsertion is transitioning from one generation to the next while maintaining a portion of the current population. This mechanism, known as the generation gap, allows for

the continuity of genetic material across generations and is crucial for the stability and convergence of the algorithm. However, it must be implemented cautiously to avoid premature convergence to local optima (Pencheva et al., 2011; Pohlheim, 2013).

Diversity within a population is a critical measure of its health and evolutionary potential. It reflects the variation in genetic material and is essential for avoiding premature convergence and encouraging exploration of the search space. Various strategies exist to measure and maintain diversity, such as fitness uniform selection and other methods (Gupta and Ghafir, 2012; Hutter, 2002; Ursem, 2002). High diversity is generally believed to enhance the algorithm's ability to escape local optima and increase the chances of finding global optima.

Evolutionary algorithms workflow

Figure 4.4 depicts the fundamental workflow of an EA in its simplest iteration (Pohlheim, 2013). The process begins with the zeroth generation, comprising an initial population, and sequentially advances through predefined steps until the optimizations conclude at the final generation. The various stages, numbered from 1 to 9, are elucidated below.

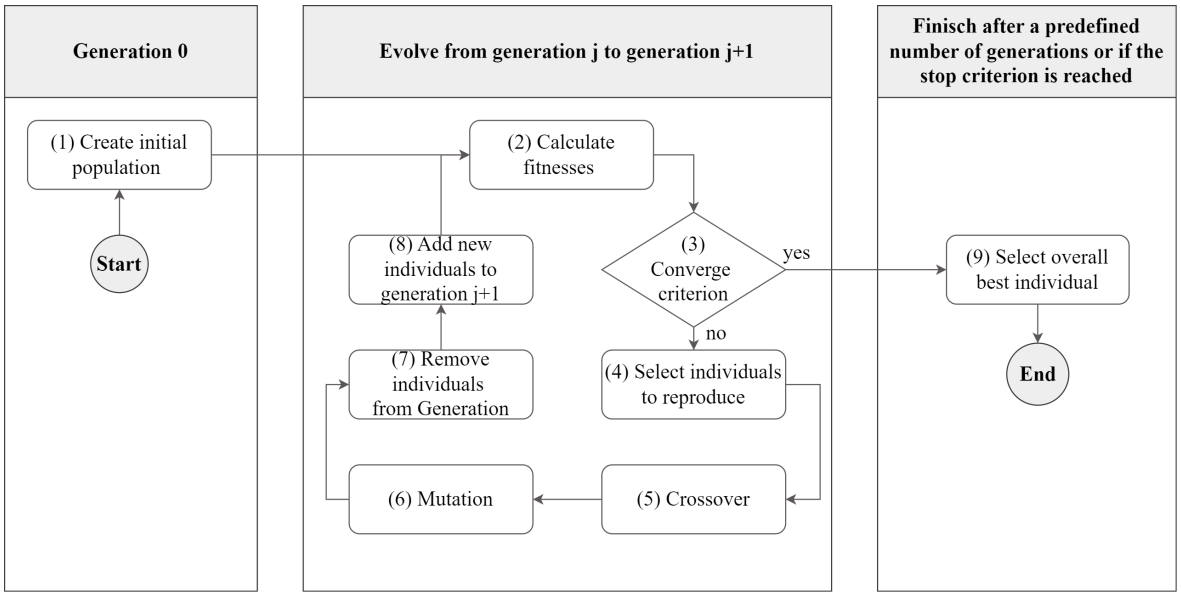

Figure 4.4: Evolutionary process in an EA.

1. Create initial population: the inception of an EA invariably involves generating an initial population. While various specialized procedures exist, a prevalent approach is to commence with a quasi-random initial population.
2. Calculate fitness: this step involves calculating the fitness of all individuals not previously assessed. These individuals may be part of the random initial population or newly created offspring.
3. Stop criterion: given finite computational resources, the optimizations must conclude at a certain juncture. Commonly employed termination criteria include a predetermined number of generations or achieving a specific fitness value.

4. Selection: through a defined selection scheme, individuals eligible for reproduction are chosen. This step is instrumental in regulating selection pressure.

5. Crossover: various crossover types combine genetic material from the selected parents to create offspring. The algorithm typically allows setting probabilities for different crossover types.

6. Mutation: post-crossover, the offspring can undergo mutation. The probability of mutation can be preconfigured.

7. Remove individuals from generation j: while some EAs operate with variable population sizes and employ alternative mechanisms, the fundamental concept is to maintain a fixed population size. To accommodate new individuals, existing ones must be removed. The remaining individuals from the current generation are then carried forward to the next.

8. Add new individuals to generation $j+1$: following the removal of a predetermined number of individuals, the generation is replenished with new individuals.

9. Select overall best individual: the optimizations process culminates with identifying the best individual after a designated number of generations or upon reaching a predetermined fitness level.

4.2.2. Gene expression programming

The Gene Expression Programming is detailed herein, particularly referring to the CFD-driven framework. The EVE code is then introduced.

Genes and expression trees

In GEP, the gene is bifurcated into two segments: the head and the tail. This division facilitates a diverse array of functional expression lengths while maintaining a fixed gene length. The head segment can incorporate terminals and functions, whereas the tail is restricted to terminals only. Terminals can be constants, variables, or inputs to the problem being solved. They are called terminals because they represent the leaves of the tree structure in GEP, where no further operations are performed on them. Functions in GEP are operations that take a certain number of arguments (terminals or the results of other functions) and perform calculations or operations on them. These functions can include arithmetic operations (like addition, subtraction, multiplication, division), logical operations, or any other domain-specific functions necessary for solving the problem at hand. The combination of terminals and functions in GEP allows the formation of symbolic expressions that can model complex relationships or perform computations. During the evolution process, GEP algorithms manipulate these symbols through genetic operations (such as mutation, crossover, and selection) to evolve solutions that best fit the given problem.

Given the head length h, the requisite maximum tail length t can be computed based on the maximum arity n_{max} (the number of input parameters of a function, e.g., 2 for

"+" and 1 for "$\sqrt{}$") of all permissible functions as follows

$$t = h(n_{max} - 1) + 1. \tag{4.2}$$

Consequently, only the head length h requires configuration, as the tail length t is derived from known variables. To illustrate the transformation of a chromosome into a parsing tree, consider terminal ($\mathbb{T}$) and function ($\mathbb{F}$) sets as follows

$$T = \{a,b,c,d,e\}, \quad F = \{\sqrt{}, +, -, *\}. \tag{4.3}$$

GEP may employ random constants generated during the initialization phase, symbolized by "?" to denote a random numerical constant's potential use. For simplicity, this feature is omitted in the subsequent example. With a head length $h = 6$, maximal arity $n_{max} = 2$, and following Eq. 4.2, the tail length becomes $t = 7$. The gene, split into head and tail for presentation, could be expressed as in the following expression.

$$\begin{array}{cccccc|ccccccc} 0 & 1 & 2 & 3 & 4 & 5 & 6 & 7 & 8 & 9 & 10 & 11 & 12 \\ \sqrt{} & * & \sqrt{} & + & - & a & b & c & d & a & c & e & b \end{array} \tag{4.4}$$

An expression tree is constructed character by character, commencing at the root node (the first allele of the chromosome) until no free edges remain. The expression tree for the chromosome in Eq. 4.4 is illustrated in Fig. 4.5, leading to the following formula:

$$\sqrt{\left(\sqrt{c-d}\right) * (a+b)}. \tag{4.5}$$

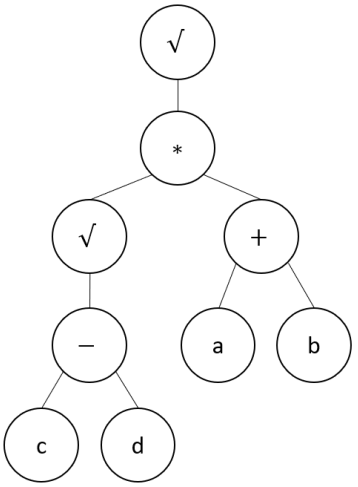

Figure 4.5: Expression tree for the chromosome in Eq. 4.4

Notably, only the initial nine symbols of the expression contribute to the formula and expression tree construction, demonstrating GEP's ability to generate formulas of varying sizes. For instance, employing the same head length $h = 6$ and sets $\mathbb{T}$ and $\mathbb{F}$ as before, but with a different chromosome configuration as Eq. 4.6, yields a distinct resultant formula (Eq. 4.7) and expression tree (Fig. 4.6). This flexibility allows GEP to create a broad spectrum of formulas based on the functions used in the head and their respective arities, integrating several aspects of GP.

$$\begin{array}{cccccc|ccccccc} 0 & 1 & 2 & 3 & 4 & 5 & 6 & 7 & 8 & 9 & 10 & 11 & 12 \\ + & * & - & + & - & * & b & c & d & a & c & e & b \end{array} \tag{4.6}$$

$$((c+d) * (a-c)) + ((e * b) - b) \tag{4.7}$$

In essence, GEP offers a robust and flexible framework for evolving diverse and complex

solutions, effectively balancing the structured approach of GP with the linear dynamics of GA, thereby marking its significance in evolutionary computation.

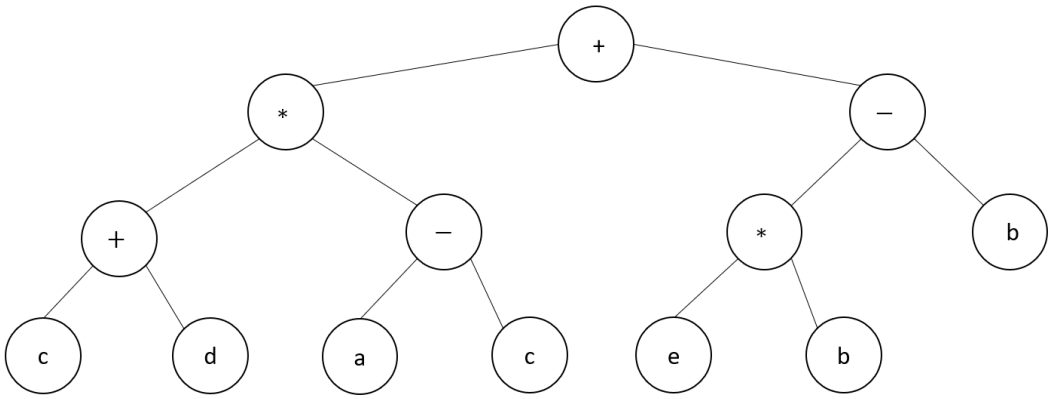

Figure 4.6: Expression tree for the chromosome in Eq. 4.6

Multi genetic chromosome

In GEP, similar to GP, it is feasible to amalgamate multiple genes into a multi-genetic chromosome. This process necessitates defining a linking function possessing an arity of two, such as the addition operator "+". An essential parameter in practical GEP implementation is the number of genes, denoted as n_{genes}, which specifies the count of genes comprising a multi-genetic chromosome. To illustrate the concept of a multi-genetic chromosome, consider combining genes from Eq. 4.4 and Eq. 4.6 into the composite structure shown in expression. 4.8.

$$\begin{array}{cc} 0\ 1\ 2\ 3\ 4\ 5\,|\,6\ 7\ 8\ 9\ 10\ 11\ 12 & 0\ 1\ 2\ 3\ 4\ 5\,|\,6\ 7\ 8\ 9\ 10\ 11\ 12 \\ \surd\ *\ \surd\ +\ -\ a\,|\,b\ c\ d\ a\ \ c\ \ \ e\ \ \ b & +\ *\ -\ +\ -\ *\,|\,b\ c\ d\ a\ \ c\ \ \ e\ \ \ b \end{array} \tag{4.8}$$

Using the linking function "+", the expressions derived from both genes in Eq. 4.5 and Eq. 4.7 can be concatenated to form a comprehensive multi-genetic expression as follows

$$\sqrt{\left(\sqrt{c-d}\right) * (a+b)} \quad + \quad ((c+d) * (a-c)) + ((e*b)-b)\,. \tag{4.9}$$

This method effectively combines the individual gene expressions into a more complex, multi-layered solution, increasing the versatility of GEP. This enhances the algorithm's capability to represent and evolve a more comprehensive array of solutions, thereby increasing the scope and potential applications of GEP in solving complex problems.

4.2.3. Training frameworks: CFD-driven method

The CFD-driven training methodology, illustrated in Fig. 4.7, evaluates turbulence models via RANS computations that subsequently guide the ML training iterations. This framework can be divided into two main segments. The first relates to the CFD solver, wherein OpenFOAM Version 7.0 is utilized to conduct RANS computations.

The complement to the CFD solver is the ML module, and GEP is the preferred choice.

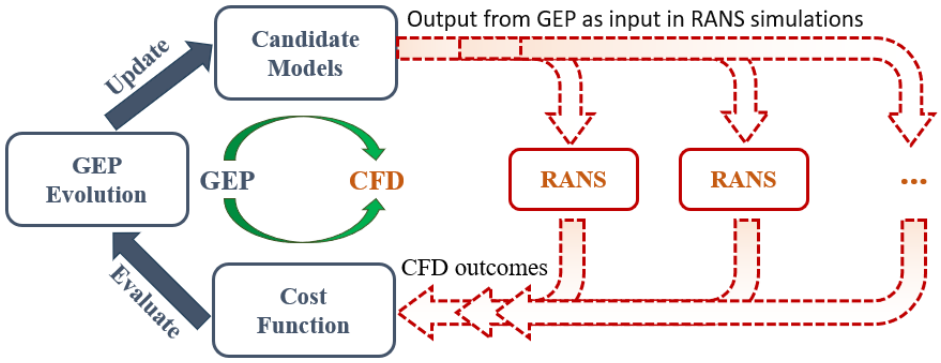

Figure 4.7: CFD-driven training scheme (inspired by Zhao et al., 2020).

Due to the precise formulation of the model equations, combining the CFD-driven training framework with the GEP method facilitates immediate integration into RANS solvers during the training process. As a result, models emerging from the CFD-driven approach are readily adaptable for use in industrial design tools. Another advantage of CFD-driven training is its versatile cost function. Rather than being limited to specific closure term components, the cost functions in CFD-driven training can be customized to emphasize any flow feature considered critical by turbulence modelers.

The training begins by generating an array of random candidate models, called individuals, from a predefined set of mathematical symbols. For this purpose, the symbols include mathematical operations, such as addition, subtraction, multiplication, variables, and constants (randomized or predefined). During each generational cycle, a designated subset of individuals undergoes evaluation, influencing their evolutionary trajectory. The chosen individuals are then integrated into RANS calculations. Integrating GEP models into the solver is achieved by referencing coefficients and variables, eliminating the need for solver recompilation with each new model candidate and thus reducing computational demands. The equations for each candidate model are transcribed to a file, which the RANS solver then accesses. The RANS solver initiates then its iterative computation by employing the GEP equation in its turbulence model. The CFD cycle concludes when either convergence is achieved, enabling the determination of the cost function through a comparison of RANS results with the ground truth or in cases of model non-convergence, where the cost function is assigned a higher value.

Since GEP operates as a global optimization approach, evaluating cost function values is crucial in model selection. Fitness functions measure the mean square deviation between the numerical prediction and the ground truth (data derived from Hi-Fi simulations, experimental results, or theoretical formulations). The GEP evolution algorithm then uses these cost functions to generate a new set of models assessed then through integrated CFD simulations. This iterative process is repeated, progressively refining the model pool until a model in a generation meets the predefined cost-effectiveness criterion.

4.2.4. The EVE code

The GEP code, called EVE, refers to a specific software tool or algorithm developed by Weatheritt and Sandberg, 2016. EVE is an academic code written in Python 3. Its framework implements the GEP algorithm by Ferreira, 2002, which evolves a population of candidate solutions over various generations towards a specified training objective. To use this framework without any expansions, the following settings have to be defined.

- The stopping tolerance to define at which fitness level the optimization ends.
- Number of generations to run at maximum.
- The seed to define the quasi-random initial population.
- The size of the population.
- The number of genes used.
- The head length of one chromosome.
- The tournament size.
- The mating size.
- The terminal and function set.
- The probabilities for mutation: one-point crossover and two-point crossover.
- Optionally, the fitness function can be changed. The default fitness function is the sum of the squared error of an individual.

After defining those values, the optimization starts with a quasi-random initial population created based on the seed at the beginning of the run. It reads in the terminal set as NumPy arrays and gets the dimensions of the terminals afterwards. This initial population is quasi-random to ensure the repeatability of runs. From there on, the steps depicted in Fig. 4.8 are done repeatedly for the set number of generations until either the stopping tolerance or the number of generations is reached.

As a selection scheme, tournament selection with elitism is implemented in EVE. The random tournament members of each tournament compete concerning the defined fitness function, and the winners are allowed to reproduce with the given probabilities for one- and two-point crossovers and mutation afterwards. Not all reproduction mechanisms mentioned by Ferreira, 2002 are implemented in EVE. Consequently, the fitness values of the newly created children are calculated after the translation into the phenotype space. For details on the translation process, see Weatheritt and Sandberg, 2016. After the offspring of the current population is done, a diversity mechanism called flood checks if the population is still diverse enough based on all the fitness values.

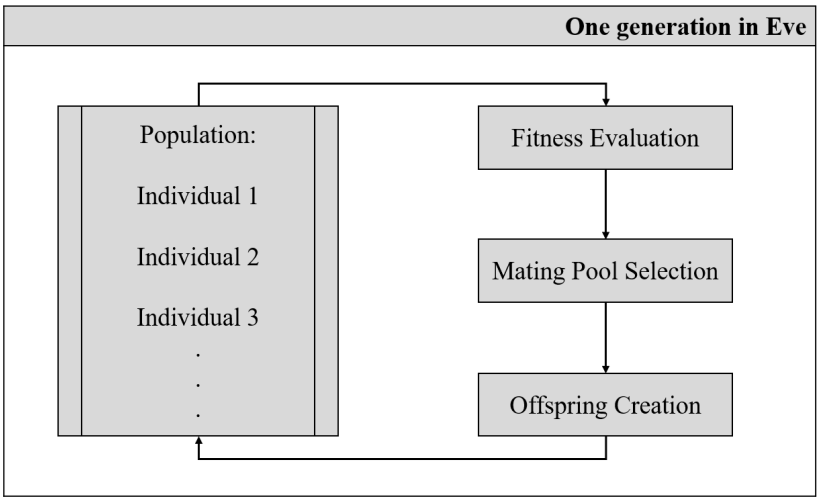

Figure 4.8: EVE framework (inspired by Weatheritt and Sandberg, 2016)

4.3. Numerical techniques

Numerous numerical techniques are available for solving the non-linear Partial Differential Equations (PDEs) that govern fluid motion. These techniques include Spectral Methods (SMs), Finite Element Methods (FEMs), and Finite Difference Methods (FDMs), among others.

SMs utilize a linear combination of continuous functions, such as sinusoids or Chebyshev polynomials, that span the entire solution domain. FEMs rely on piece-wise continuous functions that are localized to smaller sub-domains. FEM generates equations for each element independently and considers interactions between elements only when assembling these equations into a global system matrix. FDMs are based on Taylor series expansions to approximate the differential equations. While FDM offers several advantages in terms of numerical formulation, data preparation, and computational efficiency, it is generally less adaptable to complex geometries due to its inherent reliance on regular grid structures.

In contrast to these methods, the FVM approaches the problem from a fundamentally different perspective. Rather than directly solving the PDEs, the FVM focuses on the conservation of physical quantities, such as energy, mass, or momentum, across finite control volumes. This approach, which involves deriving discrete equations from the integral conservation laws, provides a more physically intuitive framework than FDMs. The control volume strategy inherent in FVM makes it particularly well-suited for applications involving complex geometries and boundary conditions.

4.3.1. Finite volume method

The FVM constitutes a pivotal approach in the discretization of governing equations within the field of CFD. Its widespread adoption and enduring popularity are attributed to its intrinsic capability to include the physical and conservation principles that are

fundamental to fluid flow dynamics. Notably, FVM are well-known for its congruence with the integral formulations of the governing equations, providing a robust framework for numerical simulation.

In employing FVM, the computational domain is subdivided into a finite number of control volumes. It is within these volumes that the integral forms of the governing equations are applied, thereby transforming the continuous domain into its discrete counterpart. This methodology facilitates the direct application of conservation laws to each control volume, effectively mirroring the physical behavior of real-world fluid flows. The governing equations introduced in Section 3.1 are expressed in their conservative form in Section 4.3.3.

The process of discretization culminates in the derivation of a system of algebraic equations that includes the entire computational domain. This system of equations represents the discretized physical phenomena and imposed boundary conditions, forming the basis for subsequent numerical analysis. The solution of this algebraic system, accomplished through suitable numerical methods, reveals the spatial distribution of flow properties across the computational domain.

Control volumes (cells)

Control volumes, or cells, form the fundamental units for discretization in CFD simulations. These cells can be either structured or unstructured, and may follow Cartesian or non-Cartesian geometries. Fig. 4.9a shows a typical three-dimensional control volume, which is characterized by a node located at its center, surrounded by adjacent nodes. Variables of interest, such as velocity or pressure, are stored at these nodal points, which are strategically placed at the control volumes' centers to facilitate numerical stability and accuracy.

Considering a control volume (V) and its nodal point (P), the adjacent nodes along the coordinate axes are typically named with capitalized letters: East, West, North, South, Higher, and Lower. These designations aid in the conceptual and computational identification of nodal relations within the grid. Conversely, lowercase letters are used to represent the control volume's surfaces, contributing to a standardized nomenclature that

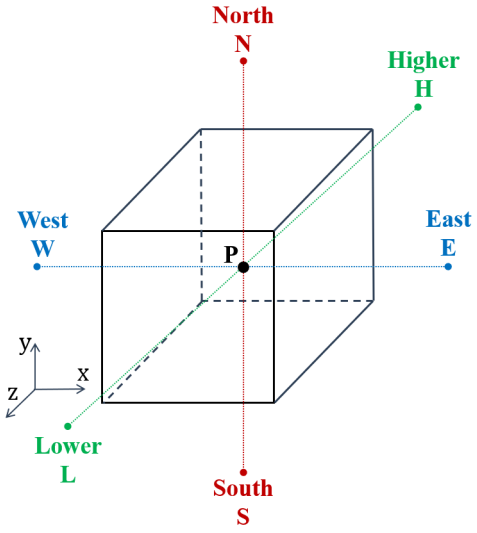

(a) Illustration of a three-dimensional control volume with central and adjacent nodes.

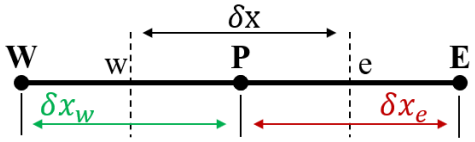

(b) A one-dimensional control volume highlighting nodes and surfaces.

Figure 4.9: Control volume.

enhances clarity in mathematical formulations. The areas of the control volumes' surfaces are denoted by A_w, A_e, A_n, A_s, A_h, and A_l, providing a basis for flux calculations across the control volume boundaries. In the case of a one-dimensional control volume, the central, eastern, and western nodes, along with the eastern and western surfaces, are illustrated in Fig. 4.9b.

4.3.2. Overview of the dual mesh approach

The DLR-TAU code, renowned for its proficiency in simulating complex aerodynamic flows, uses a Dual Mesh strategy to enhance the efficiency and accuracy of solving the Navier-Stokes equations on unstructured grids (Kroll et al., 2014).

The Dual Mesh approach incorporates two interlinked mesh structures: the primary mesh and the dual mesh, each serving a distinct purpose in the computational framework. The primary mesh forms the computational domain's backbone, composed of various elements (e.g., tetrahedra, hexahedra, prisms, and pyramids in 3D) tailored to the geometry of the object under investigation. This mesh directly applies the physical geometry and boundary conditions of the problem. Constructed from the primary mesh, the dual mesh centers around the vertices of the primary elements. A control volume is defined for each node on the primary mesh, extending to the midpoint of adjacent nodes and element centers. This setup facilitates a node-centered solution strategy, significantly impacting the computational efficiency and accuracy.

The Dual Mesh approach provides multiple advantages essential for simulating aerodynamic phenomena, which are summarized as follows (Gerhold, 2002).

- Accuracy and efficiency: by enabling a node-centered scheme on the dual mesh, TAU achieves enhanced accuracy in flux calculations across control volume boundaries, thereby improving the solution's fidelity.
- Complex geometry handling: the flexibility of the dual mesh in adapting to complex geometries ensures accurate flow physics representation throughout the computational domain.
- Parallel performance: the approach is inherently suitable for parallel computing, allowing for efficient workload distribution across multiple processors and reducing computation times for large-scale simulations.
- Solution robustness: the dual mesh contributes to the solution process's stability and robustness, especially when addressing complex flow behaviors and boundary conditions.

4.3.3. Conservative form of the governing equations

The governing equations for fluid flow, introduced in Section 3.1, are expressed in their conservative form as follows.

Mass conservation equation

$$\frac{\partial \rho}{\partial t} + \nabla \cdot (\rho \mathbf{u}) = 0, \tag{4.10}$$

where $\mathbf{u}$ represents the velocity vector.

Momentum conservation equations: in the x, y and z directions

$$\begin{aligned} \frac{\partial (\rho u)}{\partial t} + \nabla \cdot (\rho u \mathbf{u}) &= -\frac{\partial p}{\partial x} + \nabla \cdot \tau_{\mathbf{x}}, \\ \frac{\partial (\rho v)}{\partial t} + \nabla \cdot (\rho v \mathbf{u}) &= -\frac{\partial p}{\partial y} + \nabla \cdot \tau_{\mathbf{y}}, \\ \frac{\partial (\rho w)}{\partial t} + \nabla \cdot (\rho w \mathbf{u}) &= -\frac{\partial p}{\partial z} + \nabla \cdot \tau_{\mathbf{z}}, \end{aligned} \tag{4.11}$$

where $\tau_{\mathbf{i}}$ represents the viscous stress vector, incorporating the components of the viscous stress tensor, τ_{ij}, in the i-direction.

The conservative form emphasizes terms that represent the divergence of a quantity, making it particularly suited for the finite volume method. This approach ensures conservation of variables within each control volume and throughout the entire computational domain. The system consists of four equations and five unknowns: the three velocity components, pressure, and density. An additional equation, the equation of state, closes the system. Hence, the system can be solved for the unknown variables, given appropriate auxiliary conditions, including initial and boundary conditions.

Similarly, the **Energy conservation equation** can be expresses as follows

$$\frac{\partial (\rho E)}{\partial t} + \nabla \cdot (\rho \mathbf{u} E) = -\nabla \cdot (p \mathbf{u}) + \nabla \cdot (\tau \cdot \mathbf{u}) + \nabla \cdot \mathbf{q}, \tag{4.12}$$

where $\mathbf{q}$ and τ represent the heat flux vector and the Reynolds stress tensor, respectively, expressed in tensor notation.

The **generic form of the transport equations**, applicable to the governing equations for a general scalar variable ϕ, is given by

$$\frac{\partial (\rho \phi)}{\partial t} + \nabla \cdot (\rho \phi \mathbf{u}) = \nabla \cdot (\Gamma \nabla \phi) + S_{\phi}. \tag{4.13}$$

Here, ϕ represents a general scalar variable, encapsulating properties such as concentration, temperature, or any scalar field within the flow. Notably, by setting ϕ equal to 1, u, v, and w, representing the velocity components in the Cartesian coordinates, and by selecting appropriate values for the diffusion coefficient Γ, this equation can be transformed into the continuity and momentum governing equations.

On the LHD, the first term represents the transient term, indicating the rate of change of ϕ with time, and the second term represents the convective term, describing the rate of decrease of ϕ due to convection. On the RHD, the first term is the diffusive term, accounting for the rate of increase of ϕ due to diffusion, with Γ being the diffusion coefficient, the second term is the source term, denoting the rate of generation or destruction of ϕ.

In FVM, the transport equation for a general scalar variable ϕ is integrated over each control volume within the computational domain, as follows

$$\int_V \frac{\partial(\rho\phi)}{\partial t} dV + \int_V \nabla \cdot (\rho\phi \mathbf{u}) dV = \int_V \nabla \cdot (\Gamma \nabla\phi) dV + \int_V S_\phi dV. \tag{4.14}$$

This process involves converting the volume integrals of the convective and diffusive terms into surface integrals over the entire bounding surface, S, of the control volume. By using the Gauss's divergence theorem, which allows for a more straightforward evaluation of these terms, the equation transforms into

$$\int_V \frac{\partial(\rho\phi)}{\partial t} dV + \oint_S \rho\phi \mathbf{u} \cdot \mathbf{n} dS - \oint_S \Gamma \nabla\phi \cdot \mathbf{n} dS = \int_V S_\phi dV, \tag{4.15}$$

where $\mathbf{n}$ is the outward unit normal vector on the surface S. In FVM, it is required to compute fluxes at the surfaces of the control volumes, rather than at the nodes. The values of ϕ on the control volume surfaces need to be estimated by using the values of ϕ stored in the nodes.

There exists several numerical integration method to approximate the definite integral of a function over an interval. The Midpoint Rule can be applied to approximate surface integrals, particularly when discretizing a surface into small patches. For a surface divided into small elements S_i, the surface integral of a scalar field ϕ might be approximated as follows

$$\iint_S \phi \, dS \approx \sum_i \phi(\mathbf{r}_i^*) \Delta S_i,$$

where $\mathbf{r}_i^*$ is the midpoint of the ith surface element S_i, and ΔS_i is the area of the ith surface element.

4.3.4. Spatial discretization schemes

Discretization schemes play a crucial role in transforming FVM equations into algebraic equations amenable to numerical solution. Within this domain, both the upwind and central differencing schemes emerge as particularly significant for approximating spatial derivatives. The primary distinction between these schemes lies in their methodologies for representing flow direction and diffusion effects, which in turn significantly influences the accuracy, stability, and fidelity of the resultant solutions.

Central scheme

In the central differencing method the variable ϕ undergoes linear changes between adjacent nodes. Assuming Cartesian equidistant grids, as illustrated in Fig. 4.9b, the values of ϕ and its spatial derivative, $\left(\frac{\partial \phi}{\partial x}\right)$, at the control volume surface A_e can be approximated using linear interpolation as follows

$$\phi_e = \frac{\phi_P + \phi_E}{2}, \qquad \text{and} \qquad \left(\frac{\partial \phi}{\partial x}\right)_e = \frac{\phi_E - \phi_P}{\delta x_e}, \tag{4.16}$$

where ϕ_P and ϕ_E denote the values of ϕ at the central node and the node located to the east of the control volume, respectively. This approach accentuates the simplicity and effectiveness of the central differencing method in delineating the gradient of ϕ across the control volume faces. This methodology achieves second-order accuracy by relying on the symmetric evaluation of neighboring points, highlighting its efficiency in numerical schemes where high accuracy is imperative.

Artificial Dissipation in TAU. Unlike upwind schemes, which introduce numerical dissipation to stabilize the solution, central schemes use a centred stencil to approximate derivatives. They are second-order accurate and don't inherently introduce dissipation, making them useful for problems where maintaining solution accuracy is critical.

While central schemes are less dissipative, they can be prone to non-physical oscillations near discontinuities (like shock waves) due to their non-dissipative nature. Additional dissipation (artificial viscosity) must be introduced selectively to stabilize the solution without overly smearing out physical features to counteract. The dissipation has to be computed for each grid point. The approach follows the strategy described by Mavriplis and Jameson, 1990 to obtain an adequate dissipation scaling for highly stretched cells.

The matrix dissipation method introduces dissipation in a controlled manner, as proposed by Blazek, 2015. It involves calculating eigenvalues and eigenvectors of the flux Jacobian matrix, which are related to the wave speeds and modes of the system. The dissipation is then added based on these eigenvalues, ensuring that it's aligned with the characteristic waves of the flow. This way, the dissipation acts more efficiently and only where necessary, preserving the sharpness of shocks and interfaces. When applying the matrix dissipation method with central schemes, the basic discretization is done using a central scheme, and then the matrix-based dissipation is added to stabilize the solution. The amount and direction of dissipation are informed by the local flow characteristics, as determined by the Jacobian matrix of the system.

Upwind scheme

The upwind scheme modifies the computation of ϕ at the control volume surfaces to explicitly incorporate the flow direction, thus ensuring an accurate depiction of information propagation from upstream sources. In particular, the value of ϕ at the

eastern face, ϕ_e, is influenced by the flow velocity at this boundary, u_e. The assignment of ϕ_e is governed by the following conditions:

$$\phi_e = \begin{cases} \phi_P, & \text{if } u_e > 0 \text{ (indicating flow from West to East),} \\ \phi_E, & \text{if } u_e < 0 \text{ (indicating flow from East to West).} \end{cases} \tag{4.17}$$

This methodology guarantees that the value of ϕ on the eastern surface is exclusively influenced by the upstream node relative to the flow direction, significantly improving the simulation fidelity in the presence of directional convection. It offers a more precise depiction of scalar transport within the computational domain.

Despite its first-order accuracy and straightforwardness, the upwind scheme is characterized by its considerable diffusive nature, often referred to as false diffusion or numerical viscosity. The extent of false diffusion correlates directly with the grid spacing (δx), which decreases with grid refinement but does not completely disappear.

4.3.5. Time discretization - solution techniques

The conservation equations introduced in Section 4.3.3 can be converted into vector form to simplify their application in computational methods. The Navier-Stokes equations for the three-dimensional case can be written in conservative form as follows

$$\frac{\partial}{\partial t} \int_V \mathbf{W} dV = - \oint_S \mathbf{F} \cdot \mathbf{n} dS, \tag{4.18}$$

where

$$\mathbf{W} = \begin{pmatrix} \rho \\ \rho u \\ \rho v \\ \rho w \\ \rho E \end{pmatrix} \tag{4.19}$$

is the vector of conserved quantities. The flux density tensor $\mathbf{F}$ is composed of the flux vectors in the three coordinate directions as follows

$$\mathbf{F} = (\mathbf{F_i^c} + \mathbf{F_v^c}) \cdot \mathbf{e_x} + (\mathbf{G_i^c} + \mathbf{G_v^c}) \cdot \mathbf{e_y} + (\mathbf{H_i^c} + \mathbf{H_v^c}) \cdot \mathbf{e_z}, \tag{4.20}$$

with e_x, e_y, and e_z being unit vectors in the coordinate directions. The indices i and v denote the inviscid and viscous contributions, respectively. The viscous and inviscid fluxes are given by

$$\mathbf{F_i^c} = \begin{pmatrix} \rho u \\ \rho u^2 + p \\ \rho uv \\ \rho uw \\ u(\rho E + p) \end{pmatrix}, \quad \mathbf{F_v^c} = \begin{pmatrix} 0 \\ \tau_{xx} \\ \tau_{xy} \\ \tau_{xz} \\ u\tau_{xx} + v\tau_{xy} + w\tau_{xz} + q_x \end{pmatrix}, \tag{4.21}$$

$$\mathbf{G}_{\mathbf{i}}^{\mathbf{c}} = \begin{pmatrix} \rho v \\ \rho uv \\ \rho v^2 + p \\ \rho vw \\ v(\rho E + p) \end{pmatrix}, \quad \mathbf{G}_{\mathbf{v}}^{\mathbf{c}} = \begin{pmatrix} 0 \\ \tau_{xy} \\ \tau_{yy} \\ \tau_{yz} \\ u\tau_{xy} + v\tau_{yy} + w\tau_{yz} + q_y \end{pmatrix}, \tag{4.22}$$

$$\mathbf{H}_{\mathbf{i}}^{\mathbf{c}} = \begin{pmatrix} \rho w \\ \rho uw \\ \rho vw \\ \rho w^2 + p \\ w(\rho E + p) \end{pmatrix}, \quad \mathbf{H}_{\mathbf{v}}^{\mathbf{c}} = \begin{pmatrix} 0 \\ \tau_{xz} \\ \tau_{yz} \\ \tau_{zz} \\ u\tau_{xz} + v\tau_{yz} + w\tau_{zz} + q_z \end{pmatrix}. \tag{4.23}$$

The pressure is calculated by the equation of state as follows

$$p = (\gamma - 1)\rho\left(E - \frac{u^2 + v^2 + w^2}{2}\right). \tag{4.24}$$

The terms τ_{ij} in Eq. 4.21, 4.22, and 4.23 represent the viscous stress tensor components while q_i denotes the heat flux vector. These equations can be transformed into the averaged equations simply by substituting, $\tau_{ij} + \tau_{ij}^R$, for τ_{ij} and, $q_i + q_i^R$, for q_i and taking the flow variables as averaged quantities as defined in Chapter 3. In this formulation, all quantities are non-dimensionalized as follows

$$\begin{gathered} x = \frac{x^*}{L^*}, \quad y = \frac{y^*}{L^*}, \quad z = \frac{z^*}{L^*}, \\ \rho = \frac{\rho^*}{\rho_\infty^*}, \quad p = \frac{p^*}{p_\infty^*}, \quad \mu = \frac{\mu^*}{\mu_\infty^*}, \\ u = u^*\sqrt{\frac{p^*}{\rho^*}}, \quad v = v^*\sqrt{\frac{p^*}{\rho^*}}, \quad w = w^*\sqrt{\frac{p^*}{\rho^*}}, \end{gathered} \tag{4.25}$$

where the superscript $*$ denotes the dimensional variables.

From Eq. 4.18, the temporal change of the conservative variables $\mathbf{W}$ is written as

$$\frac{\partial}{\partial t}\mathbf{W} = -\frac{\oint_S \mathbf{F} \cdot \mathbf{n}\, dS}{\int_V dV}. \tag{4.26}$$

It describes the change in flow conditions within a control volume, determined by the net flux $\mathbf{F}$ through the control volume boundary, normalized by the volume. For a control volume that is stationary in both time and space and assuming $\mathbf{W}$ depending only on time, Eq. 4.26 simplifies to

$$\frac{d}{dt}\mathbf{W} = -\frac{1}{V} \cdot \mathbf{Q}^F, \tag{4.27}$$

where $\mathbf{Q}^F$ denotes the total fluxes crossing the boundaries of the control volume.

The temporal variation of the flow quantities at a generic point[1] can be generalized

[1] The notation is simplified to improve clarity. The following considerations are valid for each specific generic point.

as

$$\frac{d}{dt}\mathbf{W} + \mathbf{R} = 0. \tag{4.28}$$

Substituting from Eq. 4.27 yields an expression for the residual $\mathbf{R}$:

$$\mathbf{R} = \frac{1}{V} \cdot \mathbf{Q}^F. \tag{4.29}$$

Temporal discretization involves segmenting the time continuum into discrete intervals, a process essential for addressing problems characterized by variables that evolve over time, such as in dynamic fluid flow scenarios.

Steady state problems

First, the so-called steady-state case, in which a time-independent solution exists, is considered. From the steady-state condition $\frac{d\mathbf{W}}{dt} = 0$, Eq. 4.28 becomes

$$\mathbf{R} = 0. \tag{4.30}$$

This problem is solved by introducing the corresponding time-dependent problem with fictitious pseudo-time t^* and pursuing its steady-state solution as follows

$$\frac{d}{dt^*}\mathbf{W} + \mathbf{R} = 0. \tag{4.31}$$

The discretization concerning the fictitious pseudo-time is performed using the low-storage k-step Runge-Kutta scheme as described by Jameson et al., 1981, and it is given by

$$\begin{aligned} \mathbf{W}^{(0)} &= \mathbf{W}(n) \\ \mathbf{W}^{(1)} &= \mathbf{W}^{(0)} - \alpha_1 \Delta t^* \mathbf{R}_v^{(0)} \\ &\vdots \\ \mathbf{W}^{(a)} &= \mathbf{W}^{(0)} - \alpha_a \Delta t^* \mathbf{R}_v^{(a-1)} \end{aligned} \tag{4.32}$$

$$\mathbf{W}(n+1) = \mathbf{W}^{(a)}, \tag{4.33}$$

with

$$\mathbf{R}_v = V \cdot \mathbf{R}, \tag{4.34}$$

where Δt^* denotes the pseudo-time step width. In this equation, the residual $\mathbf{R}$ equals the fluxes $\mathbf{Q}^F$ over the control volume boundaries (see Eq. 4.26).

Time-accurate computations: dual time-stepping in TAU.

For time-accurate solutions, both global and dual time-stepping schemes are implemented in TAU. The numerical results presented in this dissertation have been achieved by using the dual time-stepping, which follows the methodology by Jameson et al., 1981, modifying the Runge-Kutta scheme to counteract instabilities associated with small physical time-steps. The temporal accuracy of the dual-time discretization can be first, second, or third order, with higher orders increasing computational demands.

The dual time-stepping method represents a sophisticated numerical strategy for efficiently solving unsteady flow problems. By transforming transient simulations into a series of quasi-steady states, this method significantly enhances the efficiency and accuracy of CFD analyses. The method is predicated on the distinction between two types of time advancement: physical time, the actual time scale over which the flow dynamics evolve; and pseudo time, an artificial time scale introduced to facilitate the attainment of steady-state solutions within each physical time step.

The workflow of the dual time-stepping method can be summarized as follows.

1. The simulation initiates with predefined flow conditions and sets the physical time to its initial value.
2. Advancement through physical time steps is undertaken, treating the flow as transient for each step to compute the flow field at subsequent time levels.
3. Within each physical time step, the flow equations undergo iterative solving in pseudo time until convergence to a steady state is achieved, thereby representing the flow field accurately at the current physical time step.
4. Upon reaching convergence in pseudo time, the solution is updated for the next physical time step, and the iterative process repeats.

The dual time-stepping method offers the following multiple advantages.

- Efficiency: this approach allows for the rapid convergence of iterative solvers, streamlining the simulation of transient flows.
- Flexibility: its compatibility with different mesh types and flow conditions enhances the method's versatility for various aerodynamic analyses.
- Accuracy: the method ensures precise control over physical time advancement, crucial for accurately capturing transient flow phenomena.

Mathematically, the dual time-stepping process can be expressed as follows. Denote $[0,T]$ the time interval and $t_0 = 0 < t_1 < \ldots < t_N = T$ a partition of $[0,T]$. The time-dependent problem is considered as follows

$$\frac{d\mathbf{W}}{dt} = -\mathbf{R}(\mathbf{W}), \tag{4.35}$$

where the notation $\mathbf{R}(\mathbf{W})$ indicates that the residual $\mathbf{R}$ for a generic dual cell was computed using the vector of conservative variables $\mathbf{W}$.

In the first step, a Backward Difference Formula (BDF) for discretizing the time derivative is employed to Eq. 4.35. The TAU-Code provides BDF of first, second, and third-order accuracy. For example, the second-order accurate BDF reads

$$\frac{3}{2\Delta t}\mathbf{W}^{n+1} - \frac{4}{2\Delta t}\mathbf{W}^{n} + \frac{1}{2\Delta t}\mathbf{W}^{n-1} = -\mathbf{R}(\mathbf{W}^{n+1}), \tag{4.36}$$

where $\mathbf{W}^j$ denotes the solution at the physical time t_j. Therefore, Eq. 4.36 represents the advancement in physical time.

The sequence of (nonlinear) steady-state problems is taken into account. Assuming that $\mathbf{W}^n$, $\mathbf{W}^{n-1}$ have already been computed, $\mathbf{W}^{n+1}$ is calculated. For this purpose, the equation in pseudo time t^* is considered as follows

$$\frac{d\mathbf{W}^{n+1}}{dt^*} = -\mathbf{R}^{DTS}(\mathbf{W}^{n+1}), \tag{4.37}$$

with the modified residual given by

$$\mathbf{R}^{DTS}(\mathbf{W}^{n+1}) \equiv \mathbf{R}(\mathbf{W}^{n+1}) + \frac{3}{2\Delta t}\mathbf{W}^{n+1} - \frac{4}{2\Delta t}\mathbf{W}^{n} + \frac{1}{2\Delta t}\mathbf{W}^{n-1}. \tag{4.38}$$

This problem can be integrated using a k-stage Runge-Kutta scheme until a steady state in fictitious pseudo-time has been reached. The steady-state solution of Eq. 4.37 is the solution of Eq. 4.36.

5

Vortex-Dominated Flow over VFE-2 at Transonic Speed

This chapter presents the main results obtained in Di Fabbio et al., 2022a, 2023. It advances the prediction of vortex-dominated flows, enhancing the understanding of various flow phenomena occurring over delta wings, particularly at transonic conditions.

Simulations of the sharp leading-edge VFE-2 wing are performed at $Ma_\infty = 0.8$, $Re_\infty = 2 \times 10^6$, and $\alpha = 20.5°$. The vortex-dominated flow is investigated by comparing IDDES and URANS outcomes with experimental data provided by the DLR (Konrath et al., 2006, 2013). The IDDES method, based on the SAneg model, is applied in the scale-resolving computations, while the SAnegRC is employed to close the RANS equations. The simulations have been performed employing the DLR-TAU code.

Section 5.1 briefly introduces the VFE-2 test case. Section 5.1.1 details the mesh characteristics, with a special focus on the requirements for HRL transition and LES mesh quality. Section 5.1.2 describes the mesh convergence study and Section 5.1.3 provides the description of the numerical approach.

The flow physics is then described and illustrated, structured into the following subtopics. The overview of the leading-edge flow with the instantaneous flow features is discussed in Section 5.2, while the analysis of mean flow features is presented in Section 5.3. Section 5.3.1 emphasizes the validation of numerical results through comparison with experimental data, focusing on mean surface pressure. Location and intensity of shock waves are also discussed. In Section 5.3.2, the vortex flow pattern and vortex-shock interaction are investigated using scale-resolving results. Finally, turbulence-related quantities, such as eddy viscosity, turbulence kinetic energy, and components of the Reynolds-stress tensor, are presented in Section 5.4.

This chapter serves as a methodological foundation for performing URANS and Hi-Fi simulations on delta wings. It also facilitates the validation of codes and approaches, and particularly, it aids in gaining expertise and knowledge. These are subsequently utilized for analyzing the flow physics of the ADS-NA2-W1 configuration, as detailed in Chapter 6.

5.1. Test case description

The VFE-2 wing is elaborated upon in Section 2.1.6, which also discusses experimental data. The operating conditions used in the CFD analysis align with these experimental conditions.

5.1.1. Mesh characteristics

Fig. 5.1 shows the computational mesh utilized to investigate the VFE-2 delta wing. Dimensionless Cartesian coordinates are introduced as $\xi = x/L$, $\eta = y/(x\tan(\varphi))$, and $\psi = z/(x\tan(\varphi))$, where L denotes the chord length in the symmetry plane.

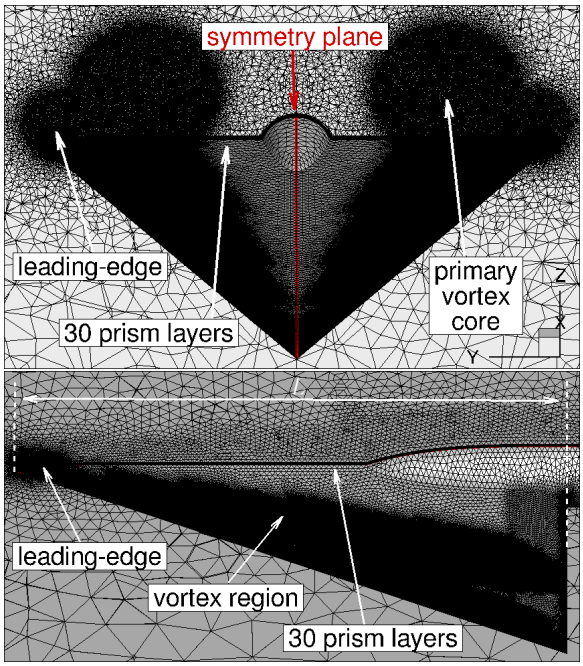

Figure 5.1: VFE-2 geometry and mesh (Di Fabbio et al., 2023)

The mesh's outer boundary consists of a spherical farfield boundary located $50L$ from the wing. Comprising approximately 32 million cells, the unstructured mesh includes up to 30 prism layers along the walls, with a wall-normal growth factor of 1.1 and the first cell thickness ensuring that $y^+ < 1$. Symmetry to the plane $y = 0$ is maintained across the mesh. Cell sizes (Δ) within the computational domain vary, with the finest cells, approximately $0.002L$ in size, located within the vortex region and near the leading-edge to resolve the onset of the shear layer.

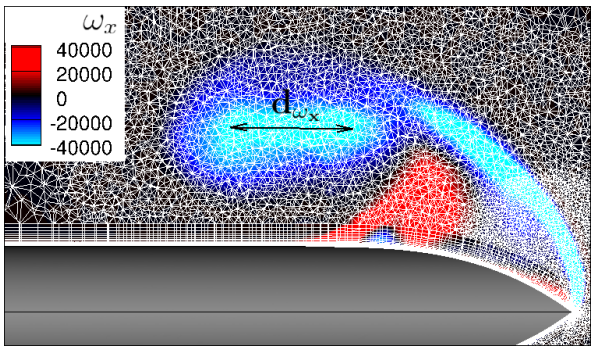

Figure 5.2: Vortex diameter (indicated by an arrow) based on the mean vorticity, IDDES results at $\xi = 0.4$.

To capture the development of turbulent scales, mesh refinement closely follows the vortex region over the wing. The grid resolution is demonstrated at $\xi = 0.4$ by the number of grid points inside the vortex diameter d_{ω_x}, computed as $N_\omega \approx 20$, derived from the mean x-vorticity distribution ω_x[1]. Although cell size slightly increases along the wing span, the ratio of the vortex diameter to cell size grows due to vortex expansion. The number of grid points inside the vortex diameter then increases.

[1]The filtering operation, denoted by an overbar, is not explicitly detailed to enhance readability. Unless specified otherwise, variables are to be interpreted as their mean values.

Computational domain's quality

The IDDES approach is selected for the scale-resolving simulations, owing to its effectiveness for sharp leading-edge delta wings. In such configurations, turbulence generation typically begins shortly after leading-edge separation within the separated shear layer, while still remaining in close proximity to the wall. The IDDES model is designed to transition to URANS mode within the wall layer, while operating in LES mode in the off-wall region. Mesh refinement at the onset of the turbulent shear layer emanating from the leading-edge is instrumental in transitioning the IDDES model into a WMLES mode, as described in Section 3.4.2. For this purpose, Fig. 5.3 depicts the mean hybrid length scale relative to the RANS length scale, $\tilde{d}/d$, where $\tilde{d}$ is expressed in Eq. 3.81 and d is the distance to the wall. Fig. 5.3 additionally presents the mesh, with the exception of $\xi = 0.95$, due to the mesh density complicating the visualization of the variables under analysis. In the thin regions close to the wall, which are fully modeled by the RANS mode, a ratio around unity is expected. Furthermore, the shear layer transition occurs in the LES mode and it enhances the model's capability to manage the shift between RANS and LES modes in the region immediately following separation. This is aimed at mitigating the impacts of the grey-area phenomenon (Peng and Jirasek, 2016; Probst et al., 2016). Besides, as the vortex core region is captured by the LES mode, the RC correction is not employed within the HRL framework.

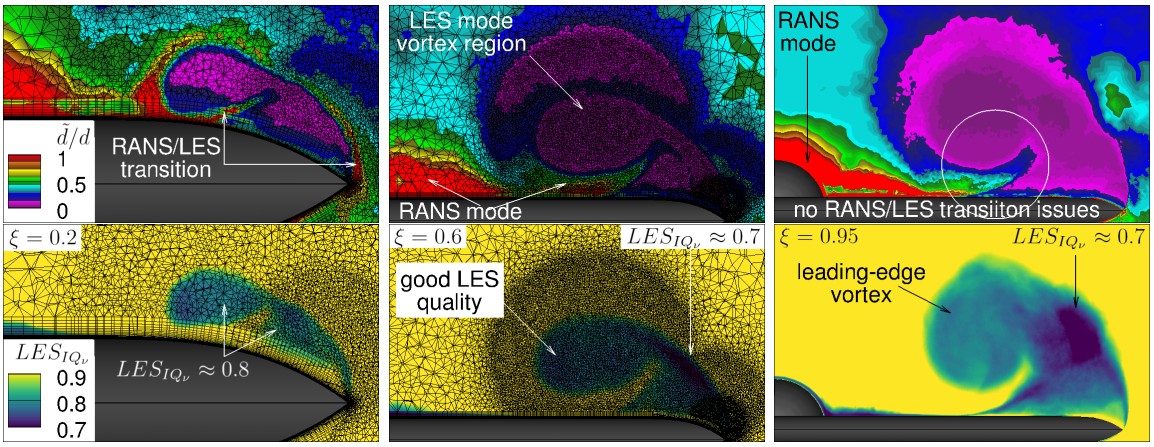

Figure 5.3: Mean hybrid length scale over RANS length scale, and mean LES_{IQ_ν}, IDDES results at $\xi = 0.2, 0.6, 0.95$.

Spatial resolution within the LES region is discussed next. To demonstrate that the current mesh resolution is capable of resolving a significant portion of the turbulence spectrum, the LES Index of Resolution Quality (LES_{IQ_ν}) is illustrated in Fig. 5.3. The LES_{IQ_ν} compares turbulent viscosity to laminar viscosity, utilizing the formulation proposed by Celik et al., 2005. This index is a dimensionless number ranging between zero and one, calibrated to simulate the ratio of resolved to total turbulent kinetic energy. An index quality greater than 0.8 is considered indicative of a good LES, while a value of 0.95 or higher is considered representative of DNS quality (Celik et al., 2009). Overall, the plots suggest a satisfactory spatial resolution within the

vortex region. Although slight weaknesses are observed in the downstream portions of the shear layer, these areas are considered to be positioned too far downstream to significantly affect the formation of the vortex core or the vortex breakdown.

5.1.2. Mesh convergence study

A study on grid resolution is undertaken to scrutinize the impact of grid discretization and to mitigate its effects. The specifications of the employed meshes are given in Table 5.1. The methodology involves methodically reducing the size of the finest mesh cell by half in successive steps. To evaluate the impact of mesh refinement, URANS simulations are executed across all four mesh configurations. In contrast, IDDES analyses are limited to the two most refined meshes, verifying the grid resolution's sufficiency in capturing essential flow dynamics.

Table 5.1: VFE-2 computational domains (Di Fabbio et al., 2023).

Acronym	Min Size	Cells
coarse	0.016 L	10 million
medium	0.008 L	21 million
fine	0.004 L	26 million
extra-fine	0.002 L	32 million

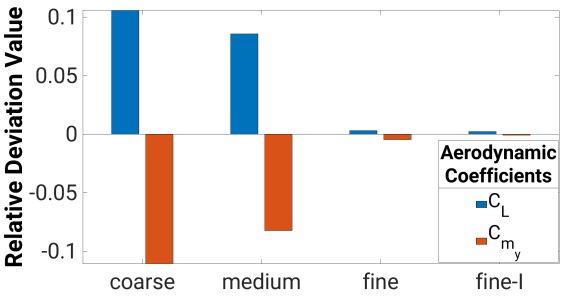

Figure 5.4: Relative deviation bar plot of the aerodynamic coefficients. "I" denotes the comparison between the IDDES results on the fine and extra-fine mesh (Di Fabbio et al., 2022a).

Figure 5.4 presents the comparative deviation in lift (C_L) and pitching moment (C_{m_y}) coefficients against the results on the finest mesh. The analysis spans both IDDES and URANS methodologies, revealing a consistent and significant diminution in grid-induced discrepancies. Mesh convergence is particularly discernible within the RANS analyses.

Moreover, an examination of the fine-I data demonstrates negligible variance in aerodynamic coefficient predictions between the fine and extra-fine meshes under the IDDES framework, substantiating the achievement of mesh convergence. Additional considerations regarding grid sensitivity are discussed in Section 5.3, focusing on the analysis of the mean surface pressure coefficient.

5.1.3. Numerical approach

An implicit dual-time stepping approach, utilizing a Backward-Euler/LUSGS implicit smoother, is employed in the unsteady simulations. To ensure the convergence of the inner iterations in the IDDES runs, Cauchy convergence criteria for several quantities, namely, volume-averaged turbulence kinetic energy, maximum Mach number, and specific aerodynamic coefficients, is applied, with tolerance values set at 1×10^{-5}. The matrix dissipation model is selected for the computation of fluxes using a central scheme. However, in the HRL approach, artificial dissipation is reduced to prevent excessive

damping of the resolved turbulent structures. Consequently, a hybrid low-dissipation, low-dispersion discretization scheme (LD2) is utilized (Probst et al., 2016).

Figure 5.5 illustrates the temporal evolution of the lift coefficient and specifies the simulated time intervals for various cases. Time is characterized by the Convective Time Unit (CTU), computed as follows:

$$CTU = L/U_\infty = 3790\mu s, \tag{5.1}$$

where L represents the characteristic length and U_∞ denotes the free-stream velocity.

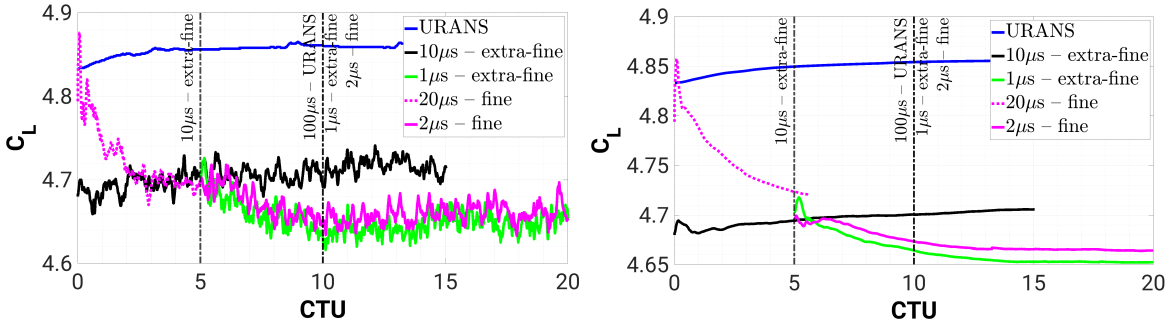

Figure 5.5: Time history of the lift coefficient, instantaneous (on the left) and run-time averaged (on the right) (Di Fabbio et al., 2023).

For URANS simulations, the time step size (Δt) is set to $100\mu s$. A period of ten CTUs is simulated before initiating time-averaging to mitigate the initial transient effects, and five flow-through times are considered in computing the mean flow field values.

To accurately resolve convective transport and capture flow characteristics, the maximum permissible time step size for IDDES runs is determined. On the extra-fine mesh, a time step size of $\Delta t = 1\mu s$ satisfactorily resolves the time scales of energy-containing eddies in the region of interest while maintaining the convective Courant-Friedrichs-Lewy number, $\mathrm{CFL} = U\Delta t/\Delta$, below one, as demonstrated in Fig. 5.6 (Spalart, 1997). To enhance the efficiency of the simulation and save computational resources, a strategy is implemented by augmenting the time step size to $\Delta t = 10\mu s$. This adjustment lead to the CFL number increasing by approximately an order of magnitude.

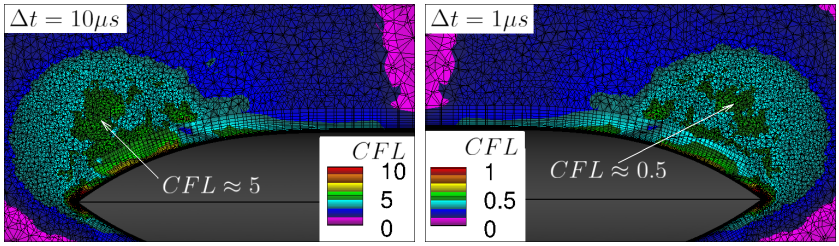

Figure 5.6: Mean convective CFL number at $\xi = 0.2$, comparison between the IDDES results with the time step size $\Delta t = 10\mu s$ and $\Delta t = 1\mu s$ (Di Fabbio et al., 2022a).

The IDDES depicted in black is conducted on the extra-fine mesh, starting from a steady-state condition. Subsequently, the simulation executes five CTUs with a time step size of $\Delta t = 10\mu s$. To calculate the flow variable statistics with an increased time step size, ten overflows with $\Delta t = 10\mu s$ are computed.

As illustrated in green, after the initial five overflows to bypass the transient phase, five CTUs are executed with a reduced time step size of $\Delta t = 1\mu s$ before commencing time-averaging for the IDDES run with a reduced time step on the extra-fine mesh. For the computation of mean flow properties, ten overflows with $\Delta t = 1\mu s$ are subsequently included. The effect of time step size is discernible when comparing the black and green lines in Fig. 5.5. With a coarser temporal resolution, the lift coefficient exhibits a near-constant behavior over time, contrasting with a noticeable decline observed upon the reduction of the time step. This demonstrates that enhanced temporal accuracy significantly improves the fidelity of the numerical results.

Figure 5.5 also presents the evolution of the IDDES run with the fine mesh, depicted in magenta, which is initialized using URANS results. No variation in the duration of the initial transient is observed. Notably, the time step sizes are doubled (as indicated in the legend of Fig. 5.4) because the size of the finest cell is increased twofold relative to the extra-fine reference mesh, as summarized in Table 5.1.

5.2. Flow overview: instantaneous flow features

As introduced in Section 2.1, over the delta wing, the flow separates at the leading-edge and subsequently rolls up to form a stable, separation-induced primary vortex. The flow reattaches to the surface as the primary vortex rolls up, and the span-wise flow beneath subsequently separates a second time to form a counter-rotating secondary vortex outboard of the primary one. The direct effect of these vortices is an additional suction footprint and, consequently, increased lift, which ultimately results in a non-linear dependence of the lift force on the angle of attack. Understanding and predicting vortex and shock wave generation and evolution are of paramount importance. The interaction between vortices and shock waves is a crucial aspect of the flow physics at transonic conditions and, therefore, is assessed in detail.

Figure 5.7a presents the vortices by illustrating the instantaneous Q-criterion iso-surfaces, which are colored based on the normalized helicity, H_n. The Q-criterion is a scalar field derived from the velocity gradient tensor, $\nabla\mathbf{U}$, used to identify vortical structures in fluid flows. It is defined as the positive second invariant of the velocity gradient tensor, which can be expressed as

$$Q = \frac{1}{2}\left(\|W_{ij}\|^2 - \|S_{ij}\|^2\right), \tag{5.2}$$

where $\|W_{ij}\|^2$ represents the norm of the vorticity tensor, indicating the local rotation, and $\|S_{ij}\|^2$ represents the norm of the rate-of-strain tensor, indicating the deformation due to shear and elongational strains. Regions where $Q > 0$ are considered to be dominated by rotational motion rather than deformation, signifying the presence of vortical structures.

The normalized helicity quantifies the alignment between the velocity field and the vorticity vectors in a flow. Vorticity is defined as the curl of the velocity field, $\boldsymbol{\omega} = \nabla \times \mathbf{U}$, and represents the local spinning motion of the fluid. The normalized helicity is expressed as follows

$$H_n = \frac{\mathbf{U} \cdot \boldsymbol{\omega}}{|\mathbf{U}||\boldsymbol{\omega}|}, \tag{5.3}$$

where, H_n measures the cosine of the angle between the velocity and vorticity vectors, ranging from −1 to 1. A value of 1 indicates that the velocity and vorticity vectors are perfectly aligned, suggesting a coherent and potentially stable vortex structure. A value of −1 implies perfect anti-alignment. A value of 0 indicates that the vectors are orthogonal, showing no direct correlation between the flow's direction and its local rotation. As depicted in Fig. 5.7a, the helicity's sign, with positive values depicted in blue and negative in red, distinguishes the rotational direction, effectively differentiating between primary and secondary vortices.

Furthermore, the Q-criterion iso-surfaces enable a qualitative evaluation of turbulence resolution within the LES domains of the IDDES simulations. The vortices exhibit noticeable turbulent fluctuations, indicating that the resolution level of the simulation is sufficient for an in-depth analysis of flow physics. The simulation grid has successfully resolved a broad spectrum of turbulent structures, facilitating a comprehensive examination of the flow's turbulent dynamics.

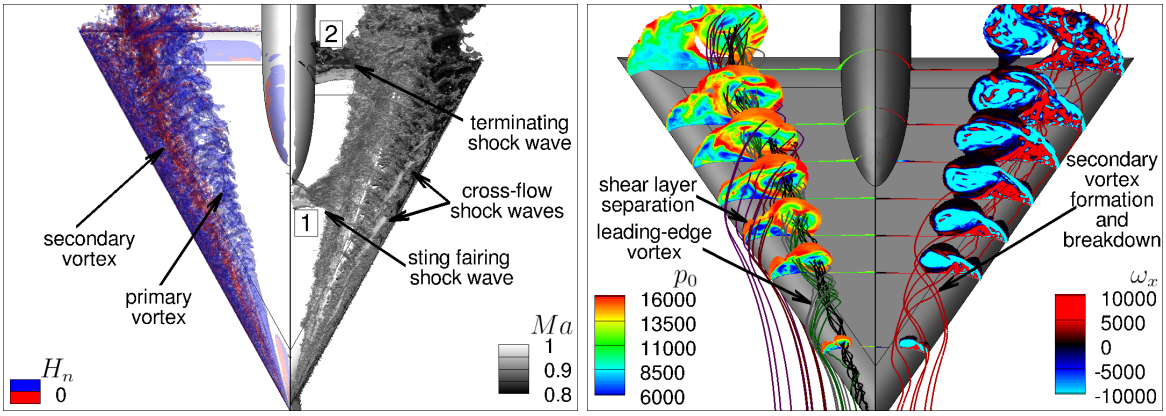

(a) Instantaneous Q-criterion iso-surface with flood contour by normalized helicity (left); pressure gradient in x-direction iso-surface with flood contour by Mach number (right).

(b) Instantaneous total pressure and primary vortex stream-traces (left); instantaneous x-direction vorticity and secondary vortex stream-traces (right).

Figure 5.7: IDDES ($\Delta t = 1\mu s$) results for the VFE-2 geometry with $Ma_\infty = 0.8$, $Re_\infty = 2 \times 10^6$, $\alpha = 20.5°$ (Di Fabbio et al., 2023).

At a transonic speed of $Ma = 0.8$, the aerodynamics become considerably more intricate compared to subsonic regimes due to the acceleration of flow above the delta wing to supersonic velocities, resulting in the manifestation of shock waves. The visualization provided in Figure 5.7a, featuring the iso-surface of the pressure gradient in the x-direction, ∇p_x, corroborates the existence of two primary shock waves: the sting fairing

and the terminating shock waves. Cross-flow shock waves are also slightly visible; however, they are analyzed in detail in the following sections.

The formation of the primary vortex, driven by the separation of the shear layer, is depicted in Figure 5.7b, which displays the instantaneous total pressure alongside the primary vortex's stream-traces. Total pressure is employed here to signify an energetic metric, offering insights into the vortex's intensity and location. To elucidate the distinct influences, streamlines in various colors are utilized. The genesis of the primary vortex occurs just downstream of the wing apex, with its high-velocity core exclusively constituted by the flow detaching from the shear layer that separates at the wing apex, as depicted by the black streamlines. Subsequently, as illustrated by the green, brown, and purple stream-traces in Figure 5.7b, the primary vortex expands in diameter, fed continuously by the shear layer extending along the wing. This process amplifies the core by encircling and infusing it with kinetic energy, thereby ensuring the vortex's sustenance and coherence.

Figure 5.7b elucidates the instantaneous x-vorticity, effectively differentiating between the primary and secondary vortices through their rotation directions, and the secondary vortex's red stream-traces located in the right half of the image. This illustration assists in examining the formation and disintegration of the secondary vortex, which is not a direct result of shear layer separation. The stream-traces forming the secondary vortex do not originate from the leading-edge's immediate vicinity. Instead, the secondary vortex emerges as a consequence of the dynamics induced by the primary vortex, with their formations being interlinked; a well-defined secondary vortex materializes only when the primary vortex exhibits sufficient strength. Subsequently, the breakdown of the secondary vortex is observed in the latter portion of the wing, downstream from the sting tip, a phenomenon that disrupts the shear layer's ability to fully roll up and merge into the primary vortex.

5.3. Mean flow features

The mean flow characteristics are scrutinized by prioritizing the validation of numerical outcomes via comparison with experimental datasets, with a particular emphasis on surface pressure. Additionally, the location and intensity of shock waves are examined. Subsequently, the vortex flow pattern and the interaction between vortex and shock are explored through the analysis of scale-resolving results[2].

5.3.1. Result validation and shock-wave locations

The suction footprint on the wing surface is primarily caused by the high tangential velocity around the inner vortex core. Figure 5.8 displays the mean surface pressure coefficient, denoted as c_p. The pressure coefficient is a dimensionless parameter used in

[2]The filtering operation, denoted by a bar, is not explicitly detailed to enhance readability. Unless specified otherwise, variables are to be interpreted as their mean values.

aerodynamics to express the pressure variations in a flow field relative to the free-stream pressure. It is defined as follows

$$c_p = \frac{p - p_\infty}{\frac{1}{2}\rho_\infty U_\infty^2}, \tag{5.4}$$

where p is the static pressure at the point of interest in the flow field, p_∞ is the free-stream static pressure, ρ_∞ is the free-stream density, and U_∞ is the free-stream velocity. The term $\frac{1}{2}\rho_\infty U_\infty^2$ corresponds to the dynamic pressure of the free-stream.

The critical or sonic pressure coefficient, c_p^*, is defined as the pressure coefficient at the point on an airfoil where the local flow speed reaches the speed of sound for the first time, indicating the onset of sonic conditions. Mathematically, it is expressed as follows

$$c_p^* = \left[\left(\frac{\gamma - 1}{\gamma + 1} Ma_\infty^2 + \frac{2}{\gamma + 1}\right)^{\frac{\gamma}{\gamma - 1}} - 1\right] \frac{2}{\gamma Ma_\infty^2}, \tag{5.5}$$

where Ma_∞ is the free-stream Mach number (Houghton et al., 2013). For the investigated test case with a specific heat ratio $\gamma = 1.4$ and a Mach number $Ma = 0.8$, it follows that the sonic pressure coefficient c_p^* is calculated to be -0.43.

To investigate the prediction of c_p, several slice planes have been extracted, as indicated in Fig. 5.8a. The distribution of c_p along the span-wise direction at chord-wise positions $\xi = 0.2, 0.4, 0.6, 0.8, 0.95$ is plotted in Fig. 5.9, comparing experimental data and simulation results (URANS, IDDES with $\Delta t = 10\mu s$ and $\Delta t = 1\mu s$ using the extra-fine mesh, and IDDES with $\Delta t = 2\mu s$ using the fine mesh).

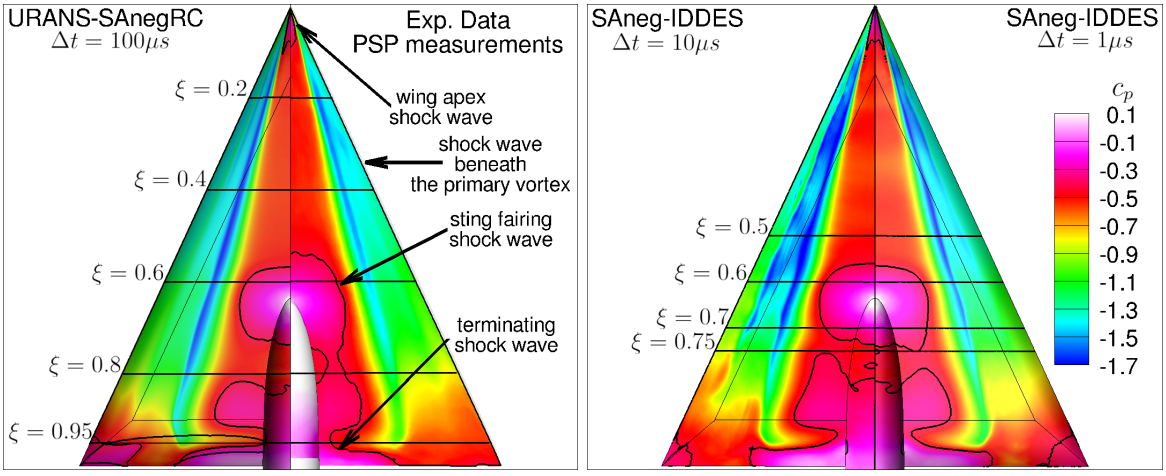

(a) URANS and Experimental Data **(b)** IDDES with $\Delta t = 10\mu s$ and $\Delta t = 1\mu s$

Figure 5.8: Mean surface coefficient of pressure, comparison between experimental and numerical data. The black contour lines indicate the sonic pressure coefficient $c_p^* = -0.43$ (Di Fabbio et al., 2022a).

The plots underscore the sensitivity of the results to both spatial and temporal resolution. The c_p distribution reveals that differences emerge between the IDDES results

obtained with the two finest meshes, despite Fig. 5.5 showing almost identical lift coefficients. Comparing the green and magenta lines, significant discrepancies are evident at the front wing for ξ = 0.2, where the formation of the leading-edge vortex begins, and the IDDES results on the "fine" mesh with $\Delta t = 2\mu s$ predict a stronger secondary vortex. This is reflected at ξ = 0.8 , where the secondary vortex is still present on the fine mesh. These discrepancies indicate that additional criteria might be necessary for mesh convergence, as integral aerodynamic coefficients seem insufficient. However, these differences are substantially mitigated across the aircraft, and the uncertainties in the IDDES results due to mesh resolution are considered significantly reduced and acceptable. Consequently, IDDES on the extra-fine mesh is regarded as the reference. It is worth noting that, in this case, for such complex configurations, achieving and demonstrating the convergence of the LES approach used in the vortex region would require an exorbitant computational expense.

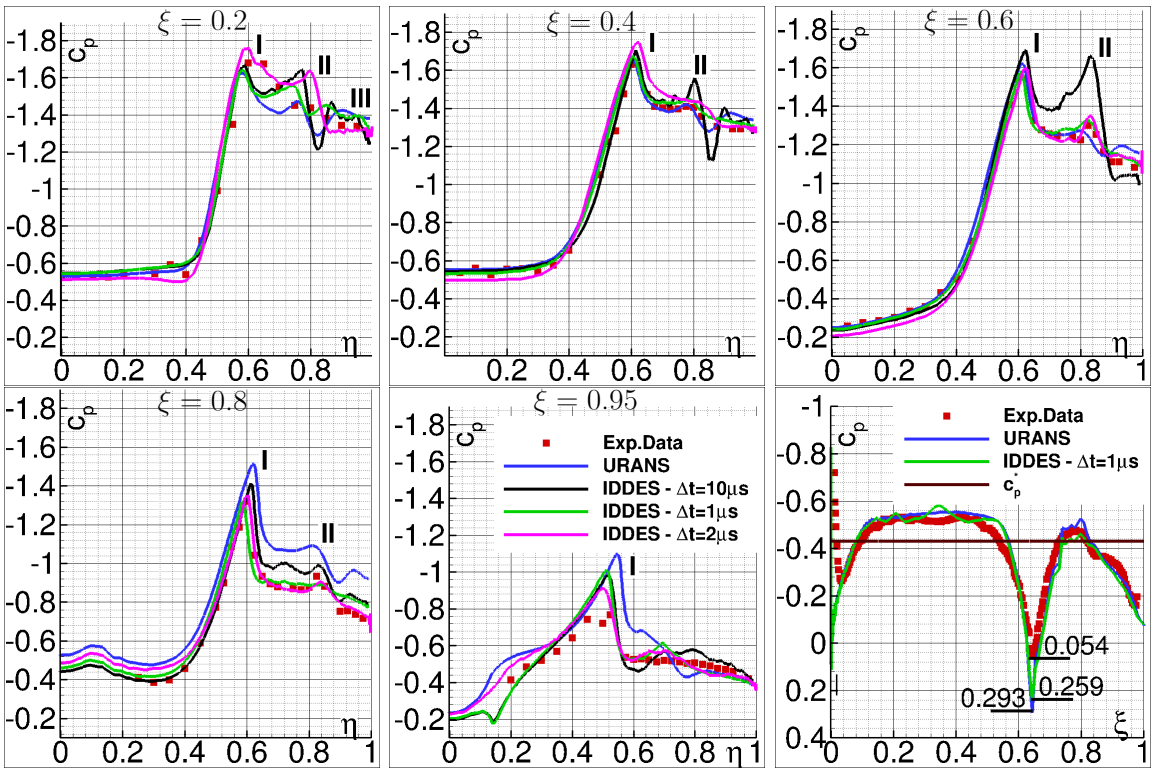

Figure 5.9: Mean surface coefficient of pressure at ξ = 0.2, 0.4, 0.6, 0.8, 0.95 and at symmetry plane η = 0 (lower right), comparison between experimental, URANS and IDDES data (Di Fabbio et al., 2022a).

Figure 5.9 demonstrates a satisfactory and suitable agreement between the IDDES results ($\Delta t = 1\mu s$) and experimental data. The IDDES results yield the closest match to the experimental observations across all numerical outcomes, particularly on the rear side of the wing. The IDDES outcomes significantly enhance the prediction of the suction footprint caused by the vortices, although some discrepancies present in the front part of the wing. The fine resolution proves especially advantageous in the apex region for mitigating the grey-area issue, which is further discussed in subsection 5.4.

The secondary and tertiary vortices, denoted by Roman numerals II and III, manifest at the peaks of c_p at $\eta \approx 0.7$ and $\eta \approx 0.85$, respectively, measured from the chordwise location $\xi = 0.2$. The tertiary vortex then vanishes in the IDDES results with $\Delta t = 1\mu s$ at $\xi = 0.4$, perfectly matching the experimental data, whereas it erroneously persists in the URANS outcomes. The experimental data suggests the overall absence of a tertiary vortex but, considering the data resolution, this phenomenon cannot be entirely ruled out. The secondary vortex peak is weak at $\xi = 0.8$ in the experimental data and disappears at $\xi = 0.95$, indicating a disintegration between these two locations. Figure 5.9 shows that in the IDDES results with $\Delta t = 1\mu s$, it bursts further upstream ($\xi < 0.8$), as also discussed in Section 5.2. It should be emphasized that increasing the time step size does not significantly impact the coefficient of pressure associated with the primary vortex. In contrast, a larger time step ($\Delta t = 10\mu s$) results in inaccurate predictions of the secondary vortex.

The numerical outcomes accurately capture the trend of the c_p curve at $\xi = 0.95$, with the notable exception of the primary vortex core region. The experiment shows a decay, whereas the simulation still predicts a strong peak of c_p caused by the vortex. The weaker vortex in the experimental data could indicate a tendency to break down near the trailing-edge. It must be acknowledged that the possibility of a measurement error in the unique sample demonstrating this phenomenon cannot be excluded. Moreover, as discussed in Section 5.3.2, close to the trailing-edge, the shear layer does not roll up to form a stable leading-edge vortex over the wing, and the suction footprint abruptly drops.

The investigation of the supersonic area over the wing and the consequent presence of shock waves are observed in Fig. 5.8, where the sonic pressure coefficient $c_p^* = -0.43$ is indicated by black contour lines. The IDDES approach best replicates the experimental results in terms of the predicted supersonic area. In the vicinity ahead of the secondary vortex, a cross-flow shock wave is observed. Figure 5.8 illustrates that the outboard-directed flow beneath the primary vortex, in close proximity to the surface, reaches supersonic speeds, thereby inducing a shock wave. This observation is corroborated by the analysis presented in Section 5.3.2. Additionally, a shock wave typical for transonic free-stream conditions is captured close to the wing apex, where critical flow conditions are reached. Finally, the contour lines of the sonic pressure coefficient indicate the presence of shock waves in proximity to the sting fairing: a first one located at about $\xi = 0.55$, and a second one closer to the trailing-edge downstream of $\xi = 0.9$. These shock waves are shown and enumerated in Fig. 5.7a. Furthermore, Fig. 5.9 displays the c_p distribution at the symmetry plane $\eta = 0$ to quantify the intensity of the aforementioned shock waves. Although the simulation results predict a higher pressure peak close to the wing apex ($\xi = 0$) and to the sting tip ($\xi \approx 0.62$), the pressure trend and the position of the shock waves above the wing are well captured by the numerical data.

5.3.2. Vortex pattern analysis

A detailed analysis of the IDDES results with $\Delta t = 1\mu s$ is performed. It is essential to understand the vortex pattern itself and how it is modified by the interaction between shock waves and vortices. For this purpose, Fig. 5.10 presents the field of

mean x-direction vorticity, ω_x, at ξ = 0.5, 0.6, 0.7, 0.75, from both experimental and IDDES outcomes. PIV data are collected only at these locations, as also illustrated in Fig. 5.8b (Konrath et al., 2013). Subsequently, Fig. 5.11 displays the mean density gradient magnitude $\|\nabla\rho\|$, the normalized mean x-direction velocity u/U_∞, and the normalized mean in-plane tangential velocity u_t/U_∞ distribution, where $u_t = \sqrt{v^2 + w^2}$. Furthermore, Fig. 5.12 illustrates the primary vortex core line extracted by considering the local maximum mean x-velocity.

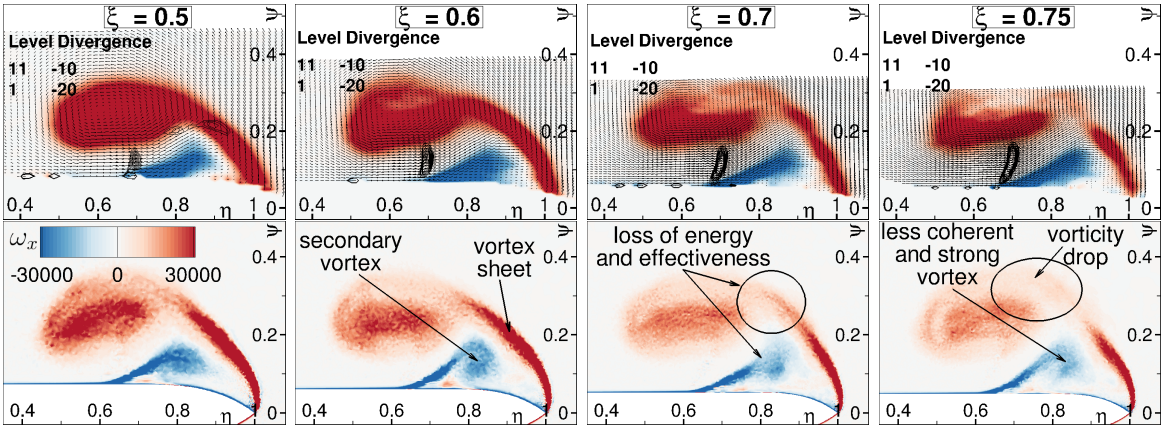

Figure 5.10: Mean x-direction vorticity distribution at ξ = 0.5, 0.6, 0.7, 0.75, comparison between experimental data (top) and IDDES outcomes (bottom). The black contour lines in the experimental data are related to the divergence of the in-plane velocity vector (Di Fabbio et al., 2022a).

Vortical structures arise from the concentration of low-energy components initially present within the boundary layer, rendering the vortex a zone of rotational flow characterized by stagnation conditions, particularly the pressure, that are inferior to those in the surrounding flow field. Consequently, the vortex can be conceptualized as an energy sink or an entropy peak, rendering it particularly susceptible to perturbations, such as shock waves (Délery, 1994). An unburst vortex exhibits a coherent structure marked by elevated axial and rotational velocities. As demonstrated in Fig. 5.10, the IDDES outcomes precisely capture both the primary and secondary vortices. Between ξ = 0.6 and ξ = 0.7, a reduction in x-direction vorticity is observed, attributable to the vortex not expanding uniformly along the stream-wise direction with an increase in the η-coordinate. According to the self-induction breakdown theory (Srigrarom and Kurosaka, 2000), the axial vorticity within the vortex induces an azimuthal velocity, subsequently causing the vorticity vector to tilt toward the azimuthal direction. The resultant gradient in azimuthal vorticity, due to enhanced circulation, prompts radial expansion of the leading-edge vortex. This radial expansion is accompanied by a sign reversal in azimuthal vorticity downstream of the vorticity gradient, where the rotation is slower compared to the upstream region. These processes culminate at a juncture where vortex filaments inwardly turn, leading to a sign reversal in axial vorticity. This phenomenon is more accurately illustrated in Fig. 5.7b, which displays the instantaneous x-vorticity.

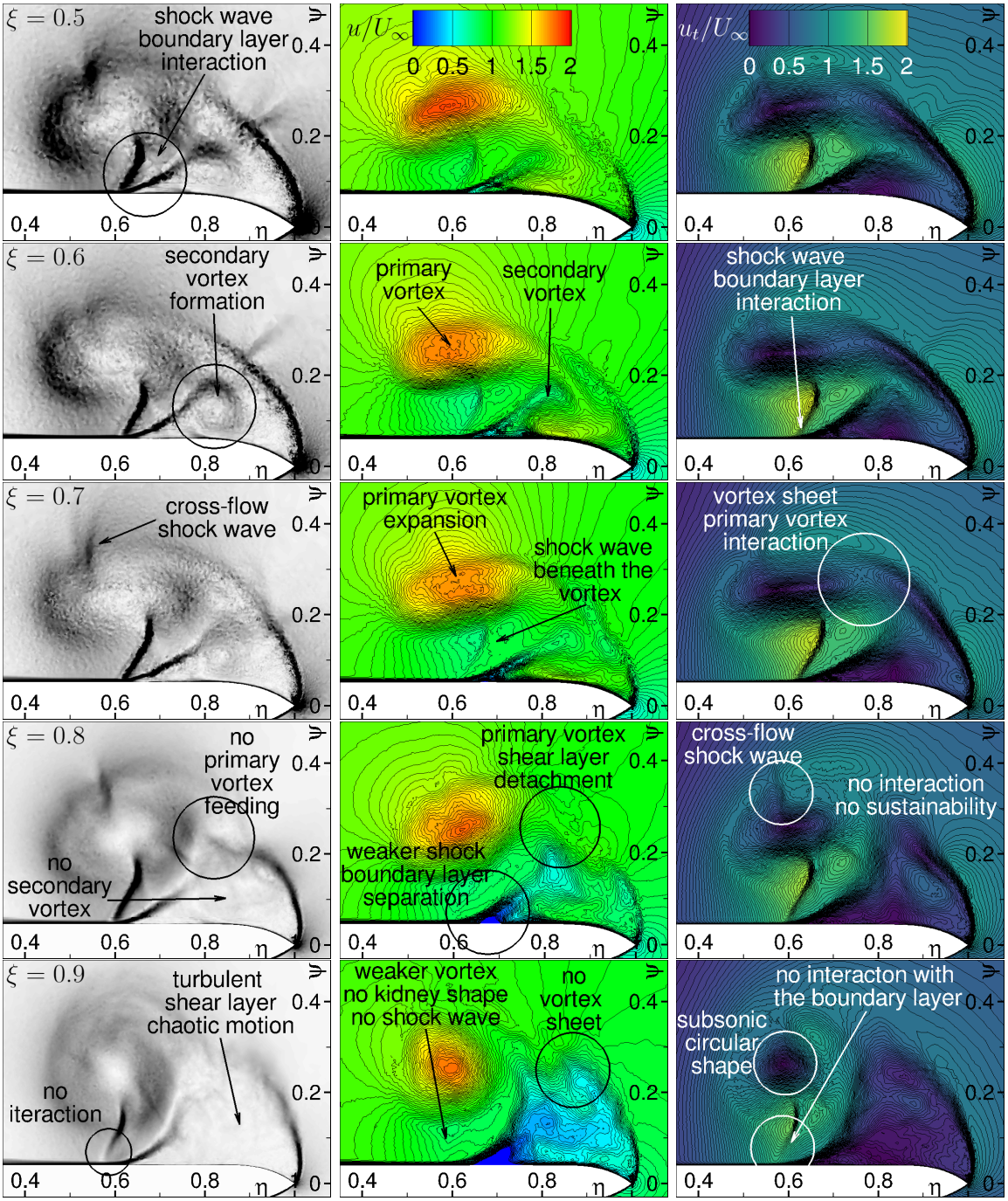

Figure 5.11: Mean density gradient magnitude, mean normalized x-direction velocity, and mean normalized in-plane tangential velocity distribution, IDDES results at ξ = 0.5, 0.6, 0.7, 0.8, 0.9 (Di Fabbio et al., 2023).

Figure 5.10 delineates regions exhibiting negative divergence of the in-plane velocity vectors, as inferred from experimental observations, providing insights into the location and morphology of the separation shock, the so-called cross-flow shock discussed in Section 2.1.5. This shock is accurately captured from the IDDES approach, as evidenced by the altered distribution of u_t, visible through the iso-contour lines in Fig. 5.11. Ad-

ditionally, the mean density gradient magnitude further elucidates this occurrence. A complex shock system is then situated beneath the leading-edge vortex. The separation shock, primarily induced by the flow acceleration in this region, substantially modifies the local flow topology. The interaction between this shock and the boundary layer on the wing's upper surface precipitates flow separation, thereby fostering the formation of the secondary vortex, as illustrated in Fig. 5.11 at $\xi = 0.6$. Besides, at transonic conditions, the leading-edge vortex assumes a kidney shape, with cross-flow shocks manifesting around the leading-edge vortex and atop the shear layer. These shocks notably influence the velocity profile and they are purportedly a consequence of the curved flow trajectories, leading to accelerations that reach thermophysical limits (Riou et al., 2010). It should be observed that the vortex shape at $\xi = 0.9$ is circular, akin to the subsonic case (analyzed in Section 2.1.1), suggesting a substantial reduction in Mach number.

Post-interaction with the shock wave in proximity of the sting tip ($\xi = 0.62$), the vortex exhibits increased vulnerability and a propensity towards breakdown. The shock interacts with the vortex core, reducing x-velocity (as seen in Fig. 5.12b at $\xi = 0.62$), and consequently diminishing the suction footprint (see Fig. 5.9 at $\xi = 0.8$). A similar trend in u_{max} is observed near other shock-vortex interactions (approximately at $\xi = 0.2$ and $\xi = 0.35$). The shock wave's width is comparable to the local mean free path of fluid particles, allowing the shock to act as a sharp discontinuity in typical aerodynamic flows. Consequently, the Mach number and normal velocity experience an abrupt reduction across the shock. The gradual nature of this drop in the plotted mean variables indicate slight temporal fluctuations in shock location on the wing. Additionally, the in-plane (tangential) velocity, ideally parallel to the shock surface, remains largely unaffected by the shock wave, as demonstrated in Fig. 5.11. Under the current flow conditions, the shock wave fails to precipitate an immediate vortex breakdown. The shock intensity escalates with an increase in the angle of attack, given its direct dependency on the incoming Mach number. Therefore, a rise in the angle of attack could provoke vortex breakdown. In cases where the shock wave does not induce vortex breakdown following shock interaction, the leading-edge vortex demonstrates a propensity to restore stability and overcome the disturbance. This resilience is attributed to the continuous sustenance of the main vortex along the wing by the shear layer originating from the leading-edge, as depicted in Fig. 5.7b. Consequently, the x-velocity within the vortex core begins to increase once more, a phenomenon observable in Figs. 5.11 and 5.12b.

Moreover, Fig. 5.11 reveals critical phenomena occurring at the rear side of the wing. As discussed in Section 5.3.1, the secondary vortex undergoes breakdown within the range of $0.7 < \xi < 0.8$ and becomes indiscernible for $\xi > 0.8$. Consequently, in this region, the primary vortex, no longer supported by the shear layer, becomes increasingly vulnerable. This behavior is corroborated by the analyses of plots at $\xi = 0.7$ and $\xi = 0.8$. At $\xi = 0.7$, the separation shock wave is still present beneath the primary vortex; the vortex sheet interacts with and feeds the primary vortex, and the secondary vortex is well-formed and coherent. In contrast, at $\xi = 0.8$, the stream-wise boundary layer separation is identified, replacing the separation shock; the secondary vortex disappears, and there is no interaction between the primary vortex and the vortex

sheet. The stream-wise boundary layer separation identified at $\xi > 0.8$ may thus act as a precursor to vortex breakdown. Indeed, the disintegration of the secondary vortex initiates chaotic motions within the shear layer, precluding its coiling and thereby affecting the sustenance and stability of the primary vortex, as observed at $\xi = 0.9$.

This observation, coupled with the analyses presented in Section 5.2, substantiates the hypothesis regarding the mechanism responsible for the primary vortex breakdown observed at increased angles of attack at transonic conditions. As the flow over the wing separates at the leading-edge and rolls up, it forms a stable, separation-induced primary vortex. Typically, the flow reattaches when the primary vortex reaches the wing surface. Under specific conditions, the span-wise flow beneath the primary vortex separates again, generating a counter-rotating secondary vortex located outward of the primary vortex. The separation shock leads to a recirculation zone and fosters the formation of the secondary vortex. The secondary vortex's existence facilitates the incorporation of the shear layer into the primary vortex. However, when the shock wave, induced by the sting tip, interacts with the primary vortex, it alters the flow dynamics, rendering the secondary vortex unsustainable. The phenomenon triggers a sudden decrease in axial velocity and results in the damping of the separation shock, which ceases to interact with the boundary layer, thereby leading to the disintegration of the secondary vortex. The fluid, previously part of the secondary vortex, transitions into turbulent motion on smaller scales, preventing the shear layer from coalescing into the primary vortex. Instead, it feeds into the turbulent flow, diminishing the primary vortex's kinetic energy source and increasing its susceptibility. This sequence is considered the beginning of the primary vortex breakdown, which becomes fully apparent at slightly higher angles of attack, as demonstrated by experimental findings (Konrath et al., 2006, 2013).

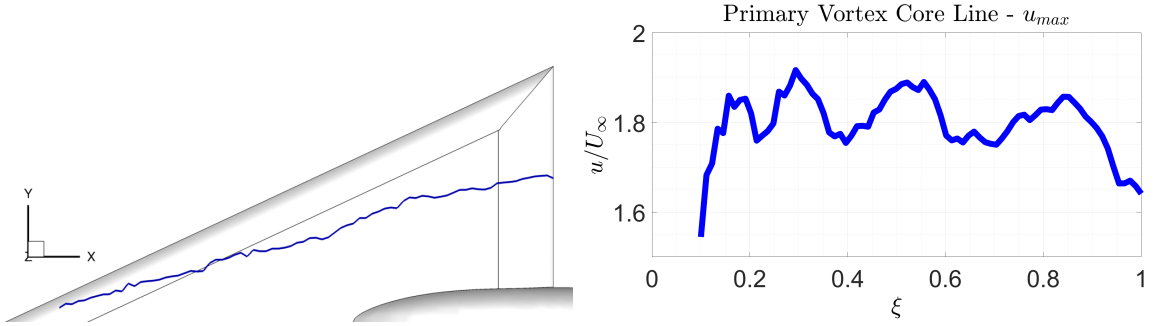

(a) Vortex core location - xy plane

(b) Normalized maximum mean x-velocity.

Figure 5.12: Primary vortex core line extracted from the IDDES outcomes (Di Fabbio et al., 2023).

5.4. Turbulence-related variables

Figure 5.13 depicts the contours of the turbulence ratio $R_t = \mu_t/\mu$, where μ represents the molecular dynamic viscosity. The modeled turbulent eddy viscosity, μ_t, is compared between URANS and IDDES methodologies. It is observed that the URANS model tends to predict significantly elevated levels of turbulent eddy viscosity within

the vortex core. The areas exhibiting high values of μ_t in the RANS model are indicative of vortex motions characterized by intense turbulence energy production, a result of pronounced flow rotation and deformation. As demonstrated in Fig. 5.13, the RC-correction mechanism mitigates the overprediction of eddy viscosity in the frontal section of the wing. Nevertheless, this correction fails to sufficiently mitigate the excessive generation of turbulent viscosity in the rear region of the vortex, which is almost an order of magnitude greater than the corresponding values observed in the HRL outcomes. The IDDES method, by using SGS eddy viscosity in regions away from the wall, highlights a significantly reduced μ_t compared to its RANS equivalent. This reduction in modeled μ_t within the LES regime is attributed to the local fine grid resolution that LES necessitates. Conversely, areas displaying elevated μ_t values within the LES framework signal strong local flow rotation or deformation and/or a relatively coarse grid resolution. Such conditions typically lead to enhanced energy dissipation of the resolved large-scale turbulence.

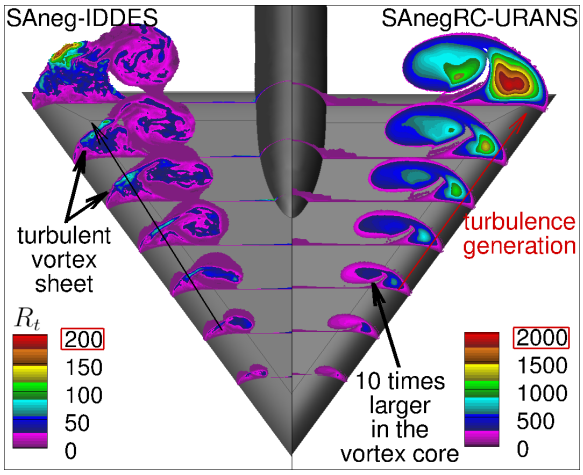

Figure 5.13: Turbulent viscosity ratio, comparison between URANS and IDDES results.

Figure 5.14a illustrates the resolved turbulence kinetic energy normalized by the square of the free-stream velocity, $K = k_t/U_\infty^2$. The term k_t could include both the modeled and resolved turbulence kinetic energy. However, since the SA model is employed, the modeled component is approximated to zero. Statistics from the resolved fluctuations are utilized to compute the resolved turbulent kinetic energy. It is important to highlight that the variable k, used in the $k\omega$SST model, refers to the turbulent kinetic energy as modeled by the turbulence model approach. The turbulence primarily influences the region surrounding the primary vortex core and the vortex sheet. The initial slice plane suggests, given the challenges associated with the grey-area issue, that K is likely underestimated during the early stages of vortical flow development, indicating a delayed emergence of resolved turbulence. This delay, known as the grey-area issue, is inherent to the IDDES modeling approach and impacts the downstream evolution of the turbulent processes, including the onset of vortex breakdown. The problem arises as the vortex formation initially occurs in near-wall regions, predominantly modeled by RANS mode. The transition from RANS to LES mode is then considered as a primary cause for the observed discrepancies in the c_p results at the wing's front, leading to a less accurate resolved vortex motion and subsequently a postponed vortex breakdown. Towards the wing's rear, the resolved turbulence kinetic energy captures the separated shear layer and turbulent transport downstream close to the leading-edge, while the separation shock modifies the K distribution beneath the primary vortex. It is important to observe the behavior of the primary vortex: in the front part, it remains stable with a low value of K, while in the rear part, particularly after interaction with the sting fairing shock,

it becomes more unstable. This instability and unsteadiness are visibly manifested through the increased magnitude of the turbulent kinetic energy.

Figure 5.14 elucidates the components of the normalized specific Reynolds stress tensor, R_{ij}, illustrating the intensity of turbulent fluctuations across three dimensions and their covariance. The components of the Reynolds-stress tensor are normalized by the free-stream velocity and the local mean density thus equating their magnitude with that of K and emphasizing turbulent fluctuations independent of their energy transport contributions. To ascertain the resolved Reynolds stresses statistics from the resolved fluctuations are computed.

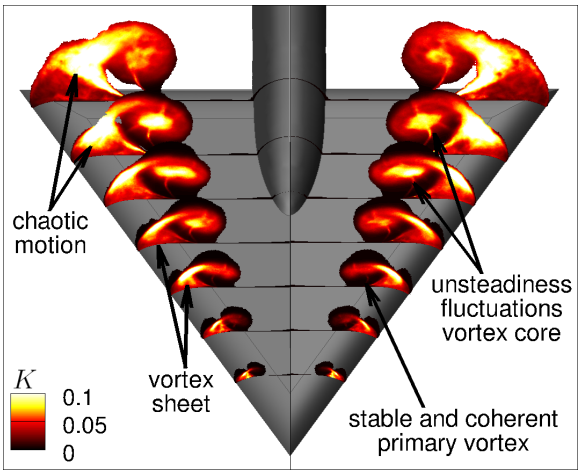

(a) Normalized turbulence kinetic energy, K.

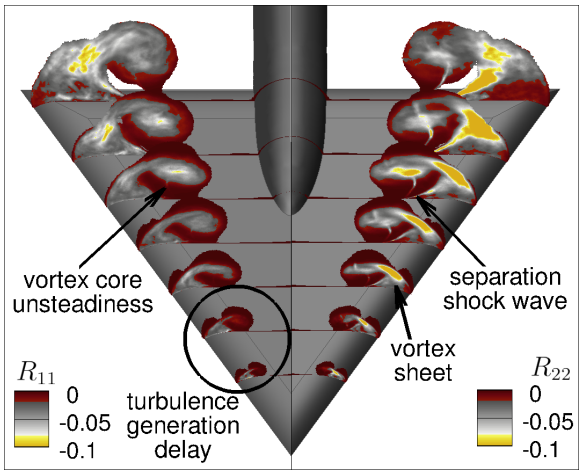

(b) Normalized Reynolds stresses, R_{11} and R_{22}.

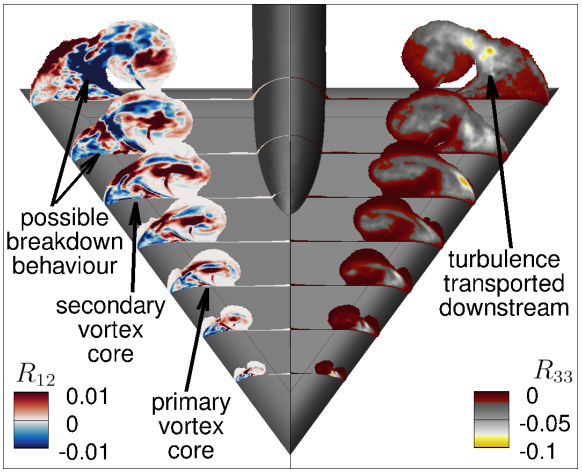

(c) Normalized Reynolds stresses, R_{12} and R_{33}.

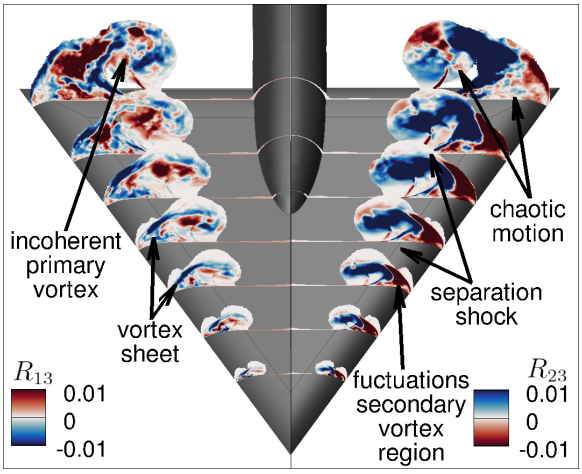

(d) Normalized Reynolds stresses, R_{13} and R_{23}.

Figure 5.14: Resolved turbulence-related quantities along the wing from the IDDES results (note the different scale in the legend boxes).

Fig. 5.14b illustrates R_{11} and R_{22}, with R_{11} depicting the turbulent dynamics of the transported turbulent shear layer, intensifying post-secondary vortex breakdown and

subsequently dispersing downstream without enriching the primary vortex. The analysis also highlights the delay in turbulence generation associated with the grey-area issue, as well as the heightened unsteadiness of the primary vortex subsequent to its interaction with the sting fairing shock. R_{22} signals fluctuations originating from the leading-edge, contributing significantly to the vortex core's turbulence kinetic energy. The vortex sheet is distinctly visible, along with the separation shock wave situated beneath the primary vortex.

Fig. 5.14c presents the covariance R_{12} and the normal component R_{33}, with R_{12} serving to identify the core of primary and secondary vortices via positive values (negative on the opposing wing side) and delineating the primary vortex boundary through peak values. A potential behavior of this component, immediately upstream of the vortex breakdown, may be discernible in the last slice plane, where positive and negative values mix in proximity to the primary vortex. This trend becomes more pronounced as it progresses downstream over the wing and is not evident in the forward section. The z-directional turbulence fluctuations are evident from R_{33}, indicating that elements transported downstream across the wing do not contribute to primary vortex formation but diverge from the wing.

Lastly, Fig. 5.14d shows covariances R_{13} and R_{23}, with R_{13} elucidating the shear layer's location, thickness, and vortex coherence, which diminishes towards the the rear wing. R_{23}, the strongest covariance component, predominantly occurs within the vortex sheet, highlighting the complex separation and roll-up processes, and is positively centered within the core (negatively on the opposite wing side), albeit less localized than R_{12}.

6

Investigation of Transonic Aerodynamics on a Triple-Delta Wing in Side-Slip Conditions

This chapter presents the main results obtained from the studies by Di Fabbio et al., 2022b,d. It aims to contribute to the field of HRL, seeking to understand their applicability to simulations of complex delta wing configurations under transonic flow conditions. For this purpose, the vortex-dominated flow around the triple-delta wing ADS-NA2-W1 aircraft is investigated by comparing URANS with Hi-Fi numerical results and experimental data provided by ADS (Hövelmann et al., 2020). The SAnegRC and $k\omega$SST model are employed to close the RANS equations, while in the scale-resolving computations, the SAneg-based IDDES and the $k\omega$-based SAS approaches are applied. The DLR-TAU code is used to perform the simulations.

Section 6.1 offers a concise introduction to the ADS-NA2-W1 test case. Section 6.1.1 elaborates on the mesh resolution, emphasizing the criteria for the transition between RANS and LES and the quality of the LES mesh. Section 6.1.2 discusses the mesh convergence study, while Section 6.1.3 delineates the numerical approach employed.

The transonic regime characterized by a Mach number of 0.85 and a Reynolds number of 12.53×10^6 is selected. The free-stream conditions are representative of highly agile delta-wing aircraft, and thus relevant to aerodynamic design topics such as maneuverability, stability, and control. Various URANS simulations are conducted at a constant side-slip angle of $\beta = 5°$, focusing on the asymmetry of the turbulent flow and varying the angle of attack within the range $12° < \alpha < 28°$. Scale-resolving simulations are performed exclusively for $\alpha = 20°$, $24°$, $28°$ due to the high computational costs.

The vortex development is analyzed in Section 6.2. The three angles of attack are categorized into distinct flow regimes and a detailed examination of the flow physics is provided. Various flow field variables are plotted to facilitate a comparison among the different datasets available. The flow physics is elucidated, with the analysis of the unsteady (instantaneous) and the mean flow features. It is important to note that the instantaneous variable capture a snapshot in time and do not account for the instability inherent to delta wing flows. The goal is to significantly advance the prediction of flow around multiple-delta wings, thereby enhancing the understanding of various flow physics phenomena that occur over the aircraft.

In Section 6.3, the numerical and experimental data are compared, focusing on the integral force and moment coefficients. Specifically, the curves for the lift, rolling, and pitching moment coefficients are presented. Furthermore, based on the distinctive behavior of the aerodynamic coefficients, several conclusions are drawn, and four different flow regimes are identified. The analyses confirm that, among the simulations presented, SAnegRC-based URANS simulations are the least accurate for modeling vortical flow over delta wings. This reinforces the need to improve the SA turbulence model's predictive accuracy using the RANS method, aiming for broader application in both academic and industry settings.

6.1. Computational domain and numerical approach

Figure 6.1 shows the ADS-NA2-W1 geometry, a 1:30-scaled version of a generic combat aircraft. A triple-delta wing characterizes this configuration, which is introduced in Section 2.1.7. The following labeling is used: leeward wing ($y > 0$) and windward wing ($y < 0$). For this configuration, the dimensionless Cartesian coordinates are introduced as follows $\xi = x/L$, $\eta = y/(b/2)$, $\psi = z/(b/2)$.

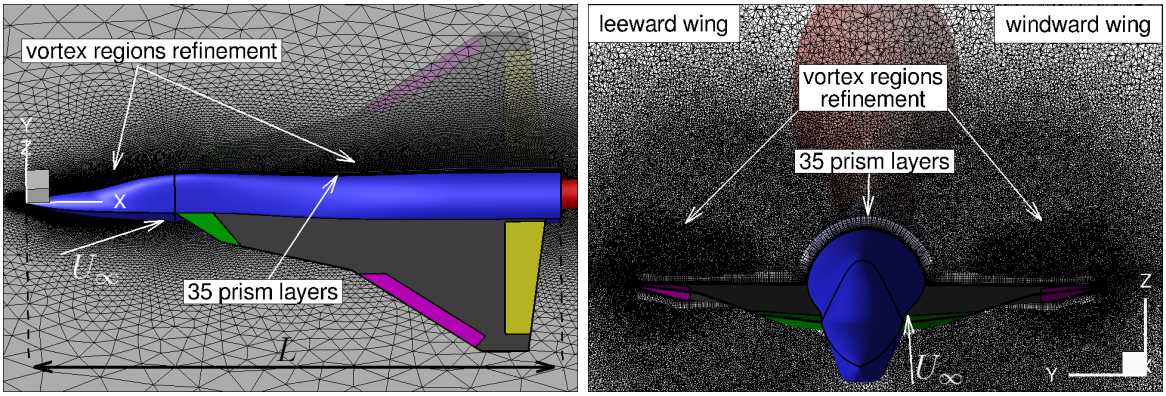

(a) Slice plane $\eta = 0$ **(b)** Slice plane $\xi = 0.3$

Figure 6.1: ADS-NA2-W1 geometry and mesh (Di Fabbio et al., 2024a).

The unstructured mesh for investigating the ADS-NA2-W1 geometry comprises approximately 40 million cells. It is constructed with 35 prism layers close to the aircraft, with the first cell layer thickness is set such that $y^+ \approx 1$, and tetrahedral volumes in all other areas. The mesh is symmetric to the plane $y = 0$. The domain's size is 50 times the characteristic length L, the aircraft's characteristic length in the symmetry plane. The computational domain is discretized using an unstructured mesh with varying cell sizes. The mesh is most refined near the leading-edge, where the inboard and outboard vortex formation begins. The finest cells are approximately 0.001 times the characteristic length, $\Delta \approx 0.001L$. This cell refinement tracks the vortices to capture strong gradients and the resolved turbulent fluctuations in the scale-resolving simulations.

To provide insights into the grid resolution, the number of grid points inside the vortex diameter is analyzed at chord-wise location $\xi = 0.55$. The vortex diameter is computed from the vorticity distribution ω_x, as presented in Chapter 5. Figure 6.2 shows the qualitative vortex measures of the diameter, indicated by an arrow, and the computational domain at chord-wise location $\xi = 0.55$. The number of grid points inside the vortex diameter is equal to $N_{\omega_x} \approx 25$.

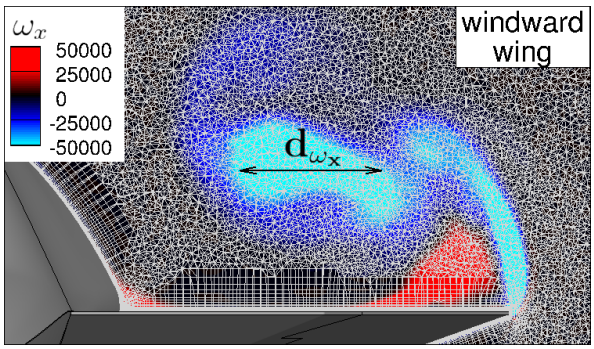

Figure 6.2: Vortex diameter (indicated by an arrow) based on the mean vorticity, IDDES results at chord-wise location $\xi = 0.55$.

6.1.1. Analysis of the mesh resolution

To enhance the understanding of the grid resolution, an analysis of essential parameters is conducted. This analysis is performed in a manner similar to that described in Chapter 5 for the VFE-2 delta wing. These considerations are based on the results obtained using the IDDES model, which necessitates the highest level of spatial and temporal accuracy. Furthermore, they are focused on the windward side of the wing, which exhibits more challenging flow conditions.

To demonstrate that the current mesh resolution is adequate for resolving a major part of the turbulence spectrum, the LES Index of Resolution Quality is illustrated in Fig. 6.3. The LES_{IQ_ν} parameter is introduced in Chapter 5 and the plots indicate that the spatial resolution within the vortex region is adequate, exhibiting still acceptable values downstream of the vortex breakdown. Besides, the $LES_{IQ_\nu} \approx 0.7$ within the vortex sheet region at $\xi = 0.55$ indicate potential studies for refinement studies in future work. Additionally, the mean cell size over the hybrid length scale, $\Delta/\tilde{d}$, depicted in Fig. 6.3, maintains a value close to unity in the vortex core, indicating the mesh's capability to effectively capture and resolve turbulent flow structures. A potential for mesh refinement is suggested where the ratio exceeds unity near the wing apex and fuselage. The regions subject to these refinements are partially incorporated into RANS mode and are not expected to significantly impact the accuracy of the simulation results. Nevertheless, a mesh refinement could enhance the transition between RANS and LES modes, thereby mitigating the grey-area issue.

Finally, Fig. 6.3 presents the mean ratio of the hybrid length scale to the RANS length scale, denoted as $\tilde{d}/d$. It elucidates the transition in the IDDES approach from RANS to LES modes. Near-wall regions, governed entirely by the RANS mode, show a ratio approaching unity. Conversely, the development of the vortex occurs within the LES domain. The transition between the two modes highlights the grey-area issue, as the vortex formation initially occurs in near-wall layers modeled by the RANS mode. The challenges associated with the grey-area, its impact on the results, and potential mitigation strategies have been extensively analyzed in the literature (Peng and Jirasek, 2016).

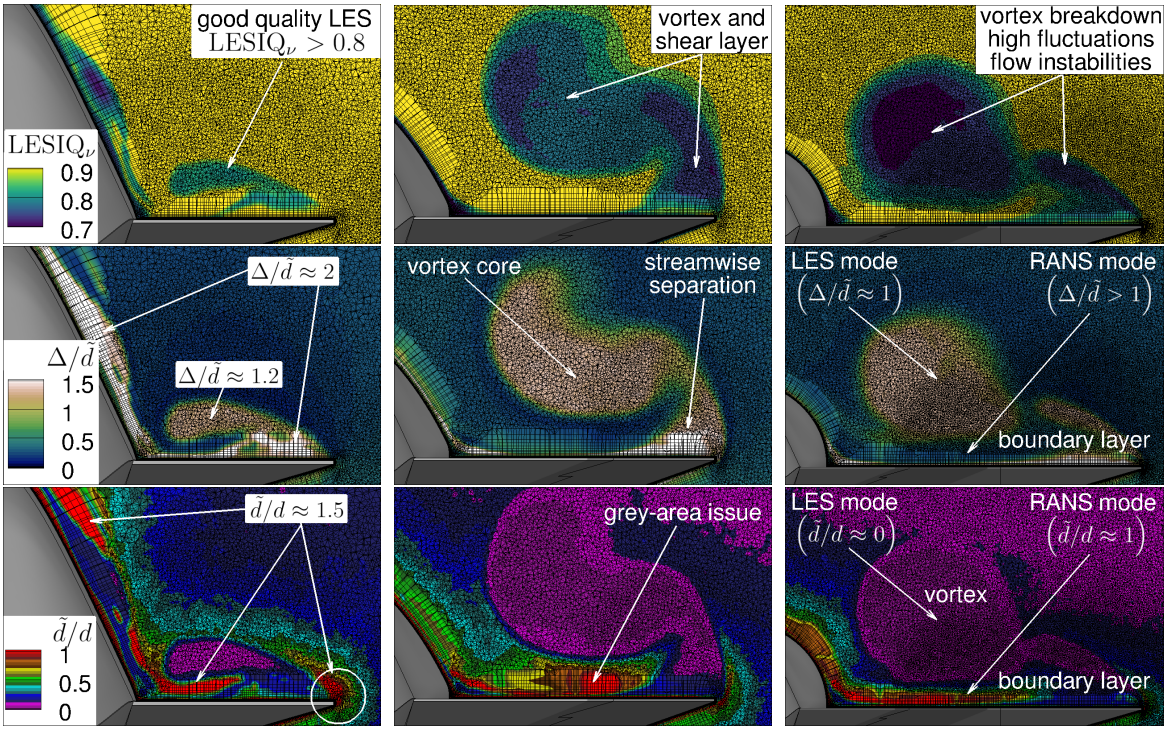

Figure 6.3: Mean LES_{IQ_ν}, mean cell size over hybrid length scale, and mean hybrid over RANS length scale, IDDES results at ξ = 0.35, 0.55, 0.75 (Di Fabbio et al., 2024a).

Considering the computational demands and challenges associated with conducting a mesh convergence study for the HRL approach, and building upon the previous analysis performed on the VFE-2, the mesh configuration is deemed appropriate for a LES within the vortex region.

6.1.2. Mesh convergence study

Three additional grid levels are considered for the SAnegRC-based URANS simulations to analyze grid effects. This approach balances computational feasibility with the need for meaningful resolution analysis. The lift and pitching moment coefficients are compared. Table 6.1 summarizes the main mesh characteristics and the values of the aerodynamic coefficients.

Table 6.1: Meshes details and aerodynamic coefficients (Di Fabbio et al., 2022d).

Mesh Acronym	Finest Cell Size	Tot. Points	C_L	C_{m_y}
3M	0.004 L	3 million	1.122	0.0025
13M	0.002 L	13 million	1.161	-0.015
35M	0.001 L	35 million	1.149	-0.013
40M (reference)	0.001 L	40 million	1.146	-0.011

Figure 6.4 shows the absolute deviation of the aerodynamic coefficients with respect to the 40M mesh for which results are presented. Even if the 35M mesh is already adequate to perform URANS, it is further refined to build the 40M mesh that is used to perform the simulations for both approaches, in order to mitigate any influence of the mesh between URANS and scale-resolving simulation outcomes.

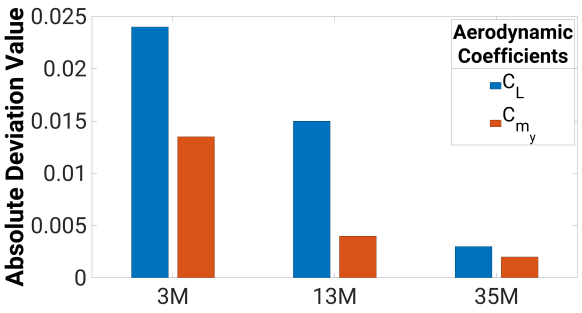

Figure 6.4: Absolute deviation bar plots (Di Fabbio et al., 2022d).

6.1.3. Numerical setup and solution techniques

Drawing on the experience gained from the VFE-2 investigation, an implicit dual-time stepping approach employing a Backward-Euler/LUSGS implicit smoother is selected. The flux computation is performed with a central scheme. To stabilize the URANS runs, an artificial dissipation for the central scheme is added with the matrix dissipation method. However, in scale-resolving simulations, IDDES and SAS, the artificial dissipation is reduced to prevent excessive damping of the resolved turbulent structures. A (hybrid) low-dissipation low-dispersion discretization scheme (HLD2) and a vorticity-sensitive sub-grid filter scale, which enhances the development of turbulent structures on anisotropic meshes, is used for the IDDES runs. A low-dissipation discretization scheme (LD) is used in the SAS runs (Probst and Reuß, 2016).

In unsteady simulations, it is crucial to account for the time a fluid element takes to traverse the aircraft, which determines the requisite physical or computational time for a reliable solution. The CTU is computed as $L/U_\infty = 2000\mu s$, where L denotes the characteristic length, and U_∞ the free-stream velocity.

For URANS simulations, a time step size of $100\mu s$ is selected. To mitigate initial transients, ten CTUs are calculated preceding five flow-through times of time-averaging until reaching statistical convergence of the mean flow properties. In Hi-Fi simulations, the maximum allowed time step size is determined to resolve convective transport and accurately capture flow characteristics. The chosen time step size, $\Delta t = 1\mu s$, adequately resolves the time scales of the energy-containing eddies in the flow of interest, ensuring the convective CFL number remains below unity in the focus region (Spalart, 1997). The simulations are initialized with the URANS results to reduce the initial transient. Fifteen CTUs are computed to reach a statistically steady flow. Subsequently, another fifteen overflows are considered to calculate statistics of the flow properties.

The CFL number is depicted in Fig. 6.5. It slightly exceeds unity near the wing apex, where the highest velocities occur. Consequently, there is a rationale for further reducing the time step size in this region. However, to balance the accuracy of the simulations with computational efficiency, the current time step value is deemed sufficient, particularly considering the temporal and sensitivity studies performed for the VFE-2 delta wing in Chapter 5. Furthermore, the CFL number decreases significantly

downstream over the aircraft due to a reduction in axial velocity, suggesting the potential for an increased time step size in these regions. For future studies, a strategy combining two different time step sizes can be devised to accelerate scale-resolving simulations without compromising accuracy.

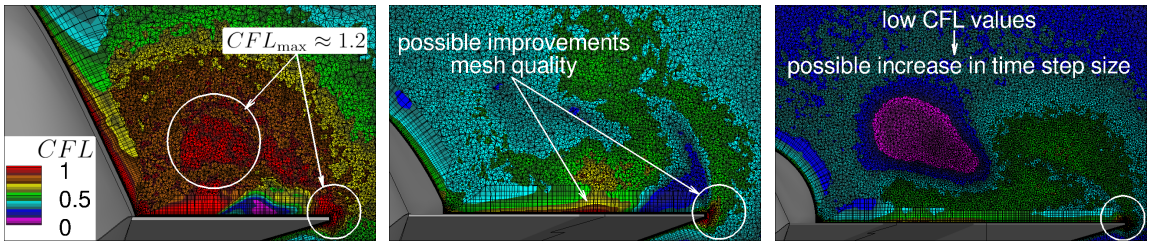

Figure 6.5: Mean convective CFL number, IDDES results at $\xi = 0.35, 0.55, 0.75$.

6.2. Vortex development: flow physics analysis

As introduced in Section 2.1 and further detailed in Chapter 5 regarding the VFE-2 delta wing, the generated vortex sheet of low aspect ratio delta wings separates at the swept leading-edge, roll-up to form a coherent vortex and induces a local low-pressure region on the suction side, contributing to the overall lift. The phenomenon known as vortex lift reaches a limiting AoA at which the vortex breaks down, characterized by an abrupt change in flow topology where the flow decelerates and diverges. This section presents the vortex development by varying the angle of attack. In particular, a relation to the discussion on vortex development can be identified, as detailed in Section 2.1.2 for the VFE-2 delta wing. The three angles of attack analyzed are categorized into distinct flow regimes (discussed in Section 6.3) and a detailed examination of the flow physics is provided.

The flow pattern of the ADS-NA2-W1 test case is further complicated by the presence of vortex merging, caused by multiple sweep angles. The side-slip angle of $\beta = 5°$ introduces an asymmetry in the flow, generating two distinct flow conditions on the leeward and windward wings. Moreover, the transonic condition creates a supersonic area over the wing, leading to various shock waves that interact with the vortices and trigger the vortex breakdown. To elucidate these phenomena, simulation results at $\alpha = 20°$, $24°$, and $28°$ are analyzed with comparisons made between URANS, Hi-Fi results, and experimental data (where available).

6.2.1. Vortex breakdown on the windward wing: $\alpha = 20°$

The analysis of vortex development commences with the second flow regime, as highlighted in Section 6.3. Specifically, numerical results for $\alpha = 20°$ obtained from employing the SAnegRC-based URANS and SAneg-based IDDES approaches are presented.

Instantaneous flow features

Over the aircraft, the flow undergoes primary separation at the leading-edge and subsequently rolls up to form a stable, separation-induced leading-edge vortex. As shown in Figs. 6.6 and 6.7, two well-distinguished vortices are present on the leeward wing, while two less distinguished (more merged) vortices are observed on the windward wing. The two vortices (outboard and inboard) are generated corresponding to the increasing sweep angles on the first and third leading-edge sections. The primary vortex induces reattached flow over the wing, and the span-wise flow under this primary vortex separates a second time to form a counter-rotating secondary vortex outboard of the primary one.

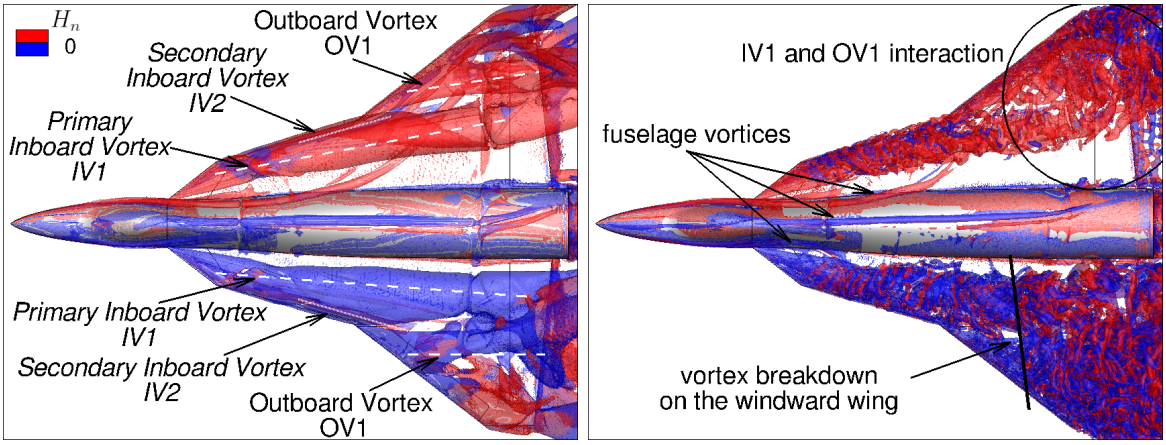

Figure 6.6: Q-criterion instantaneous iso-surface with flood contour by instantaneous normalized helicity, comparison between SAnegRC-based URANS (left) and SAneg-based IDDES (right) results with $\alpha = 20°$ and $\beta = 5°$.

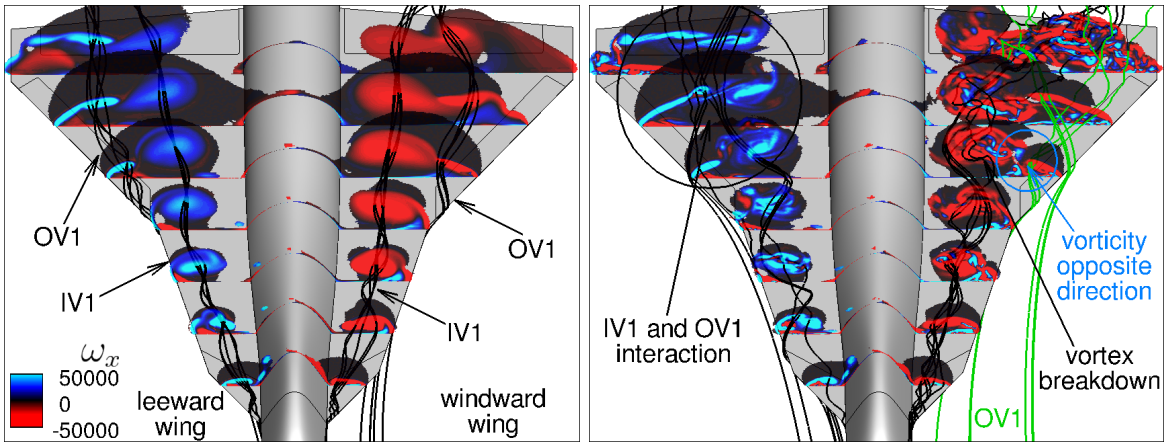

Figure 6.7: Instantaneous x-vorticity and vortex stream-traces, comparison between SAnegRC-based URANS (left) and SAneg-based IDDES (right) results with $\alpha = 20°$ and $\beta = 5°$.

Figure 6.6 illustrates the vortices using the Q-criterion iso-surface, which is colored by the normalized helicity, H_n, with positive and negative values represented in red and blue, respectively. The sense of rotation of a vortex is determined by the sign of the helicity, enabling the differentiation between counter-rotating vortices. This distinction allows for the separation of primary from secondary vortices (Levy et al., 1990), identified with the numbers 1 and 2. The inboard secondary vortex on both wings is located beneath the primary vortex. The flow under the vortices induces significant upper surface suction, resulting in large vortex-induced lift increments. Two fuselage vortices, rotating in opposite directions, are also observed, originating at the apex of the aircraft fuselage.

The onset of the inboard vortex is visualized in Fig. 6.7 from the vortex stream-traces shown together with instantaneous x-vorticity. The inboard vortex formation starts immediately downstream of the wing apex. The particles contained in the separated shear layer emanating from the leading-edge at the apex form the core of the inboard vortex and travel along the wing at very high speed. The inboard vortex then grows in size because it is fed by the shear layer all along the wing. This flow reinforces the main core by rotating around it and feeding it with kinetic energy. In this way the vortex is sustained, remains coherent and the axial velocity increases. However, this process stops at the second sweep angle increment. Indeed, the same mechanism discussed for the inboard vortex can also be seen for the outboard vortex, whose core is mainly caused by the shear layer separation at the second sweep angle increment. This leads to the conclusion that resolving separation and turbulence close to the wing apex is of primary importance for delta wing flow simulations.

On the leeward wing near the trailing-edge, as depicted in Fig. 6.7, two vortex cores are observed to be stacked atop each other, accompanied by a large separation zone near the leading-edge. An energy exchange between the vortices within the turbulent structure is noted, wherein the outboard vortex loses kinetic energy, potentially feeding and stabilizing the inboard vortex. As evidenced by the streamlines, the IDDES outcomes predict a stronger vortex-vortex interaction that leads to vortex merging.

The vortices break down within the second half of the aircraft on the windward wing. Downstream of the breakdown, the flow becomes incoherent and turbulent, as depicted only by the HRL outcomes. Examining Fig. 6.6, a preliminary qualitative assessment of the turbulence resolution in the LES regions is provided. Turbulent fluctuations within the vortices are evident, with the resolution level deemed adequate for the aims of this investigation. Larger turbulent structures are resolved by the grid, especially on the windward wing. Furthermore, Fig. 6.7 illustrates how the smaller scales are captured and resolved by the IDDES following the breakdown, showcasing the onset of turbulence fluctuations. Upstream of this phenomenon, smaller turbulence scales are not resolved, but there is no rationale for their presence, since, in principle, a coherent vortex does not constitute a turbulent phenomenon. This HRL behavior becomes even more evident when analyzing the analogous plot presented in Section 6.2.2, which features an angle of attack of 24°.

As illustrated in Fig. 6.8, where the instantaneous iso-surface of the x-direction pressure gradient, ∇p_x, is shown with a flood contour by instantaneous Mach number, several

shock waves are present over the aircraft. The interaction between leading-edge vortices and shock waves, crucial for understanding flow physics at transonic conditions, needs detailed assessment due to its potential impact on vortex breakdown. A noteworthy difference between the two approaches is the effect of the highlighted shock wave in the IDDES results, which is not evident in the URANS outcomes. Across the shock wave, pressure, density, temperature, and entropy all increase, while Mach number, velocity, normal velocity component, and total pressure decrease. This indicates that the vortex core loses velocity and kinetic energy across the shock wave.

The shock wave, proximate to the leading edge, is identified as the lambda shock, and its interaction with the vortex core can induce the breakdown of the inboard vortex on the windward wing. This phenomenon is exclusively captured by the IDDES. Figure 6.8 also shows the reduction of the Mach number behind the shock in combination with the onset of chaotic structures indicative of vortex breakdown. Therefore, the breakdown in the transonic regime could then result from a shock-vortex interaction and an accurate prediction of the shock wave location is then crucial. This aspect is further addressed in Chapter 7, by comparing these results with additional two-equation model results, namely $k\omega$SST-based URANS and SAS.

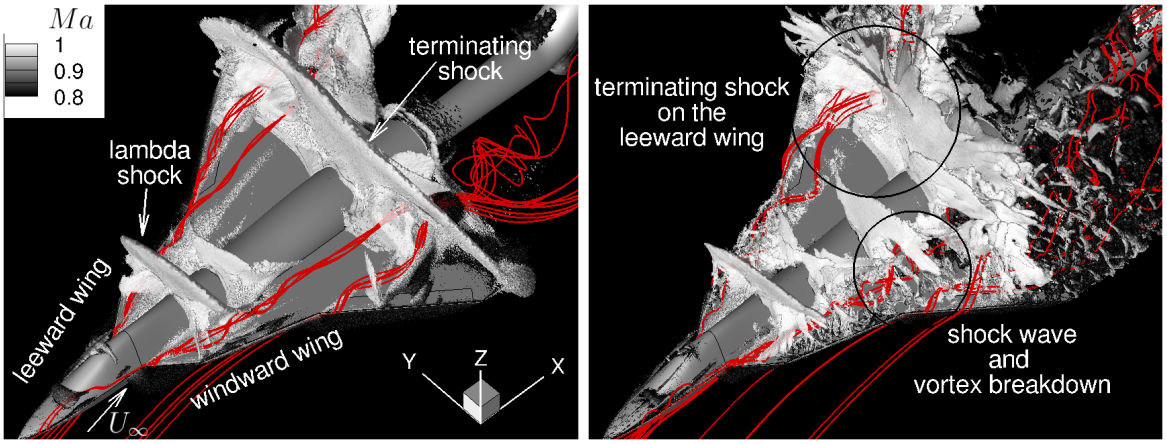

Figure 6.8: Instantaneous x-pressure gradient iso-surface with flood contour by instantaneous Mach number, comparison between SAnegRC-based URANS (left) and SAneg-based IDDES (right) results with $\alpha = 20°$ and $\beta = 5°$. Vortex stream-traces depicted in red.

Mean flow features

Fig. 6.9 depicts the mean surface coefficient of pressure on the aircraft. Three slice planes are extracted. The distribution of the mean surface coefficient of pressure, c_p, along the span-wise direction, and the mean normalized x-velocity, u/U_∞, contour at chord-wise positions $\xi = 0.35, 0.55, 0.75$ are presented in Fig. 6.10.

In the front part of the aircraft, the IDDES approach significantly enhances the results on both wings, as evidenced by the c_p at $\xi = 0.35$ in Fig. 6.10. The x-velocity contour plot at this location reveals that only the HRL approach is capable of capturing the

flow separation and the reversed flow, a phenomenon that could elucidate the superior prediction of the experimental data in this area. Nonetheless, the simulations struggle to accurately predict the flow physics proximate to the fuselage (around $-0.1 < \eta < 0.1$). The erroneous prediction of c_p near the fuselage is attributed to fuselage vortices, as indicated by the Q-criterion in Fig. 6.6. Given these vortices' proximity to the fuselage surface, they fall into the URANS region, which fails to resolve the turbulent flow accurately. Mesh refinement may ameliorate this inaccurate prediction. A detailed analysis of the HRL behavior, particularly how the hybrid model transitions from RANS to LES, is presented in Section 6.1.1.

The HRL approach captures the formation of the secondary vortex, particularly on the leeward wing at the chord-wise station $\xi = 0.55$. However, the accuracy is not as high as desired, with the negative coefficient of pressure being overestimated, as depicted in Fig. 6.10 ($0.45 < \eta < 0.35$). Furthermore, the same figure illustrates a better concordance between URANS results and experimental data on the windward wing, where the secondary vortex is accurately captured. The counter-rotating secondary vortex impacts the velocity field; the opposite sign of the vorticity field induces a negative x-velocity, leading to a reduction in the total x-velocity. This effect is observable in Fig. 6.10, near the leading-edge, where areas of low-speed flow are visible. In contrast, the IDDES outcomes predict a stream-wise separation region and the absence of the secondary vortex; a similar phenomenon observed in Chapter 5. At this location, the fuselage vortices are well-captured by the numerical outcomes, and they can also be visualized in the x-velocity contour plots. It is worth noting that other vortices are present below the aircraft, a flow region that is not investigated but can lead to potential new findings in further studies.

As previously mentioned, the onset of shear layer separation occurs in correspondence with the two sweep angles (φ_1 and φ_3), as illustrated in Fig. 2.8, on the first and third leading-edge sections. The interaction of the inboard and outboard vortices occurs in the rear part of the aircraft. In the HRL results, these two primary vortices are distinguishable in Fig. 6.10 at $\xi = 0.75$, where two peaks of axial velocity are located. The presence of two peaks of negative c_p in the experimental results for $0.4 < \eta < 0.8$ confirms the separate vortices, though their suction footprints are overestimated by the IDDES outcomes.

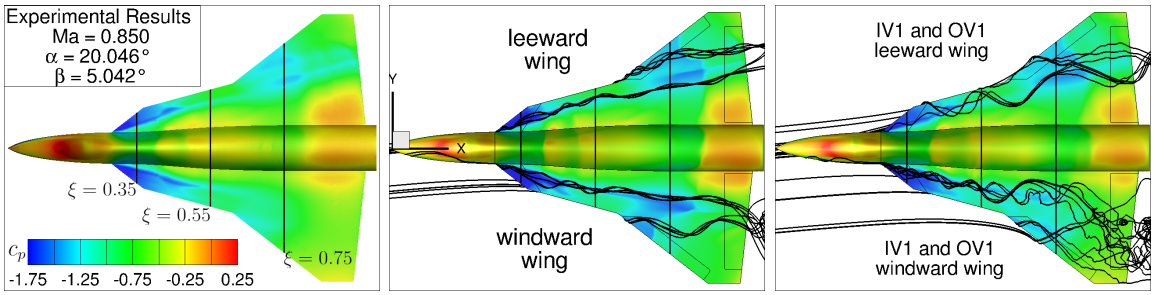

Figure 6.9: Mean surface coefficient of pressure, comparison between experimental data (left), SAnegRC-based URANS (middle) and SAneg-based IDDES (right) results with $\alpha = 20°$ and $\beta = 5°$. Vortex stream-traces depicted in black.

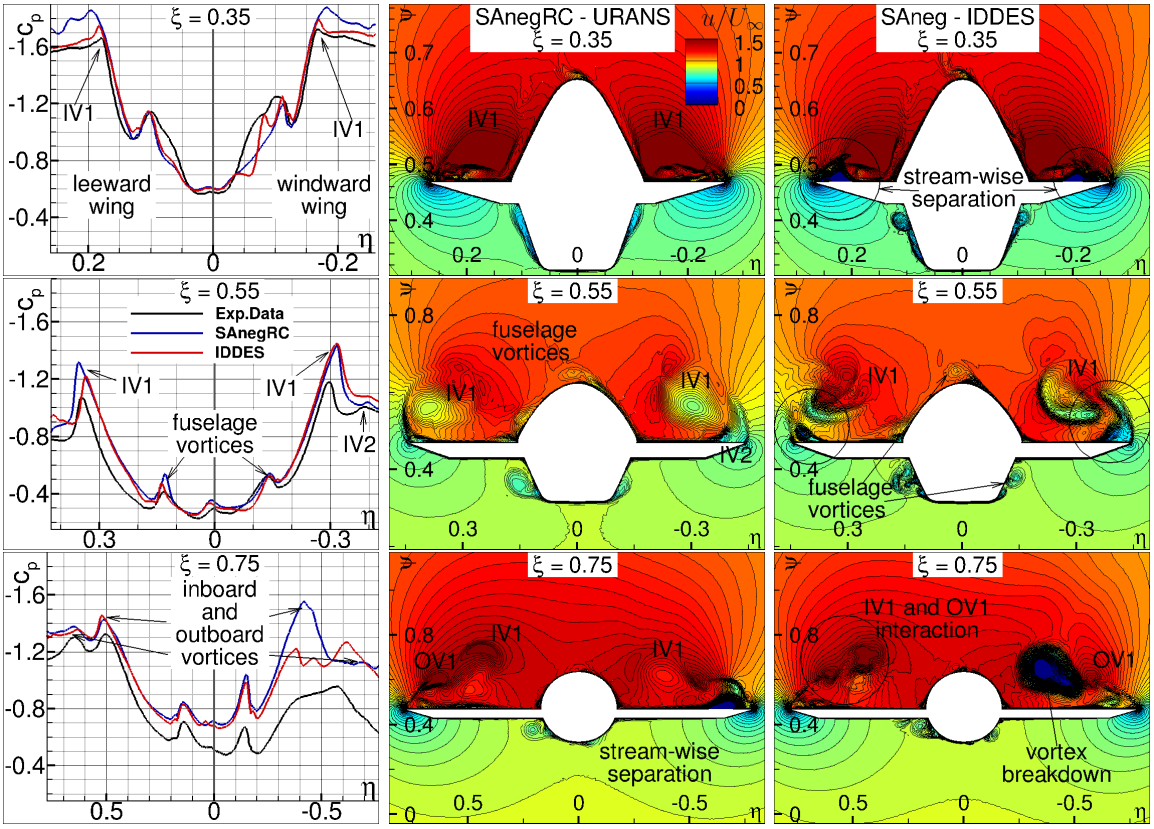

Figure 6.10: Mean surface coefficient of pressure and mean normalized x-velocity contour plots at chord-wise locations $\xi = 0.35, 0.55, 0.75$, comparison between experimental data, SAnegRC-based URANS and SAneg-based IDDES with $\alpha = 20°$ and $\beta = 5°$.

The scenario is different in the rear part of the windward wing, where the vortices break down, as discussed in the analysis of instantaneous flow features. The surface pressure coefficient in Fig. 6.10 at $\xi = 0.75$ indicates that vortex breakdown is observable in both experiment and IDDES data, albeit the suction is overestimated in the latter. The two vortices do not disintegrate simultaneously; the inboard vortex bursts first, followed by the breakdown of the outboard vortex. Indeed, the experimental data show the outboard vortex remaining coherent at location $\xi = 0.75$, evidenced by the negative peak of c_p for $\eta \approx -0.6$. The HRL outcomes predict the initial vortex breakdown, accompanied by an expansion of the vortex core and a sudden decrease in axial (and rotational) velocity. As demonstrated in Di Fabbio et al., 2022d, at chord-wise location $\xi = 0.85$, the HRL approach accurately replicate the breakdown of both main vortices, whereas the onset of vortex breakdown commences to manifest in the URANS results. The variation in the predicted onset of vortex breakdown is attributed to the upstream conditions of the vortex, with particular emphasis on the behavior of the secondary vortex. A theory underlying the mechanism of vortex breakdown is presented in Chapter 5, while Chapter 7 further elucidates this concept, advancing the understanding of vortex breakdown for improved RANS turbulence modeling.

6.2.2. Vortex breakdown fixed on the windward apex: $\alpha = 24°$

Figures analogous to those discussed in the previous section for $\alpha = 20°$ are herein presented for $\alpha = 24°$, corresponding to the third flow regime highlighted in Section 6.3. At $\alpha = 24°$, the vortex breakdown on the windward wing remains stationary at the wing apex, a finding further corroborated by the results observed at $\alpha = 28°$. Numerical results obtained from employing the SAnegRC-based URANS and SAneg-based IDDES approaches are presented.

Instantaneous flow features

As illustrated by the instantaneous Q-criterion iso-surface in Fig. 6.11, the inboard and outboard vortices are identified on the leeward wing, along with a burst vortex on the windward wing. The normalized helicity reveals that, on the leeward wing, the span-wise flow beneath the primary vortex undergoes a secondary separation, forming a counter-rotating secondary vortex outboard of the primary vortex.

The inboard and outboard vortices on the leeward wing are visualized in Fig. 6.12, as demonstrated by the vortex stream-traces alongside the instantaneous x-vorticity. Streamlines are particularly useful for identifying the core of leading-edge vortices, vortex-vortex interaction phenomena, and fuselage vortices. Comparing the outcomes depicted in Fig. 6.7 for $\alpha = 20°$ with results at $\alpha = 24°$, several observations emerge. Notably, the HRL approach predicts a weaker vortex-vortex interaction at $\alpha = 24°$. The streamlines of the two vortices no longer merge at the aircraft's rear. The inboard and outboard vortices appear also more separated in the x-vorticity contours, especially in the penultimate slice plane. These findings suggest that the vortex interaction theory, as discussed in Section 2.1.8, does not hold at high angles of attack on the leeward wing for the tested configuration under these flow conditions. Furthermore, fuselage vortices, absent at $\alpha = 20°$, become visible at higher angles of attack, suggesting increased strength due to the generated region of lower total pressure. These vortices originate from the airflow around the fuselage nose and are situated over the fuselage. Additionally, the IDDES outcomes indicate a more chaotic flow behavior on the rear side of the wing, especially near the leading edge. This observation can signify an increased vulnerability of the primary vortex, as discussed in Chapter 5.

On the windward wing, the HRL outcomes highlight the chaotic behavior of the burst vortex and the lack of coherent vortex formation from the shear layer emanating from the leading-edge. The shear layer emanating from the leading edge no longer rolls up to form a leading-edge vortex over the wing, but is instead transported downstream without inducing additional velocities on the wing surface. An immediate consequence of this phenomenon is an increase in pressure over the wing. This alteration significantly impacts the prediction of aerodynamic coefficients, a topic analyzed in Section 6.3. Moreover, a qualitative assessment of turbulence resolution within the turbulence-resolving areas reveals that turbulent fluctuations are clearly visible within the transported shear layer or burst vortex. The resolution level appears then to be suitable for an IDDES computation, as it resolves even smaller turbulent structures within the grid. As also depicted by the instantaneous x-vorticity in Fig. 6.12, the presence of chaotic structures suggests that the burst vortex impacts the leeward wing

in the rear part of the aircraft, potentially affecting the accuracy of numerical outcomes on the opposite wing. Furthermore, this effect intensifies with the angle of attack, as demonstrated in Section 6.2.3. The SAnegRC-based URANS approach fails to accurately capture this process, erroneously predicting the presence of a vortex near the windward wing apex. This method appears to stabilize and promote the presence of a coherent structure, rather than accurately simulating turbulent behavior.

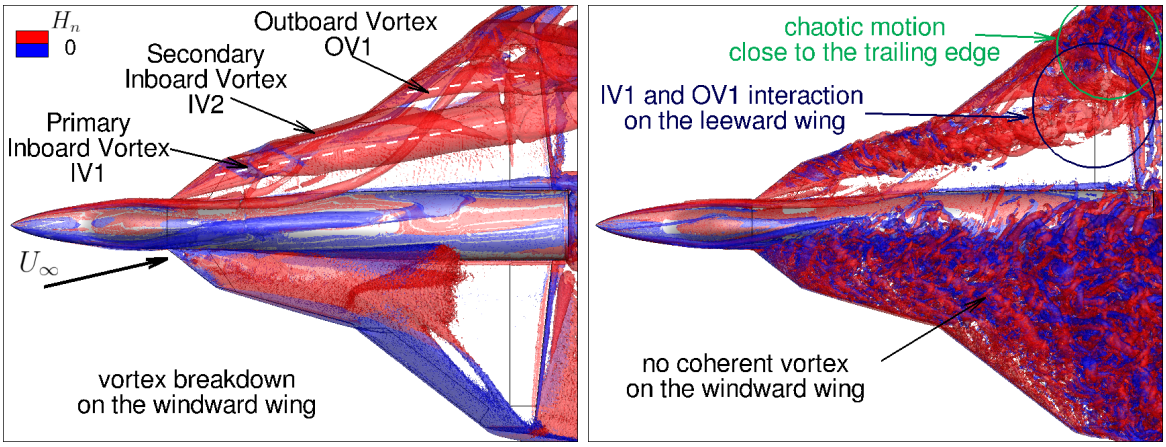

Figure 6.11: Q-criterion instantaneous iso-surface with flood contour by instantaneous normalized helicity, comparison between SAnegRC-based URANS (left) and SAneg-based IDDES (right) results with $\alpha = 24°$ and $\beta = 5°$.

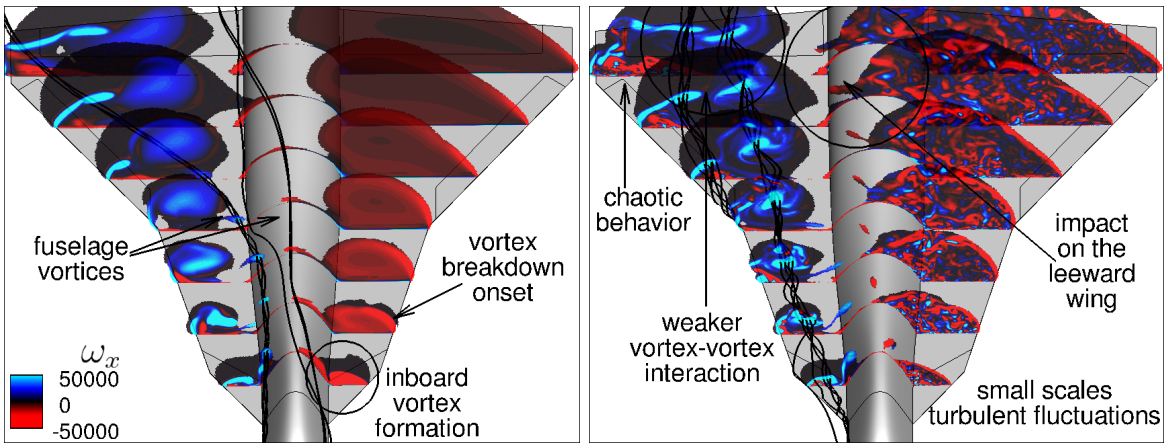

Figure 6.12: Instantaneous x-vorticity and vortex stream-traces, comparison between SAnegRC-based URANS (left) and SAneg-based IDDES (right) results with $\alpha = 24°$ and $\beta = 5°$.

Fig. 6.13 shows the instantaneous x-pressure gradient iso-surface, which reveals several shock waves over the leeward wing. In this scenario, the shock waves do not induce a vortex breakdown but interact with the inboard vortex core on the leeward wing. This interaction results in a reduction of velocity and suction footprint over the wing, as

discussed in Chapter 5. Furthermore, the vortex stream-traces depicted in Fig. 6.13 lead to additional conclusions. It is evident how the fuselage vortices converge toward the leeward wing and appear to interact with the primary vortices, thereby influencing the overall flow behavior. This observation is crucial for the analysis of the outcomes at $\alpha = 28°$. Moreover, the IDDES findings illustrate how the terminating vortex moves downstream over the wing, compared to its location at $\alpha = 20°$. It is found precisely at the point where the inboard and outboard vortices merge, specifically near the trailing edge, as confirmed by Fig. 6.14. At $\alpha = 20°$, the vortices interact and merge upstream over the wing. This interaction, stronger at $\alpha = 20°$, results in the terminating shock also moving upstream. This phenomenon can likely be attributed to the increased velocity generated by the merging of vortices over the wing.

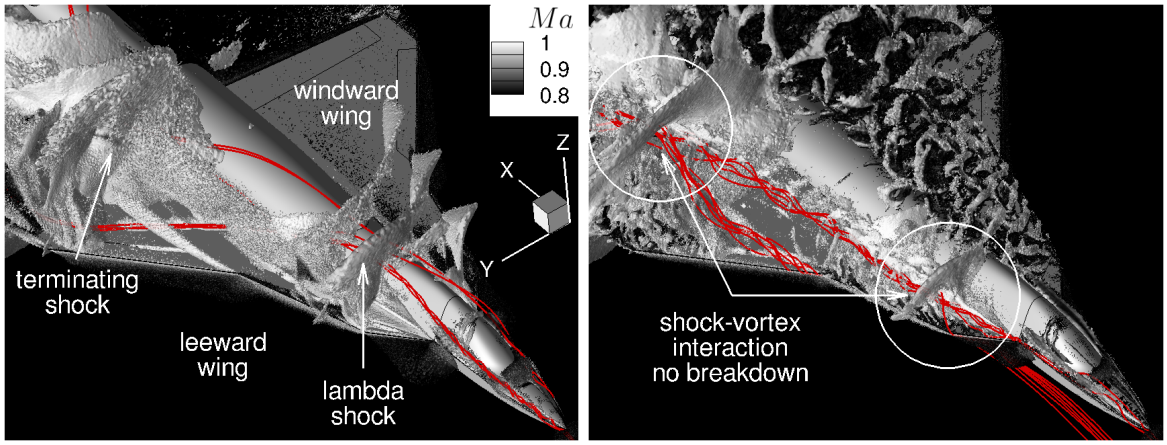

Figure 6.13: Instantaneous x-pressure gradient iso-surface with flood contour by instantaneous Mach number, comparison between SAnegRC-based URANS (left) and SAneg-based IDDES (right) results with $\alpha = 24°$ and $\beta = 5°$. Vortex stream-traces depicted in red.

Mean flow features

Figures 6.14 and 6.15 illustrate the surface coefficient of pressure over the aircraft. Regarding the leeward wing, the front part of the aircraft demonstrates how the IDDES approach enhances the simulation results. The normalized mean x-velocity, u/U_∞, contour plot in Fig. 6.15 at the chord-wise location $\xi = 0.35$ indicates that only the IDDES approach is capable of capturing the separation and reversed flow. A similar observation was made for the test case with $\alpha = 20°$, highlighting a significant difference between URANS and HRL methods in predicting the suction footprint in the front part of the wing. Accurately predicting this flow behavior is crucial, and Chapter 7 provides a detailed elucidation of the underlying reasons.

The HRL results successfully capture the secondary vortex formation, but the coefficient of pressure is still overestimated, as shown in Fig. 6.15 at $\xi = 0.55$ near the leading-edge of the leeward wing ($\eta > 0.35$). Conversely, the URANS simulations fail to accurately capture the secondary vortex formation in the c_p distribution; this phenomenon is only depicted in the x-velocity contour plot. The HRL results reveal a

pronounced shock beneath the primary vortex, accompanied by multiple fuselage vortices around the aircraft, significantly influencing the flow field. The location of the fuselage vortices differs from that observed at $\alpha = 20°$, leading to the consideration that it is influenced by the angle of attack.

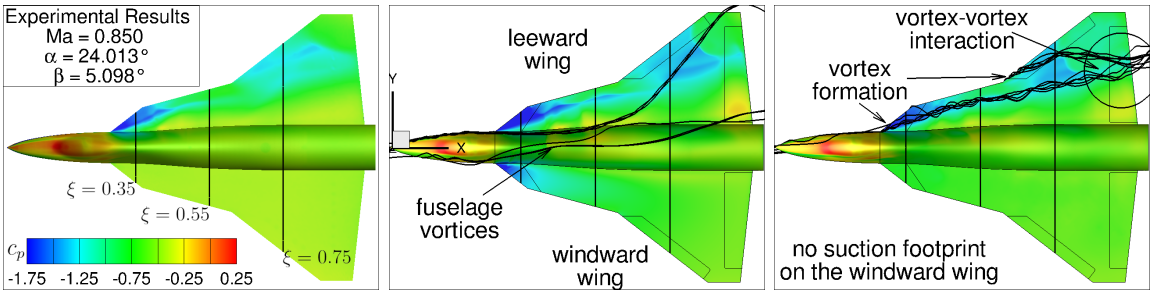

Figure 6.14: Mean surface coefficient of pressure, comparison between experimental data (left), SAnegRC-based URANS (middle) and SAneg-based IDDES (right) results with $\alpha = 24°$ and $\beta = 5°$. Vortex stream-traces depicted in black.

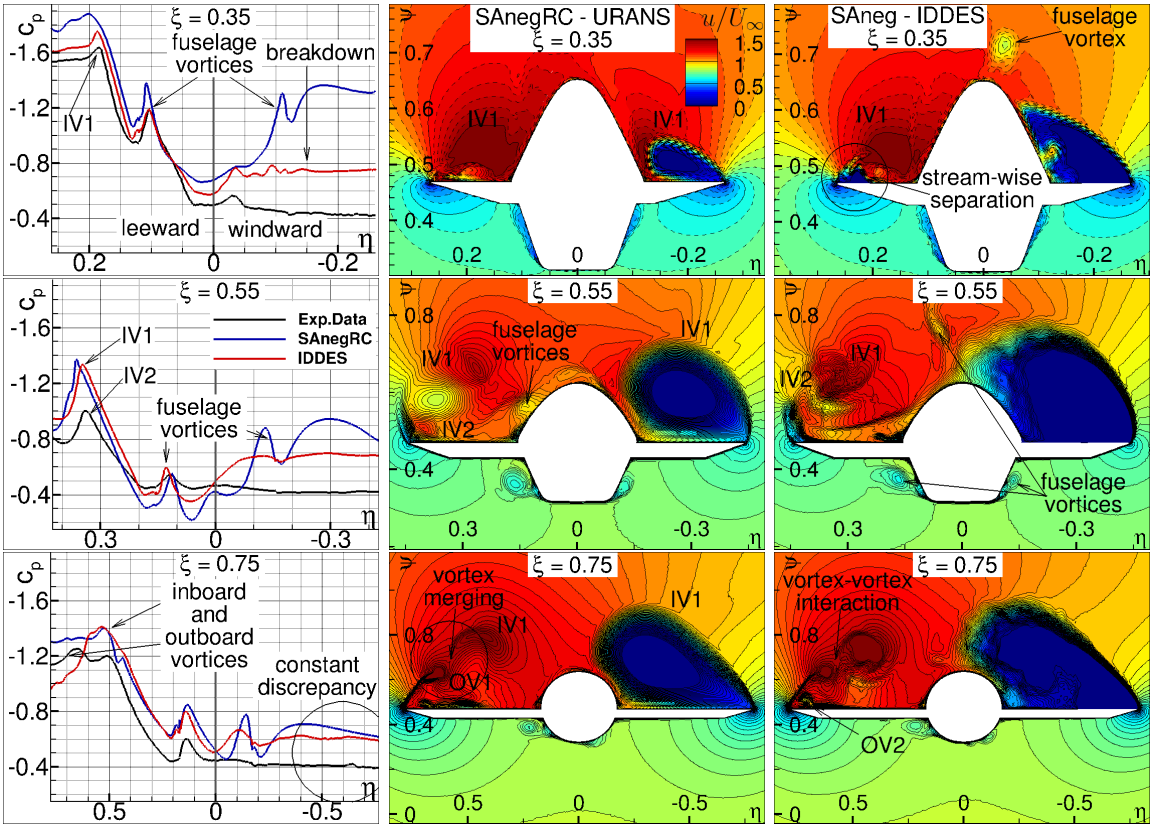

Figure 6.15: Mean surface pressure coefficient and normalized mean x-velocity contour plots at chord-wise locations $\xi = 0.35$, 0.55, 0.75, comparison between experimental data, SAnegRC-based URANS and SAneg-based IDDES with $\alpha = 24°$ and $\beta = 5°$.

Considering the IDDES results, the inboard and outboard vortices are indistinguishable and interact with each other at $\xi = 0.75$, where only a single peak in the c_p is observed. However, these vortices are distinguishable in the velocity range, complicating the interpretation of numerical results. Examination of the experimental confirm the presence of two distinct vortices at this location. The pressure coefficient reveals that the inboard vortex appears weaker and the outboard vortex stronger, compared to those observed at $\alpha = 20°$. The observed energy exchange between the vortices is hypothesized to underlie this phenomenon. This vortex-vortex interaction mechanism is contingent upon the angle of attack. At a lower angle of attack ($\alpha = 20°$), the inboard vortex, experiencing a gain in kinetic energy (manifested as an increase in velocity within the core), is theorized to be sustained by energy from the outboard vortex. This process stabilizes and accelerates the inboard vortex, maintaining its stability. However, at higher angles of attack, this interactive mechanism diminishes in efficacy, leading to a propensity for the inboard vortex to breakdown in the rear portion of the wing. The same consideration is achieved by analyzing the instantaneous flow features.

The SAnegRC-based URANS simulations inaccurately predict the pressure distribution over the windward wing, especially near the wing apex. While capturing the formation of a leading-edge vortex, this approach fails to accurately replicate the actual flow behavior, which is characterized by high turbulence and chaotic motion, as previously discussed. In contrast, the IDDES approach successfully predicts the shear layer emanating from the leading-edge and its chaotic transport downstream over the wing, albeit with a slight overestimation of the intensity of the suction footprint, as particularly shown in Fig. 6.15. The enhanced simulation of the burst vortex over the windward wing in the IDDES outcomes substantially improves the prediction of the pitching moment coefficient, as discussed in Section 6.3. It is also noteworthy that the region impacted by vortex breakdown appears more extensive in the IDDES results, which additionally predict a fuselage vortex at $\xi = 0.35$ on the windward wing. This vortex is located between the fuselage and the turbulent flow following the breakdown.

Particularly on the windward wing, the discrepancy between the IDDES and the experimental suction footprints is nearly constant. The IDDES approach entails significant approximations and assumptions regarding the resolved turbulent scales, and this constant disparity could be attributed to the high energy content of the unresolved scales of turbulence. A grid refinement study, aimed at enhancing the grid resolution, might yield improved IDDES results. Nevertheless, as discussed in Chapter 2.1.6, studies by Konrath et al., 2006, 2013 indicate that the PSP suction peak heights are underestimated due to temperature effects in certain VFE-2 test campaigns. Consequently, this issue cannot be completely disregarded.

Furthermore, a detailed analysis of the surface pressure coefficient at $\xi = 0.75$ reveals how the URANS results converge towards the IDDES results in terms of suction footprint prediction on the windward wing. This issue is less pronounced in the $k\omega$-based URANS outcomes analyzed for $\alpha = 28°$ in Section 6.2.3. The SA-based simulations appear then to have an inherent limitation in accurately capturing this type of flow behavior. Analysis of the SAnegRC-based URANS outcomes reveals anomalous flow behavior between the vortex breakdown region and the aircraft surface on the windward

wing. A thin layer within the structured grid, where turbulence is unpredicted and the flow remains attached to the surface, is observed. This behavior likely depends on the SA turbulence model formulation. Specifically, a new formulation of the destruction term, incorporating a different wall treatment, could be beneficial for improving the numerical results. Indeed, the issue appears to originate in the boundary layer, then in the treatment of the turbulence variable near the surface.

6.2.3. Vortex breakdown on the leeward wing: $\alpha = 28°$

The analysis of vortex development progresses to the fourth flow regime, as outlined in Section 6.3, with a detailed discussion of the outcomes at $\alpha = 28°$. Numerical results derived from the $k\omega$SST-based URANS and SAS approaches are presented. The IDDES approach has not been applied to the $\alpha = 28°$ test case, owing to the overall superior predictive performance of the two-equation models, a topic further elaborated in Chapter 7.

Instantaneous flow features

Figure 6.16 shows instantaneous surfaces from Q-criterion colored by Mach number. No coherent vortices are present on the windward wing. By a rough and qualitative assessment of the resolution of turbulence in the turbulence-resolving areas, turbulent fluctuations are clearly visible in the transported shear layer or burst vortex and the level of resolution seems to be appropriate for an SAS computation, since even smaller turbulent structures appear to be resolved by the grid, as corroborated by Fig. 6.17. The chaotic structures captured by SAS show how the burst vortex affects also the leeward wing in the aft part of the aircraft.

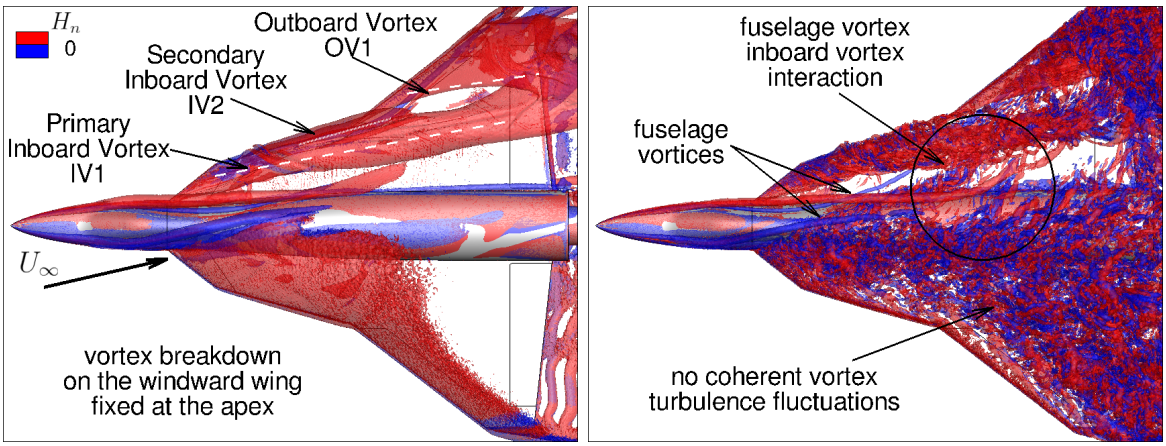

Figure 6.16: Q-criterion instantaneous iso-surface with flood contour by instantaneous normalized helicity, comparison between $k\omega$SST-based URANS (left) and SAS (right) results with $\alpha = 28°$ and $\beta = 5°$.

Vortex breakdown on the leeward wing is illustrated only through the SAS outcomes in Fig. 6.17. The URANS results do not predict this phenomenon. The x-vorticity

undergoes a change in sign, and a chaotic motion becomes visible, replacing the previously coherent vortex structure. Specifically, only the breakdown of the inboard vortex is predicted, confirming it as the first vortex to undergo bursting. Conversely, the outboard vortex appears to remain coherent.

Figure 6.17 illustrates also the fuselage vortices. Their formation is influenced by both the side-slip angle and the angle of attack, with their strength and size increasing at higher angles of attack. The fuselage vortices align with the direction of the free-stream flow and progress towards the leeward wing, significantly impacting the flow dynamics in this region. Notably, the interaction between the fuselage and the leading-edge vortex on the leeward side undergoes profound changes, as the leeward fuselage vortex eventually merges with the inboard leading-edge vortex. As corroborated by Fig. 6.18, this merging may be attributed to the occurrence of vortex breakdown. The vortex stream-traces depicted in Fig. 6.18 unequivocally illustrate the merging of the fuselage vortex with the inboard vortex, followed immediately by vortex breakdown. Furthermore, there is no observable interaction between the inboard and the outboard vortex at this angle of attack, substantiating the theory that vortex interaction on the leeward wing becomes less effective when the AoA is increased from 20° to 28°.

Furthermore, Fig. 6.17 illustrates that the vortex sheet becomes increasingly turbulent at higher angles of attack, influencing the formation and stability of the secondary vortex. Additionally, a more pronounced stream-wise flow separation is predicted near the leading edge on the rear leeward wing at $\alpha = 28°$, compared to that observed at lower angles, highlighting the increased vulnerability of the vortices.

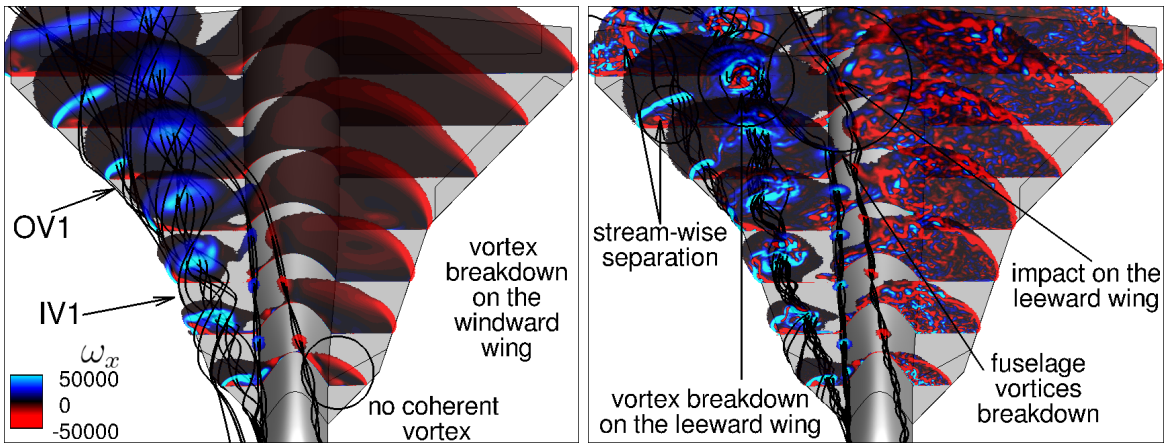

Figure 6.17: Instantaneous x-vorticity and vortex stream-traces, comparison between $k\omega$SST-based URANS (left) and SAS (right) results with $\alpha = 28°$ and $\beta = 5°$.

The shock waves occurring over the aircraft on the leeward wing are depicted in Fig. 6.18. In the SAS outcomes, the terminating shock moves in correspondence with the vortex breakdown location. This position, therefore, differs from that predicted at $\alpha = 24°$. However, in both cases, the shock occurs upon the merging of two vortices: at $\alpha = 24°$, it involves the inboard and outboard vortices, whereas at $\alpha = 28°$, it is between the inboard and fuselage vortices. Furthermore, both approaches predict the

interaction of the lambda shock with the inboard vortex on the leeward wing, and the location of this shock appears to remain consistent across test cases at various angles of attack. Therefore, its position is primarily determined by the wing geometry and the free-stream Mach number.

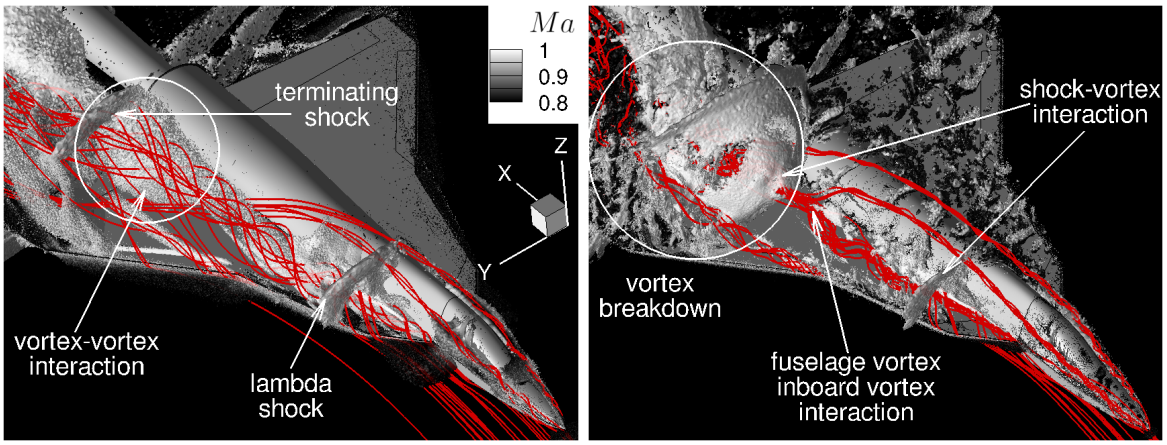

Figure 6.18: Instantaneous x-pressure gradient iso-surface with flood contour by instantaneous Mach number, comparison between $k\omega$SST-based URANS (left) and SAS (right) results with $\alpha = 28°$ and $\beta = 5°$. Vortex stream-traces depicted in red.

Mean flow features

Figures 6.19 and 6.20 depict the surface coefficient of pressure across the aircraft. The stream-wise separation is observed at $\xi = 0.35$ on the leeward wing, a phenomenon that was previously documented at $\alpha = 20°$ on the windward wing. Analysis of the surface pressure coefficient reveals that a distinction between the URANS and SAS outcomes lies in the secondary peak at $\xi = 0.55$, where the SAS outcomes predict a more pronounced secondary vortex. This observation suggests that a distinct mechanism may be responsible for the vortex breakdown on the leeward wing.

The leeward wing breakdown is exclusively predicted at $\alpha = 28°$ according to the SAS outcomes, illustrating that the pressure coefficient peak associated with the inboard vortex vanishes at the chord-wise location $\xi = 0.75$. Concurrently, the x-velocity plot evidences reversed flow. The breakdown of the outboard vortex, occurring subsequent to that of the inboard vortex, leaves the c_p peak of the outboard vortex intact at $\xi = 0.75$ for $\eta \approx 0.6$. This is corroborated by the x-velocity contour plot, which depicts the velocity peak of the outboard vortex. In contrast, the URANS method fails to predict the breakdown, and two velocity peaks corresponding to the inboard and outboard vortices are observed at $\xi = 0.75$.

Additionally, as illustrated in the x-velocity plots in Fig. 6.20, the vortex shape is also dependent on the angle of attack. The kidney-shaped configuration anticipated under transonic conditions becomes more pronounced at higher angles of attack, which may indicate an increased vulnerability of the vortex to disturbances (Riou et al., 2010). Fig. 6.20 also demonstrates how the breakdown on the windward wing affects the flow fields on the leeward wing. Particularly, at $\xi = 0.55$, the SAS outcomes reveal the

fuselage vortex bursting on the leeward wing, where the turbulent flow merges with the chaotic motion from the windward wing. This phenomenon, not predicted by the URANS outcomes, may be associated with the breakdown experienced by the inboard vortex on the leeward wing. A similar behavior near the fuselage on the leeward wing is only visible in the URANS results at $\xi = 0.75$.

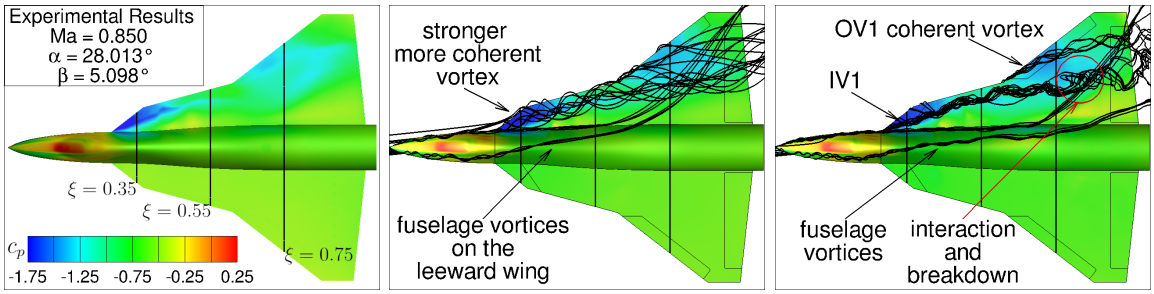

Figure 6.19: Mean surface coefficient of pressure, comparison between experimental data (left), $k\omega$SST-based URANS (middle) and SAS (right) results with $\alpha = 28°$ and $\beta = 5°$. Vortex stream-traces depicted in black.

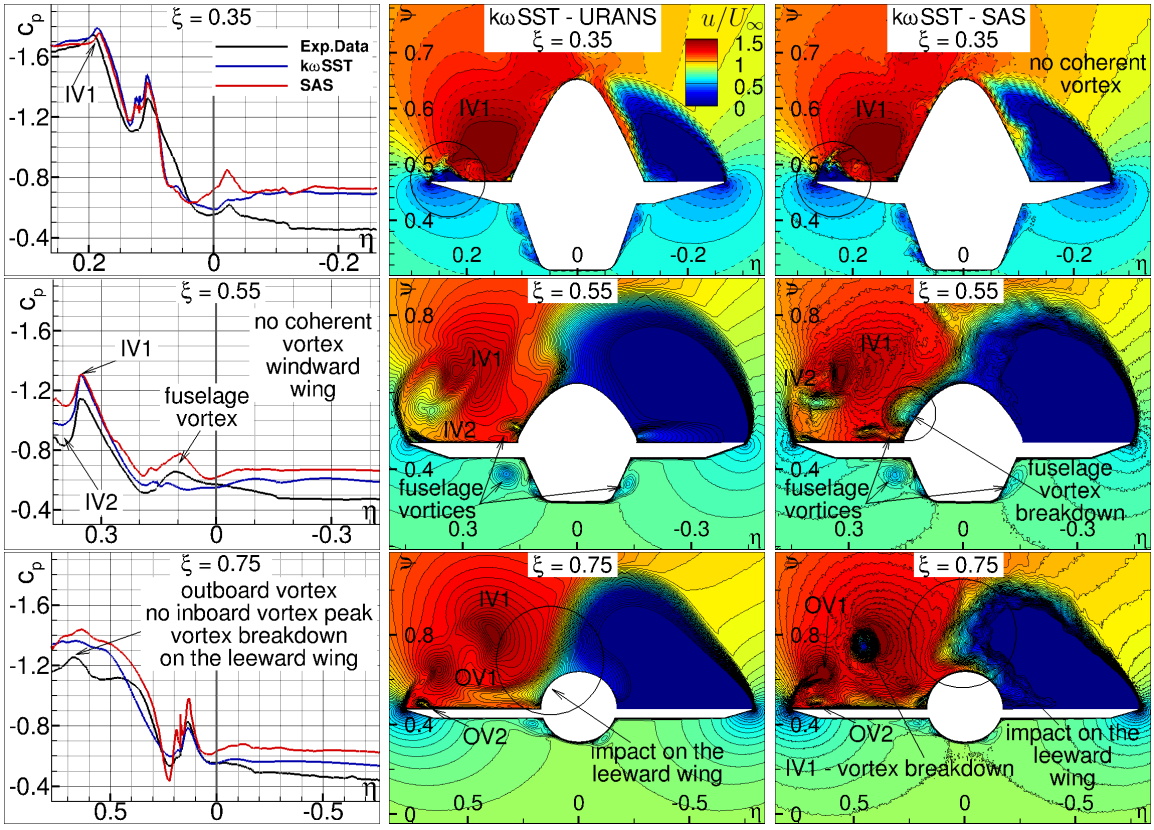

Figure 6.20: Mean surface coefficient of pressure and normalized mean x-velocity contour plots at chordwise locations $\xi = 0.35, 0.55, 0.75$, comparison between experimental data, $k\omega$SST-based URANS and SAS with $\alpha = 28°$ and $\beta = 5°$.

Both $k\omega$SST-based URANS and SAS simulations accurately predict the flow pattern over the windward wing, especially near the wing apex. They effectively capture the shear layer originating from the leading-edge and its subsequent chaotic transport downstream across the wing, albeit with a minor overestimation of the suction footprint's intensity. The $k\omega$SST model demonstrates then superior accuracy compared to the SAnegRC turbulence model in predicting such flow behavior. Possible explanations for the remaining discrepancies between the numerical predictions and experimental observations are outlined in Section 6.2.3, where they are examined in the context of the outcomes from the one-equation model.

6.3. Aerodynamic characteristic curves

Aerodynamic coefficients are dimensionless numbers that describe the aerodynamic forces and moments acting on a body in a fluid flow. These coefficients are crucial for analyzing and designing aerodynamic vehicles, such as aircraft, by allowing for comparisons across different sizes and flow conditions. Among these, the lift coefficient and the coefficients for rolling and pitching moments are of particular importance for the selected test case.

The lift, denoted by L_f to avoid confusion with the characteristic length defined as L, is the component of the total aerodynamic force perpendicular to the free-stream velocity vector, U_∞, and can be determined by integrating the pressure, p, over the aircraft's surface area, A_{ref}, considering the orientation of each surface element relative to the lift direction. The local lift force, dL_f, generated by a small surface element dA_{ref} from the local pressure difference and its orientation can be related back to the pressure coefficient and the dynamic pressure. The total lift is obtained by integrating these local contributions over the entire surface as follows

$$L_f = \iint_{A_{ref}} dL_f \; dA_{ref} = \iint_{A_{ref}} (p - p_\infty)\cos(\alpha) \; dA_{ref} = \iint_{A_{ref}} C_p \frac{1}{2}\rho_\infty U_\infty^2 \cos(\alpha) \; dA_{ref}, \quad (6.1)$$

where α is the angle of attack of each surface element, and the $\cos(\alpha)$ term projects the force in the lift direction. The lift coefficient, C_L, is calculated by normalizing the lift force by the dynamic pressure of the free-stream, $\frac{1}{2}\rho_\infty U_\infty^2$, and the reference area A_{ref} of the aircraft as follows

$$C_L = \frac{L_f}{\frac{1}{2}\rho_\infty U_\infty^2 A_{ref}} \quad (6.2)$$

This methodology requires precise knowledge of the pressure distribution over the aircraft, attainable through experimental or CFD simulations. The lift coefficient is then a dimensionless number that quantifies the lift force generated by a body, acting perpendicular to the relative wind, relative to the fluid density around the body, the velocity of the fluid, and a reference area.

The pitching moment, M_y, is a moment about the lateral axis of the aircraft, influencing its pitch attitude. The sign of M_y indicates whether the moment tends to rotate the aircraft nose-up (positive) or nose-down (negative). Conversely, the rolling moment is

a moment about the longitudinal axis, impacting the aircraft's roll angle. The pitching and rolling moments are defined as follows

$$M_y = L_f \cdot d_y, \qquad \text{and} \qquad M_x = \left(F_{\text{left}} - F_{\text{right}}\right) \cdot d_x. \tag{6.3}$$

Here, d_y represents the distance (moment arm) from the center of gravity (CG) to the point where the lift force is applied (center of pressure, CP). F_{left} and F_{right} denote the aerodynamic forces on the left and right wings, respectively, and d_x refers to the distance from the aircraft's longitudinal axis to the points of force application. The rolling moment coefficient, C_{m_x}, and the pitching moment coefficient, C_{m_y}, are dimensionless quantities characterizing M_x and M_y, respectively, per unit dynamic pressure, aircraft span (b, for the rolling moment) or mean aerodynamic chord of the wing (c_{ac}, for the pitching moment), and reference area. These coefficients are pivotal for analyzing roll stability and control, as well as pitch stability and control effectiveness. They are defined as follows

$$C_{m_x} = \frac{M_x}{\frac{1}{2}\rho_\infty U_\infty^2 A_{ref} b}, \qquad C_{m_y} = \frac{M_y}{\frac{1}{2}\rho_\infty U_\infty^2 A_{ref} c_{ac}}. \tag{6.4}$$

Figure 6.21 presents the lift coefficient curve, as well as the curves for the rolling and pitching moment coefficients, respectively. The experimental data, according to Hövelmann et al., 2020, are plotted in comparison with the numerical results. This comparison reveals interesting behavior of the force and moment coefficients, from which several conclusions can be drawn. Four distinct regimes can be identified.

1. $\alpha \leq 17.5°$, no vortex breakdown. Within this range, the lift coefficient increases almost linearly with AoA, the pitching moment is negative, stable, and decreases slowly, while the rolling moment remains nearly constant.

2. $17.5° \leq \alpha \leq 22.25°$, vortex breakdown on the windward wing. The vortex breakdown occurs on the windward, moving upstream from the trailing-edge to the leading-edge as AoA increases. This results in a gradual reduction of lift on the windward, which is not markedly evident in Fig. 6.21 because the lift on the leeward wing increases (though not with the same slope as before). This dual effect leads to a positive increase in the rolling moment. The pitching moment initially increases due to the breakdown location near the trailing-edge, causing a reduction in lift in that specific area and, consequently, a nose-up pitching of the aircraft. This effect stabilizes into a plateau of the pitching moment coefficient as the phenomenon approaches the x-coordinate of the aerodynamic center. The test case with $\alpha = 20°$ falls into this regime, with results presented in Section 6.2.1.

3. $22.25° \leq \alpha \leq 27.5°$, vortex breakdown fixed on the windward apex. At $\alpha \approx 22.25^{\circ}$, the vortex breakdown on the windward reaches the leading-edge apex and remains fixed in that position. This condition are confirmed by simulation results at $\alpha = 24°$ in Section 6.2.2. This leads to abrupt changes in the aerodynamic coefficients, with a significant drop in the lift and pitching moments, and a drastic increase in the rolling moment. Within this regime, also referred to as the post-stall regime, the shear layer emanating from the leading-edge no longer rolls up to

form a leading-edge vortex over the wing but is transported downstream without inducing additional velocities on the wing surface. As AoA increases, the lift begins to rise again due to the suction footprint on the leeward wing, with no significant changes in the integral moment coefficients.

4. $\alpha \geq 27.5°$, vortex breakdown on the leeward wing. Section 6.2.3 presents the numerical results at $\alpha = 28°$. The vortex breaks down on the leeward wing and moves upstream from the trailing-edge to the leading-edge with increasing AoA. The observations made for the windward wing are applicable to the leeward wing. The lift reduction in the rear part of the leeward wing leads to a nose-up pitching moment and a significant decrease in the rolling moment, which is of opposite sign compared to the consequence of stall on the windward wing.

The URANS and HRL results overestimate the experimental lift coefficient, but it is worth noting that the HRL results are closer to the experimental ones. The sole exception lies in the $k\omega$SST outcomes, which underestimate the lift coefficient at $\alpha = 20°$. A smooth transition between the URANS and HRL points is illustrated, but the phenomena occurring in between are not well documented in the literature and are discussed in Section 6.2. Although the sharp drop in the curve at $\alpha = 24°$ is not clearly predicted, the HRL results improve the prediction of the lift curve.

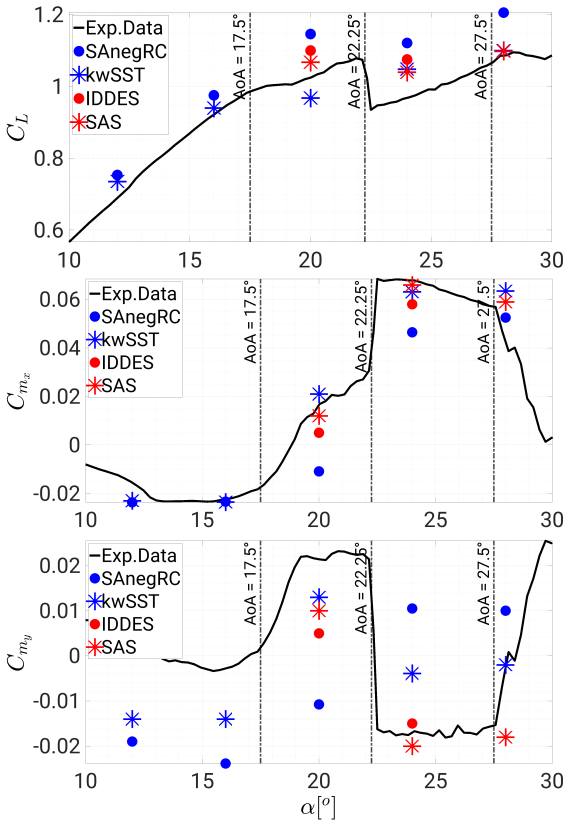

Figure 6.21: Comparison of lift, rolling, and pitching moment coefficients across AoA: experimental versus numerical data at $Ma_\infty = 0.85$, $Re_\infty = 12.53 \times 10^6$, and $\beta = 5°$.

The rolling and pitching moment coefficient curves are particularly interesting in the presence of a non-zero side-slip angle. Indeed, the integral moments respond more sensitively to variations in the flow pattern than the force coefficients do. The numerical results, except for the $k\omega$SST, underestimate the experimental rolling moment for $\alpha < 28°$. A significant deviation between the CFD results is observed at $\alpha = 20°$, attributed to the onset of vortex breakdown on the windward wing. The $k\omega$SST outcomes predict an upstream location for the vortex breakdown, leading to an overestimation of C_{m_x}, while the HRL predicts this phenomenon more downstream compared to the experimental data. The SAnegRC outcomes fail to capture the vortex breakdown entirely.

The HRL results also show a good improvement in the pitching moment values. They correctly predict the sign of C_{m_y}, indicating a nose-up pitching for $\alpha = 20°$ and nose-down pitching for $\alpha = 24°$. Conversely, the SAnegRC model significantly mispredicts this coefficient owing to an inaccurate representation of the vortex breakdown over the windward wing. In contrast, the $k\omega$SST model exhibits improved accuracy within the URANS outcomes. Generally, the HRL approach enhances the prediction of aerodynamic coefficients, achieving a notable reduction in deviations compared to the URANS results. Furthermore, significant discrepancies between the CFD results are observable at $\alpha = 28°$ due to varying predictions of vortex breakdown onset on the leeward wing. Similar observations made for $\alpha = 20°$ are applicable.

These analyses confirm that the SAnegRC-based URANS simulations exhibit the lowest accuracy in predicting vortical flow over delta wings. This finding underscores the significance of the main objective outlined in this manuscript. Following the analysis of vortex development, this manuscript shifts then focus to examining the limitations of the SA model. Subsequently, Chapter 7 proposes a straightforward and robust modification to enhance the SA model's capability in predicting vortex breakdown, with a particular emphasis on the condition at $\alpha = 20°$.

7

Towards the Understanding of Vortex Breakdown for Improved RANS Turbulence Modeling

Building upon the discussion in Chapter 6, this chapter further investigates the aerodynamics of the triple-delta wing configuration, ADS-NA2-W1, under transonic and side-slip conditions. The findings reported in Di Fabbio et al., 2022c, 2024a are further elucidated.

Outcomes from five distinct simulations employing various turbulence models are presented, including the URANS simulations utilizing the SAnegRC and the Menter $k\omega$SST models, complemented by high-fidelity results from IDDES and SAS. The different treatment of the unclosed Reynolds stresses by these models impacts both the accuracy of the solutions and the computational demands. A novel enhancement to the one-equation SA turbulence model is then introduced, referred to herein as PK, an acronym for Production-k, denoting the modeled turbulent kinetic energy. The PK model represents an evolution of the existing SA model by incorporating an additional expression for the turbulent kinetic energy into the Boussinesq assumption.

The present analysis pays attention to the flow conditions at α = 20°, highlighting the profound influence of vortex breakdown on the aerodynamic characteristics of the windward wing. It aims to illuminate the occurrence of vortex breakdown and its underlying mechanisms, with an intent to identify and rectify the deficiencies inherent in the SA turbulence model when applied to delta wing aerodynamics, as discussed in Chapter 6. Improving the accuracy of this model necessitates an understanding and meticulous examination of the factors leading to its prediction inaccuracies, including both physical phenomena and modeling challenges. This inquiry further explores the impact of turbulence modeling on CFD outcomes, highlighting the significance of turbulence-related variables.

Findings obtained using the PK model are detailed in Section 7.2, where aerodynamic coefficients and surface pressure measurements are juxtaposed against experimental (Hövelmann et al., 2020) and CFD benchmarks presented in Chapter 6. Comparative analyses with the different numerical approaches, emphasizing the complexities of flow physics and turbulence modeling, are presented in Sections 7.3 and 7.4.

These sections aim to explore the limitations and shortcomings of the SA model, thereby justifying the introduction of the PK model. Finally, a discussion on the enhancements in terms of flow physics afforded by the PK model is provided in Section 7.5.

7.1. Extension of the Boussinesq assumption

As discussed in Section 3.4.1, the SA turbulence model is constructed around a single transport equation for the eddy viscosity variable, ν_t. This eddy viscosity establishes a linear relationship, $-\overline{u_i u_j} = \nu_t S_{ij}$, in accordance with the Boussinesq assumption (Eq. 3.40). Unlike two-equation models, the SA model neglects the k term, representing turbulent kinetic energy.

An enhancement to the Boussinesq approximation within the SA model framework is proposed, introducing a modification termed the PK model. This model aims to address the original model's omission of turbulent kinetic energy by incorporating a new variable, k_{SA}, specifically designed for integration with the SA model.

By equating the production and destruction of turbulent kinetic energy (Eq. 3.83), a simplified equation for k, akin to the methodology employed in the QCR model (Rumsey et al., 2020a), is derived as follows

$$\frac{\beta^k k^2}{\nu_t} = \tau_{ij}^R \frac{\partial u_i}{\partial x_j} \quad \Rightarrow \quad k = \frac{1}{\sqrt{\beta^k}} \sqrt{\nu_t \tau_{ij}^R \frac{\partial u_i}{\partial x_j}}, \tag{7.1}$$

$$\text{where} \quad \tau_{ij}^R \frac{\partial u_i}{\partial x_j} \approx \|S_{ij}\| \tag{7.2}$$

However, applications of the QCR model have encountered numerical challenges, especially in wake zones where the turbulent viscosity, μ_t, is significant. To mitigate these issues, a strategy that suggests substituting strain rate with vorticity has been proposed (Rumsey et al., 2020b). Consequently, the revised expression for k_{SA}, representing turbulent kinetic energy within the SA model, is defined as follows

$$k_{SA} = C_k \mu_t \sqrt{2 W_{mn} W_{mn}}, \tag{7.3}$$

The calibration of the coefficient C_k is critically examined in Section 7.5, with empirical analysis determining that a value of $C_k = 3$ yields optimal results under the specified conditions and objectives of this dissertation. Eq. 7.3 is then incorporated into the Boussinesq assumption, resulting in the following formulation:

$$-\rho \overline{u_i' u_j'} = \tau_{ij}^R = 2\,\mu_t\, S_{ij}^* - k_{SA} \delta_{ij}. \tag{7.4}$$

7.2. Data comparison: validation of the CFD results

Although the flow field above the aircraft at $\alpha = 20°$ has been discussed in Section 6.2.1, an overview is briefly given herein. Leading-edge vortices, depicted in Fig. 7.1, arise

from the separation of the shear layer at the wing's leading-edge. This process initiates the formation of a stable, primary vortex that induces flow reattachment over the wing. Under certain conditions, a secondary counter-rotating vortex develops outboard of the primary one. Furthermore, fuselage vortices, illustrated in Fig 7.1, manifest on both wings, correlating with the different sweep angles of the leading-edges. The vortices on the windward wing are notably susceptible to breakdown, characterized by an abrupt change in flow topology, marked by deceleration and divergence. The location of vortex breakdown is unstable, exhibiting buffeting behavior. While a comprehensive understanding of this behavior requires analyzing the instantaneous flow characteristics due to their unsteady effects, this chapter examines the mean flow features to explore better the turbulence treatments' effects on the RANS results. The mechanisms underlying vortex breakdown are explored to enhance the understanding of both the phenomenon itself and its numerical modeling.

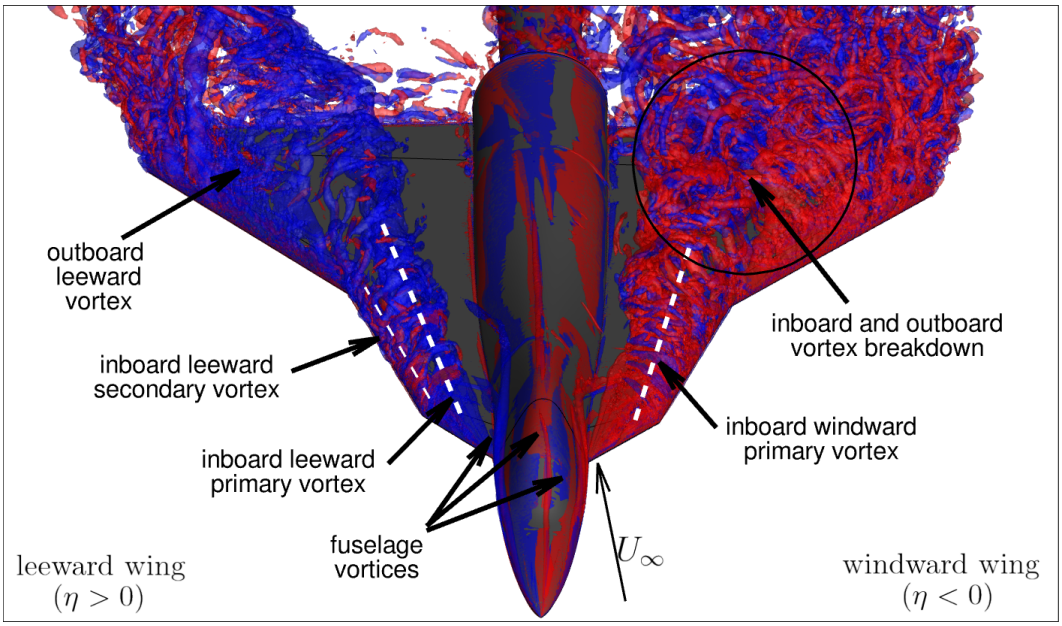

Figure 7.1: Q-criterion instantaneous iso-surface with flood contour by instantaneous normalized helicity H_n, IDDES results with $\beta = 5°$ and $\alpha = 20°$ (Di Fabbio et al., 2024a).

7.2.1. Enhancement of the aerodynamic coefficients

In the context of evaluating result accuracy within the field of aerodynamics, the curves of the rolling and pitching moment coefficients are presented. Fig. 7.2 shows the results from URANS simulations using the SAnegRC and $k\omega$SST models, and outcomes from scale-resolving simulations such as IDDES and SAS. These CFD outcomes are discussed in Chapter 6.

In addressing the significant discrepancies observed between the outcomes of various modeling approaches at $\alpha = 20°$, the differences are largely attributed to differing predictions of vortex breakdown on the windward wing. Hi-Fi data significantly refine the

accuracy of aerodynamic coefficient predictions, with the SAS methodology emerging as particularly reliable for the investigated configurations. Comparative analysis reveals that the two-equation $k\omega$SST model outperforms the SA model in terms of flow field prediction accuracy, especially by predicting the occurrence of the vortex breakdown at $\alpha = 20°$. As discussed in Chapter 6, the SAnegRC model is unable to predict the vortex breakdown on the windward wing at $\alpha = 20°$. In contrast, the PK model exhibits a significant improvement in the accuracy of aerodynamic coefficient predictions, attributed to its precise prediction of the vortex breakdown onset location.

Furthermore, across other AoAs, the PK model's performance consistently matches or surpasses that of the original SAnegRC model, thereby offering a promising solution to the constraints of the one-equation model. Even at $\alpha = 28°$, the PK outcomes represent an advancement since the model can reproduce the vortex breakdown on the leeward wing, albeit predicted too upstream compared to the experimental results. The SAnegRC model fails to replicate this phenomenon under these flow conditions ($\alpha = 28°$) as well. A comprehensive assessment of the PK model's efficacy, including a quantitative analysis of the enhancements achieved, is given in Section 7.5.

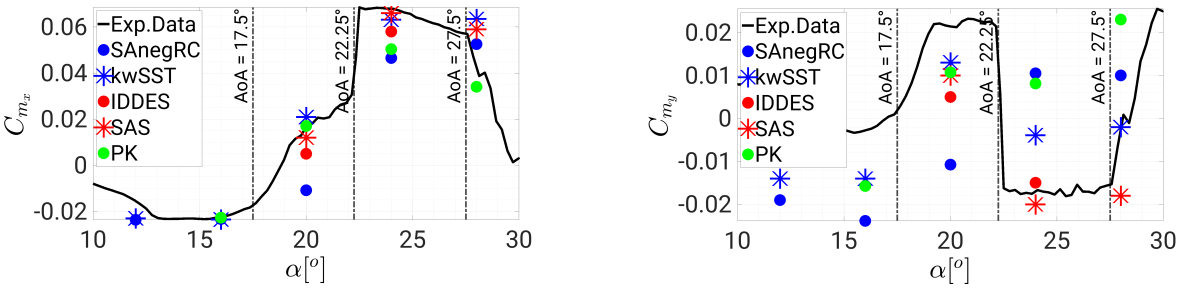

Figure 7.2: Comparison between state-of-the-art and PK model, experimental and numerical data with $Ma_\infty = 0.85$, $Re_\infty = 12.53 \times 10^6$ and $\beta = 5°$. Hi-Fi results are represented in red, while standard URANS results are in blue. PK turbulence model in green. One-equation and two-equation results are denoted with circle and star markers, respectively (Di Fabbio et al., 2024a).

7.2.2. Investigation of the suction footprint

The leading-edge vortex on delta wings triggers a localized decrease in pressure under the vortex, significantly enhancing the aircraft's lift, particularly at higher angles of attack. This phenomenon, referred to as the suction footprint, is critical for the wing's aerodynamic performance. The distribution of the mean surface pressure coefficient, c_p, on the aircraft's surface is illustrated in Fig. 7.3. An in-depth analysis of the mean surface pressure coefficient distributions is conducted across the wing's span at various chord-wise positions $\xi = 0.35, 0.55, 0.75$, as shown in Fig. 7.4.

The investigation presented in Fig. 7.4 for $\xi = 0.35$ reveals that the numerical simulations capture the intricate flow characteristics over the aircraft. Among the evaluated modeling strategies, the $k\omega$SST model and Hi-Fi simulations stand out for their accuracy in replicating surface pressure data, closely matching experimental observations.

On the contrary, the SAnegRC model shows significant deviations, highlighting its deficiencies in accurately predicting the aerodynamic behaviors noted in experimental findings. The PK model slightly improves the prediction of the SAnegRC on the windward wing, while it matches the baseline model on the leeward wing. This behavior was expected since the PK model does not modify the turbulence production term in the SA equation but simply models the isotropic part of the Reynolds stress tensor (the turbulence kinetic energy), which is still not observable over the front wing. This was discussed in Section 5.4 for the VFE-2 configuration and will be further discussed in Section 7.4 for the present configuration. Noteworthy are the variances in simulating the fuselage vortices, particularly at $\eta \approx |0.1|$ on either wing.

At the windward wing's chord-wise position of $\xi = 0.55$, the suction effect resulting from the primary inboard vortex demonstrates remarkable consistency in the outcomes derived from both the $k\omega$-based and SA-based models, when considered within their individual categories. However, significant variances are observed in the representation of the secondary vortex and the flow dynamics proximal to the leading-edge. The simulations' accuracy in capturing the secondary vortex does not reach the desired level of precision, with the negative pressure coefficient being inaccurately predicted for $|\eta| > 0.35$. In particular, the intensity of the secondary vortex, as indicated by the peak c_p values in the SAS results, tends to amplify the vortex's strength beyond what is observed in experimental data. In contrast, the $k\omega$SST model operates in the opposite manner, predicting a weaker secondary vortex.

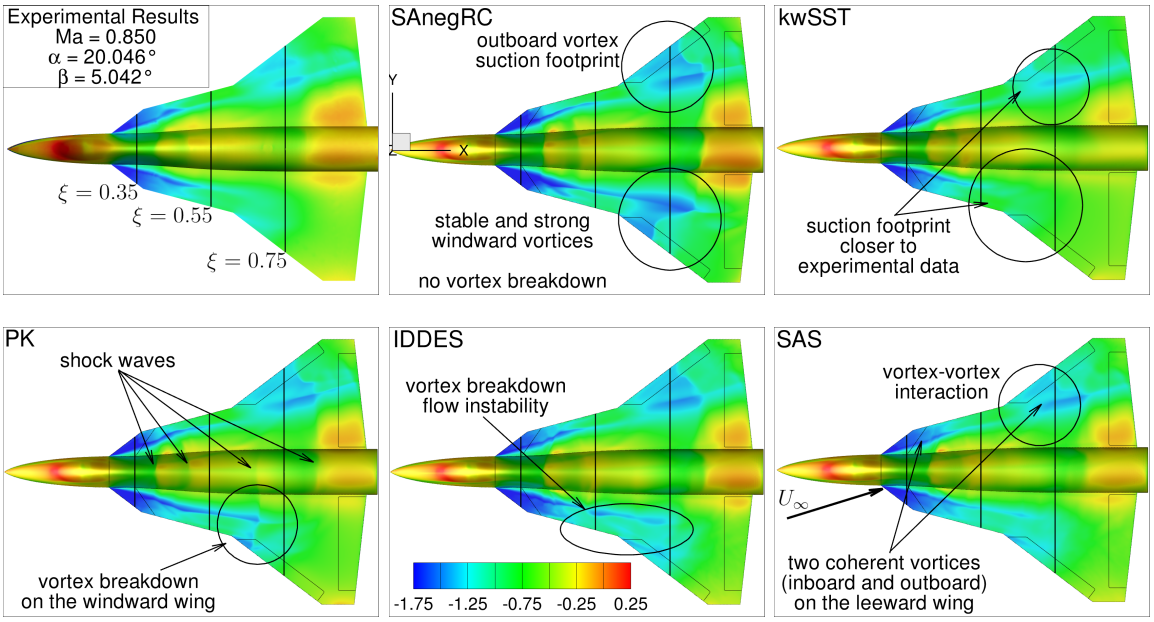

Figure 7.3: Mean surface pressure coefficient, experimental and numerical data at $\beta = 5°$ and $\alpha = 20°$. The black lines show the extracted slice planes (Di Fabbio et al., 2024a).

Accurately capturing the strength of the secondary vortex is crucial for a correct representation of the vortex breakdown process, as discussed in Chapter 5. Underestimation of the secondary vortex's intensity, characterized by a lower than expected $|c_p|$ from the secondary vortex, leads to a premature prediction of vortex breakdown locations. In the context of the one-equation model analyses, the secondary vortex is consistently identified over the windward wing in both the SAnegRC and PK model outcomes, yet it becomes indiscernible in the IDDES simulations. However, the PK model results indicate a sharp decrease in $|c_p|$ near the leading-edge, suggesting a possible onset of stream-wise flow separation. This behavior underscores the IDDES and PK models inclination towards predicting vortex breakdown, in contrast to the relative stability observed in the SAnegRC predictions. Furthermore, at $\xi = 0.55$, the fuselage vortices are well predicted by all the CFD outcomes on both wings.

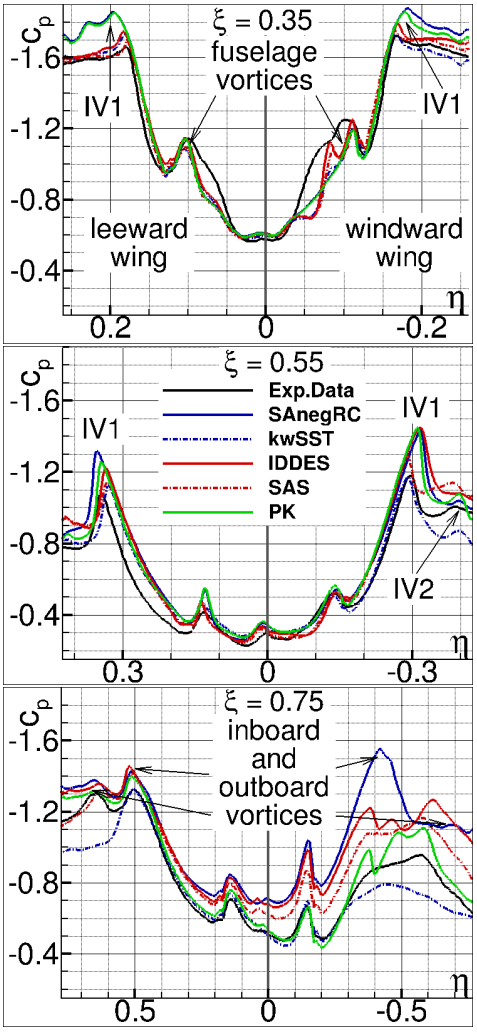

Figure 7.4: Mean pressure coefficient profiles at $\xi = 0.35$, 0.55, 0.75, experimental and CFD data at $\beta = 5°$ and $\alpha = 20°$ (Di Fabbio et al., 2024a).

At the chord-wise position of $\xi = 0.75$ on the windward wing, vortex breakdown is notably observed. The breakdown of the inboard and outboard vortices occurs sequentially, with the inboard vortex disintegrating before the outboard one. The SAnegRC model fails to capture this vortex breakdown accurately, in contrast to the PK model, which demonstrates a substantial capability to accurately simulate this critical phenomenon. With the exception of the $k\omega$SST model, which predicts the onset of vortex breakdown earlier, the other simulations tend to capture the breakdown onset occurring further downstream on the wing than what is supported by experimental evidence. Such discrepancies in the predicted locations of vortex breakdown markedly affect the variations in aerodynamic coefficients, as depicted in Fig. 7.2.

7.3. Vortex breakdown and turbulence modeling

Improving a turbulence model necessitates a thorough comprehension of the fundamental reasons for its shortcomings. Fig. 7.5 illustrates the airflow patterns over the aircraft, facilitating a comparison between the outcomes of the SAnegRC and $k\omega$SST models, thereby highlighting the impact of varying turbulence modeling approaches. Hi-Fi data are presented as the benchmark for comparison.

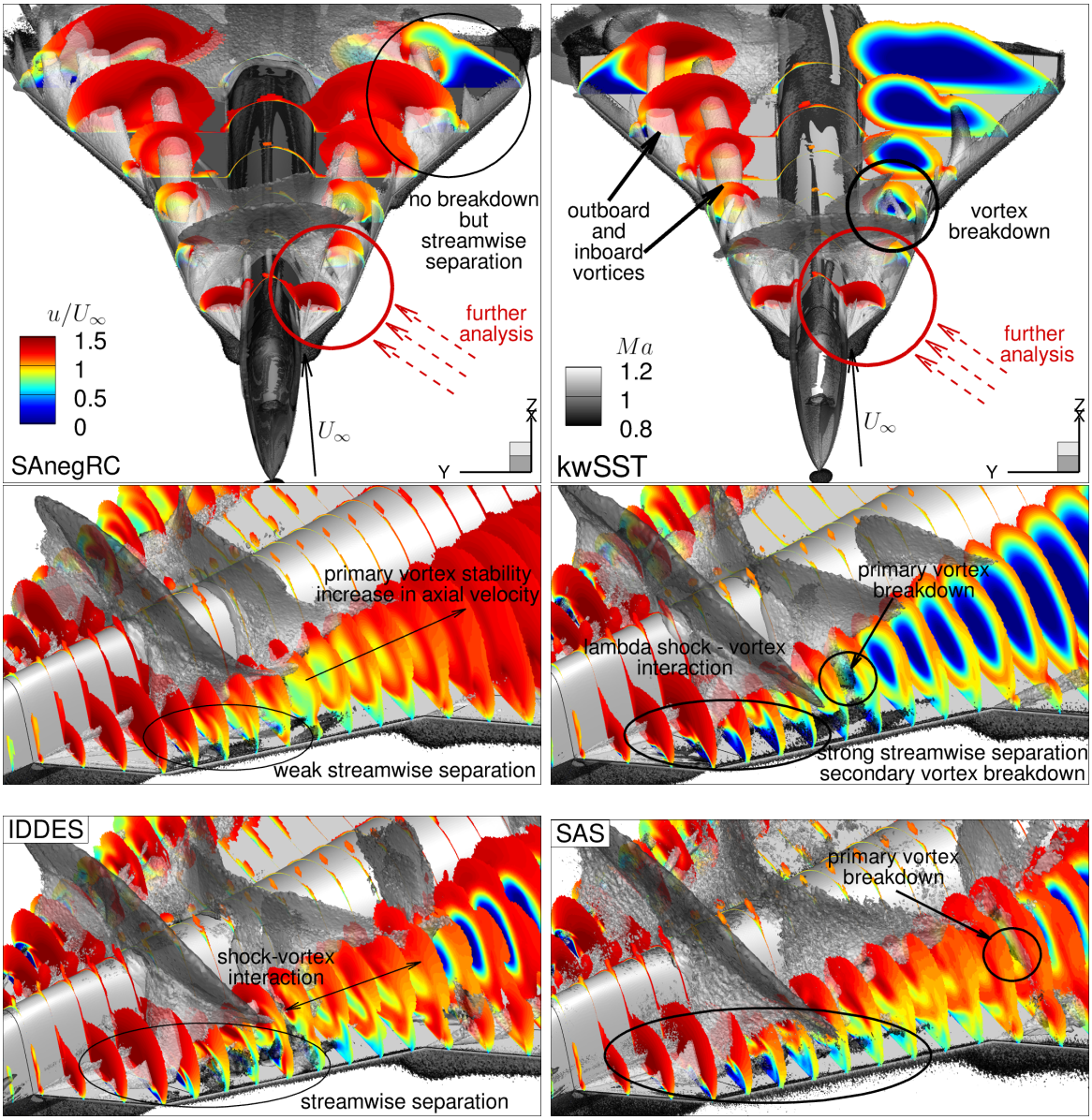

Figure 7.5: Iso-surfaces from streamwise pressure gradient and Q-criterion colored by Mach number, and slice planes showing the normalized x-velocity (Di Fabbio et al., 2024a).

A fundamental distinction exists between the examined methods, primarily highlighted by the effect of shock waves, as depicted in Fig. 7.5. This figure meticulously illustrates the interaction between shock waves and vortices, with a focus on the condition of the inboard vortex pre- and post-interaction. As the vortex core passes through the shock wave, it experiences a reduction in both velocity and kinetic energy. However, the interaction of the shock wave with the inboard vortex core is not the singular cause behind the observed breakdown. It is noteworthy that the SAnegRC model predicts the presence of the shock wave at the correct location but fails to capture the vortex breakdown, leading to the conclusion that the presence of a shock wave does not

invariably result in vortex breakdown. The vortex's inherent strength plays a crucial role in this process (Erlebacher et al., 1997). A vortex is susceptible to breakdown due to shock interaction only if it is intrinsically unstable and prone to such a breakdown.

As investigated in a collaborative research project (Rajkumar et al., 2024), the vortex breakdown location is unstable, and a buffeting behavior can be observed over the wing, leading to oscillation of the aerodynamic coefficients. For this reason, Fig. 7.5 shows the mean location of the breakdown onset for the different CFD outcomes and demonstrates how these locations distinguish themselves by influencing the value of the integral forces and moments investigated in Section 7.2.1. Based on these observations, the onset location of the breakdown phenomenon predicted by experimental data should be situated between the locations captured by the $k\omega$SST and SAS outcomes.

The mechanism elucidating the phenomenon of vortex breakdown, as delineated in Chapter 5, is employed to explain the discrepancies between the URANS outcomes, thereby demonstrating its validity to a certain extent. The inboard vortex core predominantly consists of flow from the shear layer that separates at the wing's apex. The continuous contribution of the shear layer to the inboard vortex along the wing span results in the vortex's enlargement. This incoming flow envelops the primary core, enhancing its structural integrity and maintaining its unity. This emphasizes the necessity of precisely simulating separation and turbulence near the apex in simulations of delta-wing flows. The existence of a secondary vortex lends support to this observed behavior. When this secondary vortex becomes unsustainable, it leads to the detachment of the boundary layer in the direction of the flow, resulting in the formation of a recirculation zone. Rather than merging with the secondary vortex, the fluid shifts into smaller-scale turbulent movements. This shift prevents the shear layer from integrating into the primary vortex, thus initiating a turbulent flow pattern. Consequently, the primary vortex, deprived of its kinetic energy source, is rendered more susceptible to breakdown. This hypothesis is corroborated through the analysis of Figs. 7.6 and 7.7.

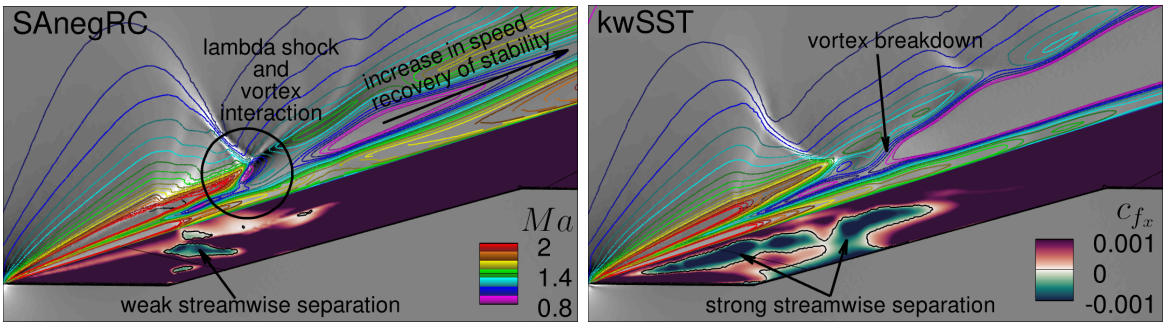

Figure 7.6: x-pressure gradient contour field with Mach number contour lines and mean x-direction friction coefficient. Black lines indicate zero mean friction coefficient (Di Fabbio et al., 2024a).

Figure 7.7 illustrates the x-vorticity on the windward side of the wing, primarily depicting the formation and degradation of the secondary vortex. Figure 7.6 reveals the

dynamics of shock-vortex interaction within the plane of the vortex core line, showcasing the presence of the lambda shock that plays a role in vortex breakdown, and displays the mean friction coefficient, c_{f_x}, in the x-direction, delineating the region of stream-wise separation.

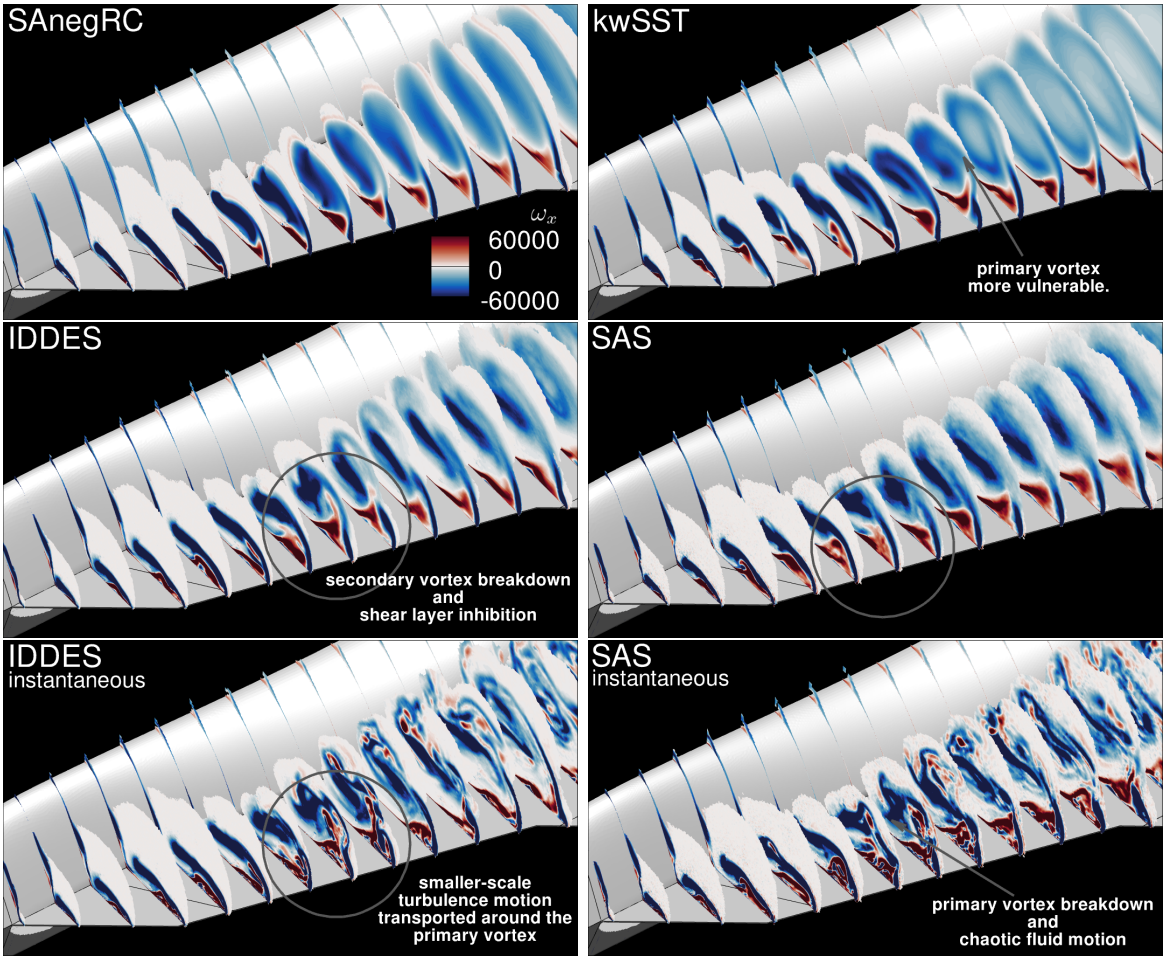

Figure 7.7: Mean and instantaneous x-vorticity, URANS, and Hi-Fi results (Di Fabbio et al., 2024a).

The analysis of SAnegRC outcomes indicates a less pronounced stream-wise separation on the wing preceding vortex disruption, with the shear layer adequately feeding the primary vortex. The consistently positive friction coefficient, except for a small area, suggests that the flow remains nearly attached to the wing's surface, maintaining vortex stability. Moreover, the velocity in the vortex core exhibits an increase following the abrupt shock interaction. The depiction of x-vorticity also portrays a stable and fully developed secondary vortex, whose formation is postponed, preventing its breakdown. In contrast, the $k\omega$SST model displays notable differences in flow behavior near the apex, including evident stream-wise flow separation, the lack of a coherent secondary vortex, and a larger area of negative friction coefficient, indicating the leading-edge vortex's pre-existing weakened state prior to interaction with the shock wave. Thus, the vortex depicted in the $k\omega$SST results is inherently more prone to breakdown than

in the SAnegRC findings, highlighting a potential shortfall in the SAnegRC model's predictive accuracy. Hi-Fi data in Fig. 7.7 substantiates and enhances this analysis, particularly when examining instantaneous plots. The illustrations demonstrate the emergence of turbulence at smaller scales, resulting from the disintegration of the secondary vortex coupled with stream-wise detachment. These fluid particles influence the behavior of the vortex sheet and begin to encircle the primary vortex, ultimately leading to its subsequent breakdown.

7.4. Model impact on turbulence-related quantities

This section presents an analysis of the impact of the turbulence model on turbulence-related quantities. A detailed discussion on eddy viscosity, including its production and destruction, is followed by an analysis of the Reynolds stress tensor. This includes understanding the effects of omitting the turbulence kinetic energy in the Boussinesq assumption within the one-equation model.

7.4.1. Eddy viscosity: turbulence production and destruction

Figure 7.8 presents the viscosity ratio contours, defined by $R_t = \mu_t/\mu$, by comparing the URANS outcomes. The RC correction strategy effectively reduces the overproduction of eddy viscosity at the wing's leading-edge. Nonetheless, this approach shows limitations at the aft portion of the vortex core, where the SAnegRC model tends to produce significantly higher eddy viscosity levels. The instability, especially subsequent to the position of the lambda shock, is somewhat mitigated by the viscous damping effects introduced by the SAnegRC model. High levels of turbulent viscosity stand in contrast to the absence of predictions for vortex breakdown, which is identified as the primary mechanism driving the generation of turbulent motion.

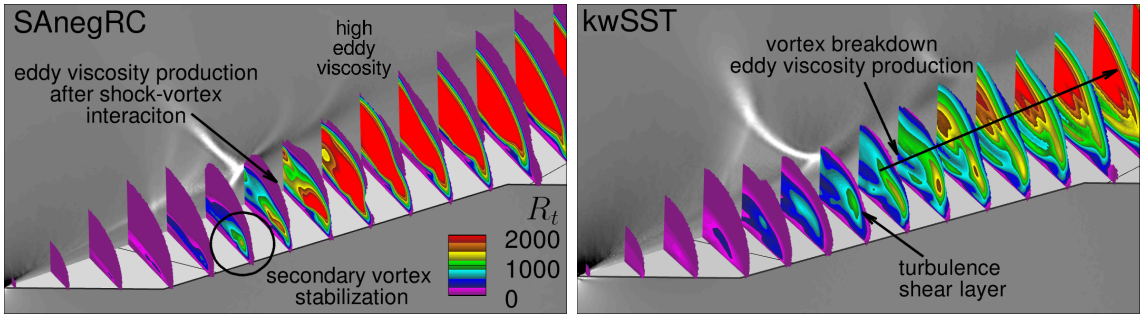

Figure 7.8: Viscosity ratio in the windward inboard vortex (Di Fabbio et al., 2024a).

The $k\omega$SST model exhibits comparable magnitudes of eddy viscosity upstream of the vortex-shock interaction, albeit manifesting generally diminished levels downstream. Prior to the vortex breakdown, an increase in eddy viscosity is predominantly noted within the separating shear layer as it forms the primary vortex. Post shock-vortex interaction and ensuing breakdown, there's a rising in eddy viscosity attributable to the

vortex's loss of coherence and the ensuing turbulent fluid motion. This phenomenon is indicative of the model's capability to accurately simulate the breakdown of vortex structure through turbulent fluctuations. Within the RANS framework, zones exhibiting elevated μ_t values typically denote vortex movements distinguished by substantial turbulence energy generation, a consequence of pronounced flow rotation and deformation (Peng and Jirasek, 2016). Consequently, areas where the vortex maintains its coherence are expected to display reduced turbulence levels. The formation of the leading-edge vortex is a naturally occurring process, independent of turbulence, as it does not involve any velocity fluctuations.

Figure 7.9 delineates the production and dissipation metrics from the $\tilde{\nu}$ and k turbulence equations. In particular, by examining the one-equation model, this analysis delineates the combination of SA and SAneg terms as articulated in Eqs. 3.61 and 3.65, with a summary provided in Table 7.1. Additionally, the rotation correction coefficient, f_{r1}, as defined in Eq. 3.67, is depicted to offer further insights.

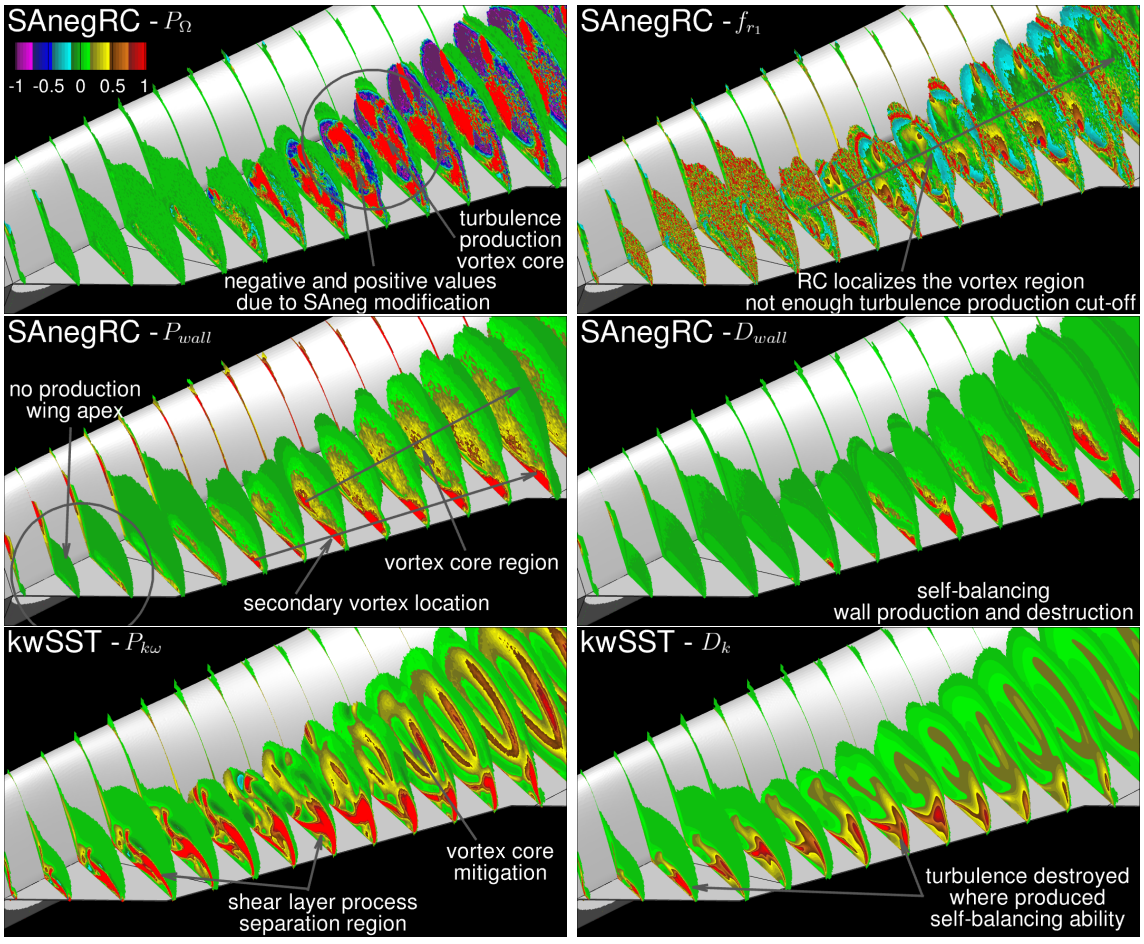

Figure 7.9: Source terms of the turbulence equations written in Table 7.1. All the values have been normalized (Di Fabbio et al., 2024a).

Near the apex and leading-edge of the wing, where the vortex originates, the SA model exhibits negligible turbulence production. "These outcomes corroborate the discrepan-

cies highlighted in capturing the flow behavior near the leading edge on the windward wing at $\alpha = 24°$ in Chapter 6. Within the vortex core, especially post shock interaction, the production term becomes significantly pronounced, explaining the heightened turbulent viscosity observed in this region. The model also oscillates between positive and negative values, a phenomenon attributed to the RC correction. Such fluctuations underscore the challenges in accurately quantifying turbulent viscosity, with additional efforts to avoid negative values, which are both unrealistic and non-physical, resulting in an increase in the absolute turbulent viscosity measure.

Moreover, the term associated with wall production elucidates that turbulence is predominantly generated at the site of the secondary vortex, which is observed to be stable and well-formed. This scenario contrasts with the relatively inconsequential role of the destruction term, which only partially offsets the impact of wall production. Furthermore, despite the RC factor's efficacy in delineating the vortex core, it does not curtail turbulence generation adequately. The SAnegRC model produces excessive turbulence within the coherent core of the vortex, leading to its erroneous stabilization. Since eddy viscosity acts to attenuate rotational motion, a more viscous flow exhibits slower rotation. An increase in the Rossby number, the ratio of axial to tangential velocity, is then generated signifying enhanced vortex stability (Riou et al., 2010).

The $k\omega$SST model accurately predicts turbulence production in the region of flow separation and somewhat reduces turbulence within the vortex core due to its specific formulation, as detailed in Section 3.4.3. Furthermore, the observation that the destruction term manifests where the turbulent kinetic energy is both generated and reaches peak levels, underscores the two-equation model's inherent ability to self-regulate and adjust the levels of turbulent viscosity. This self-balancing feature is less pronounced in the one-equation model, especially within the context of vortical flows, suggesting the need for a differentiated strategy in dealing with such complex configurations in CFD simulations.

Table 7.1: Source terms of the turbulence equations illustrated in Fig. 7.9

	Production Term	Wall Production Term
SA	$P_{\Omega_{SA}} = \left[c_{b_1}\left(1 - f_{t2}\right)\Omega - c_{b_1} f_{t2}\overline{s}\right]\tilde{\nu}$	$P_{wall_{SA}} = c_{b_1}\overline{s}\tilde{\nu}$
SAneg	$P_{\Omega_{SAneg}} = c_{b_1}\left(1 - c_{t3}\right)\Omega\tilde{\nu}$	$P_{wall_{SAneg}} = 0$
SA-RC	$P_{\Omega_{SA-RC}} = f_{r1} P_{\Omega_{SA}}$	$P_{wall_{SA-RC}} = f_{r1} P_{wall_{SA}}$
k-eq	$P_{k\omega} = \tau_{ij}^{R}\dfrac{\partial u_i}{\partial x_j}$	-
	(Wall) Destruction Term	
SA	$D_{wall_{SA}} = \left[c_{w1} f_w - \dfrac{c_{b1}}{\kappa^2} f_{t2}\right]\left(\dfrac{\tilde{\nu}}{d}\right)^2$	
SAneg	$D_{wall_{SAneg}} = -c_{w1} f_w \left(\dfrac{\tilde{\nu}}{d}\right)^2$	
SA-RC	$D_{wall_{SA-RC}} = D_{wall_{SA}}$	
k-eq	$D_k = \beta^* \rho\omega k$	

7.4.2. Boussinesq assumption and Reynolds stress tensor

A comparative examination of the Reynolds stresses between the SAnegRC and $k\omega$SST models highlights the significance of turbulence modeling, and more precisely, the implications of omitting explicit turbulence kinetic energy in the SA model. Indeed, the potential influence of Reynolds stress anisotropy on the inaccuracies observed in URANS simulations is unable to explain the variances observed between the results obtained by SA and $k\omega$SST models, as both models incorporate the Boussinesq approximation. Hi-Fi data is utilized for benchmark purposes.

Reynolds stresses quantify the intensity of turbulent fluctuations across three dimensions. These stresses comprise both the resolved and the modeled components. Within the context of the mean flow-field, the modeled Reynolds stresses are derived utilizing the Boussinesq approximation presented in Eq. 3.40. To compute the resolved Reynolds stresses statistics from the resolved fluctuations are computed. Figures 7.10 and 7.11 illustrate two normalized normal components of the Reynolds stress tensor, $R_{(ij)}$, on the windward wing. As introduced in Chapter 5, they are normalized against the free-stream velocity and local mean density, reflecting the variance of the velocity components.

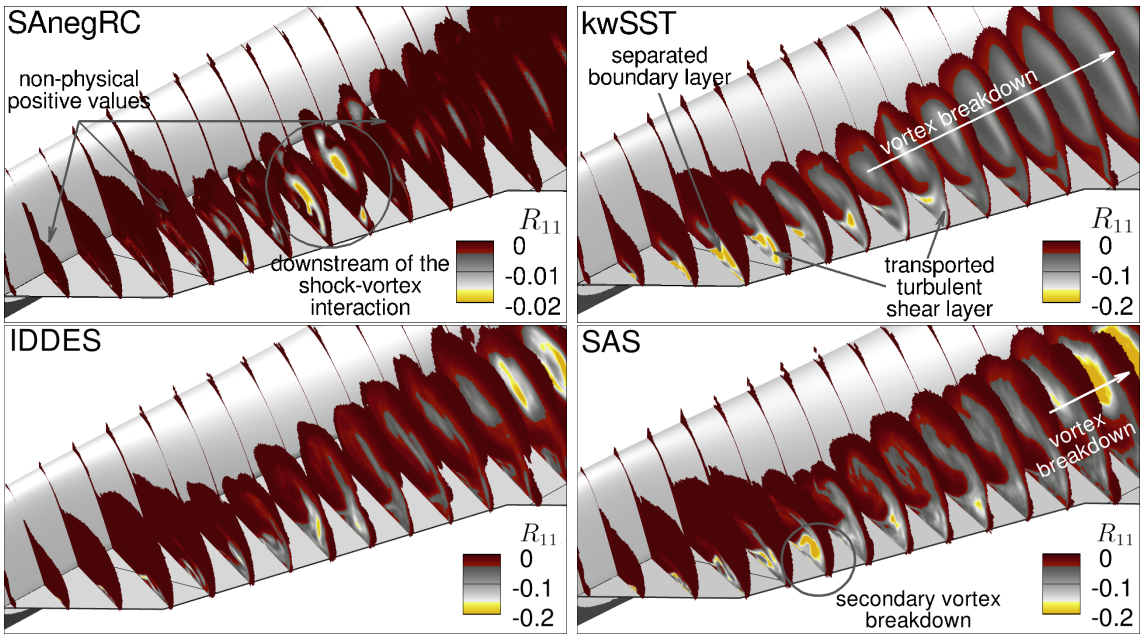

Figure 7.10: Normalized specific Reynolds stresses, R_{11} (Di Fabbio et al., 2024a).

The outcomes derived from the SAnegRC model exhibit non-physical positive values for $R_{(ii)}$, contradicting the expectation for these values to be negative, a consequence of the negative sign applied to squared velocity fluctuations. This discrepancy is notably absent in the findings associated with the $k\omega$SST model. The inclusion of k, as delineated in Eq. 3.40 and depicted in Fig. 7.12, accounts for the observed difference in the $k\omega$SST results, ensuring a more accurate representation of turbulence characteristics. In the one-equation turbulence model, the turbulent kinetic energy is assumed to

be zero, a simplification that leads to inaccuracies in predicting the normal Reynolds stresses. This observation underscores the importance of the isotropic term from the Boussinesq approximation, represented as $2/3\rho k\delta_{ij}$. The absence of this term may result in a significant disparity in the Reynolds stress magnitudes observed between different modeling approaches, indicating the need for an alternative approach to incorporate the isotropic term of the Boussinesq hypothesis into one-equation models.

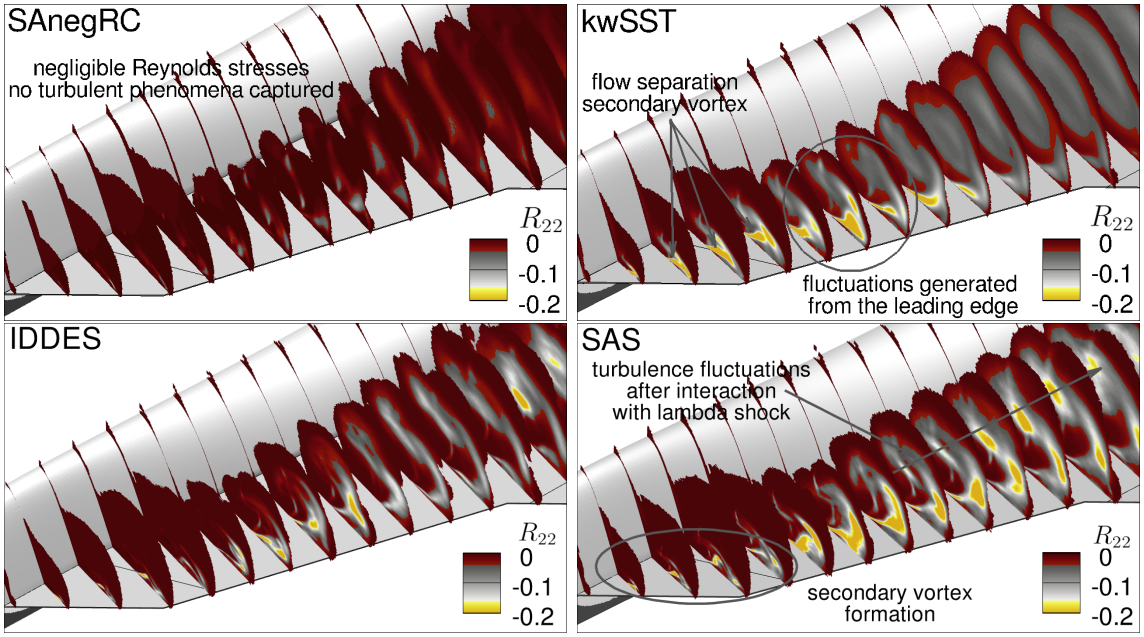

Figure 7.11: Normalized specific Reynolds stresses, R_{22} (Di Fabbio et al., 2024a).

Additionally, the R_{11} component highlights the turbulent characteristics of the shear layer, particularly within the $k\omega$SST model outcomes. The stream-wise turbulent motion becomes increasingly noticeable in the separated boundary layer and intensifies following the vortex breakdown, facilitating the downstream transport of turbulence kinetic energy. Prior to the breakdown, velocity fluctuations within the leading-edge vortex core are observed, attributed to the stochastic displacement of the vortex core (Menke and Gursul, 1997). R_{22} highlights the genesis of fluctuations as the flow transitions away from the leading-edge, serving as a significant contributor to the turbulence kinetic energy within the vortex core.

In the context of the SAnegRC model, R_{11} exhibits significant negative values downstream of the shock-vortex interaction, emphasizing the transient nature of these phenomena. The averaged Navier-Stokes equations primarily account for the divergence of the Reynolds stress tensor. The influence of turbulence on the averaged momentum equation is represented by the body force $f = \partial\tau_{ij}^R/\partial x_i$, as discussed in Section 3.3.3. This observation implies that a positive gradient within the Reynolds stress tensor serves as a propulsive force, accelerating the airflow over the aircraft, and conversely, a negative gradient indicates a deceleration force. Consequently, the turbulence model might erroneously augment the stability of a coherent vortex subsequent to its interaction with the shock wave. In contrast, a negative gradient is observed in the vicinity

of the interaction, signifying the sudden deceleration of the flow. Furthermore, the τ_{22} values are markedly lower when compared to those from the $k\omega$SST model, indicating a discrepancy in the turbulence modeling between the two approaches.

To deepen the discussion on Reynolds stress and facilitate a comprehensive understanding of the associated dynamics, Figs. 7.13, 7.14 and 7.15 are introduced to exhibit the covariance components of the Reynolds stress tensor. These visualizations provide insights into the underlying turbulence structure and its impact on vortex dynamics.

The Reynolds stress R_{12} primarily indicates the vortex core and the region of the separated shear layer near the leading-edge, where its value is positive, and consequently, the covariance $\overline{u'v'}$ is negative. This signifies that fluctuations in the x and y directions are opposite in sign. The SAnegRC outcomes exhibit lower values of R_{12} compared to other CFD outcomes, especially in the region of the secondary vortex. Here, it is possible to visualize its formation and disintegration, followed by the consequent stream-wise separation, which leads to high levels of turbulence generation. It is also noteworthy to highlight the opposite sign of this component predicted at the location of the shock wave by the SAnegRC results, as marked in Fig. 7.13.

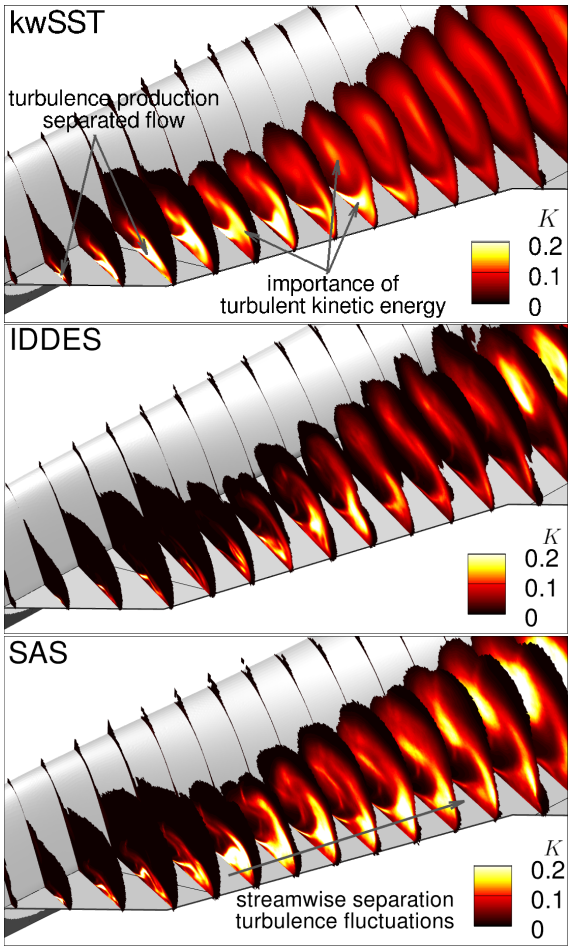

Figure 7.12: Normalized turbulent kinetic energy, K (Di Fabbio et al., 2024a).

The Reynolds stress R_{13} is positive within the stream-wise separated boundary layer but turns negative within the same region after the occurrence of the shock wave. This effect is observed in correspondence with the interruption of the primary vortex feeding process by the vortex sheet and is not present in the SAnegRC outcomes. It is also noteworthy to highlight how this component is divided into two parts inside the vortex core in the URANS outcomes; on the upper side, it is positive, with fluctuations in the x and z directions being opposite in sign, while on the lower side, it is negative, with fluctuations concordant in sign. This trend is not as evident in the Hi-Fi data, where the behavior of this component is more chaotic within the vortex core region. Furthermore, the color scale shows that R_{13} is the weakest covariance component.

As illustrated in Fig. 7.15, R_{23} primarily influences the shear layer, where the complex separation process and vortex rolling-up occur. Within the shear layer, it is negative, whereas it becomes positive in the vortex core. The Hi-Fi data provide a more accurate

prediction of the vortex sheet, including its thickness and location. Furthermore, a peak in this component is discernible in correspondence with the secondary vortex disintegration, which causes a reduction in the vortex sheet length and decreases its effectiveness in feeding the primary vortex. The SAnegRC model does not exhibit these processes and phenomena, showcasing only a high value of this component inside the vortex core.

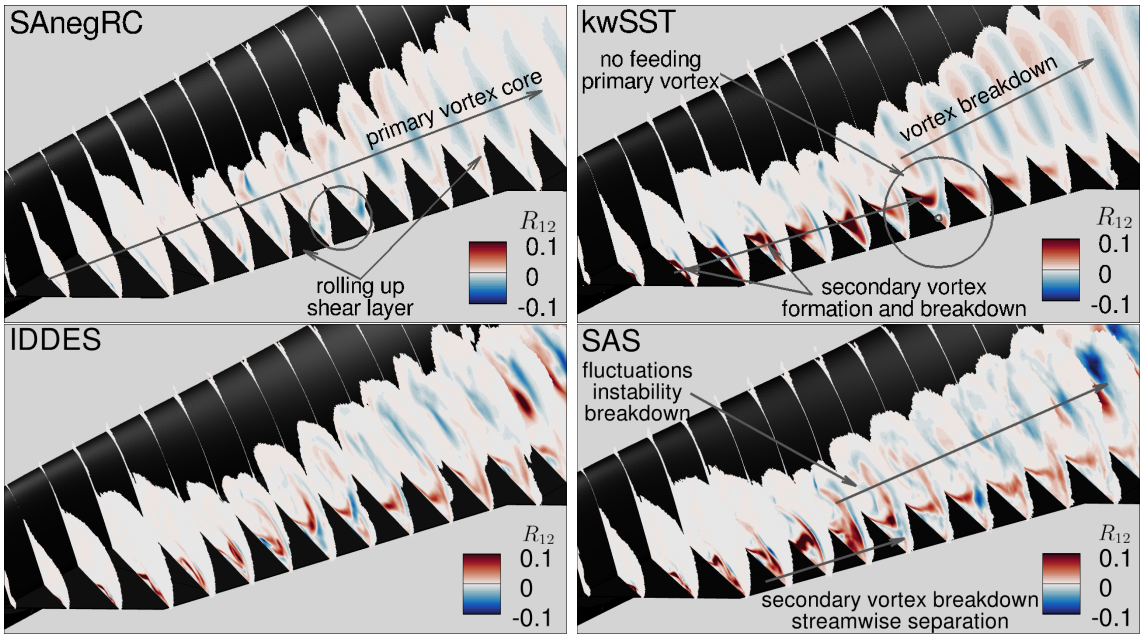

Figure 7.13: Normalized specific Reynolds stress, R_{12}.

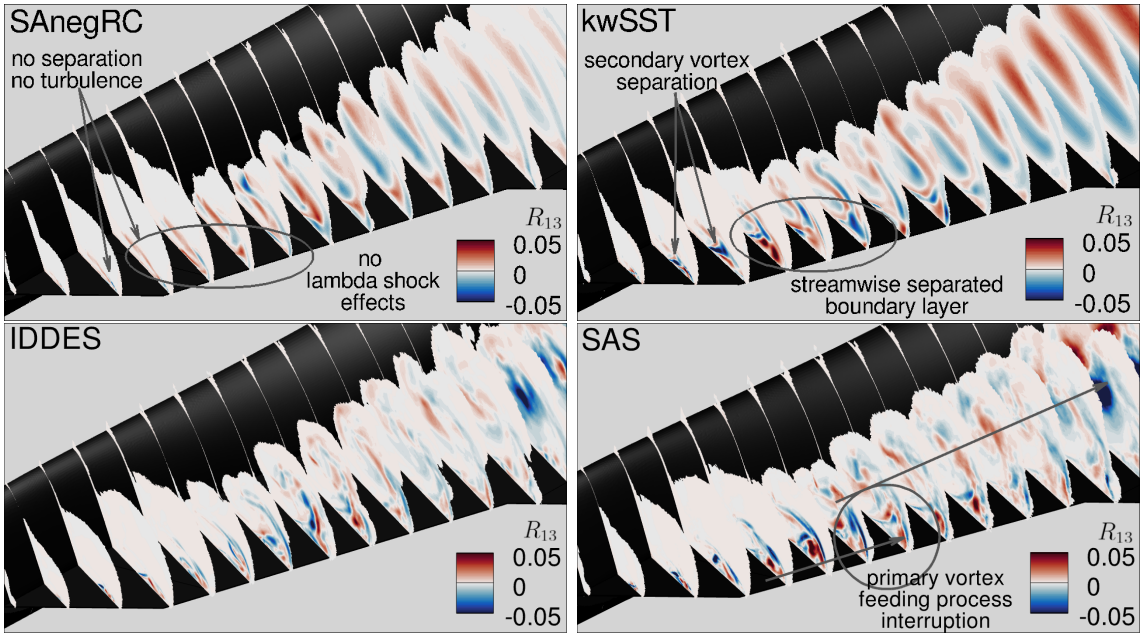

Figure 7.14: Normalized specific Reynolds stress, R_{13}.

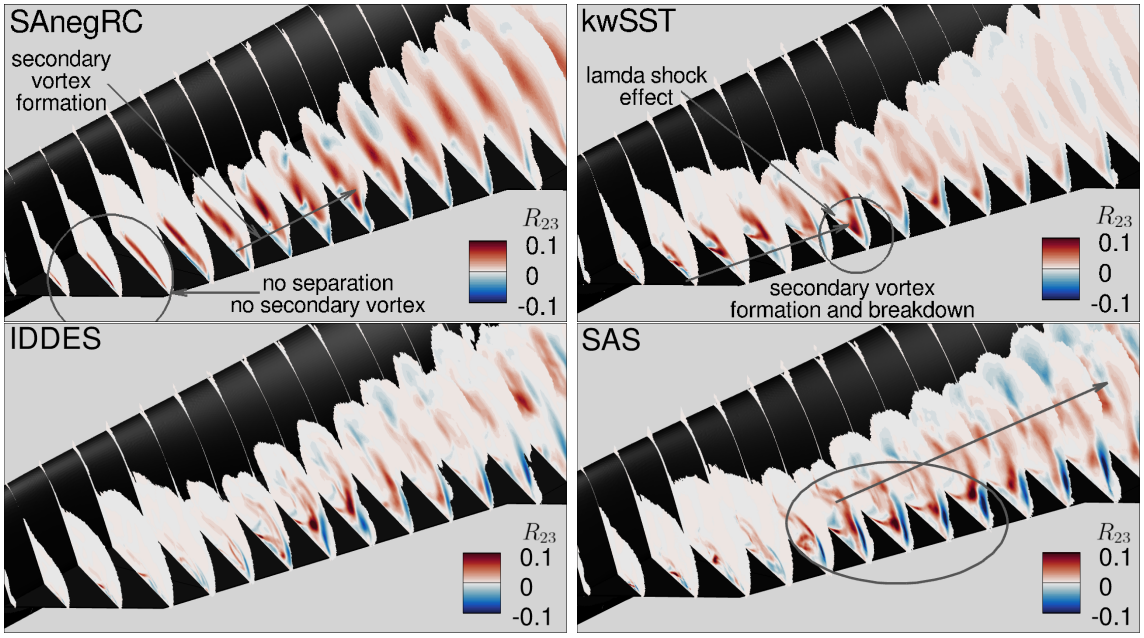

Figure 7.15: Normalized specific Reynolds stress, R_{23}.

7.5. Improved one-equation results

As outlined in Section 7.1, calibrating the constant C_k necessitates an analysis of the turbulence kinetic energy, which is illustrated in Fig. 7.12. The initial estimate for C_k has been then derived through the application of findings from the $k\omega$SST model .By reversing Eq. 7.3, the coefficient C_k can be expressed as follows

$$C_k = \frac{k}{\mu_t \sqrt{2 W_{mn} W_{mn}}}, \tag{7.5}$$

where the variables on the RHS are computed from the $k\omega$SST outcomes. Figure 7.16 shows the values of the coefficient C_k calculated by applying Eq. 7.5. The results show the relation between vorticity magnitude and turbulent kinetic energy in the vortex core and suggest setting the value to 3.

Furthermore, a range of C_k values is tested to identify the optimal value, thereby substantiating the credibility of the proposed enhancement. A quantitative assessment is conducted to compare simulation outcomes with empirical data, involving the calculation of the aerodynamic coefficient's relative deviation for $\alpha = 20°$, as depicted in Fig. 7.17. This comparison included C_k values of $C_{cr2} = 2.5$, derived from the QCR methodology (Rumsey et al., 2020b), 3.0, and $1/\sqrt{\beta_c^*} = 3.\overline{3}$, based on the Bradshaw hypothesis (Bradshaw et al., 1967), alongside the CFD results previously elucidated. Considering outcomes from previous research (Di Fabbio et al., 2022c), the novel model also exhibits enhanced stability and robustness compared to the QCR model, characterized by a more efficient convergence rate.

By analyzing the results achieved with the variation of C_k, several conclusions can be drawn regarding the behavior of this coefficient and its impact on the flow physics. Firstly, the calibration of C_k is identified as pivotal, requiring precise adjustments to accurately predict the location of vortex breakdown onset. With an increase in C_k, the breakdown point moves further up the wing, ultimately aligning with the experimentally observed position. Beyond this point, the pitching moment coefficient shows reduced sensitivity to changes in C_k. Conversely, the rolling moment coefficient, C_{m_x}, exhibits considerable sensitivity to variations in C_k, reflecting its significant influence on the aerodynamic characteristics of the leeward wing. The implementation of the PK turbulence model notably improves the precision in predicting aerodynamic coefficients, thereby achieving a substantial reduction in deviations when compared to those observed with the SAnegRC model. Optimal performance is attained when C_k is set to 3, and further detailed analysis are provided.

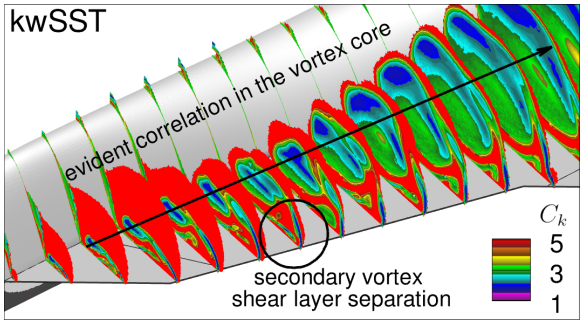

Figure 7.16: Relation between vorticity magnitude and turbulent kinetic energy through C_k (Di Fabbio et al., 2024a).

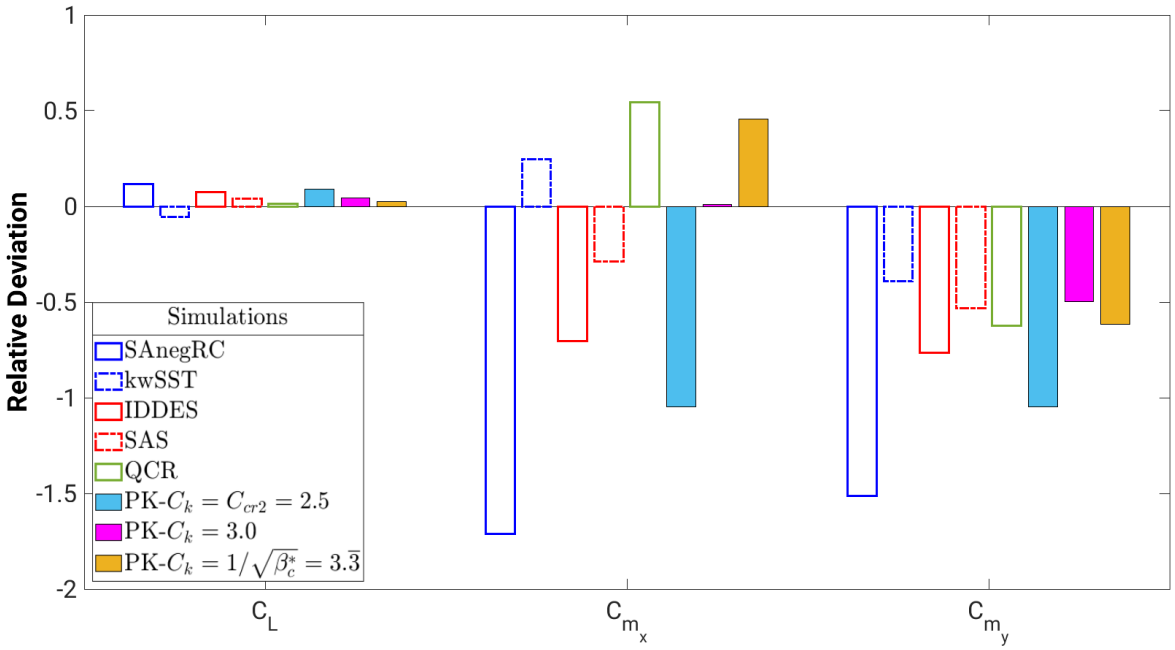

Figure 7.17: Aerodynamic coefficients deviation at $\alpha = 20°$ (Di Fabbio et al., 2024a).

Figure 7.18 shows the flow dynamics above the aircraft as predicted by the PK turbulence model, with C_k set at 3. The PK model excels in predicting the behavior and instability of the secondary vortex, evidenced by a more distinct stream-wise separation initiating at the leading-edge, as illustrated by the x-direction friction coefficient.

Additionally, this model achieves a more precise representation of the lambda shock, thereby enhancing the fidelity of shock-vortex interaction predictions. The Mach contour delineations generated by the PK model exhibit a closer resemblance to those obtained by the $k\omega$SST model shown in Fig. 7.6, albeit with the vortex breakdown transpiring further downstream. In the $k\omega$SST-based URANS results, the breakdown appears at the exact location of the interaction with the lambda shock, whereas in the PK outcomes, its location is further downstream. This behavior may be attributed to the intensity and extent of the separation area close to the leading-edge, which is decidedly more pronounced in the $k\omega$SST outcomes. Nonetheless, the PK model proficiently predicts the vortex breakdown location on the wing, aligning closely with experimental findings and achieving a position that more accurately reflects the Hi-Fi data.

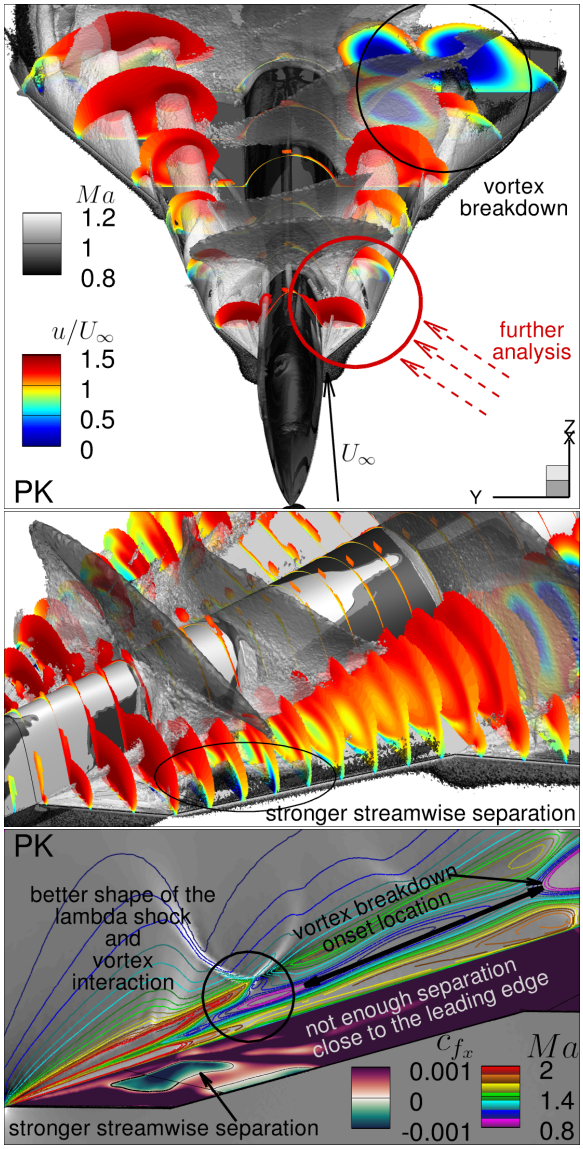

Figure 7.18: PK outcomes: leading-edge vortices, vortex-shock interaction, stream-wise separation, and vortex breakdown (Di Fabbio et al., 2024a).

Figure 7.19 presents the turbulence-related metrics derived from the PK model outcomes, highlighting its enhanced turbulence modeling. Notably, the viscosity ratio predictions more closely align with those recorded by the $k\omega$SST model, indicating a significant improvement in modeling fidelity. This model identify the turbulence within the vortex core, especially after the interaction with the lambda shock, and particularly near the leading-edge where the vortex sheet appears. The normal Reynolds stresses and the turbulent kinetic energy also depict the chaotic motion subsequent to the stream-wise separation following the burst of the secondary vortex.

By extending Boussinesq's hypothesis, the PK model effectively overcomes the limitations observed in traditional one-equation RANS approaches, accurately predicting the Reynolds normal stresses without yielding to the inaccuracies previously noted, such as unjustified and non-physical positive values. Through this advancement, the PK model significantly refines the understanding of the flow physics around a delta wing under transonic conditions, marking a pivotal enhancement over conventional one-equation

RANS models. The ongoing refinement of the PK model, particularly through the optimization of the coefficient C_k via a process that incorporates a flow field-dependent variation function, may represent a promising route for further research. Such advancements could potentially lead to even more accurate and reliable predictions of complex aerodynamic behaviors, while maintaining efficiency and robustness, thereby contributing valuable insights into the design and analysis of aerospace vehicles operating under a wide range of conditions.

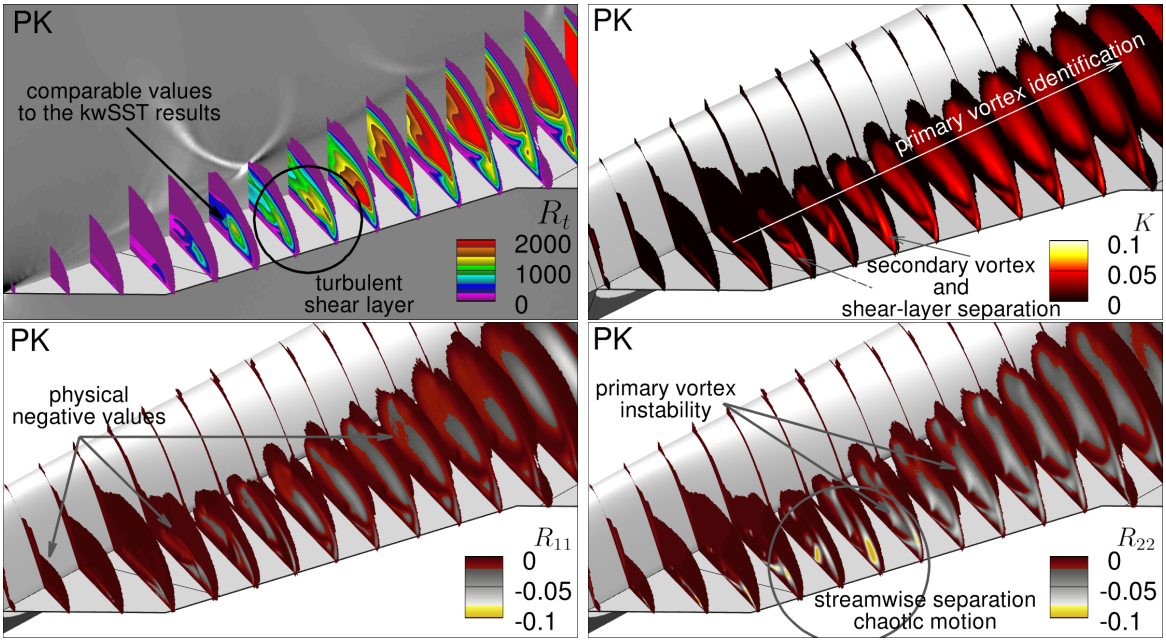

Figure 7.19: PK outcomes: viscosity ratio; normalized turbulent kinetic energy and normalized normal Reynolds stresses (Di Fabbio et al., 2024a).

Finally, as illustrated by the aerodynamic coefficients in Fig. 7.2, the PK model does not significantly improve numerical predictions at α = 24°. However, it successfully captures the vortex breakdown at α = 20° and 28° on the windward and leeward wings, respectively. This discrepancy may be attributed to multiple factors, with no universal solutions readily apparent. However, considering the analysis conducted at α = 24° in Section 6.2.2 and the observed flow physics on the wing, it may be hypothesized that the primary challenge lies in capturing the turbulent motion generated on the windward wing. In this scenario, no coherent vortex is generated, and the breakdown has reached the wing's apex. As discussed in Section 6.2.2, the SAnegRC model does not accurately capture this phenomenon, and the PK model exhibits similar limitations. This issue stems from the intrinsic limitations of the model's formulation, which fails to generate the necessary turbulence near the leading-edge, as corroborated from the analysis conduced in Section 7.4.1. To address this challenge, new formulations of the one-equation model are explored through modifications of the production and destruction terms and the incorporation of machine learning techniques. The significant outcomes are detailed in Chapter 8.

8

Towards an Enhanced One-Equation Turbulence Model by Gene Expression Programming

This chapter elucidates the findings reported in Di Fabbio et al., 2024b, aiming to enhance RANS modeling capabilities through two innovative methodologies, which are introduced in Section 8.1. The first strategy involves extending the linear Boussinesq hypothesis to more accurately capture and model Reynolds stress anisotropy, thereby improving the predictive accuracy, as detailed in Section 8.1.1. The second strategy focuses on the development of an enhanced one-equation turbulence model, discussed in Section 8.1.2, aiming to more accurately represent turbulence production and destruction within the flow field. In both strategies, the SA model is employed, either in its standard form for the first strategy or with modifications for the second. These modifications involve adjusting coefficients in the production and destruction terms of the original SA equation and potentially developing a new formulation of these terms, leading to a novel eddy viscosity turbulence equation.

A machine learning techniques is employed, specifically GEP, which is introduced in Section 4.2.2. As described in Section 4.2.3, a CFD-driven framework is used to integrate GEP with the OpenFOAM solver for computing the RANS simulations. This integration enables the real-time evaluation of expressions generated by the machine learning algorithm.

At the initial stage, as presented in Section 8.2, four fundamental flows from the NASA challenge validation cases, the flat plate, channel, jet, and wall-mounted hump (accessible at `https://turbmodels.larc.nasa.gov`), are considered to evaluate the performance of the proposed models. These cases, characterized by complex flow dynamics such as significant wall curvature, pronounced flow separation, and exceptionally high Reynolds numbers, are crucial for the optimization phase of the model. The flow cases are analyzed individually, in a single-case CFD-driven training approach, followed by a comprehensive analysis of the derived model expressions. Following the evaluation and validation of the methodologies based on these fundamental cases, Section 8.3 discusses the training and numerical investigation of the VFE-2 delta wing configuration.

8.1. Methodology for improved one-equation model

The two methodologies applied for improving the one-equation turbulence model predictions are presented. Section 8.1.1 discusses the extension of the linear Boussinesq hypothesis to more accurately capture and model Reynolds stress anisotropy. Section 8.1.2 elucidates the development of an advanced one-equation turbulence model.

8.1.1. Extra-Anisotropic Reynolds Stress Modeling

Advancements in turbulence modeling have led to the exploration of EARSMs, which offer a refined approach over the traditional Boussinesq hypothesis by incorporating an additional anisotropic stress component, a_{ij}, into the Reynolds stress tensor representation as follows[1]

$$\tau_{ij}^R = \frac{2}{3}\rho k\delta_{ij} - 2\mu_t S_{ij}^* + a_{ij}. \tag{8.1}$$

Such EARSM-based closures can be represented in a dimensionless form, as given by

$$a_{ij}^* = \sum_k f^{(k)}(I_1, I_2, \ldots, I_n)V_{ij}^k, \tag{8.2}$$

which involves a summation of basis tensors, V_{ij}^k, each multiplied by functions of the invariants, $f^{(k)}$. Considering the purpose of this work and the selected test cases, three basis tensors and two invariants are utilized. Indeed, the application of three fundamental basis tensors alongside two invariants constitutes the standard methodology for analyzing two-dimensional flows (Pope, 1975). Furthermore, extending this framework to encompass three-dimensional cases, such as the VFE-2 delta wing, effectively simplifies the model's complexity. The employed basis tensors and invariants are thus defined as follows

$$\begin{gathered} V_{ij}^1 = s_{ij}, \quad V_{ij}^2 = s_{ik}\omega_{kj} - \omega_{ik}s_{kj}, \quad V_{ij}^3 = s_{ik}s_{kj} - \frac{1}{3}\delta_{ij}s_{mn}s_{mn}, \\ I_1 = s_{mn}s_{mn}, \quad I_2 = \omega_{mn}\omega_{mn}. \end{gathered} \tag{8.3}$$

The dimensionless anisotropic stress tensor, a_{ij}^*, represented by a combination of basis tensor, V_{ij}^k, and scalar invariants, I_k, is formulated through symbolic regression via the GEP framework (Weatheritt and Sandberg, 2016). This technique aims to identify the coefficients $f^{(k)}$, which are functions of the invariants, utilizing training datasets.

The tensors and invariants originate from the dimensionless strain rate tensor $s_{ij} = t_l S_{ij}^*$ and rotation rate tensor $\omega_{ij} = t_l W_{ij}$. Following the methodology proposed by Weatheritt and Sandberg, 2016, the turbulence timescale, t_l, must be derived when applying the SA turbulence model, due to the inability to compute the specific dissipation ratio, ω, directly from its equation (Eq. 3.84). Drawing inspiration from the QCR approach (Rumsey et al., 2020a), the timescale is computed based on the magnitude

[1] The sign of the Boussinesq equation has been inverted relative to Eq. 3.40 to align with the model's implementation in OpenFOAM, thereby ensuring easier implementation and facilitating a better understanding of the obtained results.

of the velocity gradient tensor as follows

$$t_l = \frac{1}{\sqrt{\frac{\partial u_m}{\partial x_n}\frac{\partial u_m}{\partial x_n}}}, \tag{8.4}$$

$$\text{where} \quad \sqrt{\frac{\partial u_m}{\partial x_n}\frac{\partial u_m}{\partial x_n}} = \sqrt{u_x^2 + u_y^2 + u_z^2 + v_x^2 + v_y^2 + v_z^2 + w_x^2 + w_y^2 + w_z^2}. \tag{8.5}$$

Subsequently, the dimensionalized anisotropic stress tensor a_{ij} is derived from the modeled dimensionless form a_{ij}^* as follows

$$a_{ij} = \frac{2\mu_t a_{ij}^*}{t_l}, \tag{8.6}$$

resulting in a revised Reynolds stress tensor equation given by

$$\tau_{ij}^R = \frac{2}{3}\rho k\delta_{ij} - 2\mu_t S_{ij}^* + \frac{2\mu_t a_{ij}^*}{t_l} = \frac{2}{3}\rho k\delta_{ij} - 2\mu_t\left(S_{ij}^* - \frac{a_{ij}^*}{t_l}\right). \tag{8.7}$$

The model employing this methodology is designated as SA+a_{ij}. The training of the GEP model commences with an initial set of EASMs. Throughout the optimization, the basis tensor V_{ij}^k remain unaltered, whereas the coefficients $f^{(k)}$, subject to I_k, are determined. These functions are generated randomly, presenting distinct functional structures and arbitrary constants. Each candidate model has 4 genes, representing unique coefficients for V_{ij}^k. The expression length for the coefficient function is primarily governed by the gene's head length and the truncation level of its expression tree. In this investigation, the head length is set to 5, the maximum size of the expression tree is limited to 12, and the population size is established at 400. For a comprehensive insight into the configuration parameters of GEP, readers are referred to the following references (Fang et al., 2023; Weatheritt and Sandberg, 2016, 2017; Zhao et al., 2020). In addition, the EVE code, which is utilized in this work and based on the GEP algorithms, is introduced in Section 4.2.

8.1.2. The enhanced one-equation model

The predominant source of numerical prediction error in the SA model is attributed to the production and destruction terms, which are expected to counterbalance each other, as elucidated and addressed by Moioli et al., 2019, 2022. Similar considerations are discussed in the dissertation towards the end of Chapter 6. Consequently, the diffusion terms of the standard SA turbulence model in Eq. 3.61 remains unaltered without further derivation or modification. The focus will be on devising a novel formulation for the terms of production and destruction. The enhancement of the SA model is then explored by adjusting these terms via GEP optimization. The modified equation, henceforth referred to as SA+PD, is proposed as follows

$$\frac{\partial\tilde{\nu}}{\partial t} + u_j\frac{\partial\tilde{\nu}}{\partial x_j} = C_P\tilde{S}\tilde{\nu} - C_D\left(\frac{\tilde{\nu}}{d}\right)^2 + \frac{1}{\sigma}\left[\frac{\partial}{\partial x_j}\left((\nu+\tilde{\nu})\frac{\partial\tilde{\nu}}{\partial x_j}\right) + c_{b2}\frac{\partial\tilde{\nu}}{\partial x_i}\frac{\partial\tilde{\nu}}{\partial x_i}\right], \tag{8.8}$$

where the coefficients $C_P(I_1, I_2)$ and $C_D(I_1, I_2)$ are functions of invariants I_1 and I_2, as defined in Eq. 8.3. The same GEP settings detailed in Section 8.1.1 are kept for this methodology as well, even though, in this case, the optimization process aims to find the best values for the coefficients C_P and C_D in front of the production and destruction terms of the original SA model. Therefore, using the standard Boussinesq assumption, an attempt has been made to modify the turbulence's production and destruction, optimizing the SA equation for various case studies.

Alternatively, an enhanced one-equation turbulence model is derived from the well-established $k-\omega$ model, introduced in Section 3.4.3. By substituting the k and ω equations, Eq. 3.83 and Eq. 3.84 respectively, the ν_t equation can be derived as follows

$$\frac{D\nu_t}{Dt} = \frac{1}{\omega}\left(\frac{Dk}{Dt} - \nu_t\frac{D\omega}{Dt}\right) = (1-\gamma_\omega)\frac{\tau_{ij}^R}{\omega}\frac{\partial u_i}{\partial x_j} - \beta^k k + \beta^\omega \nu_t \omega + \dots, \tag{8.9}$$

where the dissipation terms are omitted because, as previously explained, the scope is to derive a new formulation for the production and destruction terms. The Reynolds stress tensor τ_{ij}^R is computed using the Boussinesq assumption, where the isotropic term $2/3\rho k\delta_{ij}$ is neglected. However, it does not play any role in incompressible cases.

The terms on the RHS can be reformulated by substituting $k = \nu_t\omega$, resulting in the ν_t equation as follows

$$\frac{D\nu_t}{Dt} = 2(1-\gamma_\omega)\nu_t\frac{S_{ij}^*}{\omega}\frac{\partial u_i}{\partial x_j} - (\beta^k - \beta^\omega)\nu_t\omega + \frac{1}{\sigma}\left[\frac{\partial}{\partial x_j}\left((\nu+\tilde{\nu})\frac{\partial\tilde{\nu}}{\partial x_j}\right) + c_{b2}\frac{\partial\tilde{\nu}}{\partial x_i}\frac{\partial\tilde{\nu}}{\partial x_i}\right], \tag{8.10}$$

which include the original formulation of the SA diffusion terms. It is worth noting that the new production term has the advantage that changes of τ_{ij}^R are reflected in itself as well, and not just in the Boussinesq assumption. In this way, a kind of double optimization is possible while modeling the anisotropy of the Reynolds stress.

The specification of ω requires a distinct formulation, since the ω equation cannot be applied to appropriately model the production and destruction terms in Eq. 8.10. Firstly, the destruction term is considered. The turbulence length scale, l_t, is equated to the wall distance, $l_t = d$, within the context of the one-equation model. This assumption facilitates the scaling of turbulence kinetic energy as $k \propto \nu_t^2/d^2$, as demonstrated by Bradshaw et al., 1967. Consequently, the relationship between ω and the wall distance is derived as follows

$$k \propto \frac{\nu_t^2}{d^2} \quad \text{and} \quad \omega \propto \frac{k}{\nu_t} \quad \rightarrow \quad \omega \propto \frac{\nu_t}{d^2}. \tag{8.11}$$

Accordingly, the formulation of the destruction term aligns with the original model as outlined in Eq. 3.61, where $D = (\beta^k - \beta^\omega)(\nu_t/d)^2$, introducing a new coefficient or function to calibrate the term.

In terms of the production term, the specific dissipation rate, ω, is conceptualized as a parameter used to render the deviatoric strain rate tensor, S_{ij}^*, dimensionless. Considering the analyses presented in Section 8.1.1, ω is reformulated based on the

magnitude of the velocity gradient tensor, expressed as $\omega = 1/t_l$, with the timescale t_l in Eq. 8.4.

Adhering to the definitions stipulated in the baseline SA model (Spalart and Allmaras, 1992) and presented in Section 3.4.1,

$$\nu_t = \tilde{\nu} f_{v1}, \quad \text{where} \quad f_{v1} = \frac{\xi^3}{\xi^3 + c_{v1}^3}, \quad \text{and} \quad \xi = \frac{\tilde{\nu}}{\nu}, \tag{8.12}$$

and maintaining the original form of the diffusion term, the enhanced one-equation turbulence model for the variable $\tilde{\nu}$ is delineated as follows

$$\frac{D\tilde{\nu}}{Dt} = 2(1-\gamma_\omega) t_l S_{ij}^* \frac{\partial u_i}{\partial x_j} \tilde{\nu} - (\beta^k - \beta^\omega) \left(\frac{\tilde{\nu}}{d}\right)^2 + \frac{1}{\sigma} \left[\frac{\partial}{\partial x_j} \left((\nu + \tilde{\nu}) \frac{\partial \tilde{\nu}}{\partial x_j} \right) + c_{b2} \frac{\partial \tilde{\nu}}{\partial x_i} \frac{\partial \tilde{\nu}}{\partial x_i} \right]. \tag{8.13}$$

To mitigate the dependency on wall distance and enhance the model's versatility, a novel formulation of the destruction term is introduced, analogous to the original SA model but with modifications to better address flows distant from walls. This adjustment is particularly crucial in HRL methodologies (Spalart et al., 2006), where a blending function, f_d, facilitates a smooth transition between RANS and LES modes based on the proximity to the wall. The blending function, expressed in Eq. 3.74, facilitates the dynamic adjustment of the destruction term, enabling it to accurately represent both near-wall and free-stream behaviors, through the following expression:

$$\tilde{D} = \frac{\tilde{\nu}}{d^2} - f_d \cdot \min\left(\frac{\tilde{\nu}}{d^2} - \sqrt{\beta^*} |S_{ij}|^2 t_l, 0 \right). \tag{8.14}$$

Here, $\beta^* = 0.09$, as identified by Wilcox, 1998, and $|S_{ij}| = \sqrt{2 S_{ij} S_{ij}}$ represents the magnitude of the strain rate tensor. Therefore, $\tilde{D} = \tilde{\nu}/d^2$ when $f_d = 0$ (near the wall) and transitions to $\tilde{D} = \sqrt{\beta^*} |S_{ij}|^2 t_l$ when $f_d = 1$ (away from the wall), ensuring that the destruction term's value is not only preserved but potentially increased in areas with significant strain rates to adequately counterbalance the production term.

The enhanced model, denoted as CSA (Coupled Spalart-Allmaras model), integrates these modifications while retaining the core structure of the original SA formulation and it is written as follows

$$\frac{D\tilde{\nu}}{Dt} = 2 c_{b1} t_l S_{ij}^* \frac{\partial u_i}{\partial x_j} \tilde{\nu} - c_{w1} f_w \tilde{D} \tilde{\nu} + \frac{1}{\sigma} \left[\frac{\partial}{\partial x_j} \left((\nu + \tilde{\nu}) \frac{\partial \tilde{\nu}}{\partial x_j} \right) + c_{b2} \frac{\partial \tilde{\nu}}{\partial x_i} \frac{\partial \tilde{\nu}}{\partial x_i} \right], \tag{8.15}$$

where the production and destruction coefficients are substituted with the original ones from the SA model, as presented in Section 3.4.1. Indeed, the original coefficient formulations from the SA model have been successfully tested, demonstrating the balanced and well-constructed nature of the new equation. For this reason, they are utilized in the new formulation, although significant potential remains for further improvements by employing the CSA equation.

Modeling the anisotropy of Reynolds stresses following the first approach has been conducted using both the SA model in Eq. 3.61 and the new CSA model in Eq. 8.15

as turbulence closure equation. The same GEP settings detailed in Section 8.1.1 are employed. The CSA turbulence equation enables the simultaneous optimization of Reynolds stresses and the production term, similar to the approach taken for the two-equation $k\omega$SST model (Weatheritt and Sandberg, 2016). The model employing this methodology is designated as CSA+a_{ij}. The two approaches discussed above are then interconnected.

8.2. NASA validation cases

This section details the outcomes of extensive optimizations of RANS turbulence models, aimed at enhancing their predictive accuracy for a range of fundamental flows. The following four NASA challenge validation cases are considered to perform the training process.

- **2DZP**: 2D Zero Pressure Gradient Flat Plate.
- **2DFDC**: 2D Fully-Developed Channel Flow at a high Reynolds number.
- **2DWMH**: 2D NASA Wall-Mounted Hump with Flow Separation.
- **ASJ**: Axisymmetric Subsonic Jet.

The computational domain is not discussed herein, as it can be downloaded from `https://turbmodels.larc.nasa.gov`, where all necessary information is provided. These are standard validation cases that are well-known in the field of turbulence modeling research.

For each case, specific quantities are meticulously defined for computing the cost functions. For the flat plate case, emphasis is placed on the stream-wise friction coefficient and the velocity profile at a stream-wise position of $x/L = 0.97$, measured relative to the distance from the wall. The training for the channel flow case is informed by the velocity profile at a stream-wise location of $x/h = 500$, also relative to the wall distance. The axisymmetric subsonic jet case focuses on the stream-wise velocity and shear stress profiles at downstream positions $x/D_{\text{jet}} = 15$ and 20. Lastly, for the wall-mounted hump case, the cost function incorporates both the friction and pressure coefficients along the surface of the hump, as well as the stream-wise velocity profiles at axial positions immediately before and after the separation bubble, specifically at $x/c = 0.9$, 1.0, and 1.1.

For the RANS simulations, the rhoPimpleFoam solver is explicitly used for the compressible jet, while the other cases utilize simpleFoam within the OpenFOAM framework, discussed in Section 4.1. In this OpenFOAM simulation configuration, the numerical schemes are tailored for a steady-state analysis. The gradient computations default to a Gaussian linear approach, with a specific cell-limited modification applied to the velocity gradient to enhance numerical stability. The divergence schemes are meticulously selected for different variables: a bounded linear upwind scheme is used for velocity fluxes, ensuring accuracy while preventing numerical oscillation; an upwind scheme is adopted for the turbulence model variable, $\tilde{\nu}$, favoring stability; and a

standard Gauss linear scheme is applied for the effective viscosity multiplied by the deviatoric tensor of velocity gradient, aiming for a balance between accuracy and stability. The Laplacian terms employ a Gauss linear corrected scheme to improve accuracy by correcting for mesh non-orthogonality. Linear interpolation is used as the default for intermediate values, and the surface normal gradients are corrected to account for mesh irregularities, ensuring that the simulation results are both accurate and reliable[2].

Five simulation results have been compared with the experimental data. The methodologies presented in Section 8.1 are thus tested.

1. **SA**: SA turbulence model by applying the Boussinesq assumption.
2. **SA+a_{ij}**: SA turbulence model by optimizing τ_{ij}^R modeling the Reynolds stress anisotropy, as introduced in Section 8.1.1. GEP provides the coefficients $f^{(1)}$, $f^{(2)}$, $f^{(3)}$ that multiply the basis tensors $V_{ij}^1, V_{ij}^2, V_{ij}^3$ for modeling a_{ij}.
3. **SA+PD**: Boussinesq assumption applied with an optimized version of the SA turbulence model in Eq. 8.8. The original production and destruction coefficients of the SA equation, c_{b1} and $c_{w1}f_w$ respectively, have been substituted with C_P and C_D found through GEP optimization.
4. **CSA**: new CSA one-equation turbulence model in Eq. 8.15 by applying the Boussinesq assumption.
5. **CSA+a_{ij}**: new CSA one-equation turbulence model in Eq. 8.15 by optimizing τ_{ij}^R modeling the Reynolds stress anisotropy, as introduced in Section 8.1.1. The modeled a_{ij} is also included in the new turbulence production term in Eq. 8.15 by noticing that $2\tilde{\nu}S_{ij}^* = \tau_{ij}^R/f_{\nu 1}$. It allows to optimize with the same 3 coefficients ($f^{(1)}$, $f^{(2)}$, $f^{(3)}$) both the anisotropy tensor and the turbulence production term. The employed production term thus becomes $P = 2c_{b1}\left(S_{ij}^* t_l - a_{ij}^*\right)\dfrac{\partial u_i}{\partial x_j}\tilde{\nu}$.

Some variables related to the boundary layer theory need to be defined before presenting the results. In turbulent boundary layers, the dimensionless variables u^+ and y^+ are commonly defined to facilitate the analysis of velocity profiles and the scaling of turbulence near walls. The non-dimensional velocity, u^+, is defined as follows

$$u^+ = \frac{u}{u_\tau}, \tag{8.16}$$

where u denotes the local fluid velocity parallel to the wall, and u_τ is the friction velocity, given by

$$u_\tau = \sqrt{\frac{\tau_w}{\rho}}, \tag{8.17}$$

with τ_w representing the wall shear stress and ρ the fluid density. Similarly, the dimensionless wall-normal distance, y^+, is given by

$$y^+ = \frac{y u_\tau}{\nu}, \tag{8.18}$$

[2]The numerical approach is described by following the OpenFOAM parameters nomenclature, ensuring ease of understanding and reproducibility.

where y is the physical distance from the wall, and ν is the kinematic viscosity of the fluid. These definitions are essential for the characterization of flow dynamics in the viscous sub-layer of turbulent boundary layers. These dimensionless parameters are crucial in the analysis of near-wall turbulent flows, facilitating the universal representation of velocity profiles and the scaling of turbulence statistics.

Furthermore, the momentum thickness, θ, is a fundamental parameter in boundary layer theory that characterizes the velocity profile relative to the free-stream. It is defined as follows

$$\theta = \int_0^\delta \left(1 - \frac{u}{U_\infty}\right)\left(\frac{u}{U_\infty}\right) dy, \tag{8.19}$$

where u is the fluid velocity parallel to the wall at a distance y from the wall, U_∞ is the free-stream velocity, and δ represents the boundary layer thickness. The parameter y denotes the distance normal to the wall, extending from the wall to the edge of the boundary layer where the flow velocity is approximately 99% of the free-stream velocity, U_∞.

The Reynolds number based on momentum thickness, Re_θ, is a dimensionless quantity used to characterize the flow within the boundary layer, defined as follows

$$Re_\theta = \frac{\rho U \theta}{\mu}. \tag{8.20}$$

This Reynolds number is crucial for understanding the transition from laminar to turbulent flow, with higher values indicating increasingly turbulent flow characteristics.

8.2.1. Flat plate

Figure 8.1 presents the comparison of the friction coefficient, c_f, along the flat plate and the velocity profile at $x/L = 0.97$ as functions of the distance from the wall. These numerical results are compared against experimental data from White and Majdalani, 2006. Table 8.1 summarizes the expressions found by the GEP training.

The SA model provides velocity predictions that align well with theoretical expectations concerning the distance from the wall. However, the model tends to underpredict or overpredict the c_f for Re_θ below or above 7500, respectively. Except for the CSA+a_{ij} model, all models exhibit certain deviations in accurately predicting the friction coefficient, yet conform to the logarithmic velocity profile. The SA+PD modifications fail to enhance the performance of the SA model for the flat plate test case. This outcome is attributed to the coefficients already being tailored for such conditions. Conversely, integrating the SA+a_{ij} modification substantially improves the prediction of the c_f only in the downstream region of the flat plate. Finally, the development of a new formulation for the one-equation turbulence model (referred to as CSA) emerges as a viable solution in this context. It demonstrates stability and consistency with the SA model, while also facilitating more precise optimization through GEP. The enhanced optimization capability of the CSA+a_{ij} model can be attributed to the optimization of Reynolds stress anisotropy coupled with the production term.

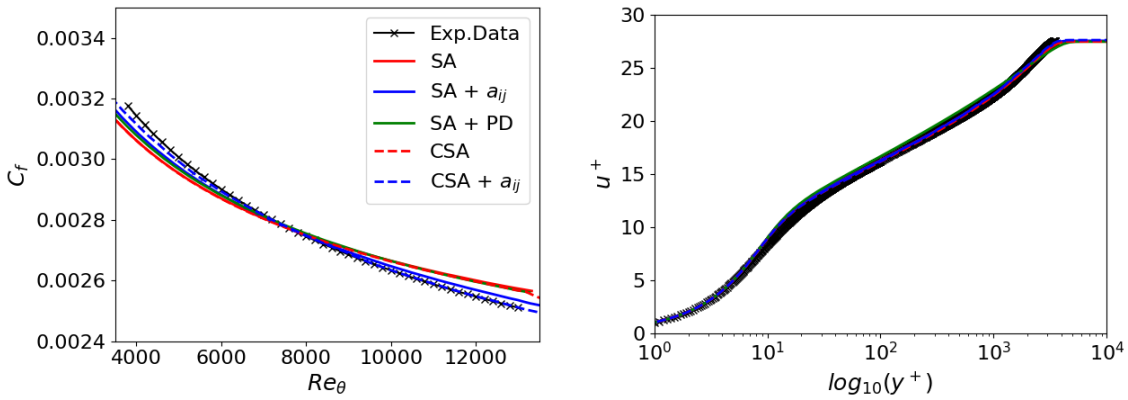

Figure 8.1: 2DZP: friction coefficient and velocity profile (Di Fabbio et al., 2024b).

Table 8.1: 2DZP: GEP expressions. Numbers rounded to the third decimal place.

	$f^{(1)}$	$f^{(2)}$	$f^{(3)}$
SA+a_{ij}	$-0.097I_2I_1^2 - 0.097I_2I_1$	$-I_2I_1^2 - 2.15I_2I_1 - 0.183I_2$	$3.903I_1 + 8.153$
CSA+a_{ij}	$-0.01I_2^2 + 0.001I_1I_2 - 0.002I_2 + 0.0001I_1 - 0.0001$	$0.097I_1 - 5I_2 + 0.294$	$0.43I_1 + 2.21894$
	C_P	C_D	
SA+PD	$0.097I_1 - 0.097I_2 + 0.43$	$1.911I_1 + I_2 + 3.546$	

8.2.2. Channel flow

The velocity profile at $x/h = 500$ is depicted in Fig. 8.2. All models demonstrate close agreement with the theoretical results (White and Majdalani, 2006). Each model accurately represents then the vertical stratification across the viscous sub-layer, logarithmic layer, and turbulent core, even in scenarios characterized by very high Reynolds numbers. Such findings underscore the efficacy of the HRL blending function integrated into the destruction term of the CSA model, confirming its ability to maintain the integrity of the law of the wall with a well-represented velocity profile. The expressions derived through GEP training are summarized in Table 8.2.

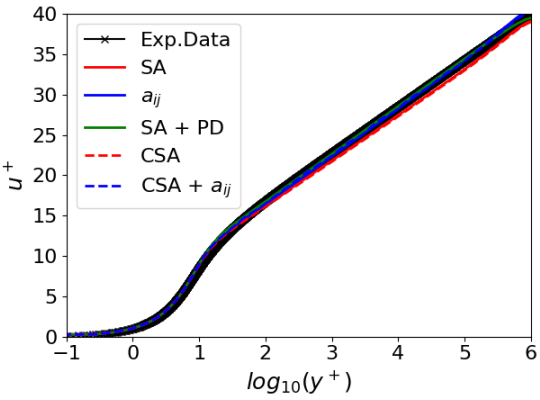

Figure 8.2: 2DFDC: law of the wall (Di Fabbio et al., 2024b).

Table 8.2: 2DFDC: GEP expressions. Numbers rounded to the third decimal place.

	$f^{(1)}$	$f^{(2)}$	$f^{(3)}$
SA+a_{ij}	$0.205I_1^2 + 0.205I_2I_1 - 0.001I_1$	$2I_1I_2^2 + 0.216I_2 - 0.089$	$2I_2^2 + I_1I_2 + 7I_2 + 2I_1 + 6$
CSA+a_{ij}	$0.097I_2 - 0.005$	$-0.15I_1^2 + 0.087I_1 - 2I_2$	$-1.15I_2 - 2.527$
	C_P	C_D	
SA+PD	$0.205I_2 + 1.485$	$-0.43I_2I_1 - 2.198I_1 + 2.518I_2 + 12.870$	

8.2.3. Wall-mounted hump

Figures 8.3, 8.4, and 8.5 juxtapose the numerical results with experimental data from Seifert et al. (2002) for the wall-mounted hump test case.

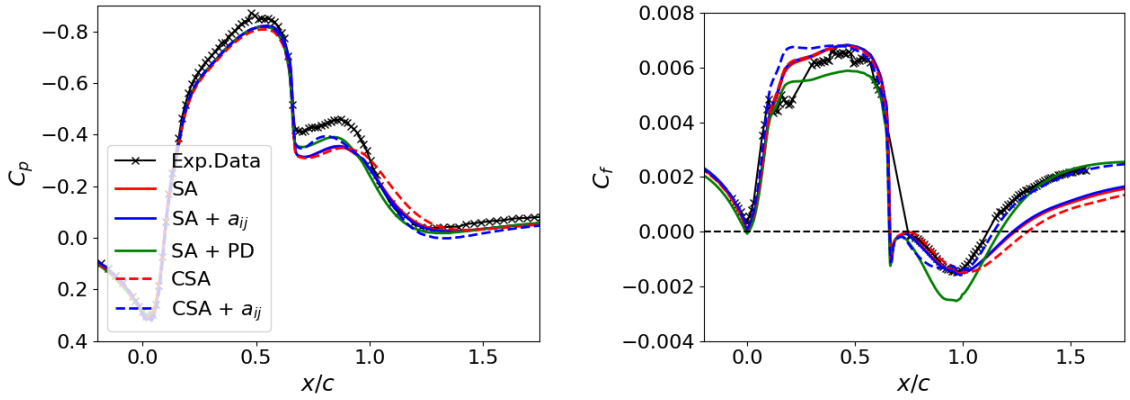

Figure 8.3: 2DWMH: friction and pressure coefficients (Di Fabbio et al., 2024b).

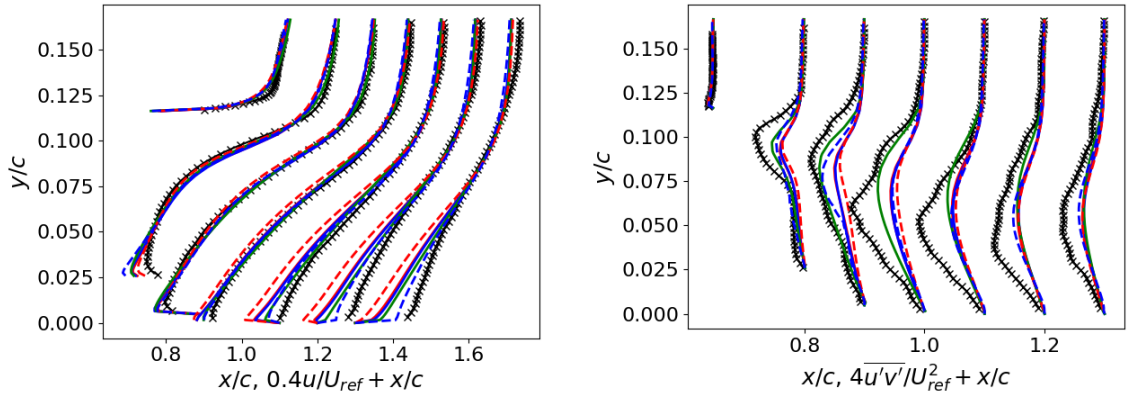

Figure 8.4: 2DWMH: velocity and Reynolds stress profiles (Di Fabbio et al., 2024b).

Figure 8.3 presents the pressure and friction coefficients along the surface. The reattachment point, indicative of the separation bubble's extent, is delineated at the juncture where $c_f = 0$. Notable discrepancies are observed adjacent to and beyond the separation bubble. Specifically, the SA model tends to underestimate both coefficients following the bubble, mirroring the deviation observed for the flat plate. However, the discrepancies in the friction coefficient for the hump case are more pronounced compared to those in the flat plate scenario.

Figure 8.4 illustrates the velocity and shear stress profiles at selected locations around the hump. Analysis of the velocity profiles reveals increased deviation near the hump's surface, while the shear stress profiles exhibit significant differences in the vicinity of the separation bubble. Despite not being explicitly included in the cost functions, the Reynolds stress profile are accurately represented by the CSA+a_{ij} and SA+PD models. The CSA model exhibits slight deviations from the SA model but demonstrates alignment with the results of the $k\omega$SST model reported in the literature (Rumsey and Coleman, 2022). With the exception of the SA+a_{ij}, all models subjected to training enhance the accuracy of numerical predictions. Thus, the modification of Reynolds stresses through the modeling of the anisotropic tensor alone proves inadequate for accurately predicting the reattachment point. Enhancement in the prediction necessitates the modification and the training of the production term. Notably, the CSA+a_{ij} model achieves outcomes highly consistent with the reference data, marking one of the most accurate predictions rendered by a one-equation model to date (Rumsey and Coleman, 2022).

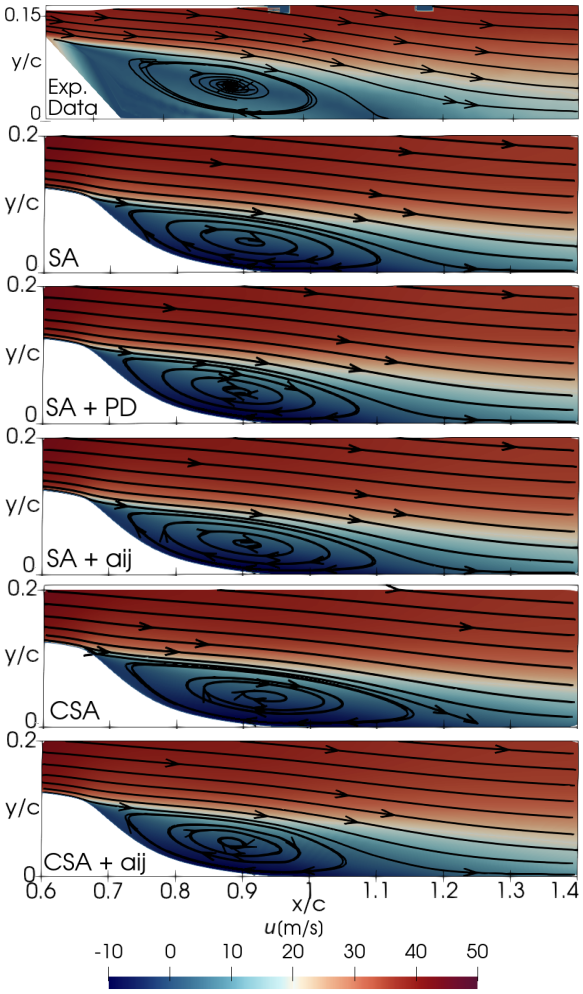

Figure 8.5: 2DWMH: velocity contour plots (Di Fabbio et al., 2024b).

Figure 8.5 illustrates the efficacy of the trained models through the contour of the velocity flow field. Streamlines are utilized to illustrate separation bubbles, facilitating a comparison between experimental and numerical data. As indicated in Figs. 8.3 and 8.5, experimental analyses approximate the reattachment point at $x/c = 1.1$, whereas the SA model predicts it at $x/c = 1.2$. Flow fields generated by the CSA+a_{ij} and SA+PD models exhibit notable congruence, adjusting the reattachment closer to $x/c = 1.12$, whereas the SA+a_{ij} model does not significantly alter it. The trained

models, except for SA+a_{ij}, accurately depict the flow dynamics along the hump's down ramp, closely mirroring experimental observations. Expressions derived from GEP training for the hump case are written in Table 8.3, warranting a comprehensive analysis.

Table 8.3: 2DWMH: GEP expressions. Numbers rounded to the third decimal place.

	$f^{(1)}$	$f^{(2)}$	$f^{(3)}$
SA+a_{ij}	$-2I_2I_1^2 - I_1 + I_2 + 0.205$	$-I_2^2 + I_1I_2 - 0.097I_2 - 2I_1 + 1$	-2.160
CSA+a_{ij}	$-I_1^2 - 0.911I_2I_1 + 1.911I_2^2$	0	$I_2I_1 - 0.903I_1 - 0.108$
	C_P	C_D	
SA+PD	$-0.205I_1 + I_2 - 0.170$	$4 - I_1I_2$	

Figure 8.6 presents the $f^{(1)}$ contour along with streamlines for the CSA+a_{ij} model, alongside the coefficients C_P and C_D for the SA+PD model. As elucidated by Fang et al., 2023, the coefficient $f^{(1)}$ plays a pivotal role in Eq. 8.2, meriting an in-depth examination. Within the separation zone, $f^{(1)}$ demonstrates oscillatory behavior, ranging from 0.6 to −0.6, indicative of simulation unsteadiness. It is suggested that these results could benefit from time-averaging to mitigate such oscillations. For the SA+PD model, coefficients C_P and C_D exhibit stable values of approximately 0.3 and 3.7, respectively, with C_P exceeding the original model's coefficient, c_{b1}. The negative value of $f^{(1)}$ leads to an increase in turbulence production, a similar effect to that caused by the C_P coefficient. These expressions are derived as functions of the invariants I_1 and I_2.

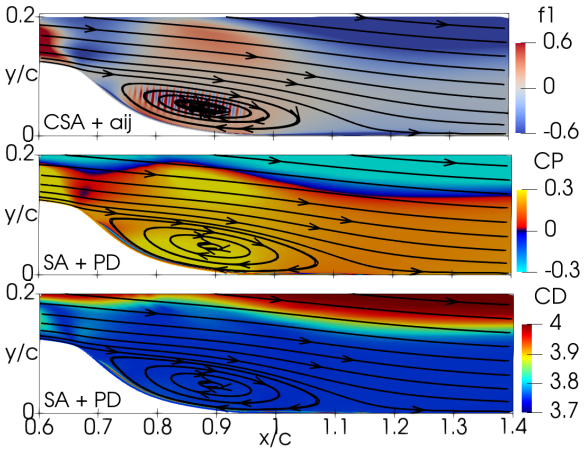

Figure 8.6: 2DWMH: $f^{(1)}$, C_P, and C_D contours and streamlines (Di Fabbio et al., 2024b).

The dynamic interplay between these invariants is graphically illustrated in Fig. 8.7. Given that the invariants are normalized by the velocity gradient tensor's magnitude, the axes are limited to unity. The function $f^{(1)}$ assumes a positive value when the magnitude of vorticity (I_2) surpasses that of the strain rate (I_1), and vice versa. In the separation zone, I_1 and I_2 are closely matched, leading to oscillations of $f^{(1)}$ between positive and negative values. This trend is less pronounced for the C_P coefficient, which shows steadiness. Furthermore, the C_D coefficient peaks at a value of 4 and diminishes with increasing invariants, suggesting that enhancing the production term is crucial when vorticity dominance over strain rate is observed, and conversely, the destruction term should be attenuated.

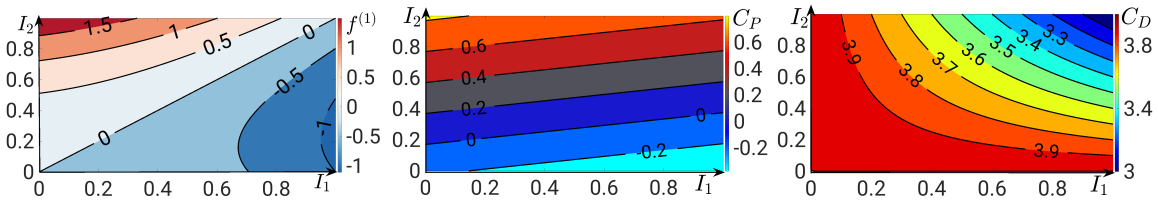

Figure 8.7: 2DWMH: expressions as function of the invariants (Di Fabbio et al., 2024b).

8.2.4. Axisymmetric subsonic jet

Figures 8.8 and 8.9 illustrate the velocity and shear stress profiles of the jet case along the jet axis and at selected cross-sections. The CSA+a_{ij} and SA+PD models demonstrate notable improvements, effectively reducing diffusion and enhancing the accuracy of mean flow and second-moment profiles.

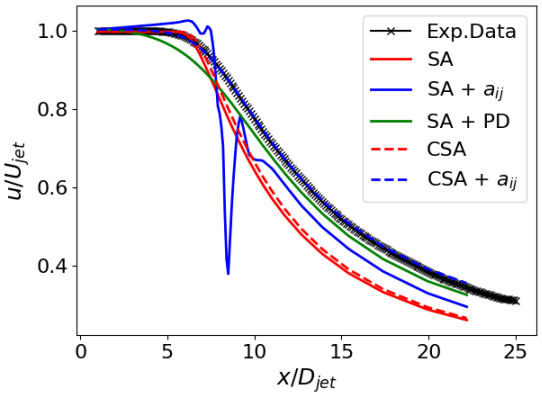

Figure 8.8: ASJ: velocity profiles along the jet axis (Di Fabbio et al., 2024b).

While the improvements in shear stress profiles are not as marked as those in the velocity profiles, they remain significant, especially considering that RANS models are primarily focused on mean flow characteristics. In the jet case, the SA model's destruction term, as delineated in Eq. 3.61, exhibits limited relevance due to its dependency on wall distance. The CSA model, which incorporates the HRL blending function, effectively addresses this limitation. Furthermore, the SA+a_{ij} model does not achieve convergence and demonstrates undesirable non-stationary effects, highlighting the need for further research to understand the contributing factors to these observations.

Figure 8.10 presents the flow field contours to evaluate the performance of the trained models. The flow fields predicted by the CSA+a_{ij} and SA+PD models show significant similarities, notably narrowing the jet radius and extending the jet length compared to the baseline simulation. Along the jet centerline, the velocity exhibits a slower decrement, which is indicative of diminished diffusion effects (Fang et al., 2023).

It is important to acknowledge that these modifications uniformly influence the entire jet, rather than implementing different adjustments across the laminar ($x/D_{jet} \leq 5$), transition ($5 < x/D_{jet} \leq 10$), and fully turbulent ($10 < x/D_{jet} \leq 25$) regions. Notably, a less precise prediction of stream-wise velocity in the transition region is observed for all trained models in Fig. 8.9. However, this outcome aligns with expectations, given that the trained model prioritizes turbulence mixing, supported by a cost function centered on velocity profiles within the fully turbulent zone.

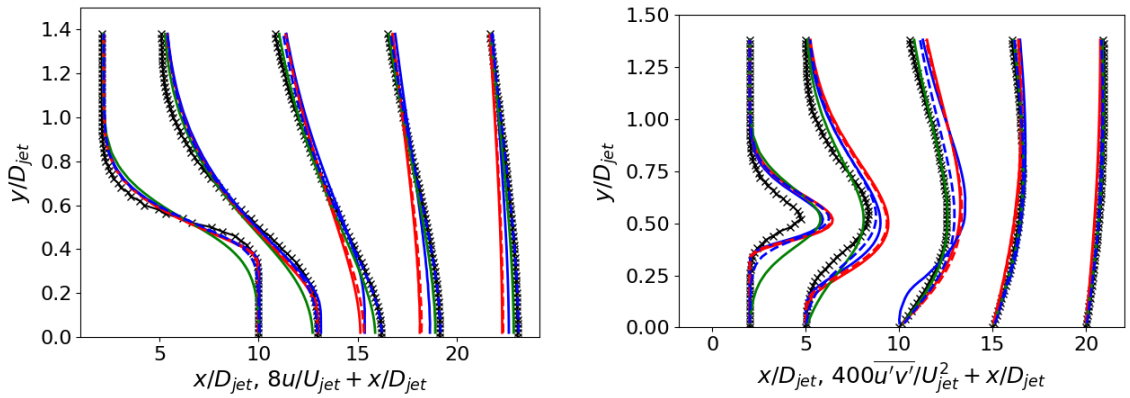

Figure 8.9: ASJ: velocity and Reynolds stress profiles (Di Fabbio et al., 2024b).

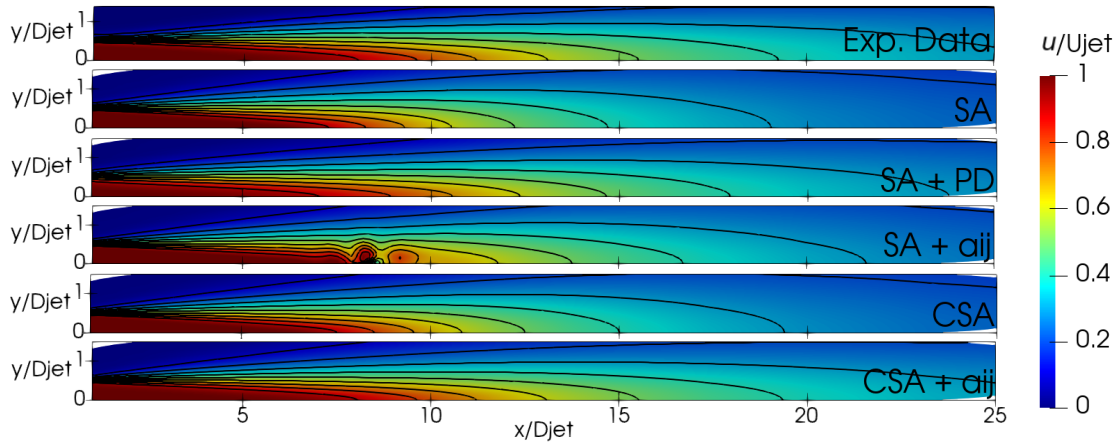

Figure 8.10: ASJ: normalized velocity contour plots (Di Fabbio et al., 2024b).

Table 8.4 presents the expressions derived through GEP training. Figures 8.11 depicts the $f^{(1)}$ contour for the CSA+a_{ij} model, alongside the coefficients C_P and C_D for the SA+PD model. Fig. 8.12 shows these expressions as functions of the invariants, I_1 and I_2. In the jet region, the function $f^{(1)}$ is characterized by a uniform value of 0.01. Indeed, considering its dependence on the two invariants, I_1 and I_2, the function $f^{(1)}$ exhibits a negligible value, except under conditions of high vorticity and significant strain-rate stress.

The coefficients C_P and C_D maintain positive values, except when I_1 exceeds I_2 by at least an order of magnitude. Upon examining the contour field, the coefficients C_P and C_D are observed to remain stable at values of approximately 0.1 and 0.195, respectively, with C_P being lower than the original model's coefficient, c_{b1}, suggesting that the trained model necessitates reduced production compared to the original model. Similarly, the small positive value of $f^{(1)}$ leads to a decrease in turbulence production. This contrasts with the results analyzed for the hump case, which indicate

a need for decreased turbulence production. Such behavior underscores the difficulty of developing a generic model capable of accurately representing multiple scenarios. Notable variations of these parameters are detected near the jet axis. They are likely attributable to velocity gradient values corresponding to the boundary condition.

Table 8.4: ASJ: GEP expressions. Numbers rounded to the third decimal place.

	$\boldsymbol{f^{(1)}}$	$\boldsymbol{f^{(2)}}$	$\boldsymbol{f^{(3)}}$
SA+a_{ij}	$-0.205I_2 - 0.0307$	$-I_2 - 0.163$	$-I_2^2 - 2I_1I_2 - 2.971I_2 - 6.174I_1 + 0.358$
CSA+a_{ij}	$0.144I_1^3 + 0.776I_2I_1^2 - 0.056I_1^2 - 0.3I_2I_1$	$I_1I_2 - 2I_2 + 0.081$	$-I_1 - 0.85$
	$\boldsymbol{C_P}$	$\boldsymbol{C_D}$	
SA+PD	$0.218I_2 - 0.013I_1$	$0.038I_1I_2 - 0.003I_2 + 0.185$	

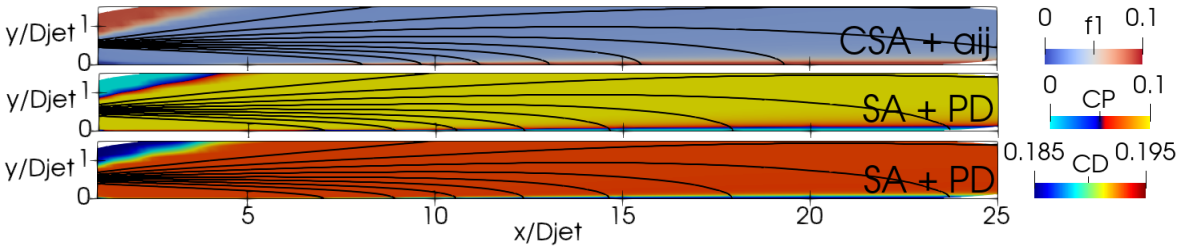

Figure 8.11: ASJ: $f^{(1)}$, C_P, and C_D contours and streamlines (Di Fabbio et al., 2024b).

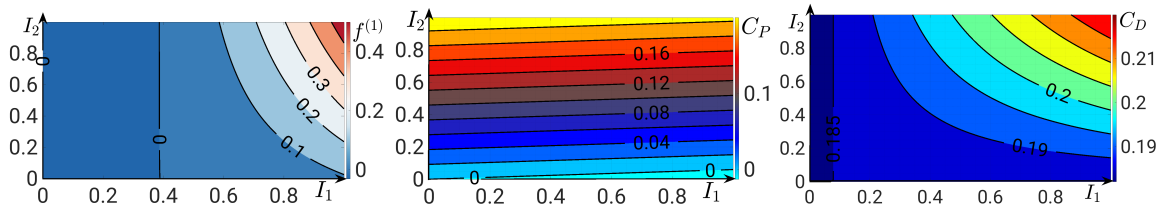

Figure 8.12: ASJ: expressions as function of the invariants (Di Fabbio et al., 2024b).

8.3. GEP training on the VFE-2 delta wing

Upon the assessment of methodologies across the foundational cases, the CFD-driven GEP training is performed on the VFE-2 delta wing configuration, illustrated in Fig. 8.13 and introduced in Section 2.1.6. The analysis has been conducted at an angle of attack of 23°, operating at $Re = 1 \times 10^6$ and $Ma = 0.07$. The selected cost function incorporated the evaluation of pressure coefficients across the wing's surface

at diverse span-wise locations, specifically at $\xi = 0.2$, 0.4, 0.6, 0.8, and 0.95. The experimental data can be found in the literature (Furman and Breitsamter, 2009) and are further discussed by Tangermann et al., 2012. The flow over the wing is characterized by a vortex system on its upper surface and it is discussed in detail in Chapter 5. At a sufficiently high angles of attack ($\alpha = 23°$), vortex breakdown occurs, significantly altering the downstream flow field. Traditional eddy viscosity models struggle to accurately capture such vortex breakdown phenomena. Therefore, in line with the methodologies applied to the NASA validation cases, the new turbulence models are evaluated, with CFD-driven training undertaken to refine the predictions of the one-equation model.

The computational grid, depicted in Figure 8.13, employs an unstructured mesh comprising approximately 661.000 cells, featuring 30 prism layers adjacent to the wing surface to ensure a first cell layer thickness that achieves $y^+ = 1$, while polyhedral volumes populate the remaining domain. Given the symmetrical flow conditions, simulations were restricted to the half-wing to save computational resources. Cell size within the computational domain is variable, with areas necessitating heightened resolution, specifically around and atop the wing, receiving focused refinement. The leading and trailing-edges received particular attention during mesh design. To enhance mesh quality and ensure well-defined surface normal, the sharp leading edge was slightly rounded in the model, a modification that negligibly affects flow dynamics. The primary aim of the mesh design was not to probe mesh convergence but rather to illustrate the GEP method's capacity to develop turbulence models for such configurations, even without high mesh resolution. Regarding the numerical approach, the same settings applied for the investigation of the NASA validation cases are used with the exception of the turbulence variable, $\tilde{\nu}$, where in this test case, the linear interpolation is employed.

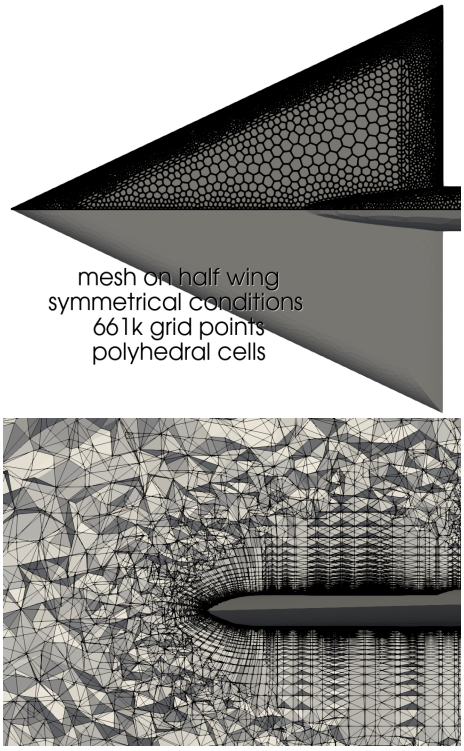

Figure 8.13: VFE2: geometry and mesh.

Figure 8.14 presents cross-sectional plots of the surface pressure coefficient, c_p, at various stream-wise locations along the wing, as illustrated in the top view in Fig. 8.15. At the first cross-section ($\xi = 0.2$), the suction peak is slightly underpredicted by all simulations, except for the results from the SA+a_{ij} model. This suggests that the resolution near the vortex formation area is adequate, leading to accurate vortex strength predictions, except for the SA baseline and CSA models, which indicate a weaker vortex. Notably, with the exception of the SA+a_{ij} model, neither simulations nor experiments capture a second peak indicative of a secondary vortex, suggesting its absence over the wing. Notably, the SA+a_{ij} model predicts a stronger primary vortex compared to other models, which in turn successfully induces the presence of the secondary vortex.

At $\xi = 0.4$, only the SA+a_{ij} and CSA+a_{ij} models accurately match the primary peak observed experimentally. This accuracy implies that modeling anisotropy enhances vortex formation and turbulence production near the leading edge. This behavior also corroborates the conclusions drawn at the end of Chapter 7. While the isotropic part of the Reynolds stress tensor enables the prediction of vortex breakdown, it does not enhance turbulence production near the wing apex. In contrast, the anisotropic part effectively fulfills this role, predicting an enhanced vortical motion of the flow in proximity to the wing apex. The secondary peak is discernible in the numerical results from SA+a_{ij} and SA+PD models, whereas the CSA+a_{ij} model predict the secondary vortex breakdown, indicative of the primary vortex's increased instability. Indeed, Figs. 8.15 and 8.16 reveal that this model predicts a vortex breakdown further upstream over the wing, compared to the other CFD outcomes.

In the third cross-section at $\xi = 0.6$, the GEP models excellently capture the experimental data, accurately predicting the pressure pea associated with the primary vortex. Although the primary peak is slightly underpredicted, the improvement over baseline SA results is significant, and the position of the primary vortex closely matches the experimental observations. Furthermore, the SA+a_{ij} model predicts a strong and stable secondary vortex, diverging from other observations. The subsequent cross-section at $\xi = 0.8$ is located downstream of the primary vortex breakdown, as predicted by the experiments. Indeed, as investigated by Tangermann et al., 2012, the experimental flow field visualizations indicate vortex breakdown occurring at approximately 60% of the root chord length. However, even though the CFD outcomes do not predict the vortex breakdown at this location, no significant discrepancies are observable between the experimental and the numerical data. Finally, in the last cross-section, only a weak indication of the primary vortex is detected before reaching the

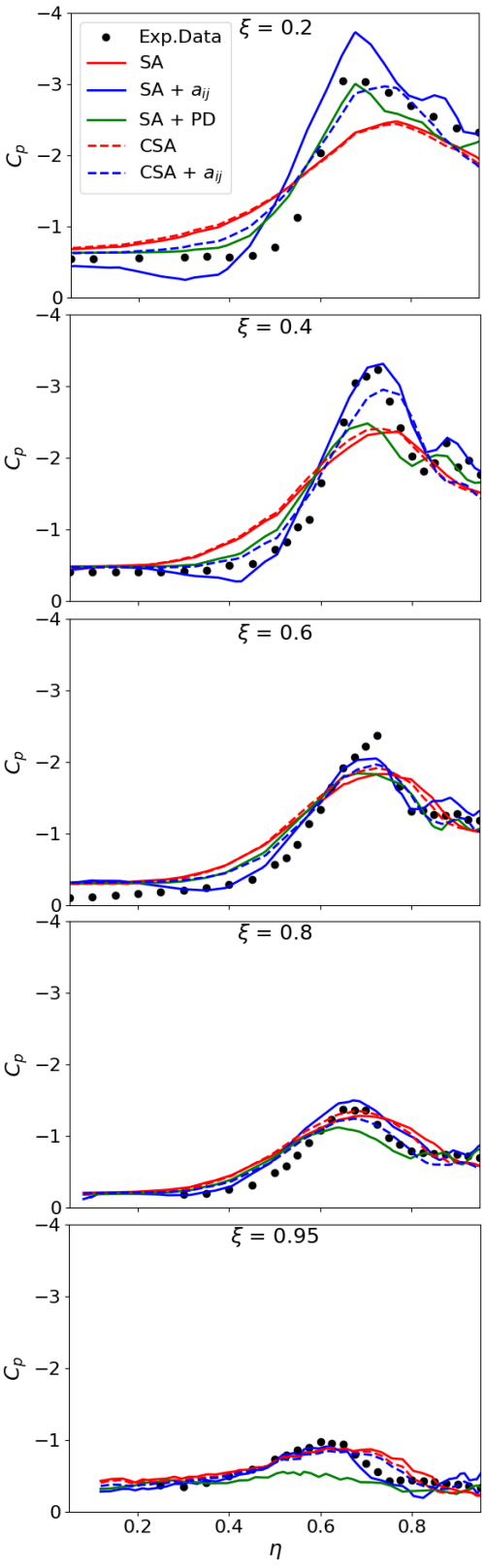

Figure 8.14: VFE2: surface pressure coefficient at different ξ locations over the wing.

trailing edge, with all simulations, except for SA+PD, accurately predicting the pressure peak location consistent with experimental findings.

To facilitate a comprehensive analysis of the flow field and visualize the onset of vortex breakdown, velocity field cutting planes are depicted in Figs. 8.15 and 8.16. Specifically, Fig. 8.16 presents the normalized axial velocity, u/U_∞, at ξ = 0.5, 0.6, 0.7, 0.8, 0.95. Initial observations from the slice planes indicate that both experimental and simulation data identify an axial velocity peak within the vortex core. However, the experiment shows the high-velocity region extending closer to the wing surface, contrasting with the simulations' depiction of a more circular area projecting upwards (Tangermann et al., 2012). Moreover, the new models generate a more robust and stable vortex with enhanced core velocity compared to the baseline SA results, attributed to increased turbulence production near the leading edge. This adjustment is critical for accurately predicting the surface pressure coefficient, as illustrated in Fig. 8.14.

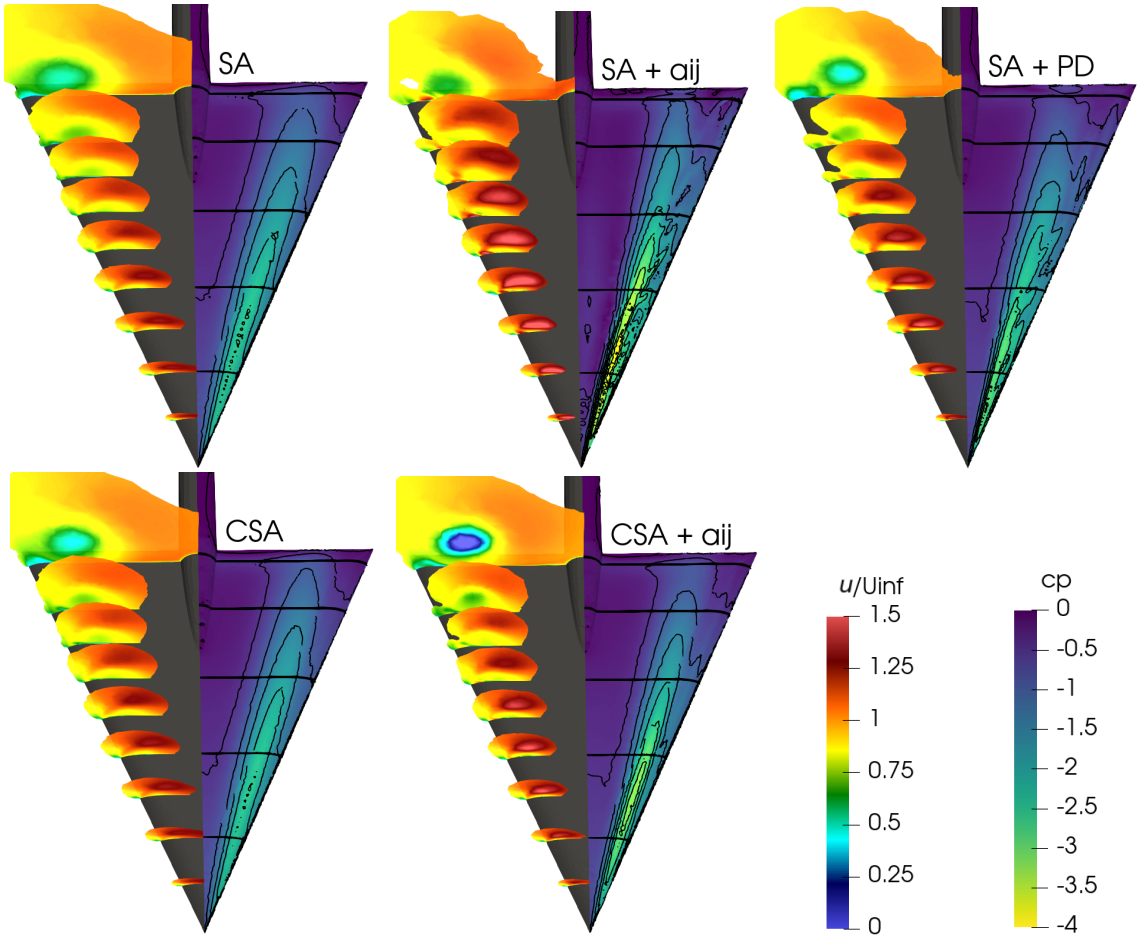

Figure 8.15: VFE2: surface pressure coefficient and normalized x-velocity.

Figure 8.15 reveals that vortex breakdown is notably pronounced in the numerical results of the SA+PD and CSA+a_{ij} models, with the CSA model surpassing the SA model in predicting the flow field above the wing. Conversely, the SA+a_{ij} model predicts a downstream vortex breakdown, owing to its depiction of a more stable and

robust secondary vortex. Although the simulations do not predict the onset of vortex breakdown at $\xi = 0.6$ as observed in experiments (Furman and Breitsamter, 2009; Tangermann et al., 2012), signs of breakdown become apparent around $\xi = 0.8$. Advancing to $\xi = 0.95$, the vortex breakdown is more distinctly captured in RANS simulations, demonstrating flow separation that leads to the formation of a vortex breakdown. A noticeable reduction in the primary vortex core velocity accompanies the stream-wise separation in the secondary vortex region at $\xi = 0.8$. Unlike experimental observations, simulations do not showcase the classic signs of vortex breakdown, characterized by an abrupt drop in velocity within the vortex core. The discrepancy between the accurate prediction of the surface pressure coefficient and the less precise prediction of the velocity flow field may arise from the formulation of the fitness function, which focuses solely on the surface pressure coefficient. Incorporating velocity profiles into the training process, akin to the approach for the jet and hump cases, could offer a potential solution. Moreover, the coarse mesh resolution could be responsible for the behavior observed in the CFD results, and a mesh convergence study can be conducted to address this possibility.

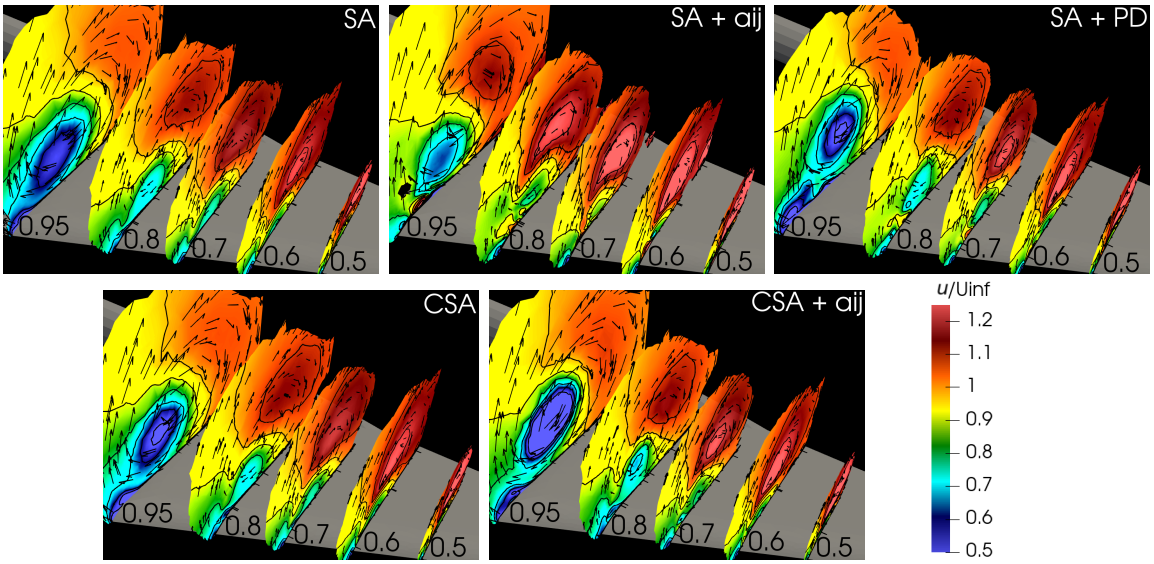

Figure 8.16: VFE2: normalized x-velocity, contour and in-plane vectors at locations $\xi = 0.5, 0.6, 0.7, 0.8, 0.95$.

Table 8.5 presents the expressions derived through GEP training. Figures 8.17 depicts the $f^{(1)}$ contour for the CSA+a_{ij} model, alongside the coefficients C_P and C_D for the SA+PD model. Fig. 8.18 shows these expressions as functions of the invariants. The function $f^{(1)}$ response to variations in I_2 (representing vorticity magnitude) is relatively stable, yet it exhibits an escalation with an increase in I_1 (denoting strain rate magnitude), especially outside the vortex region. It predominantly shows positive values, with exceptions occurring in areas of diminished strain stress magnitude, typically coinciding with the vortex core's location. In fact, within the formulation of the production term in the CSA+a_{ij} model, a positive value coincides with a decrease in production, and vice versa.

Table 8.5: VFE2: GEP expressions. Numbers rounded to the third decimal place.

	$f^{(1)}$	$f^{(2)}$	$f^{(3)}$
SA+a_{ij}	$-0.152I_2I_1 + 2I_1 - 0.152I_2 + 0.063$	$0.089I_1 - 0.089I_1I_2$	$3I_1^2 - 1.038I_1$
CSA+a_{ij}	$0.388I_2I_1^2 + 0.388I_1^2 - 0.15I_2I_1 - 0.15I_1$	$1.43I_1 - I_2 - 1.089$	$-2.01455I_1 - 0.702983I_2 - 0.15$

	C_P	C_D
SA+PD	$2I_1I_2$	$4I_1^2 + 4I_2I_1 + 21.388I_1 + 5I_2 + 20.485$

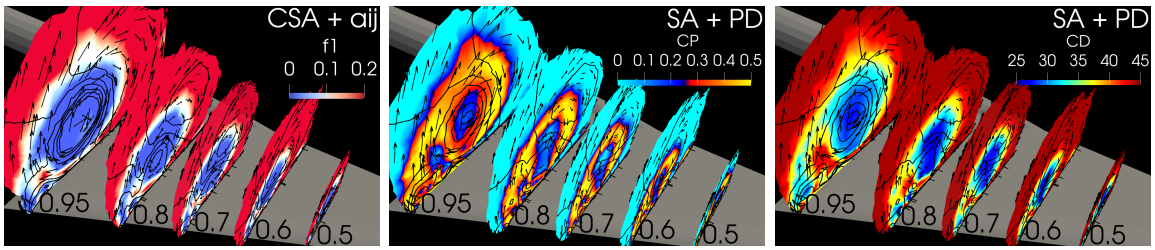

Figure 8.17: VFE2: $f^{(1)}$, C_P, and C_D contours and streamlines.

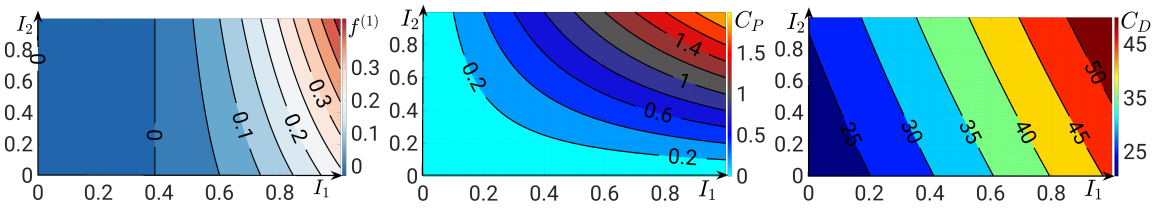

Figure 8.18: VFE2: expressions as function of the invariants.

The coefficients C_P and C_D consistently exhibit positive values. Specifically, C_P demonstrates a significant rise with the augmentation of both invariants, whereas C_D shows heightened sensitivity to variations in I_1. The coefficients effectively delineate the vortex region, adjusting their magnitudes to reflect the flow physics. An increase in turbulence production within the vortex sheet and a reduction within the vortex core are observed. The original model coefficient, c_{b1}, appears to be adequate in the vortex region but insufficient to reproduce the turbulence generation in the vortex sheet, as also discussed in Section 7.4.1. Conversely, the destruction coefficient exhibits an upward trend moving from the vortex core towards the free-stream.

9

Conclusions and Outlook

The objectives of the thesis are concisely articulated in bullet points in Section 1.2.1, presented logically and sequentially. The conclusions are structured to follow the same order ensuring readability and ease of understanding.

Chapter 5 provides deep insights into the transonic flow field around the VFE-2 delta wing. Outcomes from SAnegRC-based URANS and SAneg-based IDDES are utilized. The flow physics is elucidated by examining both mean and instantaneous flow features in detail. This chapter establishes a methodological foundation for performing URANS and Hi-Fi simulations on delta wings, facilitating the validation of computational codes and methodologies. Moreover, it is instrumental in acquiring expertise and knowledge, which are subsequently applied to analyze the flow physics of the ADS-NA2-W1 configuration.

The IDDES approach is highlighted as a promising approach for simulating flow around delta wings at transonic conditions, potentially standing as a reference model for such cases across more demanding conditions and configurations. Appropriate cell and time step sizes unveil critical flow characteristics, establishing these simulations as a vital tool for enhancing understanding of delta wing aerodynamics under transonic conditions. The sensitivity of outcomes to temporal and spatial resolutions are thoroughly addressed, ensuring high predictive accuracy. The numerical results are validated against experimental data, with a specific focus on the mean surface pressure coefficient. Furthermore, shock wave behaviors are explored, resulting in both surface pressure distributions and shock wave positions being accurately captured by the numerical simulations.

The interaction between leading-edge vortices and shock waves is analyzed, demonstrating the capability of the scale-resolving method to replicate these complex interactions. The formation of the primary vortex, driven by the separated shear layer from the leading edge, is examined and revels the importance of capturing turbulence at the leading-edge apex. Additionally, the formation and breakdown of the secondary vortex are investigated, offering hypotheses to elucidate the underlying processes and mechanisms of vortex breakdown.

As the flow over the wing separates at the leading-edge and rolls up, it forms a stable, separation-induced primary vortex. Typically, the flow reattaches when the primary

vortex reaches the wing surface. Under specific conditions, the span-wise flow beneath the primary vortex separates again, generating a counter-rotating secondary vortex located outward of the primary vortex. The separation shock leads to a recirculation zone and fosters the formation of the secondary vortex. The secondary vortex's existence facilitates the incorporation of the shear layer into the primary vortex. However, when the shock wave, induced by the sting tip, interacts with the primary vortex, it alters the flow dynamics, rendering the secondary vortex unsustainable. The phenomenon triggers a sudden decrease in axial velocity and results in the damping of the separation shock, which ceases to interact with the boundary layer, thereby leading to the disintegration of the secondary vortex. The fluid, previously part of the secondary vortex, transitions into turbulent motion on smaller scales, preventing the shear layer from coalescing into the primary vortex.

Discussions expand to encompass turbulence-related variables. The modeled turbulent eddy viscosity is compared between URANS and IDDES methodologies. It is observed that the URANS model tends to predict significantly elevated levels of turbulent eddy viscosity within the vortex core. The components of the Reynolds stress tensor are utilized to visualize various flow phenomena over the wing, including the vortex sheet, primary and secondary vortices, and the separation shock wave. A slight delay in the onset of resolved turbulence development is unveiled, characterized by an initial underestimation of resolved turbulent kinetic energy. This underestimation influences the development of downstream turbulent processes. This observation, in conjunction with recognized challenges in the grey-area of turbulence modeling within HRL frameworks, indicates the potential need for adjustments to HRL turbulence models in future research.

The investigation of vortex-dominated flow around the triple-delta wing ADS-NA2-W1, aimed at enhancing the understanding of flow physics phenomena at transonic speeds, is detailed in Chapter 6. Employing both URANS and scale-resolving simulations, it examines the applicability of current CFD methods. URANS simulations are conducted with a constant side slip angle ($\beta = 5°$), highlighting the asymmetric turbulent flow across a range of attack angles ($12° < \alpha < 28°$), whereas high-fidelity simulations are limited to $\alpha = 20°$, $24°$, $28°$ due to computational constraints.

Detailed discussions of the flow field are segmented into analyses of both instantaneous and mean flow features, inclusive of aerodynamic integral coefficients. The vortex development is elaborated. At $\alpha = 20°$, two distinct vortices on the leeward wing and two less distinct (merged) vortices undergoing breakdown on the windward wing are documented. For $\alpha = 24°$, distinct vortices on the leeward wing and a burst or incoherent vortex at the leading edge apex on the windward wing are observed. At $\alpha = 28°$, a breakdown of the vortices on the leeward wing is also noted.

Employing the IDDES and SAS numerical methods shows promising improvements, enhancing aerodynamic coefficient predictions and significantly reducing deviations from experimental results. The accuracy of integral moment coefficients (pitching and rolling) is closely associated with the prediction of the vortex breakdown onset position, influencing the suction footprint over the wings and the surface pressure coefficient distribution post-vortex breakdown across the aircraft. Particularly for $\alpha = 20°$, the

predicted vortex breakdown by the IDDES approach represents a notable improvement. This phenomenon is not captured by the SAnegRC-based URANS outcomes.

On the windward wing at $\alpha = 24°$, the HRL outcomes highlight the chaotic behavior of the burst vortex and the lack of coherent vortex formation from the shear layer emanating from the leading-edge. The shear layer emanating from the leading edge no longer rolls up to form a leading-edge vortex over the wing, but is instead transported downstream without inducing additional velocities on the wing surface. An immediate consequence of this phenomenon is an increase in pressure over the wing. This alteration significantly impacts the prediction of aerodynamic coefficients. The SAnegRC-based URANS approach fails to accurately capture this process, erroneously predicting the presence of a vortex near the windward wing apex. Therefore, the SAnegRC-based URANS simulations inaccurately predict the pressure distribution over the windward wing, especially near the wing apex. This method appears to stabilize and promote the presence of a coherent structure, rather than accurately simulating turbulent behavior.

The fuselage vortices converge toward the leeward wing and appear to interact with the primary vortices, thereby influencing the overall flow behavior. The IDDES findings illustrate how the terminating vortex moves downstream over the wing, compared to its location at $\alpha = 20°$. It is found precisely at the point where the inboard and outboard vortices merge, specifically near the trailing edge. At $\alpha = 20°$, the vortices interact and merge upstream over the wing. This interaction results in the terminating shock also moving upstream.

Vortex breakdown on the leeward wing is illustrated only through the SAS outcomes at $\alpha = 28°$. The formation of fuselage vortices is influenced by both the side-slip angle and the angle of attack, with their strength and size increasing at higher angles of attack. The interaction between the fuselage and the leading-edge vortex on the leeward side undergoes profound changes, as the leeward fuselage vortex eventually merges with the inboard leading-edge vortex. This merging is followed immediately by vortex breakdown and then may be attributed to the occurrence of this phenomenon. Furthermore, there is no observable interaction between the inboard and the outboard vortex at this angle of attack, substantiating the theory that vortex interaction on the leeward wing becomes less effective when the angle of attack is increased from 20° to 28°.

Both $k\omega$SST-based URANS and SAS simulations accurately predict the flow pattern over the windward wing, especially near the wing apex. They effectively capture the shear layer originating from the leading-edge and its subsequent chaotic transport downstream across the wing, albeit with a minor overestimation of the suction footprint's intensity. The $k\omega$SST model demonstrates then superior accuracy compared to the SAnegRC turbulence model in predicting such flow behavior. These analyses demonstrate that SAnegRC-based URANS simulations exhibit the lowest accuracy in predicting vortical flow over delta wings. Following the analysis of vortex development, this manuscript then shifts its focus to examining the reasons behind the limitations of the SA model, aiming to improve its accuracy.

Chapter 7 presents further insights into the findings of transonic flow around the ADS-NA2-W1 aircraft at $\alpha = 20°$. In addition to the simulations introduced in Chapter 6, the PK model is presented. It introduces a novel and simplified extension to the Boussinesq assumption, conceived for the SAnegRC turbulence model, to emulate the turbulent kinetic energy effect observed in the $k\omega$SST outcomes. While the SAnegRC model fails to predict vortex breakdown, the PK model accurately captures this phenomenon, markedly improving the prediction of aerodynamic coefficients and substantially reducing deviations observed with the SAnegRC results.

Vortex breakdown occurs due to shock interaction only if the primary vortex is inherently unstable and predisposed to such breakdown. The variable predictions of the vortex breakdown onset location are ascribed to the vortex's upstream conditions, with the shear-layer separation near the wing apex and secondary vortex formation being particularly significant. The SAnegRC model displays weaker stream-wise separation on the wing upstream of the vortex breakdown, in contrast to the $k\omega$SST results, which show pronounced stream-wise flow separation near the wing apex without a coherent secondary vortex. The leading edge's shear-layer does not adequately feed then the primary vortex. The primary vortex predicted by the $k\omega$SST model is intrinsically more susceptible to breakdown than that predicted by the SAnegRC model. The PK model effectively captures more pronounced stream-wise separation near the leading edge, achieving a more accurate depiction of the lambda shock shape and enhancing the reliability of shock-vortex interaction predictions.

The SAnegRC model fails to generate turbulence near the wing apex or leading edge where vortex formation occurs. Additionally, within the vortex core, particularly post-shock encounter, the production term becomes highly active, resulting in elevated turbulent viscosity levels. The $k\omega$SST model accurately predicts turbulence generation in the separation region and partially mitigates production within the vortex. The PK model aligns viscosity ratio values more closely with those observed in the $k\omega$SST model. In the one-equation model, assuming k to be zero leads to non-physical values for normal Reynolds stresses. The isotropic component of the Boussinesq assumption, crucial in this case, is then integrated into the one-equation PK model.

The PK method shows promise in improving the physics predicted by one-equation RANS around delta wings in transonic conditions. Further research is essential to refine the k_{SA} function, a critical step to enhance the model's applicability and accuracy across various flow conditions. Notably, the PK model successfully captures also the vortex breakdown at 28° on the leeward wing, yet it does not significantly enhance numerical predictions at $\alpha = 24°$. This discrepancy may be attributed to multiple factors, with no universal solutions readily apparent. However, considering the analysis conducted at $\alpha = 24°$ in Chapter 6, and the observed flow physics on the wing, it may be hypothesized that the primary challenge lies in capturing the turbulent motion generated on the windward wing. In this scenario, no coherent vortex is generated, and the breakdown has reached the wing's apex. The SAnegRC model does not accurately capture this phenomenon, and the PK model exhibits similar limitations. This issue stems from the intrinsic limitations of the model's formulation, which fails to generate the necessary turbulence near the leading-edge. To address this challenge, new formu-

lations of the one-equation model are explored through modifications of the production and destruction terms and the incorporation of machine learning techniques.

Chapter 8 explores enhancements to RANS modeling capabilities through two methodologies by using a CFD-driven GEP framework. The first method employs the standard SA model to close the RANS equations, aiming to improve predictive accuracy by extending the linear Boussinesq hypothesis to model the Reynolds stress anisotropy. The second method builds upon the Boussinesq hypothesis to augment RANS modeling performance, conceptualizing an enhanced one-equation turbulence model designed to refine turbulence production and destruction mechanisms.

Four fundamental flows from the NASA challenge validation cases are utilized for the training process. Following the evaluation of these fundamental cases, the VFE-2 delta wing configuration is numerically trained and analyzed. The flow cases are considered individually, leading to an in-depth analysis of the derived model expressions.

In the context of NASA validation cases, the SA+a_{ij} model consistently fails to outperform the baseline and sometimes demonstrates instability. Thus, merely modifying Reynolds stresses through anisotropic tensor modeling proves insufficient for enhancing the RANS capability using the SA turbulence model for the investigations at hand. The CSA model performs similarly to SA, but its formulation effectively couples with anisotropic formulations for Reynolds stresses in the CSA+a_{ij} model. The introduction of a new production term is advantageous as changes in τ_{ij} reflect not only in the Boussinesq assumption but also in itself, enabling a sort of double optimization while modeling Reynolds stress anisotropy. Likewise, as demonstrated by the results accuracy of the SA+PD model, adjustments to the production and destruction terms in the SA model facilitate effective optimization of model performance. The expressions found through GEP underscore the need for a significant alteration in the production term contingent on vorticity or strain stress magnitude, explaining the superior results of the CSA+a_{ij} and SA+PD models over the SA+a_{ij} model.

Considering the VFE-2 configuration, vortex breakdown is most apparent in the numerical outcomes of SA+PD and CSA+a_{ij}. The CSA model also surpasses the SA model in flow field prediction above the wing. The SA+a_{ij} model predicts a more downstream vortex breakdown, attributed to its predicting of a more stable and robust secondary vortex. This analysis underscores CFD-driven GEP's capacity to develop turbulence models for such intricate configurations without excessive and prohibitive mesh resolution.

In summary, the CSA+a_{ij} and SA+PD models exhibit superior accuracy, suggesting two research directions for optimizing the SA model: either through refining the coefficients in its original formulation or by introducing a new version that incorporates the Reynolds stress tensor in the production term to model its anisotropy. Additionally, optimizing the baseline CSA model by training its coefficients and/or constants presents an opportunity for further enhancements. Future studies may aim to improve the generalizability of data-driven turbulence models, focusing on optimizing their performance across various flow conditions and configurations during the training phase. However, it is worth noting that, for instance, outcomes from jet simulations suggest a need for increased turbulence production, whereas results for the hump case indicate a

need for decreased turbulence production. This contrast underscores the challenge in developing a generic model capable of accurately representing multiple scenarios.

In subsequent studies, the efficacy of these models and their integrations will be evaluated across more intricate configurations, such as the ADS-NA2-W1 triple delta wing, to ascertain their applicability and potential for further refinement. A meticulous examination of the outcomes will facilitate a comprehensive understanding of the merits and demerits of the proposed models, thereby enriching the knowledge surrounding turbulence modeling. This dissertation lays then the groundwork and motivates future efforts to develop a modified constitutive relation for specific applications, focusing on devising a one-equation turbulence model adept at accurately simulating leading-edge vortices.

Finally, the CFD-driven framework can be expanded to incorporate the DLR-TAU code through the development of interfacing code, thereby facilitating the coupling with the GEP code. Such an enhancement would afford increased versatility in selecting test cases for training, as well as the capability to tailor turbulence models specifically for applications on military aircraft operating under transonic conditions.

References

Agrawal, S., Barnett, R. M., and Robinson, B. A. (1992). "Numerical investigation of vortex breakdown on a delta wing". AIAA Journal 30 (3), pp. 584–591.

Akolekar, H., Waschkowski, F., Zhao, Y., Pacciani, R., and Sandberg, R. D. (2021). "Transition modeling for low pressure turbines using computational fluid dynamics driven machine learning". Energies 14 (15).

Akolekar, H., Weatheritt, J., Hutchins, N., Sandberg, R., Laskowski, G., and Michelassi, V. (2019). "Development and use of machine-learnt algebraic Reynolds stress models for enhanced prediction of wake mixing in low-pressure turbines". Journal of Turbomachinery 141 (4).

Alaya, E., Grabe, C., and Eisfeld, B. (2022). "Evolutionary Algorithm applied to Differential Reynolds Stress Model for Turbulent Boundary Layer subjected to an Adverse Pressure Gradient". AIAA Aviation Forum. Chicago, IL.

Allan, M., Badcock, K., Barakos, G., and Richards, B. (2004). "Wind-tunnel interference effects on a 70 delta wing". The Aeronautical Journal 108 (1088), pp. 505–513.

Allan, M., Badcock, K., Barakos, G., and Richards, B. (2005). "Wind-tunnel interference effects on delta wing aerodynamics computational fluid dynamics investigation". Journal of Aircraft 42 (1), pp. 189–198.

Allmaras, S. and Johnson, F. (2012). "Modifications and clarifications for the implementation of the Spalart-Allmaras turbulence model". Seventh International Conference on Computational Fluid Dynamics. Big Island, HI.

Anderson, J. (2016). Fundamentals of Aerodynamics (6th ed.) McGraw-Hill Education.

Arolla, S. and Durbin, P. (2013). "Modeling rotation and curvature effects within scalar eddy viscosity model framework". International Journal of Heat and Fluid Flow 39, pp. 78–89.

Ashley, H., Katz, J., Jarrah, M., and Vaneck, T. (1991). "Survey of research on unsteady aerodynamic loading of delta wings". Journal of Fluids and Structures 5 (4), pp. 363–390.

Asnaghi, A., Svennberg, U., and Bensow, R. (2019). "Evaluation of curvature correction methods for tip vortex prediction in SST k- ω turbulence model framework". International Journal of Heat and Fluid Flow 75, pp. 135–152.

Baker, J. (1987). "Reducing bias and inefficiency in the selection algorithm". Genetic Algorithms and their Applications: Proceedings of the Second International Conference on Genetic Algorithms. Ed. by J. Grefenstette. Vol. 206. Naval Research Laboratory, pp. 14–21.

Baldwin, B. and Lomax, H. (1978). "Thin-layer approximation and algebraic model for separated turbulent flows". 16th aerospace sciences meeting. Huntsville, AL.

Blazek, J. (2015). “Chapter 5 - Unstructured Finite-Volume Schemes”. Computational Fluid Dynamics: Principles and Applications (Third Edition). Ed. by J. Blazek. Oxford: Butterworth-Heinemann, pp. 121–166.

Blickle, T. and Thiele, L. (1996). “A comparison of selection schemes used in evolutionary algorithms”. Evolutionary Computation 4 (4), pp. 361–394.

Boussinesq, J. (1877). Essai sur la théorie des eaux courantes. Imprimerie Nationale.

Bradshaw, P., Ferriss, D., and Atwell, N. (1967). “Calculation of boundary-layer development using the turbulent energy equation”. Journal of Fluid Mechanics 28 (3), pp. 593–616.

Breitsamter, C. (2008). “Unsteady flow phenomena associated with leading-edge vortices”. Progress in Aerospace Sciences 44 (1), pp. 48–65.

Brennenstuhl, U. and Hummel, D. (1982). “Vortex formation over double-delta wings”. Congress of the International Council of the Aeronautical Sciences.

Brown, G. and Lopez, J. (1990). “Axisymmetric vortex breakdown Part 2. Physical mechanisms”. Journal of Fluid Mechanics 221, pp. 553–576.

Brunton, S., Noack, B., and Koumoutsakos, P. (2020). “Machine learning for fluid mechanics”. Annual review of fluid mechanics 52, pp. 477–508.

Celik, I., Klein, M., and Janicka, J. (2009). “Assessment Measures for Engineering LES Applications”. Journal of Fluids Engineering 131.3.

Celik, I., Cehreli, Z., and Yavuz, I. (2005). “Index of Resolution Quality for Large Eddy Simulations”. Journal of Fluids Engineering 127 (5), pp. 949–958.

Chu, J. (1996a). Experimental surface pressure data obtained on 65° delta wing across Reynolds number and Mach number ranges. Vol. 1 - Sharp Leading Edge. National Aeronautics and Space Administration, Langley Rearch Center.

Chu, J. (1996b). Experimental surface pressure data obtained on 65° delta wing across Reynolds number and Mach number ranges. Vol. 2 - Small Radius Leading Edge. National Aeronautics and Space Administration, Langley Rearch Center.

Chu, J. (1996c). Experimental surface pressure data obtained on 65° delta wing across Reynolds number and Mach number ranges. Vol. 3 - Medium Radius Leading Edge. National Aeronautics and Space Administration, Langley Rearch Center.

Chu, J. (1996d). Experimental surface pressure data obtained on 65° delta wing across Reynolds number and Mach number ranges. Vol. 4 - Large Radius Leading Edge. National Aeronautics and Space Administration, Langley Rearch Center.

Craft, T., Launder, B., and Suga, K. (1996). “Development and application of a cubic eddy-viscosity model of turbulence”. International Journal of Heat and Fluid Flow 17 (2), pp. 108–115.

Crippa, S. and Rizzi, A. (2008). “Steady, Subsonic CFD Analysis of the VFE-2 Configuration and Comparison to Wind Tunnel Data”. 46th AIAA Aerospace Sciences Meeting and Exhibit. Reno, Nevada.

Cummings, R., Forsythe, J., Morton, S., and Squires, K. (2003a). “Computational challenges in high angle of attack flow prediction”. Progress in Aerospace Sciences 39 (5), pp. 369–384.

Cummings, R., Morton, S., and Siegel, S. (2003b). “Computational simulation and experimental measurements for a delta wing with periodic suction and blowing”. Journal of Aircraft 40 (5), pp. 923–931.

Cummings, R., Morton, S., and Siegel, S. (2003c). "Computational simulation and PIV measurements of the laminar vortical flowfield for a delta wing at high angle of attack". 41st Aerospace Sciences Meeting and Exhibit. Reno, Nevada.

Cummings, R. and Schütte, A. (2012). Assessment of Stability and Control Prediction Methods for NATO Air and Sea Vehicles.

Cummings, R. and Schütte, A. (2013). "Detached-Eddy Simulation of the vortical flow field about the VFE-2 delta wing". Aerospace Science and Technology 24 (1), pp. 66–76.

Deb, K., Pratap, A., Agarwal, S., and Meyarivan, T. (2002). "A Fast and Elitist Multiobjective Genetic Algorithm: NSGA-II". IEEE Transactions on Evolutionary Computation 6 (2), pp. 182–197.

Degani, D. and Schifft, L. (1986). "Computation of turbulent supersonic flows around pointed bodies having crossflow separation". Journal of Computational Physics 66 (1), pp. 173–196.

Délery, J. (1994). "Aspects of vortex breakdown". Progress in Aerospace Sciences 30 (1), pp. 1–59.

Di Fabbio, T., Tangermann, E., and Klein, M. (2022a). "Flow pattern analysis on a delta wing at transonic speed". AIAA SciTech Forum. San Diego, California.

Di Fabbio, T., Tangermann, E., and Klein, M. (2022b). "Investigation of Leading-Edge Vortices on a Triple-Delta-Wing Configuration using Scale-Adaptive Simulation". 33rd Congress of the International Council of the Aeronautical Sciences. Stockholm, Sweden.

Di Fabbio, T., Tangermann, E., and Klein, M. (2022c). "Investigation of Reynolds stresses prior to vortex breakdown on a triple-delta wing at transonic condition". 12th International Symposium on Turbulence and Shear Flow Phenomena. Osaka, Japan.

Di Fabbio, T., Tangermann, E., and Klein, M. (2022d). "Investigation of transonic aerodynamics on a triple-delta wing in side slip conditions". CEAS Aeronautical Journal 13 (2), pp. 453–470.

Di Fabbio, T., Tangermann, E., and Klein, M. (2023). "Analysis of the vortex-dominated flow field over a delta wing at transonic speed". The Aeronautical Journal 127 (1317), pp. 1–18.

Di Fabbio, T., Tangermann, E., and Klein, M. (2024a). "Towards the understanding of vortex breakdown for improved RANS turbulence modeling". Aerospace Science and Technology 146.

Di Fabbio, T., Fang, Y., Tangermann, E., Sandberg, R. D., and Klein, M. (2024b). "Strategies for Enhancing One-Equation Turbulence Model Predictions Using Gene-Expression Programming". Fluids 9 (8).

Dol, H., Kok, J., and Oskam, B. (2002). "Turbulence modelling for leading-edge vortex flows". 40th AIAA Aerospace Sciences Meeting & Exhibit. Reno, Nevada.

Donohoe, S. and Bannink, W. (1997). "Surface reflective visualizations of shock-wave/vortex interactions above a delta wing". AIAA Journal 35 (10), pp. 1568–1573.

Donohoe, S., Houtman, E., and Bannink, W. (1995). "Surface reflective visualization system study to vortical flow over delta wings". Journal of Aircraft 32 (6), pp. 1359–1366.

Duraisamy, K., Iaccarino, G., and Xiao, H. (2019). “Turbulence Modeling in the Age of Data”. Annual Review of Fluid Mechanics 51, pp. 357–377.

Duraisamy, K., Spalart, P., and Rumsey, C. (2017). Status, emerging ideas and future directions of turbulence modeling research in aeronautics. Tech. rep. NASA Langley Research Center.

Durbin, P. (2018). “Some recent developments in turbulence closure modeling”. Annual Review of Fluid Mechanics 50, pp. 77–103.

Edeling, W., Cinnella, P., Dwight, R., and Bijl, H. (2014). “Bayesian estimates of parameter variability in the k-ϵ turbulence model”. Journal of Computational Physics 258, pp. 73–94.

Ekaterinaris, J. and Schiee, L. (1990a). “Numerical simulation of the effects of variation of angle of attack and sweep angle on vortex breakdown over delta wings”. 8th Applied Aerodynamics Conference.

Ekaterinaris, J. and Schiee, L. (1990b). “Vortical flows over delta wings and numerical prediction of vortex breakdown”. 28th Aerospace Sciences Meeting.

Erickson, G. and Rogers, L. (1987). “Experimental study of the vortex flow behavior on a generic fighter wing at subsonic and transonic speeds”. 19th AIAA, Fluid Dynamics, Plasma Dynamics, and Lasers Conference. Honolulu, HI.

Ericsson, L. (2003). “Multifaceted influence of fuselage geometry on delta-wing aerodynamics”. Journal of Aircraft 40 (1), pp. 204–206.

Erlebacher, G., Hussaini, M., and Shu, C. (1997). “Interaction of a shock with a longitudinal vortex”. Journal of Fluid Mechanics 337, pp. 129–153.

Escudier, M. (1988). “Vortex breakdown: Observations and explanations”. Progress in Aerospace Sciences 25 (2), pp. 189–229.

Fang, Y., Zhao, Y., Waschkowski, F., Ooi, A., and Sandberg, R. (2023). “Toward More General Turbulence Models via Multicase Computational-Fluid-Dynamics-Driven Training”. AIAA Journal 61 (5), pp. 2100–2115.

Favre, A. (1965). The equations of compressible turbulent gases. Tech. rep. Aix-marseille univ (France) inst de mecanique statistique de la turbulence.

Ferreira, C. (2002). “Gene expression programming in problem solving”. Soft computing and industry: recent applications. Springer, pp. 635–653.

Ferreira, C. (2006a). Gene expression programming: mathematical modeling by an artificial intelligence. Springer.

Ferreira, C. (2006b). “Gene expression programming: a new adaptive algorithm for solving problems”. Complex Systems 13 (2), pp. 87–129.

Fleming, P. and Purshouse, R. (2002). “Evolutionary algorithms in control systems engineering: a survey”. Control Engineering Practice 10 (11), pp. 1223–1241.

Fritz, W. and Cummings, R. (2008). “What was learned from the numerical simulations for the VFE-2”. 46th AIAA Aerospace Sciences Meeting and Exhibit. Reno, Nevada.

Furman, A. and Breitsamter, C. (2009). “Experimental investigations on the VFE-2 configuration at TU Munich, Germany”. NATO STO, Summary Report of Task Group AVT-113 21, pp. 1–51.

Gerhold, T. (2002). “Overview of the Hybrid Rans Code TAU”. Ed. by N. Kroll and J. K. Fassbender. Vol. 89. Notes on Numerical Fluid Mechanics and Multidisciplinary Design. Springer Verlag, pp. 81–92.

Goertz, S. (2003). “Time-accurate Euler simulations of a full-span delta wing at high incidence”. 21st AIAA Applied Aerodynamics Conference. Orlando, Florida.

Goertz, S. and Le Moigne, Y. (2003). “Detached-Eddy simulations of a full-span delta wing at high incidence”. 21st AIAA Applied Aerodynamics Conference. Orlando, Florida.

Gordnier, R. (1997). “Numerical simulation of a 65-degree delta-wing flowfield”. Journal of Aircraft 34 (4), pp. 492–499.

Gordnier, R. and Visbal, M. (2005). “Compact Difference Scheme Applied to Simulation of Low-Sweep Delta Wing Flow.” AIAA Journal 43 (8), pp. 1744–1752.

Govinda, K., Bocci, G., Verma, S., Hassan, M. M., Holmes, J., Yang, J. J., Sirimulla, S., and Oprea, T. I. (2021). “A machine learning platform to estimate anti-SARS-CoV-2 activities”. Nature Machine Intelligence 3 (6), pp. 527–535.

Greenshields, C. (2019). OpenFOAM v7 User Guide. London, UK: The OpenFOAM Foundation.

Greenshields, C. and Weller, H. (2022). Notes on computational fluid dynamics: General principles. Reading, UK: CFD Direct Ltd.

Gupta, D. and Ghafir, S. (2012). “An overview of methods maintaining diversity in genetic algorithms”. International journal of emerging technology and advanced engineering 2 (5), pp. 56–60.

Gursul, I. and Xie, W. (2000). “Origin of vortex wandering over delta wings”. Journal of Aircraft 37 (2), pp. 348–350.

Gursul, I. (1994). “Unsteady flow phenomena over delta wings at high angle of attack”. AIAA Journal 32 (2), pp. 225–231.

Gursul, I. (2004). “Recent developments in delta wing aerodynamics”. The Aeronautical Journal 108 (1087), pp. 437–452.

Gursul, I. (2005). “Review of unsteady vortex flows over slender delta wings”. Journal of Aircraft 42 (2), pp. 299–319.

Gursul, I. and Yang, H. (1995). “On fluctuations of vortex breakdown location”. Physics of Fluids 7 (1), pp. 229–231.

Haghiri, A., Lav, C., and Sandberg, R. (2020). “Data-driven turbulence modelling for improved prediction of ship airwakes”. 33rd Symposium on Naval Hydrodynamics. Osaka, Japan, pp. 1–17.

Hellsten, A. (1998). “Some improvements in Menter’s k-omega SST turbulence model”. 29th AIAA, Fluid Dynamics Conference. Albuquerque, New Mexico.

Hemsch, M. and Luckring, J. (1990). “Connection between leading-edge sweep, vortex lift, and vortex strength for delta wings”. Journal of Aircraft 27 (5), pp. 473–475.

Hitzel, S. (2022a). “Combat Aircraft Vortex Interaction - Design, Physics & CFD-Tools”. AIAA SciTech Forum. San Diego, California.

Hitzel, S. (2022b). “Status of Vortex Interaction on Combat Aircraft - Physics Understood, Simulation Tool Demands, Quality & Cost”. AIAA SciTech Forum. San Diego, California.

Hitzel, S., Winkler, A., and Hövelmann, A. (2020). “Vortex Flow Aerodynamic Challenges in the Design Space for Future Fighter Aircraft”. New Results in Numerical and Experimental Fluid Mechanics XII. Ed. by A. Dillmann, G. Heller, E. Krämer, C. Wagner, C. Tropea, and S. Jakirlić. Springer International Publishing, pp. 297–306.

Hofmann, D. (2015). “A Genetic Programming Approach to Generating Musical Compositions”. Evolutionary and Biologically Inspired Music, Sound, Art and Design. Ed. by C. Johnson, A. Carballal, and J. Correia. Cham: Springer International Publishing, pp. 89–100.

Holland, J. (1992). “Genetic algorithms”. Scientific American, a division of Nature America, Inc. 267 (1), pp. 66–73.

Houghton, E., Carpenter, P., Collicott, S., and Valentine, D. (2013). “Chapter 7 - Airfoils and Wings in Compressible Flow”. Aerodynamics for Engineering Students. Sixth Edition. Boston: Butterworth-Heinemann, pp. 427–477.

Hövelmann, A., Winkler, A., Hitzel, S., Richter, K., and Werner, M. (2020). “Analysis of Vortex Flow Phenomena on Generic Delta Wing Planforms at Transonic Speeds”. New Results in Numerical and Experimental Fluid Mechanics XII. Ed. by A. Dillmann, G. Heller, E. Krämer, C. Wagner, C. Tropea, and S. Jakirlić. Cham: Springer International Publishing, pp. 307–316.

Howard, J., Patankar, S., and Bordynuik, R. (1980). “Flow Prediction in Rotating Ducts Using Coriolis-Modified Turbulence Models”. Journal of Fluids Engineering 102.4, pp. 456–461.

Huang, X. and Hanff, E. (1992). “Prediction of leading-edge vortex breakdown on a delta wing oscillating in roll”. 10th Applied Aerodynamics Conference. Palo Alto, California.

Hummel, D. (1981). Experimental investigation of the flow on the suction side of a thin delta wing. Tech. rep.

Hutter, M. (2002). “Fitness uniform selection to preserve genetic diversity”. Proceedings of the 2002 Congress on Evolutionary Computation. Vol. 1, pp. 783–788.

Jameson, A., Schmidt, W., and Turkel, E. (1981). “Numerical solution of the Euler equations by finite volume methods using Runge Kutta time stepping schemes”. 14th Fluid and Plasma Dynamics Conference. Palo Alto, California, p. 1259.

Jiang, C., Vinuesa, R., Chen, R., Mi, J., Laima, S., and Li, H. (2021). “An interpretable framework of data-driven turbulence modeling using deep neural networks”. Physics of Fluids 33 (5).

Jobe, C. (2004). “Vortex breakdown location over 65 delta wings empiricism and experiment”. The Aeronautical Journal 108 (1087), pp. 475–482.

Johari, H. and Moreira, J. (1998). “Direct measurement of delta-wing vortex circulation”. AIAA Journal 36 (12), pp. 2195–2203.

Johnson, A., Meyerson, E., De La Parra, J., Savas, T., Miikkulainen, R., and Harper, C. (2019). “Flavor-cyber-agriculture: Optimization of plant metabolites in an open-source control environment through surrogate modeling”. PLoS One 14 (4).

Jones, W. and Launder, B. (1972). “The prediction of laminarization with a two-equation model of turbulence”. International Journal of Heat and Mass Transfer 15 (2), pp. 301–314.

Jumper, E., Nelson, R., and Cheung, K. (1993). “A simple criterion for vortex breakdown”. 31st Aerospace Sciences Meeting. Reno, Nevada, p. 866.

Jupp, M., Coton, F., and Green, R. (1999). “A statistical analysis of the surface pressure distribution on a delta wing”. The Aeronautical Journal 103 (1025), pp. 349–357.

Kalkhoran, I. and Smart, M. (2000). “Aspects of shock wave-induced vortex breakdown”. Progress in aerospace sciences 36 (1), pp. 63–95.

Kasten, C., Fahr, J., and Klein, M. (2022a). “An efficient way of introducing gender into evolutionary algorithms”. IEEE Transactions on Evolutionary Computation 27 (4).

Kasten, C., Shin, J., Sandberg, R., Pfitzner, M., Chakraborty, N., and Klein, M. (2022b). “Modeling subgrid-scale scalar dissipation rate in turbulent premixed flames using gene expression programming and deep artificial neural networks”. Physics of Fluids 34 (8).

Kengelman, J. and Roos, F. (1989). “Effects of leading-edge shape and vortex burst on the flowfield of a 70-degree-sweep delta-wing”. 27th Aerospace sciences meeting. Reno, Nevada.

Kengelman, J. and Roos, F. (1990). “The flowfields of bursting vortices over moderately swept delta wings”. 28th Aerospace Sciences Meeting. Reno, Nevada.

Kolmogorov, A. (1991). “The local structure of turbulence in incompressible viscous fluid for very large Reynolds”. Proc. R. Soc. Lond. A 434 (1890), pp. 9–13.

Konrath, R., Klein, C., Engler, R., and Otter, D. (2006). “Analysis of PSP results obtained for the VFE-2 65° delta wing configuration at sub-and transonic speeds”. 44th AIAA Aerospace Sciences Meeting and Exhibit. Reno, Nevada.

Konrath, R., Klein, C., and Schröder, A. (2013). “PSP and PIV investigations on the VFE-2 configuration in sub- and transonic flow”. Aerospace Science and Technology 24 (1), pp. 22–31.

Koza, J. (1994). “Genetic programming as a means for programming computers by natural selection”. Statistics and Computing 4, pp. 87–112.

Kramer, O. (2017). “Genetic Algorithms”. Genetic Algorithm Essentials. Cham: Springer International Publishing, pp. 11–19.

Kroll, N., Langer, S., and Schwöppe, A. (2014). “The DLR flow solver TAU-status and recent algorithmic developments”. 52nd Aerospace Sciences Meeting. National Harbor, Maryland.

Kumar, A. (1999). “Role of flow-consistent grid in CFD”. Computers & fluids 28 (3), pp. 265–280.

Lambourne, N. and Bryer, D. (1961). “The bursting of leading-edge vortices-some observations and discussion of the phenomenon”. Aeronautical Research Council Reports And Memoranda.

Langdon, W. B., Poli, R., McPhee, N. F., and Koza, J. R. (2008). “Genetic programming: An introduction and tutorial, with a survey of techniques and applications”. Computational intelligence: A compendium, pp. 927–1028.

Launder, B., Priddin, C., and Sharma, B. (1977). “The Calculation of Turbulent Boundary Layers on Spinning and Curved Surfaces”. Journal of Fluids Engineering 99 (1), pp. 231–239.

Launder, B., Reece, G., and Rodi, W. (1975). “Progress in the development of a Reynolds-stress turbulence closure”. Journal of fluid mechanics 68 (3), pp. 537–566.

Lav, C., Haghiri, A., and Sandberg, R. (2021). “RANS predictions of trailing-edge slot flows using heat-flux closures developed with CFD-driven machine learning”. Journal of the Global Power and Propulsion Society 2021, pp. 1–13.

Lav, C., Philip, J., and Sandberg, R. (2019a). “A new data-driven turbulence model framework for unsteady flows applied to wall-jet and wall-wake flows”. Turbo Expo: Power for Land, Sea, and Air. American Society of Mechanical Engineers.

Lav, C., Sandberg, R., and Philip, J. (2019b). “A framework to develop data-driven turbulence models for flows with organised unsteadiness”. Journal of Computational Physics 383, pp. 148–165.
Lee, M. and Ho, C.-M. (1990). “Lift force of delta wings”.
Leonard, A. (1975). “Energy cascade in large-eddy simulations of turbulent fluid flows”. 18, pp. 237–248.
Levy, Y., Degani, D., and Seginer, A. (1990). “Graphical visualization of vortical flows by means of helicity”. AIAA Journal 28 (8), pp. 1347–1352.
Ling, J., Kurzawski, A., and Templeton, J. (2016). “Reynolds averaged turbulence modelling using deep neural networks with embedded invariance”. Journal of Fluid Mechanics 807, pp. 155–166.
Longo, J. (1995). “Compressible inviscid vortex flow of a sharp edge delta wing”. AIAA Journal 33 (4), pp. 680–687.
Lovell, D. (2001). Military vortices. Tech. rep.
Lowson, M. (1991). “Visualization measurements of vortex flows”. Journal of Aircraft 28 (5), pp. 320–327.
Lowson, M. and Riley, A. (1995). “Vortex breakdown control by delta wing geometry”. Journal of Aircraft 32 (4), pp. 832–838.
Luckring, J. (2002a). “Reynolds number and leading-edge bluntness effects on a 65-deg delta wing”. 40th AIAA Aerospace Sciences Meeting & Exhibit. Reno, Nevada.
Luckring, J. (2002b). “Transonic Reynolds Number and Leading-Edge Bluntness Effects on a 65 deg Delta Wing”. 40th AIAA Aerospace Sciences Meeting & Exhibit. Reno, Nevada.
Luckring, J. (2004). “Compressibility and leading-edge bluntness effects for a 65-deg delta wing”. 42nd AIAA Aerospace Sciences Meeting and Exhibit. Reno, Nevada, p. 765.
Luckring, J. (2013). “Initial experiments and analysis of blunt-edge vortex flows for VFE-2 configurations at NASA Langley, USA”. Aerospace Science and Technology 24 (1), pp. 10–21.
Luckring, J., Boelens, O., Breitsamter, C., Hövelmann, A., Knoth, F., Malloy, D., and Deck, S. (2016). “Objectives, approach, and scope for the AVT-183 diamond-wing investigations”. Aerospace Science and Technology 57.
Man, K.-F., Tang, K. S., and Kwong, S. (2001). Genetic algorithms: concepts and designs. Springer Science & Business Media.
Mary, I. (2003). “Large eddy simulation of vortex breakdown behind a delta wing”. International Journal of Heat and Fluid Flow 24 (4), pp. 596–605.
Mavriplis, D. and Jameson, A. (1990). “Multigrid solution of the Navier-Stokes equations on triangular meshes”. AIAA Journal 28 (8), pp. 1415–1425.
Menke, M., Yang, H., and Gursul, I. (1999). “Experiments on the unsteady nature of vortex breakdown over delta wings”. Experiments in Fluids 27 (3), pp. 262–272.
Menke, M. and Gursul, I. (1997). “Unsteady nature of leading edge vortices”. Physics of Fluids 9.10, pp. 2960–2966.
Menter, F. (1993). “Zonal two equation kw turbulence models for aerodynamic flows”. 23rd fluid dynamics, plasmadynamics, and lasers conference. Orlando, Florida.
Menter, F. (1994). “Two-equation eddy-viscosity turbulence models for engineering applications”. AIAA Journal 32 (8), pp. 1598–1605.

Menter, F. (1997). "Eddy Viscosity Transport Equations and Their Relation to the $k-\epsilon$ Model". Journal of Fluids Engineering 119 (4), pp. 876–884.

Menter, F. and Egorov, Y. (2010). "The Scale-Adaptive Simulation Method for Unsteady Turbulent Flow Predictions. Part 1: Theory and Model Description". Flow, Turbulence and Combustion 85 (1), pp. 113–138.

Menter, F., Matyushenko, A., and Lechner, R. (2020). "Development of a Generalized K-ω Two-Equation Turbulence Model". New Results in Numerical and Experimental Fluid Mechanics XII. Ed. by A. Dillmann, G. Heller, E. Krämer, C. Wagner, C. Tropea, and S. Jakirlić. Cham: Springer International Publishing, pp. 101–109.

Milano, M. and Koumoutsakos, P. (2002). "Neural network modeling for near wall turbulent flow". Journal of Computational Physics 182 (1), pp. 1–26.

Miller, D. and Wood, R. (1984). "Leeside flows over delta wings at supersonic speeds". Journal of Aircraft 21 (9), pp. 680–686.

Mitchell, A. and Délery, J. (2001). "Research into vortex breakdown control". Progress in Aerospace Sciences 37 (4), pp. 385–418.

Mitchell, A., Molton, P., Barberis, D., and Délery, J. (2000). "Characterization of vortex breakdown by flow field and surface measurements". 38th Aerospace Sciences Meeting and Exhibit. Reno, Nevada.

Mitchell, A., Morton, S., Forsythe, J., and Cummings, R. (2006). "Analysis of delta-wing vortical substructures using detached-eddy simulation". AIAA Journal 44 (5), pp. 964–972.

Moioli, M., Breitsamter, C., and Sørensen, K. (2018). "Turbulence model conditioning for vortex dominated flows based on experimental results". 31st Congress of the International Council of the Aeronautical Sciences, pp. 9–14.

Moioli, M., Breitsamter, C., and Sørensen, K. (2019). "Parametric data-based turbulence modelling for vortex dominated flows". International Journal of Computational Fluid Dynamics 33 (4), pp. 149–170.

Moioli, M., Breitsamter, C., and Sørensen, K. (2022). "Turbulence Modeling for Leading-Edge Vortices: An Enhancement Based on Experimental Data". AIAA Journal 60 (3), pp. 1382–1399.

Morton, S., Forsythe, J., Mitchell, A. M., and Hajek, D. (2002). "DES and RANS simulations of delta wing vortical flows". 40th AIAA Aerospace Sciences Meeting & Exhibit. Reno, Nevada.

Mühlenbein, H. and Schlierkamp-Voosen, D. (2005). "Analysis of selection, mutation and recombination in genetic algorithms". Evolution and Biocomputation: Computational Models of Evolution. Springer, pp. 142–168.

Müller, J. and Hummel, D. (1999). "An analysis of vortex breakdown predicted by a time-accurate Euler code". New Results in Numerical and Experimental Fluid Mechanics II: Contributions to the 11th AG STAB/DGLR Symposium Berlin, Germany 1998. Ed. by W. Nitsche, H.-J. Heinemann, and R. Hilbig. Wiesbaden: Vieweg+Teubner Verlag, pp. 331–338.

Murman, E. and Rizzi, A. (1986). "Applications of Euler equations to sharp edge delta wings with leading edge vortices". AGARD Applications of Computational Fluid Dynamics in Aeronautics.

Nagano, Y., Pei, C., and Hattori, H. (2000). "A new low-Reynolds-number one-equation model of turbulence". Flow, Turbulence and Combustion 63 (1-4), pp. 135–151.

NATO Science and Technology Organization (2018). Vortex Interaction Effects Relevant to Military Air Vehicle Performance. Accessed on 2024-03-18. URL: https://www.sto.nato.int/Lists/test1/activitydetails.aspx?ID=16476.

Nelson, R. and Pelletier, A. (2003). "The unsteady aerodynamics of slender wings and aircraft undergoing large amplitude maneuvers". Progress in Aerospace Sciences 39 (2-3), pp. 185–248.

Newsome, R. (1986). "Euler and Navier-Stokes solutions for flow over a conical delta wing". AIAA Journal 24 (4), pp. 552–561.

OpenAI (2024). Images inspired by the Eurofighter Typhoon, Concorde and Space Shuttle during Ascent. https://openai.com/dall-e. Generated by DALL · E. Accessed on 04.03.2024.

Parish, E. and Duraisamy, K. (2016). "A paradigm for data-driven predictive modeling using field inversion and machine learning". Journal of Computational Physics 305, pp. 758–774.

Parmee, I. (2012). Evolutionary and adaptive computing in engineering design. Springer Science & Business Media.

Parneix, S., Laurence, D., and Durbin, P. (1998). "A Procedure for Using DNS Databases". Journal of Fluids Engineering 120.1, pp. 40–47.

Payne, F., Ng, T., and Nelson, R. (1987). "Experimental study of the velocity field on a delta wing". 19th AIAA, Fluid Dynamics, Plasma Dynamics, and Lasers Conference.

Payne, F., Ng, T., Nelson, R., and Schiff, L. (1986). Visualization and flow surveys of the leading edge vortex structure on delta wing planforms. Reno, Nevada.

Pencheva, T., Atanassov, K., and Shannon, A. (2011). "Generalized nets model of offspring reinsertion in genetic algorithms". Annual of "Informatics" Section of the Union of Scientists in Bulgaria 4, pp. 29–35.

Peng, S.-H. and Jirasek, A. (2016). "Verification of RANS and hybrid RANS-LES modelling in computations of a delta-wing flow". 46th AIAA Fluid Dynamics Conference. Washington, D.C.

Pfnür, S. and Breitsamter, C. (2019). "Leading-edge vortex interactions at a generic multiple swept-wing aircraft configuration". Journal of Aircraft 56 (6), pp. 2093–2107.

Pohlheim, H. (2013). Evolutionäre Algorithmen: Verfahren, Operatoren und Hinweise für die Praxis. Springer-Verlag.

Polhamus, E. (1971). "Predictions of vortex-lift characteristics by a leading-edge suctionanalogy". Journal of Aircraft 8 (4), pp. 193–199.

Pope, S. B. (1975). "A more general effective-viscosity hypothesis". Journal of Fluid Mechanics 72 (2), pp. 331–340.

Pope, S. B. (2000). "Turbulent Flows, Cambridge University Press, Cambridge, UK". Combustion and Flame 125, pp. 1361–62.

Probst, A., Löwe, J., Reuß, S., Knopp, T., and Kessler, R. (2016). "Scale-resolving simulations with a low-dissipation low-dispersion second-order scheme for unstructured flow solvers". AIAA Journal 54 (10), pp. 2972–2987.

Probst, A. and Reuß, S. (2016). "Progress In Scale-Resolving Simulations with the DLR-TAU Code". Deutscher Luft- und Raumfahrtkongress. Braunschweig, Deutschland.

Rajkumar, K., Di Fabbio, T., Tangermann, E., and Klein, M. (2024). "Physical aspects of vortex-shock dynamics in delta wing configurations". Physics of Fluids 36 (6).

Rediniotis, O., Stapountzis, H., and Telionis, D. (1993). "Periodic vortex shedding over delta wings". AIAA Journal 31 (9), pp. 1555–1562.

Reif, B. P., Durbin, P., and Ooi, A. (1999). "Modeling rotational effects in eddy-viscosity closures". International journal of heat and fluid flow 20 (6), pp. 563–573.

Reissmann, M., Hasslberger, J., Sandberg, R., and Klein, M. (2021). "Application of gene expression programming to a-posteriori LES modeling of a Taylor Green vortex". Journal of Computational Physics 424.

Reynolds, O. (1895). "On the dynamical theory of incompressible viscous fluids and the determination of the criterion". Philosophical transactions of the royal society of London (186), pp. 123–164.

Riou, J., Garnier, E., and Basdevant, C. (2010). "Compressibility effects on the vortical flow over a 65 sweep delta wing". Physics of Fluids 22 (3).

Rizzi, A. and Eriksson, L.-E. (1985). "Computation of inviscid incompressible flow with rotation". Journal of Fluid Mechanics 153, pp. 275–312.

Rizzi, A., Jirásek, A., Lamar, J. E., Crippa, S., Badcock, K. J., and Boelens, O. J. (2009). "Lessons learned from numerical simulations of the F-16XL aircraft at flight conditions". Journal of Aircraft 46 (2), pp. 423–441.

Rizzi, A. and Müller, B. (1988). "Comparison of Euler and Navier-Stokes solutions for vortex flow over a delta wing". The Aeronautical Journal 92 (914), pp. 145–153.

Rizzi, A. and Purcell, C. (1987). "On the computation of transonic leading-edge vortices using the Euler equations". Journal of Fluid Mechanics 181, pp. 163–195.

Robinson, B., Barnett, R., and Agrawal, S. (1994). "Simple numerical criterion for vortex breakdown". AIAA Journal 32 (1), pp. 116–122.

Rumsey, C., Carlson, J., Pulliam, T., and Spalart, P. (2020a). "Improvements to the Quadratic Constitutive Relation Based on NASA Juncture Flow Data". AIAA Journal 58.

Rumsey, C., Lee, H., and Pulliam, T. (2020b). "Reynolds-Averaged Navier-Stokes Computations of the NASA Juncture Flow Model Using FUN3D and OVERFLOW". AIAA Scitech Forum.

Rumsey, C. and Coleman, G. (2022). NASA Symposium on Turbulence Modeling: Roadblocks, and the Potential for Machine Learning. Tech. rep.

Russel, A., Peshkin, D., Werner, M., and Eccleston, S. (2022). "Assessment of Hybrid Delta Wing Vortex Flow Investigation - Part II at Transonic Conditions". AIAA SciTech Forum. San Diego, California.

Sandberg, R., Tan, R., Weatheritt, J., Ooi, A., Haghiri, A., Michelassi, V., and Laskowski, G. (2018). "Applying machine learnt explicit algebraic stress and scalar flux models to a fundamental trailing edge slot". Journal of Turbomachinery 140 (10).

Schiavetta, L., Boelens, O., Crippa, S., Cummings, R., Fritz, W., and Badcock, K. (2009). "Shock effects on delta wing vortex breakdown". Journal of Aircraft 46 (3), pp. 903–914.

Schmitt, F. (Oct. 2007). "About Boussinesq's turbulent viscosity hypothesis: historical remarks and a direct evaluation of its validity". Comptes Rendus Mécanique 335.9-10, pp. 617–627.

Schoepplein, M., Weatheritt, J., Sandberg, R., Talei, M., and Klein, M. (2018). "Application of an evolutionary algorithm to LES modelling of turbulent transport in premixed flames". Journal of Computational Physics 374, pp. 1166–1179.

Schütte, A. and Werner, M. (2022). "Turbulence Model Effects on the Prediction of Transonic Vortex Interaction on a Multi-Swept Delta Wing". AIAA SciTech Forum. San Diego, California.

Schütte, A., Boelens, O., Oehlke, M., Jirásek, A., and Loeser, T. (2012a). "Prediction of the flow around the X-31 aircraft using three different CFD methods". Aerospace Science and Technology 20 (1), pp. 21–37.

Schütte, A., Hummel, D., and Hitzel, S. (2012b). "Flow physics analyses of a generic unmanned combat aerial vehicle configuration". Journal of Aircraft 49 (6), pp. 1638–1651.

Schütte, A. and Marini, R. (2020). "Computational Aerodynamic Sensitivity Studies for Generic Delta Wing Planforms". New Results in Numerical and Experimental Fluid Mechanics XII. Ed. by A. Dillmann, G. Heller, E. Krämer, C. Wagner, C. Tropea, and S. Jakirlić. Cham: Springer International Publishing, pp. 338–348.

Secretan, J., Beato, N., D'Ambrosio, D., Rodriguez, A., Campbell, A., Folsom-Kovarik, J., and Stanley, K. (2011). "Picbreeder: A case study in collaborative evolutionary exploration of design space". Evolutionary Computation 19 (3), pp. 373–403.

Seifert, J. (2012). "SAGITTA-Nationale Forschungskooperation für fortschrittliche UAV-Technologien im Rahmen der Open Innovation Initiative von Cassidian". 61th Deutscher Luft-und Raumfahrtkongress.

Shan, H., Jiang, L., and Liu, C. (2000). "Direct numerical simulation of three-dimensional flow around a delta wing". 38th Aerospace Sciences Meeting and Exhibit. Reno, Nevada.

Shih, T.-H. (1997). Modeling of turbulent swirling flows. National Aeronautics and Space Administration, Lewis Research Center, Institute for Computational Mechanics in Propulsion.

Shur, M., Strelets, M., Travin, A., and Spalart, P. (2000). "Turbulence modeling in rotating and curved channels: assessing the Spalart-Shur correction". AIAA Journal 38 (5), pp. 784–792.

Shur, M., Spalart, P., Strelets, M., and Travin, A. (2008). "A hybrid RANS-LES approach with delayed-DES and wall-modelled LES capabilities". International Journal of Heat and Fluid Flow 29.6, pp. 1638–1649.

Singh, A. P., Medida, S., and Duraisamy, K. (2017). "Machine-learning-augmented predictive modeling of turbulent separated flows over airfoils". AIAA Journal 55 (7), pp. 2215–2227.

Smirnov, P. and Menter, F. (2009). "Sensitization of the SST Turbulence Model to Rotation and Curvature by Applying the Spalart–Shur Correction Term". Journal of Turbomachinery 131 (4).

Spalart, P. and Bogue, D. (2003). "The role of CFD in aerodynamics, off-design". The Aeronautical Journal 107 (1072), pp. 323–329.

Spalart, P. (1997). "Comments on the Feasibility of LES for Wings and on the Hybrid RANS/LES Approach". Proceedings of the First AFOSR International Conference on DNS/LES, 1997, pp. 137–147.

Spalart, P. (2000). “Strategies for turbulence modelling and simulations”. International Journal of Heat and Fluid Flow 21 (3), pp. 252–263.

Spalart, P. and Allmaras, S. (1992). “A one-equation turbulence model for aerodynamic flows”. 30th aerospace sciences meeting and exhibit. Reno, Nevada, p. 439.

Spalart, P., Deck, S., Shur, M., Squires, K., Strelets, M., and Travin, A. (2006). “A new version of detached-eddy simulation, resistant to ambiguous grid densities”. Theoretical and computational fluid dynamics 20, pp. 181–195.

Spall, R. E., Gatski, T. B., and Grosch, C. E. (1987). “A criterion for vortex breakdown”. The Physics of fluids 30 (11), pp. 3434–3440.

Srigrarom, S. and Kurosaka, M. (2000). “Shaping of delta-wing planform to suppress vortex breakdown”. AIAA Journal 38 (1), pp. 183–186.

Stabnikov, A. and Garbaruk, A. (2016). “Testing of modified curvature-rotation correction for k-ω SST model”. 769 (1).

Stanbrook, A. and Squiref, L. (1964). “Possible types of flow at swept leading edges”. Aeronautical Quarterly 15 (1), pp. 72–82.

Suddul, G., Dookhitram, K., Bekaroo, G., and Shankhur, N. (2020). “An Evolutionary MultiLayer Perceptron Algorithm for Real Time River Flood Prediction”. 2020 Zooming Innovation in Consumer Technologies Conference, pp. 109–112.

Tangermann, E., Furman, A., and Breitsamter, C. (2012). “Detached Eddy Simulation compared with Wind Tunnel Results of a Delta Wing with Sharp Leading Edge and Vortex Breakdown”. 30th AIAA Applied Aerodynamics Conference. New Orleans, Louisiana.

Towfighi, J. and Rockwell, D. (1993). “Instantaneous structure of vortex breakdown on a delta wing via particle image velocimetry”. AIAA Journal 31 (6), pp. 1160–1162.

Tracey, B., Duraisamy, K., and Alonso, J. (2015). “A machine learning strategy to assist turbulence model development”. 53rd AIAA aerospace sciences meeting. Kissimmee, Florida.

Tsinober, A. (2001). An informal introduction to turbulence. Springer Science & Business Media.

Ursem, R. K. (2002). “Diversity-guided evolutionary algorithms”. International Conference on Parallel Problem Solving from Nature. Springer, pp. 462–471.

Visbal, M. (1996). “Computed unsteady structure of spiral vortex breakdown on delta wings”. Fluid Dynamics Conference. New Orleans, LA.

Visbal, M. and Gaitonde, D. (1999). “High-order-accurate methods for complex unsteady subsonic flows”. AIAA Journal 37 (10), pp. 1231–1239.

Visbal, M. and Gordnier, R. (2003). “On the structure of the shear layer emanating from a swept leading edge at angle of attack”. 33rd AIAA fluid dynamics conference and exhibit. Orlando, Florida.

Wang, J.-X., Huang, J., Duan, L., and Xiao, H. (2019). “Prediction of Reynolds stresses in high-Mach-number turbulent boundary layers using physics-informed machine learning”. Theoretical and Computational Fluid Dynamics 33, pp. 1–19.

Wang, J.-X., Wu, J.-L., and Xiao, H. (2017). “Physics-informed machine learning approach for reconstructing Reynolds stress modeling discrepancies based on DNS data”. Physical Review Fluids 2 (3).

Weatheritt, J. and Sandberg, R. (2015). "Use of Symbolic Regression for construction of Reynolds-stress damping functions for Hybrid RANS/LES". 53rd AIAA Aerospace Sciences Meeting. Kissimmee, Florida.

Weatheritt, J. and Sandberg, R. (2016). "A novel evolutionary algorithm applied to algebraic modifications of the RANS stress–strain relationship". Journal of Computational Physics 325, pp. 22–37.

Weatheritt, J. and Sandberg, R. (2017). "The development of algebraic stress models using a novel evolutionary algorithm". International Journal of Heat and Fluid Flow 68, pp. 298–318.

Wentz, W. and Kohlman, D. (1971). "Vortex breakdown on slender sharp-edged wings". Journal of Aircraft 8 (3), pp. 156–161.

White, F. and Majdalani, J. (2006). Viscous fluid flow. Vol. 3. McGraw-Hill New York.

Wilcox, D. (1988). "Reassessment of the scale-determining equation for advanced turbulence models". AIAA Journal 26 (11), pp. 1299–1310.

Wilcox, D. (1998). Turbulence modeling for CFD. La Canada, California: DCW Indust.

Wilcox, D. (2001). "Turbulence modeling-an overview". 39th Aerospace Sciences Meeting and Exhibit. Reno, Nevada.

Wilsby, O. and Sandberg, R. (2019). "Data-Driven RANS Closures for Trailing Edge Noise Predictions". 25th AIAA/CEAS Aeroacoustics Conference. Delft, The Netherlands.

Wray, T. and Agarwal, R. (2015). "Low-Reynolds-Number One-Equation Turbulence Model Based on k–ω Closure". AIAA Journal 53 (8), pp. 2216–2227.

Wu, J.-L., Xiao, H., and Paterson, E. (2018). "Physics-informed machine learning approach for augmenting turbulence models: A comprehensive framework". Physical Review Fluids 3 (7).

Xu, X., Waschkowski, F., Ooi, A., and Sandberg, R. (2022). "Towards robust and accurate Reynolds-averaged closures for natural convection via multi-objective CFD-driven machine learning". International Journal of Heat and Mass Transfer 187.

Zaharie, D. (2009). "Influence of crossover on the behavior of differential evolution algorithms". Applied Soft Computing 9 (3), pp. 1126–1138.

Zanin, B. Y. (2013). Flow topology on a delta wing at a high angle of attack. Modified by the author. This work is licensed under the Creative Commons Attribution 4.0 International License. To view a copy of this license, visit `https://creativecommons.org/licenses/by-sa/4.0/`.

Zhang, W., Ma, Z., Yu, Y., and Chen, H. (2010). "Applied new rotation correction κ–ω SST model for turbulence simulation of centrifugal impeller in the rotating frame of reference". Journal of Hydrodynamics 22 (5), pp. 404–407.

Zhang, X. and Agarwal, R. (2018). "Development of Various Rotation and Curvature Corrections for Eddy-Viscosity Turbulence Models". 2018 AIAA Aerospace Sciences Meeting. Kissimmee, Florida.

Zhang, Z., Ye, S., Yin, B., Song, X., Wang, Y., Huang, C., and Chen, Y. (2021). "A semi-implicit discrepancy model of Reynolds stress in a higher-order tensor basis framework for Reynolds-averaged Navier–Stokes simulations". AIP Advances 11 (4).

Zhang, Z. and Duraisamy, K. (2015). "Machine learning methods for data-driven turbulence modeling". 22nd AIAA computational fluid dynamics conference. Dallas, Texas.

Zhao, Y., Akolekar, H., Weatheritt, J., Michelassi, V., and Sandberg, R. (2020). "RANS turbulence model development using CFD-driven machine learning". Journal of Computational Physics 411.

Zhou, B., Diskin, B., Gauger, N., Pardue, J., Chernikov, A., Tsolakis, C., Drakopoulos, F., and Chrisochoides, N. (2019). "Hybrid RANS/LES simulation of vortex breakdown over a delta wing". AIAA Aviation Forum. Dallas, Texas.

Zhu, L., Zhang, W., Kou, J., and Liu, Y. (2019). "Machine learning methods for turbulence modeling in subsonic flows around airfoils". Physics of Fluids 31 (1).

Zhu, L., Zhang, W., and Tu, G. (2022). "Generalization enhancement of artificial neural network for turbulence closure by feature selection". Advances in Aerodynamics 4 (1), pp. 1–24.

A

Implementation-Ready Turbulence Models

A.1. Boussinesq Extension Models

A.1.1. The PK Model

An enhancement to the Boussinesq approximation within the SA model framework is proposed, introducing a modification termed the PK (production of turbulent kinetic energy) model.

The Boussinesq assumption is extended to include the isotropic term, proposing a new formulation for the turbulent kinetic energy, k_{SA}, within the SA turbulence model:

$$-\rho\overline{u_i' u_j'} = \tau_{ij}^R = 2\mu_t S_{ij}^* - k_{SA}\delta_{ij}, \tag{A.1}$$

where

$$k_{SA} = C_k \mu_t \sqrt{2W_{mn}W_{mn}}. \tag{A.2}$$

The coefficient C_k is calibrated through empirical analysis, with a recommended value of 3.

A.1.2. Extra-Anisotropic Reynolds Stress Model

EARSMs refine the traditional Boussinesq hypothesis by incorporating an anisotropic stress component, a_{ij}, into the Reynolds stress tensor:

$$\tau_{ij}^R = \frac{2}{3}\rho k\delta_{ij} - 2\mu_t S_{ij}^* + a_{ij}. \tag{A.3}$$

This anisotropic component a_{ij} is represented in dimensionless form as follows

$$a_{ij}^* = \sum_k f^{(k)}(I_1, I_2, \ldots, I_n) V_{ij}^k. \tag{A.4}$$

The functions $f^{(k)}$ are optimized using GEP based on training datasets. Since, the application of 3 fundamental basis tensors alongside 2 invariants constitutes the standard methodology for analyzing 2D flows, the basis tensors V_{ij}^k and invariants I_n are

expressed as

$$V_{ij}^1 = s_{ij}, \quad V_{ij}^2 = s_{ik}\omega_{kj} - \omega_{ik}s_{kj}, \quad V_{ij}^3 = s_{ik}s_{kj} - \frac{1}{3}\delta_{ij}s_{mn}s_{mn}, \\ I_1 = s_{mn}s_{mn}, \quad I_2 = \omega_{mn}\omega_{mn}. \tag{A.5}$$

The tensors and invariants originate from the dimensionless strain rate tensor $s_{ij} = t_l S_{ij}^*$ and rotation rate tensor $\omega_{ij} = t_l W_{ij}$. The turbulence timescale t_l is computed as

$$t_l = \frac{1}{\sqrt{\frac{\partial u_m}{\partial x_n}\frac{\partial u_m}{\partial x_n}}}, \tag{A.6}$$

and the dimensionalized anisotropic stress tensor a_{ij} is derived as

$$a_{ij} = \frac{2\mu_t a_{ij}^*}{t_l}, \tag{A.7}$$

leading to the modified Reynolds stress tensor

$$\tau_{ij}^R = \frac{2}{3}\rho k\delta_{ij} - 2\mu_t\left(S_{ij}^* - \frac{a_{ij}^*}{t_l}\right). \tag{A.8}$$

The formulation of a_{ij}^* is presented in Chapter 8.

A.2. RANS Turbulence Models

A.2.1. Spalart-Allmaras

SA formulation for free shear flows.

$$\frac{\partial \nu_t}{\partial t} + u_j\frac{\partial \nu_t}{\partial x_j} = c_{b1}S\nu_t + \frac{1}{\sigma}\left[\frac{\partial}{\partial x_j}\left(\nu_t\frac{\partial \nu_t}{\partial x_j}\right) + c_{b2}\frac{\partial \nu_t}{\partial x_i}\frac{\partial \nu_t}{\partial x_i}\right]. \tag{A.9}$$

SA formulation for wall-bounded flows.

$$\frac{\partial \tilde{\nu}}{\partial t} + u_j\frac{\partial \tilde{\nu}}{\partial x_j} = c_{b1}\left(1 - f_{t2}\right)\tilde{S}\tilde{\nu} - \left[c_{w1}f_w - \frac{c_{b1}}{\kappa^2}f_{t2}\right]\left(\frac{\tilde{\nu}}{d}\right)^2 + \frac{1}{\sigma}\left[\frac{\partial}{\partial x_j}\left(\left(\nu + \tilde{\nu}\right)\frac{\partial \tilde{\nu}}{\partial x_j}\right) + c_{b2}\frac{\partial \tilde{\nu}}{\partial x_i}\frac{\partial \tilde{\nu}}{\partial x_i}\right], \tag{A.10}$$

with

$$c_{b1} = 0.1355, \quad \sigma = \frac{2}{3}, \quad c_{b2} = 0.622, \quad \kappa = 0.41, \\ c_{w1} = \frac{c_{b1}}{\kappa^2} + \frac{1 + c_{b2}}{\sigma}, \quad c_{w2} = 0.3, \quad c_{w3} = 2.0, \\ c_{v1} = 7.1, \quad c_{t3} = 1.1, \quad c_{t4} = 0.5. \tag{A.11}$$

A non-dimensional smoothing function f_ω, based on the dimensionless mixing length,

$$r = \frac{\nu_t}{S\kappa^2 d^2}, \tag{A.12}$$

is applied to the destruction factor. The function is defined as follows

$$f_\omega(r) = g\left[\frac{1+c_{\omega3}^6}{g^6+c_{\omega3}^6}\right]^{\frac{1}{6}}, \quad \text{where} \quad g = r + c_{\omega2}(r^6 - r). \tag{A.13}$$

A smoothing function f_{v1} is applied as follows

$$\nu_t = \tilde{\nu} f_{v1}, \quad \text{where} \quad f_{v1} = \frac{\chi^3}{\chi^3 + c_{v1}^3} \quad \text{with} \quad \chi = \frac{\tilde{\nu}}{\nu}. \tag{A.14}$$

$\tilde{S}$ is expressed as follows

$$\tilde{S} = S + \frac{\tilde{\nu}}{\kappa^2 d^2} f_{v2}, \quad \text{with} \quad f_{v2} = 1 - \frac{\chi}{1+\chi f_{v1}}. \tag{A.15}$$

The function f_{t2} is formulated as follows

$$f_{t2} = c_{t3} \exp\left(-c_{t4}\chi^2\right). \tag{A.16}$$

For compressible flow simulations, additional compressibility corrections are introduced, exemplified by

$$C_{\tilde{\nu}} = -\frac{1}{\sigma}(\nu + \tilde{\nu})\frac{\partial \rho}{\partial x_k}\frac{\partial \tilde{\nu}}{\partial x_k} \tag{A.17}$$

Consequently, the **compressibility-corrected SA** equation is expressed as

$$\begin{aligned}\frac{\partial(\rho\tilde{\nu})}{\partial t} + \frac{\partial(\rho\tilde{\nu}u_j)}{\partial x_j} = {} & c_{b1}(1-f_{t2})\tilde{S}\rho\tilde{\nu} - \left[c_{w1}f_w - \frac{c_{b1}}{\kappa^2}f_{t2}\right]\rho\left(\frac{\tilde{\nu}}{d}\right)^2 \\ & + \frac{1}{\sigma}\left[\frac{\partial}{\partial x_j}\left(\rho(\nu+\tilde{\nu})\frac{\partial\tilde{\nu}}{\partial x_j}\right) + c_{b2}\rho\frac{\partial\tilde{\nu}}{\partial x_i}\frac{\partial\tilde{\nu}}{\partial x_i}\right] \\ & - \frac{1}{\sigma}(\nu+\tilde{\nu})\frac{\partial\rho}{\partial x_k}\frac{\partial\tilde{\nu}}{\partial x_k}.\end{aligned} \tag{A.18}$$

The SA model with negative eddy viscosity correction (**SAneg**) is expressed as

$$\frac{\partial\tilde{\nu}}{\partial t} + u_j\frac{\partial\tilde{\nu}}{\partial x_j} = c_{b1}(1-c_{t3})\Omega\tilde{\nu} + c_{w1}f_w\left(\frac{\tilde{\nu}}{d}\right)^2 + \frac{1}{\sigma}\left[\frac{\partial}{\partial x_j}\left((\nu+\tilde{\nu}f_n)\frac{\partial\tilde{\nu}}{\partial x_j}\right) + c_{b2}\frac{\partial\tilde{\nu}}{\partial x_i}\frac{\partial\tilde{\nu}}{\partial x_i}\right], \tag{A.19}$$

with

$$f_n = \frac{c_{n1}+\chi^3}{c_{n1}-\chi^3} \qquad \text{and} \qquad c_{n1} = 16. \tag{A.20}$$

The coefficient c_{t3} is set at 1.2.

The SA model with a streamline curvature correction (**SA-RC**), modifying the production term with a rotation function as follows

$$f_{r1} = (1+c_{r1})\frac{2r^*}{1+r^*}\left[1 - c_{r3}tan^{-1}(c_{r2}\tilde{r})\right] - c_{r1}. \tag{A.21}$$

Specifically, the first term on the RHS of the SA-RC equation is given by

$$c_{b1}(f_{r1} - f_{t2})\hat{S}\hat{\nu}. \tag{A.22}$$

The various terms are defined as follows

$$\begin{aligned}
&r^* = \frac{S}{\omega}, \qquad \tilde{r} = \frac{2\omega_{ik}S_{jk}}{D^4}\left(\frac{DS_{ij}}{Dt} + (\varepsilon_{imn}S_{jn} + \varepsilon_{jmn}S_{in})\Omega'_m\right),\\
&S_{ij} = \frac{1}{2}\left(\frac{\partial u_i}{\partial x_j} + \frac{\partial u_j}{\partial x_i}\right), \qquad \omega_{ij} = \frac{1}{2}\left[\left(\frac{\partial u_i}{\partial x_j} - \frac{\partial u_j}{\partial x_i}\right) + 2\varepsilon_{mji}\Omega'_m\right],\\
&S^2 = 2S_{ij}S_{ij}, \qquad \omega^2 = 2\omega_{ij}\omega_{ij}, \qquad D^2 = \frac{1}{2}\left(S^2 + \omega^2\right),\\
&c_{r1} = 1.0, \qquad c_{r2} = 12, \qquad c_{r3} = 1.0.
\end{aligned} \tag{A.23}$$

A.2.2. Menter $k-\omega$ Shear Stress Transport

The transport equation for turbulent kinetic energy is given by

$$\frac{\partial(\rho k)}{\partial t} + \frac{\partial(\rho k u_j)}{\partial x_j} = P_k - \beta^k \rho\omega k + \frac{\partial}{\partial x_j}\left[(\mu + \sigma_k\mu_t)\frac{\partial k}{\partial x_j}\right]. \tag{A.24}$$

Similarly, the transport equation for the dissipation rate is expressed as

$$\frac{\partial(\rho\omega)}{\partial t} + \frac{\partial(\rho\omega u_j)}{\partial x_j} = \frac{\gamma_\omega\omega}{k}P_k - \beta^\omega\rho\omega^2 + \frac{\partial}{\partial x_j}\left[(\mu + \sigma_\omega\mu_t)\frac{\partial\omega}{\partial x_j}\right] + \frac{\rho\sigma_d}{\omega}\frac{\partial k}{\partial x_j}\frac{\partial\omega}{\partial x_j}. \tag{A.25}$$

The turbulent eddy viscosity is given by

$$\mu_t = \frac{\rho k}{\omega}, \tag{A.26}$$

and the turbulence production term $P_{k\omega}$ is defined as

$$P_k = \tau_{ij}^R\frac{\partial u_i}{\partial x_j}, \tag{A.27}$$

where the Reynolds stress tensor τ_{ij}^R is evaluated using the Boussinesq assumption.

Menter Baseline. Menter's Baseline model combines the $k-\omega$ model for near-wall regions with the $k-\varepsilon$ model for the free-stream. The transition between these models is smoothly handled by blending the closure coefficients ϕ (where ϕ represents the set $\{\beta_k, \beta_\omega, \gamma_\omega, \sigma_k, \sigma_\omega, \sigma_d\}$) using the blending function F_1:

$$\phi = F_1\phi^{(i)} + (1 - F_1)\phi^{(o)}, \tag{A.28}$$

where $F_1 = \tanh(G_1^4)$ and G_1 is calculated using:

$$G_1 = \min\left[\max\left(\Gamma_1, \Gamma_2\right), \Gamma_3\right]. \tag{A.29}$$

The arguments are defined as

$$\Gamma_1 = \frac{\sqrt{k}}{0.09\omega d}, \qquad \Gamma_2 = \frac{500\mu}{\rho\omega d^2}, \qquad \Gamma_3 = \frac{2\sigma_d^{(o)} k}{\mathrm{CD}_\omega^{(o)} d^2}, \tag{A.30}$$

with

$$\mathrm{CD}_\omega^{(o)} = \max\left(\sigma_d^{(o)} \frac{\rho}{\omega} \frac{\partial k}{\partial x_j} \frac{\partial \omega}{\partial x_j}, 10^{-20}\right). \tag{A.31}$$

Menter SST. The SST model is an extension of the BSL model, improving its response to adverse pressure gradients and flow separation by modifying the eddy viscosity μ_t:

$$\mu_t = \frac{\rho a_1 k}{\max(a_1\omega, \Omega F_2)}, \tag{A.32}$$

where $a_1 = 0.31$ and $F_2 = \tanh(G_2^2)$ with $G_2 = \max(2\Gamma_1, \Gamma_2)$.

The standard values for the constants in the Menter SST model are:

$$\gamma = 0.553, \quad \beta = 0.075, \quad \beta^* = 0.09, \quad \sigma_k = 0.85, \quad \sigma_{\omega 1} = 0.5, \quad \sigma_{\omega 2} = 0.856 \tag{A.33}$$

A.2.3. Spalart-Allmaras with trained Production and Destruction

The modified equation, henceforth referred to as SA+PD, is proposed as follows

$$\frac{\partial \tilde{\nu}}{\partial t} + u_j \frac{\partial \tilde{\nu}}{\partial x_j} = C_P \tilde{S} \tilde{\nu} - C_D \left(\frac{\tilde{\nu}}{d}\right)^2 + \frac{1}{\sigma}\left[\frac{\partial}{\partial x_j}\left((\nu + \tilde{\nu})\frac{\partial \tilde{\nu}}{\partial x_j}\right) + c_{b2}\frac{\partial \tilde{\nu}}{\partial x_i}\frac{\partial \tilde{\nu}}{\partial x_i}\right], \tag{A.34}$$

where the coefficients $C_P(I_1, I_2)$ and $C_D(I_1, I_2)$ are functions of invariants I_1 and I_2, and are optimized using GEP based on training datasets. The formulations of C_P and C_D are presented in Chapter 8.

A.2.4. Coupled Spalart-Allmaras

The enhanced model, denoted as CSA, is written as follows

$$\frac{D\tilde{\nu}}{Dt} = 2c_{b1} t_l S_{ij}^* \frac{\partial u_i}{\partial x_j}\tilde{\nu} - c_{w1} f_w \tilde{D}\tilde{\nu} + \frac{1}{\sigma}\left[\frac{\partial}{\partial x_j}\left((\nu + \tilde{\nu})\frac{\partial \tilde{\nu}}{\partial x_j}\right) + c_{b2}\frac{\partial \tilde{\nu}}{\partial x_i}\frac{\partial \tilde{\nu}}{\partial x_i}\right]. \tag{A.35}$$

The original coefficient formulations from the SA model have been successfully tested, demonstrating the balanced and well-constructed nature of the new equation.

The dynamic adjustment of the destruction term, enabling it to accurately represent both near-wall and free-stream behaviors, is obtained through the following expression:

$$\tilde{D} = \frac{\tilde{\nu}}{d^2} - f_d \cdot \min\left(\frac{\tilde{\nu}}{d^2} - \sqrt{\beta^*}|S_{ij}|^2 t_l, 0\right), \tag{A.36}$$

where the shielding function f_d is defined as

$$f_d = 1 - \tanh\left((8r_d)^3\right), \quad \text{with} \quad r_d = \frac{\mu + \mu_t}{\rho(\kappa d^2)\max\left[\sqrt{\frac{\partial u_i}{\partial x_j}\frac{\partial u_i}{\partial x_j}}, 10^{-10}\right]}. \tag{A.37}$$

Here, $\beta^* = 0.09$, and $|S_{ij}| = \sqrt{2S_{ij}S_{ij}}$ represents the magnitude of the strain rate tensor. Besides, the turbulence timescale t_l is computed as

$$t_l = \frac{1}{\sqrt{\frac{\partial u_m}{\partial x_n}\frac{\partial u_m}{\partial x_n}}}. \tag{A.38}$$

A.2.5. Coupled Spalart-Allmaras with trained extra-anisotropy

The new CSA one-equation turbulence model is coupled with the optimization of τ_{ij}^R by modeling the Reynolds stress anisotropy. The modeled a_{ij} is also included in the new turbulence production term which thus becomes

$$P = 2c_{b1}\left(S_{ij}^* t_l - a_{ij}^*\right)\frac{\partial u_i}{\partial x_j}\tilde{\nu}. \tag{A.39}$$

The CSA+a_{ij} turbulence model equation then reads

$$\frac{D\tilde{\nu}}{Dt} = 2c_{b1}\left(S_{ij}^* t_l - a_{ij}^*\right)\frac{\partial u_i}{\partial x_j}\tilde{\nu} - c_{w1}f_w\tilde{D}\tilde{\nu} + \frac{1}{\sigma}\left[\frac{\partial}{\partial x_j}\left((\nu + \tilde{\nu})\frac{\partial\tilde{\nu}}{\partial x_j}\right) + c_{b2}\frac{\partial\tilde{\nu}}{\partial x_i}\frac{\partial\tilde{\nu}}{\partial x_i}\right]. \tag{A.40}$$

The formulation of a_{ij}^* is presented in Chapter 8.

A.3. Hybrid RANS/LES Turbulence Models

A.3.1. SA-based Improved Delayed Detached Eddy Simulation

DES integrates LES modeling in regions distant from wall boundaries while transitioning to RANS modeling in near-wall boundary layer regions. For integrating the SA model within the DES framework to exhibit both URANS and LES behavior, the distance d is replaced with a modified distance $\widetilde{d}$, defined as

$$\widetilde{d}_{DES} \equiv \min\left[d, \Delta_{DES}\right], \quad \text{with} \quad \Delta_{DES} = C_{DES}\Psi\Delta. \tag{A.41}$$

Here, C_{DES} is a constant set to 0.65 as recommended for homogeneous turbulence conditions, and Ψ is a low Reynolds number correction.

In the **DDES** model, the hybrid length scale, $\widetilde{d}$, becomes

$$\widetilde{d}_{DDES} \equiv d - f_d\max\left[0, d - \Delta_{DES}\right], \tag{A.42}$$

where the shielding function f_d is defined as

$$f_d = 1 - \tanh\left((8r_d)^3\right), \quad \text{with} \quad r_d = \frac{\mu + \mu_t}{\rho(\kappa d^2)\max\left[\sqrt{\frac{\partial u_i}{\partial x_j}\frac{\partial u_i}{\partial x_j}}, 10^{-10}\right]}. \tag{A.43}$$

The **WMLES** branch of the IDDES is designed to activate only under specific conditions. It employs the hybrid length scale, $\widetilde{d}_{WMLES}$, defined as follows

$$\widetilde{d}_{WMLES} = f_\beta(1 + f_e)d + (1 - f_\beta)\Delta_{DES}. \tag{A.44}$$

Here, f_β, the empirical blending function, is expressed as

$$f_\beta = \min\left[2\exp\left(-9\alpha^2\right), 1\right], \quad \text{with} \quad \alpha = 0.25 - \frac{d}{\Delta}. \tag{A.45}$$

The secondary empirical function, f_e, is defined as

$$f_e = \max\left[(f_{e1} - 1), 0\right]\Psi f_{e2}, \tag{A.46}$$

where f_{e_1} and f_{e2} are given by

$$\begin{aligned} f_{e_1} &= \begin{cases} 2\exp(-11.09\alpha^2), & \text{if } \alpha \geq 0 \\ 2\exp(-9.0\alpha^2), & \text{if } \alpha < 0 \end{cases} \\ f_{e_2} &= 1 - \max\left[\tanh\{(c_t^2 r_{d_t})^3\}, \tanh\{(c_l^2 r_{d_l})^{10}\}\right]. \end{aligned} \tag{A.47}$$

Here, Ψ represents an optional low Reynolds number correction, while r_{d_t} and r_{d_l} denote the turbulent and laminar portions of the r_d parameter. The constants $c_t = 1.63$ and $c_l = 3.55$ are effective with the SA model.

A modified DDES length scale expression allows for blending in a manner that guarantees the realization of the desired branch, contingent on the presence of resolved turbulent content within the boundary layer, as follows

$$\widehat{d}_{DDES} = \widetilde{f}_d d + (1 - \widetilde{f}_d)\Delta_{DES}, \tag{A.48}$$

where

$$\widetilde{f}_d = \max\left[1 - f_{d_t}, f_\beta\right], \quad f_{d_t} = 1 - \tanh\left[(8r_{d_t})^3\right]. \tag{A.49}$$

This functional replacement for the DDES length scale essentially facilitates the blending of the DDES and WMLES length scale definitions through the following expression:

$$\widetilde{d}_{IDDES} = \widetilde{f}_d(1 + f_e)d + (1 - \widetilde{f}_d)\Delta_{IDDES}. \tag{A.50}$$

The IDDES hybrid length scale ensures the desired WMLES behavior in simulations containing resolved turbulent content within the boundary layer.

Additionally, the DES filter width in the IDDES formulation is explicitly modified to include the wall distance, d, as follows

$$\Delta_{IDDES} = \min\left\{\max\left[C_w d, C_w\Delta, \Delta_n\right], \Delta\right\}, \qquad \text{with} \qquad C_w = 0.15. \tag{A.51}$$

Here, Δ_n denotes the grid spacing in the wall-normal direction, which can be ambiguous for complex geometries with multiple walls.

A.3.2. $k\omega$-based Scale Adaptive Simulation

SAS's turbulence model incorporates an additional source term or function, Q_{SAS}, into the turbulence dissipation rate Eq. A.25 that responds to locally resolved turbulence. This term is mathematically expressed as

$$Q_{SAS} = \max\left[\rho\zeta_2 S^2\left(\frac{L_m}{L_{vK}}\right)^2 - F_{SAS}\frac{2\rho k}{\sigma_\phi}\max\left(\frac{1}{k^2}\frac{\partial k}{\partial x_j}\frac{\partial k}{\partial x_j}, \frac{1}{\omega^2}\frac{\partial \omega}{\partial x_j}\frac{\partial \omega}{\partial x_j}\right), 0\right], \tag{A.52}$$

with $\zeta_2 = 1.755$, $\sigma_\phi = \frac{2}{3}$, and $F_{SAS} = 1.25$. The length L_m is defined as follows

$$L_m = c_\mu^{-\frac{1}{4}}\frac{\sqrt{k}}{\omega}, \tag{A.53}$$

with $c_\mu = 0.09$ and $\kappa = 0.41$. The von Kármán length scale, $L_{\nu K}$, is defined as

$$L_{\nu K} = \kappa\frac{U'}{U''}, \quad \text{where} \quad U' = \sqrt{2S_{ij}S_{ij}} \quad \text{and} \quad U'' = \sqrt{\frac{\partial^2 u_i}{\partial x_k^2}\frac{\partial^2 u_i}{\partial x_j^2}}. \tag{A.54}$$